

NASA Contractor Report 145217-1

(NASA-CR-145217-App-1) WIND TUNNEL
INVESTIGATION OF ROTOR LIFT AND PROPULSIVE
FORCE AT HIGH SPEED: DATA ANALYSIS (Boeing
Vertol Co., Philadelphia, Pa.) 211 p
HC A13/MF A11

N78-10020

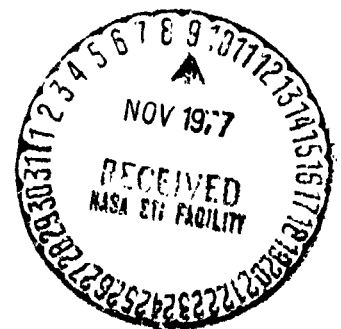
Unclas
CSCL D1A 33/02 51963

Wind Tunnel Investigation of Rotor Lift and Propulsive Force at High Speed Data Analysis

Frank McHugh
Ross Clark
Mary Solomon

CONTRACT NAS1-14317
OCTOBER 1977

NASA
National Aeronautics and
Space Administration
Langley Research Center
Hampton, Virginia 23665





**Wind Tunnel Investigation of
Rotor Lift and Propulsive Force
at High Speed
Data Analysis**

**Frank McHugh
Ross Clark
Mary Soloman**

October 1977

**Prepared Under Contract No. NAS 1-14317
for**

**National Aeronautics and Space Administration
Langley Research Center
by**

BOEING VERTOL COMPANY
A DIVISION OF THE BOEING COMPANY

**P.O. BOX 16858
PHILADELPHIA, PENNSYLVANIA 19142**

D210-11135-1

TABLE OF CONTENTS

	<u>PAGE</u>
ABSTRACT	iv
FOREWORD	v
LIST OF FIGURES	vi
LIST OF TABLES	xiv
NOMENCLATURE	xv
1.0 SUMMARY	1
2.0 INTRODUCTION	27
3.0 MODEL DESCRIPTION AND INSTRUMENTATION	29
3.1 Test Stand	29
3.2 Model Details	29
3.3 Instrumentation	35
4.0 DATA REDUCTION	39
5.0 TEST PROGRAM	46
5.1 Objectives	46
5.2 Test Procedures	47
5.3 Test Operating Conditions	49
5.4 Run Log	49
6.0 TEST DATA ANALYSIS	54
6.1 Lift and Propulsive Force Limits	55
6.2 Blade Load Growth Approaching Limits	74
6.3 Cruise Rotor Performance	109
6.4 Rotor Control Power in Proximity of Stall	133
6.5 Advancing Tip Mach Number Effects on Limits	144
6.6 Blade Flapping Response	147
6.7 Rotor Operation in Stall	148
6.8 Model Configuration Performance	162
6.9 Correlation of Theory with Test Data	171
6.10 Effect of Torsional Stiffness on High Advance Ratio Characteristics	181
7.0 CONCLUSIONS	188
8.0 RECOMMENDATIONS	192

1

ABSTRACT

This document presents the basic test data obtained during the Lift-Propulsive Force Limit Wind Tunnel Test conducted during 1976 at the Boeing Vertol Wind Tunnel. Included are the rotor control positions, blade loads and six components of rotor force and moment, corrected for hub tares. Performance and blade loads are presented as the rotor lift limit is approached at fixed levels of rotor propulsive force coefficients and rotor tip speeds. Performance and blade load trends are presented for fixed levels of rotor lift coefficient as propulsive force is increased to the maximum obtainable by the model rotor. Test data is also included that defines the effect of stall proximity on rotor control power. The analysis of the data is presented in Volume I and the basic test data plots are presented in Volumes II and III.

FOREWORD

This report was prepared by the Boeing Vertol Company for the National Aeronautics and Space Administration, Langley Research Center, under NASA contract NAS1-14317. It presents the test data and analysis from the Lift-Propulsive Force Limit Wind Tunnel Test. The analysis of the data establishes the useful flight envelope and the characteristics of a conventional rotor in high speed flight. The results are presented in three volumes:

- 1 Wind Tunnel Investigation of Rotor Lift and
Propulsive Force Limits at High Speed -
- Data Analysis -
- 2 Wind Tunnel Investigation of Rotor Lift and
& -3 Propulsive Force Limits at High Speed -
- Test Data Appendix -

Mr. J. L. Jenkins (NASA Langley) was the technical monitor for this work.

The Boeing Vertol Program Manager was F. J. McHugh and was assisted in the testing, data presentation and report preparation by Ross Clark, Aerodynamics Tech. Rep.

LIST OF FIGURES

<u>FIGURE NO.</u>		<u>PAGE</u>
1.1	Single Rotor Helicopter (SRH) Rotor Test Stand Wind Tunnel Installation	15
1.2	Lift Limit Defined by Aerodynamic Capability .	16
1.3	Effect of Propulsive Force Requirements on Maximum Lift	17
1.4	Lift-Propulsive Force Limit	18
1.5	Summary of Alternating Blade Root Torsion Load Growth as Lift Limit is Approached	19
1.6	Radial and Azimuthal Distribution of Blade Torsion Loads, $\mu = 0.50$, $C_T'/\sigma = 0.0894$, $X/qd^2\sigma = 0.05$	20
1.7	Rotor Effective Drag for Performance Summary - $V_T = 620$ FT/SEC	21
1.8	Summary of Maximum Effective Lift-Drag Ratio .	22
1.9	Effect OF Stall Proximity on Longitudinal Control Power Rotor Moments & Inplane Forces at $\mu = 0.53$, $X/qd^2\sigma = 0.05$	23
1.10	Effect of Rotor Speed on Maximum Lift Limit .	24
1.11	Effect of Propulsive Requirement on Model Configuration Performance, $C_T'/\sigma = 0.08$	25
1.12	Effect of Torsional Stiffness on Rotor Effective Drag $\mu = 0.57$, $X/qd^2\sigma = 0.05$	26
3.1	SRH Rotor Test Stand with RTS Hub & Stack . .	30
3.2	Blade Construction	33
3.3	Frequency Spectrum for 1/10 Scale CH-47B Rotor	34
3.4	Longitudinal & Lateral Cyclic Envelope as Influenced by Collective	36
3.5	Blade Load Instrumentation Location	37

LIST OF FIGURES

<u>FIGURE NO.</u>		<u>PAGE</u>
4.1	Data Acquisition System	40
4.2	Model Force & Moment Convention	42
5.1	Summary of Test Operating Conditions	50
6.1.1	Lift Limit Defined by Aerodynamic Capability .	63
6.1.2	Lift Limit Not Defined by Blade Loads	64
6.1.3	Maximum Lift Limit	65
6.1.4	Lift Distribution Estimated from Torsion Loads at $\mu = 0.20$ and $X/qd^2\sigma = 0.05$	66
6.1.5	Lift Distribution Estimated from Torsion Loads at $\mu = 0.50$ and $X/qd^2\sigma = 0.05$	67
6.1.6	Effect of Propulsive Force Requirements on Maximum Lift Limit	68
6.1.7	Propulsive Force Limit not Defined by Stall . .	69
6.1.8	Propulsive Force Limit not Defined by Aerodynamics	70
6.1.9	Maximum Propulsive Force Limit Achieved during Testing Limit Defined by Lag Stop	71
6.1.10	Lift-Propulsive Force Envelope at the Lift Limit	72
6.1.11	Lift-Propulsive Force Limit	73
6.2.1	Frequency Spectrum for 1/10 Scale CH-47B Rotor	86
6.2.2	Summary of Alternating Blade Root Torsion Loads	87
6.2.3	Summary of Alternating Blade Root Flap Bending Loads	88
6.2.4	Summary of Alternating Root Chord Bending Loads.	89
6.2.5	Effect of Rotor Lift on Radial Distribution of Blade Torsion Load at $\mu = 0$	90

LIST OF FIGURES

<u>FIGURE NO.</u>		<u>PAGE</u>
6.2.6	Effect of Rotor Lift on Radial Distribution of Blade Torsion Load at $\mu = 0.20$, $X/qd^2\sigma = 0.05$	91
6.2.7	Effect of Rotor Lift on Radial Distribution of Blade Torsion Load at $\mu = 0.40$, $X/qd^2\sigma = 0.05$	92
6.2.8	Effect of Rotor Lift on Radial Distribution of Blade Torsion Load at $\mu = 0.50$, $X/qd^2\sigma = 0.05$	94
6.2.9	Effect of Rotor Lift on Radial Distribution of Blade Torsion Load at $\mu = 0.57$, $X/qd^2\sigma = 0.05$	95
6.2.10	Effect of Approaching the Lift Limit on the Blade Torsion Load at $\mu = 0$	96
6.2.11	Effect of Approaching the Lift Limit on the Blade Torsion Load at $\mu = 0.02$	97
6.2.12	Effect of Approaching Lift Limit on the Blade Torsion Load at $\mu = 0.40$	98
6.2.13	Effect of Approaching the Lift Limit on the Blade Torsion Load at $\mu = 0.50$	99
6.2.14	Effect of Approaching the Lift Limit on the Blade Torsion Load at $\mu = 0.57$	100
6.2.15	Radial & Azimuthal Distribution of Blade Torsion Loads, $\mu = 0.20$, $C_T'/\sigma = 0.1238$, $X/qd^2\sigma = 0.05$	101
6.2.16	Radial & Azimuthal Distribution of Blade Torsion Loads, $\mu = 0.20$, $C_T'/\sigma = 0.1333$, $X/qd^2\sigma = 0.05$	102
6.2.17	Radial and Azimuthal Distribution of Blade Torsion Loads, $\mu = 0.50$, $C_T'/\sigma = 0.0894$, $X/qd^2\sigma = 0.05$	103

LIST OF FIGURES

<u>FIGURE NO.</u>		<u>PAGE</u>
6.2.18	Radial & Azimuthal Distribution of Blade Torsion Loads, $\mu = 0.50$, $C_T^1/\sigma = 0.1029$, $X/qd^2\sigma = 0.05$	104
6.2.19	Azimuthal Variation in Flap Bending Load & Estimation of Major Areas of Rotor Lift $\mu = 0.20$, $C_T^1/\sigma = 0.1238$, $X/qd^2\sigma = 0.05$	105
6.2.20	Azimuthal Variation in Flap Bending Load & Estimation of Major Areas of Rotor Lift $\mu = 0.20$, $C_T^1/\sigma = 0.1333$, $X/qd^2\sigma = 0.05$	106
6.2.21	Azimuthal Variation in Flap Bending Load & Estimation of Major Areas of Rotor Lift $\mu = 0.50$, $C_T^1/\sigma = 0.0894$, $X/qd^2\sigma = 0.05$. . .	107
6.2.22	Azimuthal Variation in Flap Bending Load & Estimation of Major Areas of Rotor Lift $\mu = 0.50$, $C_T^1/\sigma = 0.1029$, $X/qd^2\sigma = 0.05$	108
6.3.1	Rotor Performance Summary at $V_T = 620$ FT/SEC .	115
6.3.2	Rotor Effective Drag for Performance Summary $V_T = 620$ FT/SEC	116
6.3.3	Summary of Maximum Effective Lift-Drag Ratio .	117
6.3.4	Shaft Angle of Attack for Performance Summary $V_T = 620$ FT/SEC	118
6.3.5	Collective Pitch for Performance Summary $V_T = 620$ FT/SEC	119
6.3.6	Longitudinal Cyclic Pitch for Performance Summary $V_T = 620$ FT/SEC	120
6.3.7	Lateral Cyclic Pitch for Performance Summary $V_T = 620$ FT/SEC	121
6.3.8	Effect of Propulsive Force on Rotor Power Required at Constant Lift, $\mu = 0.40$	122
6.3.9	Effect of Propulsive Force on Rotor Power Required at Constant Lift, $\mu = 0.50$	123
6.3.10	Effect of Propulsive Force on Rotor Power Required at Constant Lift, $\mu = 0.61$	124

LIST OF FIGURES

<u>FIGURE NO.</u>		<u>PAGE</u>
6.3.11	Summary of Rotor Propulsive Efficiency	125
6.3.12	Rotor Performance Summary At $V_T = 570$ FT/SEC . .	126
6.3.13	Rotor Effective Drag for Performance Summary $V_T = 570$ FT/SEC	127
6.3.14	Shaft Angle of Attack for Performance Summary $V_T = 570$ FT/SEC	128
6.3.15	Collective Pitch for Performance Summary $V_T = 570$ FT/SEC	129
6.3.16	Longitudinal Cyclic Pitch for Performance Summary $V_T = 570$ FT/SEC	130
6.3.17	Lateral Cyclic Pitch for Performance Summary $V_T = 570$ FT/SEC	131
6.3.18	Alternating Blade Root Torsion Loads for Performance Summary at $V_T = 570$ FT/SEC	132
6.4.1	Effect of Stall Proximity of Longitudinal Control Power - Rotor Moments & Inplane Forces at $\mu = 0.20$, $X/qd^2\sigma = 0.05$	135
6.4.2	Effect of Stall Proximity on Lateral Control Power - Rotor Moments & Inplane Forces at $\mu = 0.20$, $X/qd^2\sigma = 0.05$	136
6.4.3	Effect of Stall Proximity on Rotor Control Power - Rotor Lift & Power Variation at $\mu = 0.20$, $X/qd^2\sigma = 0.05$	137
6.4.4	Effect of Stall Proximity on Longitudinal Control Power - Rotor Moments & Inplane Forces at $\mu = 0.40$, $X/qd^2\sigma = 0.05$	138
6.4.5	Effect of Stall Proximity on Lateral Control Power - Rotor Moments & Inplane Forces at $\mu = 0.40$, $X/qd^2\sigma = 0.05$	139
6.4.6	Effect of Stall Proximity on Rotor Control Power - Rotor Lift & Power at $\mu = 0.40$, $X/qd^2\sigma = 0.05$	140

LIST OF FIGURES

<u>FIGURE NO.</u>		<u>PAGE</u>
6.4.7	Effect of Stall Proximity on Longitudinal Control Power Rotor Moments & Inplane Forces at $\mu = 0.53$, $X/qd^2\sigma = 0.05$	141
6.4.8	Effect of Stall Proximity on Lateral Control Power - Rotor Moments & Inplane Forces at $\mu = 0.53$, $X/qd^2\sigma = 0.05$	142
6.4.9	Effect of Stall Proximity on Rotor Control Power - Rotor Lift & Power at $\mu = 0.53$, $X/qd^2\sigma = 0.05$	143
6.5.1	Effect of Rotor Speed on Maximum Lift Limit .	146
6.7.1	Rotor Performance with & Without Tip Stall for Same Lift & Propulsive Force	152
6.7.2	Rotor Operation with & Without Tip Stall for Same Lift & Propulsive Force	153
6.7.3	Rotor Attitude & Control Positions for Operation With & Without Tip Stall for Same Lift & Propulsive Force	154
6.7.4	Alternating Blade Loads for Operating With & Without Tip Stall for Same Lift & Propulsive Force	155
6.7.5	Comparison of Outboard Torsion Load Wave Form for Operation in & Out of Stall $\mu = 0.53$, $X/qd^2\sigma = 0.05$	156
6.7.6	Comparison of Flap Bending Load Wave Form for Operation In & Out of Stall $\mu = 0.53$, $X/qd^2\sigma = 0.05$	157
6.7.7	Comparison of Chord Bending Load Wave Form for Operation In & Out of Stall $\mu = 0.53$, $X/qd^2\sigma = 0.05$	158
6.7.8	Alternating Blade Root Torsion Loads With & Without Tip Stall for Same Lift & Propulsive Force	159

LIST OF FIGURES

<u>FIGURE NO.</u>		<u>PAGE</u>
6.7.9	Tip Stall Effects on Maximum Lift Limit	160
6.7.10	Model Configuration Rotor Power Required	161
6.8.1	Model Configuration Performance $C_T/\sigma = 0.08$, $X/qd^2\sigma = 0.05$	166
6.8.2	Model Configuration Effective Lift to Drag Ratio $C_T/\sigma = 0.08$, $X/qd^2\sigma = 0.05$	167
6.8.3	Shaft Angle of Attack & Control Positions Associated with Model Configuration Performance $C_T/\sigma = 0.08$, $X/qd^2\sigma = 0.05$	168
6.8.4	Alternating Blade Root Torsion Loads for Model Configuration $C_T/\sigma = 0.08$, $X/qd^2\sigma = 0.05$	169
6.8.5	Effect of Propulsive Requirement on Model Configuration Performance, $C_T/\sigma = 0.08$	170
6.9.1	Comparison of Predicted Rotor Performance with Test Data for Conventional Rotor Using SRIBR Program	176
6.9.2	Comparison of Full Scale Rotor Control Position Prediction with Model Test Data	177
6.9.3	Comparison of Mid Span Torsion Prediction with Test Data $\mu = .53$, $C_T/\sigma = 0.08$, $X/qd^2\sigma = 0.05$	178
6.9.4	Comparison of Root Torsion Prediction with Test Data $\mu = 0.53$, $C_T/\sigma = 0.08$, $X/qd^2\sigma = 0.05$	179
6.9.5	Comparison of Root Torsion Prediction with Test Data - Prediction Corrected for Mid Span Load Discrepancy, $\mu = 0.53$, $C_T/\sigma = 0.08$, $X/qd^2\sigma = 0.05$	180

LIST OF FIGURES

<u>FIGURE NO.</u>		<u>PAGE</u>
6.10.1	Frequency Spectrum for Torsionally Soft Blade	184
6.10.2	Effect of Torsional Stiffness on Rotor Power, $\mu = 0.57$, $X/qd^2\sigma = 0.05$	185
6.10.3	Effect of Torsional Stiffness on Rotor Effective Drag $\mu = 0.57$, $X/qd^2\sigma = 0.05$	186
6.10.4	Effect of Torsional Stiffness on Blade Root Torsion Load $\mu = 0.57$, $X/qd^2\sigma = 0.05$	187

LIST OF TABLES

<u>Table</u>		<u>Page</u>
3.1	Summary of Rotor Blade Physical Properties	32
5.1	Run Log	51

NOMENCLATURE

<u>Symbol</u>	<u>Definition</u>	<u>Units</u>
A	Rotor Area (πR^2)	$m^2 (ft^2)$
A ₁ , a ₁	1st Harmonic Longitudinal Flapping Angle	rad(deg)
A ₁	Lateral Cyclic (- θ at $\psi = 0^\circ$)	rad(deg)
B ₁ , b ₁	1st Harmonic Lateral Flapping Angle	rad(deg)
B ₁	Longitudinal Cyclic (- θ at $\psi = 90^\circ$)	rad(deg)
CB12	Alternating Root Chord Bending Moment at 12% Blade Radius (P+P)/2	Nm(in-lb)
CB53	Alternating Mid Span Chord Bending Moment at 53% Blade Radius (P+P)/2	Nm(in-lb)
CDE/SB	Rotor Effective Drag Coefficient = $DE/\rho AV_{TIP}^2 \sigma$	
CH/SB	Rotor Longitudinal Force Coefficient = $HFORCE/\rho AV_{TIP}^2 \sigma$	
CPMB	Rotor Pitching Moment = $PM/\rho AV_{TIP}^2 R$	
CP/SB	Rotor Power Coefficient = $Q/\rho AV_{TIP}^2 R \sigma$	
CRMB	Rotor Rolling Moment Coefficient = $RM/\rho AV_{TIP}^2 R$	
CT'/SB	Rotor Lift Coefficient = $L/\rho AV_{TIP}^2 \sigma$	
CX/SB	Rotor Propulsive Force Coefficient = $X/\rho AV_{TIP}^2 \sigma$	
CY/SB	Rotor Side Force Coefficient = $S.F./\rho AV_{TIP}^2 \sigma$	
FB12	Alternating Root Flap Bending at 12% Blade Radius (P+P)/2	Nm(in-lb)
FB22	Alternating Inboard Flap Bending Moment at 22% Blade Radius (P+P)/2	Nm(in-lb)

<u>Symbol</u>	<u>Definition</u>	<u>Units</u>
FB48	Alternating Mid Span Flap Bending Moment at 48% Blade Radius $(P+P)/2$	Nm (in-lb)
FB79	Alternating Outboard Flap Bending Moment at 79% Blade Radius $(P+P)/2$	Nm (in-lb)
PM	Hub Pitching Moment	Nm (ft-lb)
Q	Rotor Torque	Nm (lb-ft)
R	Rotor Radius	m (ft)
RM	Hub Rolling Moment	Nm (ft-lb)
SF	Rotor Side Force	N (lb)
T	Rotor Thrust	N (lb)
TB12	Alternating Root Torsion at 12% Blade Radius = $(P+P)/2$	Nm (in-lb)
TB20	Alternating Inboard Torsion at 20% Blade Radius = $(P+P)/2$	Nm (in-lb)
TB51	Alternating Mid Span Torsion at 51% Blade Radius = $(P+P)/2$	Nm (in-lb)
TB81	Alternating Outboard Torsion at 81% Blade Radius = $(P+P)/2$	Nm (in-lb)
V	Tunnel Velocity	m/s (ft/s)
V _{TIP}	Rotor Tipspeed	m/s (ft/s)
X	Rotor X Force	N (lb)
α_s	Shaft Angle of Attack	rad(deg)
θ	Collective Pitch	rad(deg)
μ	Advance Ratio = V/V_{TIP}	

<u>Symbol</u>	<u>Definition</u>	<u>Units</u>
ρ	Tunnel Density	Kg/m^2 (slugs/ft ³)
σ	Rotor Solidity $bc/\pi R$	

1.0 SUMMARY

Current sophisticated rotor analyses and exploratory wind tunnel test indicated a potential for operating a conventional rotor in the 200 to 300 knot speed regime existed. The test data, obtained at low rotor tip speed, were minimal and required verification at full scale tip speeds. The results were encouraging enough to obtain support from NASA for the lift and propulsive force limit test that explores the high-speed regime to define the capabilities and limitations of the conventional rotor. To accomplish this test program objective, the Single Rotor Helicopter (SRH) Rotor Test Stand, shown in Figure 1.1 was used. This model is designed as a fully integrated system, containing necessary power plant controls and data measuring transducers to simulate any desired configuration of conventional helicopter or isolated rotor. The testing was performed with a 1/10 scale CH-47B rotor which has a cambered airfoil section from root to tip, linear twist of -7 degrees and three blades.

The general purpose of the test as defined above was divided into distinct tasks or objectives. These objectives will be addressed in the following paragraphs in the order of importance to the overall program purpose.

Test Objective 1: Determine the maximum lift and propulsive force obtainable from an articulated rotor for advance ratios of 0.4 to 0.67.

A sweep in rotor lift was made at a fixed rotor propulsive force coefficient ($X/qd^2\sigma$), increasing the lift until a limit defined by aerodynamic capability, blade loads or control capability was reached. Since collective pitch defined the rotor lift, this variation was used to establish any aerodynamic limitation on lift. Figure 1.2 presents a typical variation of rotor lift coefficient (C_T/σ) with collective pitch ($\theta_{.75R}$) at an advance ratio (μ) of 0.53 for three levels of propulsive force coefficient ($X/qd^2\sigma$) of 0.025, 0.05 and 0.10. At the lower level of rotor lift, the sensitivity to collective is very high but as C_T/σ becomes greater than 0.08 the sensitivity gradually decreases to a point where further increases in collective pitch produces either no change or a decrease in rotor lift coefficient. This indicates the lift is limited by the aerodynamic capability of this model rotor system.

The most critical load monitored during the test was alternating blade root torsion because it was the primary indicator of blade stall and had the smallest margin with the anticipated loads. Maximum measured torsion loads never exceeded 60 percent of the allowable, so loads were never the cause for limiting testing. There were only a few cases where longitudinal or lateral cyclic capability limited the testing and not the aerodynamic capability.

A summary of the rotor lift limits for the basic propulsive force coefficient of 0.05 is presented with the solid line in Figure 1.3 from hover ($\mu = 0.0$) to 225 knots ($\mu = 0.61$). The trend of lift limit with advance ratio decreases linearly up to a $\mu = 0.35$, beyond this value the lift decreases rapidly to a C_T'/σ of 0.098 at $\mu = 0.45$. From $\mu = 0.45$ to 0.50 the lift limit rises rapidly and levels off at a value of $C_T'/\sigma = 0.112$ out to $\mu = 0.53$. After this advance ratio the lift limit drops to C_T'/σ of 0.072 at 225 knots ($\mu = 0.61$).

In Figure 1.3, a summary of the lift limits at propulsive force coefficients ($X/qd^2\sigma$) of 0.025, 0.10 and 0.20 are also presented and compared with the basic lift limit at a propulsive force coefficient of $X/qd^2\sigma = 0.05$. Reducing the $X/qd^2\sigma$ to 0.025 resulted in no change between $\mu = 0.40$ and 0.50 but there was an increase in lift limit (C_T'/σ) of 0.008 at an advance ratio of 0.53. Increasing $X/qd^2\sigma$ from 0.05 to 0.10 resulted in a decrease in lift limit (C_T'/σ) of 0.01 between $\mu = 0.40$ to 0.50 and the decrement in lift limit (C_T'/σ) increases to 0.03 beyond an advance ratio of 0.50. Similar changes were established when the propulsive force coefficient was increased from 0.10 to 0.20.

To define the propulsive force limit, a sweep in propulsive force coefficient was made at a fixed level of rotor lift coefficient. Propulsive force was increased until a limit was defined by aerodynamic capability, blade loads or control capability. The testing was limited at a level 9 to 10 times greater than the basic propulsive force by a physical limitation of the model - the lag stops. The lead-lag motion was not large (less than 2 degrees) but the steady lag was large at these high levels of propulsive force, thus causing the blade to bang on the lag stops.

The maximum lift obtained at specific level of propulsive force or the maximum propulsive force obtained at fixed levels of rotor lift combine to establish the limitation on the operational capability of the model rotor system. This is presented in Figure 1.4 as the variation of rotor lift coefficient with rotor propulsive force coefficient for each advance ratio. Superimposed on Figure 1.4 is an equivalent flat plate drag area loading $GW/fe = 1500 \text{ lb/ft}^2$, a drag level representative of an advanced helicopter. This establishes the flight envelope for the model rotor system and specifies that the rotor can operate at a rotor lift coefficient $C_L'/\sigma = 0.10$ up to an advance ratio of 0.57 or 210 knots. Flight at an advance ratio of 0.61 or 225 knots can be achieved when operating at a $C_L'/\sigma = 0.08$. This answers the repeatedly asked question - can the conventional rotor

operate at useful lift levels in high speed forward flight without auxiliary lift or auxiliary propulsion? - with a firm YES.

Test Objective 2: Establish the blade load growth as the lift approaches the limit.

Loads data was measured in conjunction with testing to define the lift-propulsive force limits. Torsion, flap and chord bending loads were measured at ten locations on the blade. This instrumentation was utilized during the initial phase of the testing with blades on to determine the frequency spectrum of the rotor. At the normal operating tip speed the first torsion mode was 6.1/rev and would be the frequency ratio at which the blade would respond when encountering stall. During the testing this extensive instrumentation provided the depth of data coverage required not only to define the blade load growth as lift approached the limit, but also to assist in the development of an understanding of the operation of the rotor in the high speed regime. A summary of the alternating blade root torsion loads are presented in Figure 1.5 for a propulsive force coefficient ($X/qd^2\sigma$) of 0.05 at advance ratios of 0.0 to 0.61. The general trend exhibited a very slight increase in loads with rotor lift coefficients up to C_{T1}/σ of approximately 0.09 and advance ratios of 0.50. At higher lift levels the growth in alternating root torsion significantly increase. There is a second change in the slope, becoming

almost asymptotic, indicating a trend normally associated with stall and the lift limit. The growth in alternating flap and chord bending loads with rotor lift coefficient were similar to the trends exhibited by torsion; i.e., as the maximum lift limit is approached, the loads increase rapidly.

Referring to Figure 1.5 the alternating torsion load growth at an advance ratio of 0.50 shows a moderate sensitivity up to a lift level of $C_T/\sigma = 0.095$ and beyond that level there is a sharp increase in the sensitivity. Are these two load growth trends caused by conventional stall occurring in different areas of the rotor disc? In an effort to define the answer to this question it is necessary to combine the radial and azimuthal load variation and discuss them together as: the azimuthal variation of the outboard portion of the blade ($r/R = 0.81$ to 1.00), mid blade ($r/R = 0.50$ to 0.81) and the inboard portion of the blade ($r/R = 0.12$ to 0.50). Figure 1.6 shows these three incremental torsional load variations for a $C_T'/\sigma = 0.0894$ at $\mu = 0.50$. The outboard load variation is a uniform level of torsional load from 30 degrees to 270 degrees rotor azimuth with increases maximizing between 120 degrees to 160 degrees. A very low level of torsion load is evident near 280 degrees and 20 degrees rotor azimuth. For the mid blade variation there is a significant increase in nose down load at 150 degrees azimuth typical of stall while at 300 degrees azimuth the load becomes slightly positive, indicative

of operation at negative section angle of attack. In the inboard portion of the blade there is an increase in nose down load at 150 degrees azimuth representing stall. At 300 degrees azimuth there is a large increase in nose up load indicating negative stall and operation at extremely large negative angles of attack. There is a decrease in torsion load to zero between 60 and 90 degrees on the inboard portion of the blade indicating operation at negative section angles of attack.

For rotor lift near the lift limit there is an increase in load sensitivity to rotor lift for higher advance ratios. This is a result of operating at higher lift levels on the mid and outboard portions of the blade and developing a large area of positive stall in all three areas of the rotor. The region of negative stall becomes larger and also contributes to the increased load sensitivity to lift.

Test Objective 3: Obtain cruise rotor performance for
advance ratios of 0.40 to 0.67.

During the testing performed to define the lift limit, performance data was obtained from lift levels as low as C_T/σ of 0.04 up to the limit defined in Figure 1.3. This data is representative of steady level cruise performance for the 1/10 scale CH47B rotor. Figure 1.7 presents the summary of the rotor performance in terms of the rotor effective drag coefficient (C_{D_e}/σ) variation with rotor lift. Rotor effective drag coefficient is defined below:

$$C_{D_e}/\sigma = (C_p/\sigma)/\mu + C_x/\sigma$$

There is a large improvement in rotor effective drag from an advance ratio of 0.10 to 0.20. A slight increase in effective drag coefficient is shown as the advance ratio is increased to $\mu = 0.40$. For advance ratios of 0.45, 0.50 and 0.53 the effective drag level is slightly increased over an advance ratio of 0.40 and they are all approximately the same. The effective drag gradually increases with advance ratio up to 0.61 reaching a level that is equal to that of an advance ratio of $\mu = 0.10$. The general trend evident for each of the advance ratios is that the effective drag starts to increase significantly at lift levels well below the lift limit but in the lift level that is incurring inboard stall.

Rotor lift to effective drag ratio is a measure of cruise efficiency. The slope to any point on Figure 1.7 provides the L/D_E and the position of each advance ratio on this figure indicates their efficiency relative to each other. A summary of the maximum rotor L/D_E is presented in Figure 1.8 indicating a peak value of 9.5 at $\mu = 0.28$. The trend from $\mu = 0.40$ to 0.61 resembles the lift limit trend showing a dip at an advance ratio of 0.45 and a lower peak of 4.5 at $\mu = 0.53$.

The strain gages and wire bundles for the torsion, flap and chord bending loads were mounted externally on the blade. This produces lumps and spanwise surface irregularities that increase the basic drag of the airfoil section. From testing performed under the HLH program, data was obtained to define an increment in section drag

coefficient ($\Delta C_D = 0.02$) for instrumentation and wire bundles on the blades used in the Lift-Propulsive Force Limit test. Utilizing this ΔC_D , an estimate of the change in rotor effective drag coefficient was made and the associated impact on the maximum effective lift drag ratio. This was added to Figure 1.8 and indicates that the peak in maximum L/D_E increases to approximately 13.5 at $\mu = 0.28$. The second peak in L/D_E increases to 7.0 at an advance ratio of 0.53.

Test Objective 4: Determine the sensitivity of the rotor forces and moments to rotor control inputs as the lift limit is approached.

During the testing to determine the maximum lift limits, perturbations in longitudinal and lateral cyclic were made from the trimmed operating conditions. This was accomplished at 90 percent and 70 percent of the maximum lift to determine if there was any decrease in the incremental forces and moments generated. Figure 1.9 presents the impact of incremental longitudinal cyclic on the rotor pitching moment and longitudinal force as well as the cross coupling effects on rotor rolling and side force for an advance ratio of 0.53. The sensitivity of rotor pitching moment and longitudinal force are slightly increased when operating near the lift limit as shown in Figure 1.9. The sensitivities become slightly greater in the cross coupling terms of rotor rolling

moment and side force when operating near stall. The lateral control characteristics are less affected by operation near stall than the longitudinal control characteristics. At $\mu = 0.53$ there was no effect on the thrust or power sensitivities to longitudinal or lateral cyclic. The conclusion drawn is that there is a negligible effect on the control power resulting from operation at 90 percent of the lift limit at all speeds up to an advance ratio of 0.53.

Test Objective 5: Define the effect of advancing tip Mach number on the lift and propulsive force limits.

To determine the effect of advancing tip Mach number, a nominal increment of 0.05 in Mach number was selected which required reducing the rotor tip speed to approximately 570 ft/sec. The lift limit testing was performed in the same manner as described previously and a summary of the lift limit variation with advance ratio for 570 ft/sec is shown in Figure 1.10, with a dashed line. It shows a continuous decrease in the limit from an advance ratio of 0.45 to 0.64. To define the relative change in the limits resulting from this 0.05 change in Mach number, the lift limit of Figure 1.3, for $X/qd^2\sigma = 0.05$, is superimposed on Figure 1.10. The most significant difference in the limit is the distinct change in shape. For the lower tip speed there is no dip in lift limit at an advance ratio of 0.45. The result is a lower lift limit

of 0.50 and 0.60 by approximately $\Delta C_T^i/\sigma = 0.01$, but beyond $\mu = 0.60$ the lower tip speed has a definite advantage with the more shallow rate of change in lift limit with advance ratio. Further analysis is required to fully understand and establish the reason for these results.

Test Objective 6: Determine the blade flapping response to a step input in cyclic as the lift limit is approached.

An instrumentation failure prevented measuring blade flapping and a quantitative answer was not achieved but a qualitative one was provided each time the rotor hub moments were trimmed to zero. The hydraulic control system had very rapid response and any input command to the collective or cyclic controls resulted in a step input. Visual observation of the rotor indicated that the blade flapping was highly damped since the rotor stabilized very rapidly without any rotor wobble.

Testing in the higher advance ratio regions made evident that a rotor can operate at a fixed level of propulsive force and lift with and without tip stall. This can occur at all levels of lift and there appears to be two distinct operating conditions: one significantly worse from the performance and blade loads considerations. At an advance ratio of 0.53 there is an increase in power of approximately 30 percent resulting from this stalled operation. The

corresponding impact on the lift limit causes a decrease in rotor lift coefficient of 0.006.

The data presentations up to this point in the discussion has addressed maximum lift, maximum propulsive force or maximum effective lift to drag ratio; always defining the limit to the capability of the rotor system. It is equally important to define the capability for a fixed lift and equivalent flat plate drag requirement to simulate the rotor under normal operation and be representative of a model configuration. The definition of this configuration is as follows:

- o Reduced drag levels, representative of an advanced helicopter ($X/qd^2\sigma = 0.05$)
- o Normal operating lift ($C_T/\sigma = 0.08$)
- o Normal operating speed 620 ft/sec

The performance for this configuration in terms of effective rotor lift to drag ratio is slightly less than that shown in Figure 1.8. A comparison of this level of performance with that obtained at a propulsive force coefficient of 0.10, representative of current helicopter drag levels is shown in Figure 1.11 in the form of power required curves. There is a 25 to 30 percent reduction in total rotor power required achieved by reducing the propulsive force requirement with drag reduction from $X/qd^2\sigma$ of 0.10 to 0.05. Shown also on this figure is the power required for $X/qd^2\sigma = 0.025$ and the extrapolation

between advance ratios to the ultimate capability - zero drag. The 25 to 30 percent reduction in total power required for $X/qd^2\sigma = 0.05$ takes the configuration halfway to the ultimate goal and adds greater emphasis to the accomplishment of drag reduction. With the cost of fuel increasing dramatically and energy conservation being carefully considered in the development of the next generation helicopter, drag reduction and cleanup becomes a very high priority effort.

At the end of the first portion of the test program, one lift limit test data run was performed at an advance ratio of 0.57 with a set of rotor blades that are geometrically the same but the torsional stiffness is reduced by approximately 45 percent. Figure 1.12 presents the performance obtained for the soft GJ blade compared to the standard blade summarized earlier. The maximum lift measured for the soft GJ blade is 0.086, the standard blade has reached a C_T'/σ of 0.094 and has not reached a maximum. Effective rotor drag variation with rotor lift is presented in Figure 1.12 and shows a difference of $\Delta C_{D_E}/\sigma_B = 0.040$. The soft GJ blade was instrumented out to 55 percent of the radius but the standard blade was instrumented out to 80 percent and these instrumentation leads could account for this difference in C_{D_E}/σ_B . The maximum effective rotor lift to drag ratio is approximately 3.2 for the soft GJ blade and 2.9 for the standard blade, not correcting for the difference in external instrumentation. A comparison of the alternating blade

root torsion loads indicated that the load growth on the soft GJ blade is larger and the load becomes 20 percent higher at $C_T'/\sigma = 0.082$.

The lift propulsive force limit test provided a large amount of test data and only a portion of it has been examined in depth. From the data analysis included in this report, the overall conclusion reached is that the conventional rotor and pure helicopter has the capability to operate in excess of 200 knots without wings and auxiliary propulsion. Since this 6 foot diameter model could operate effectively up to 225 knots, a full scale rotor with improved planform, twist and structural characteristics should have the capability to expand this operational envelope and provide a more efficient helicopter.

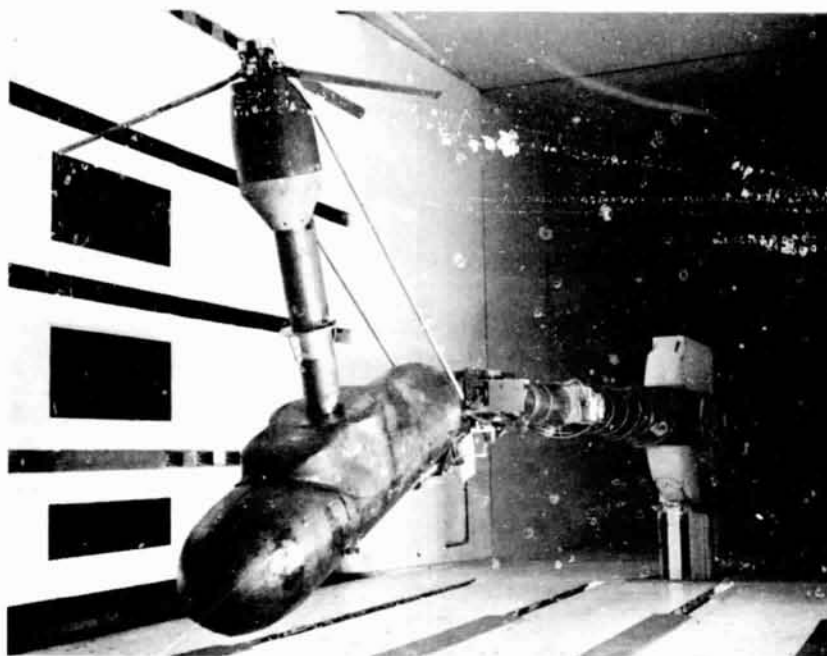


FIGURE 1.1 SINGLE ROTOR HELICOPTER (SRH) ROTOR TEST STAND
WIND TUNNEL INSTALLATION

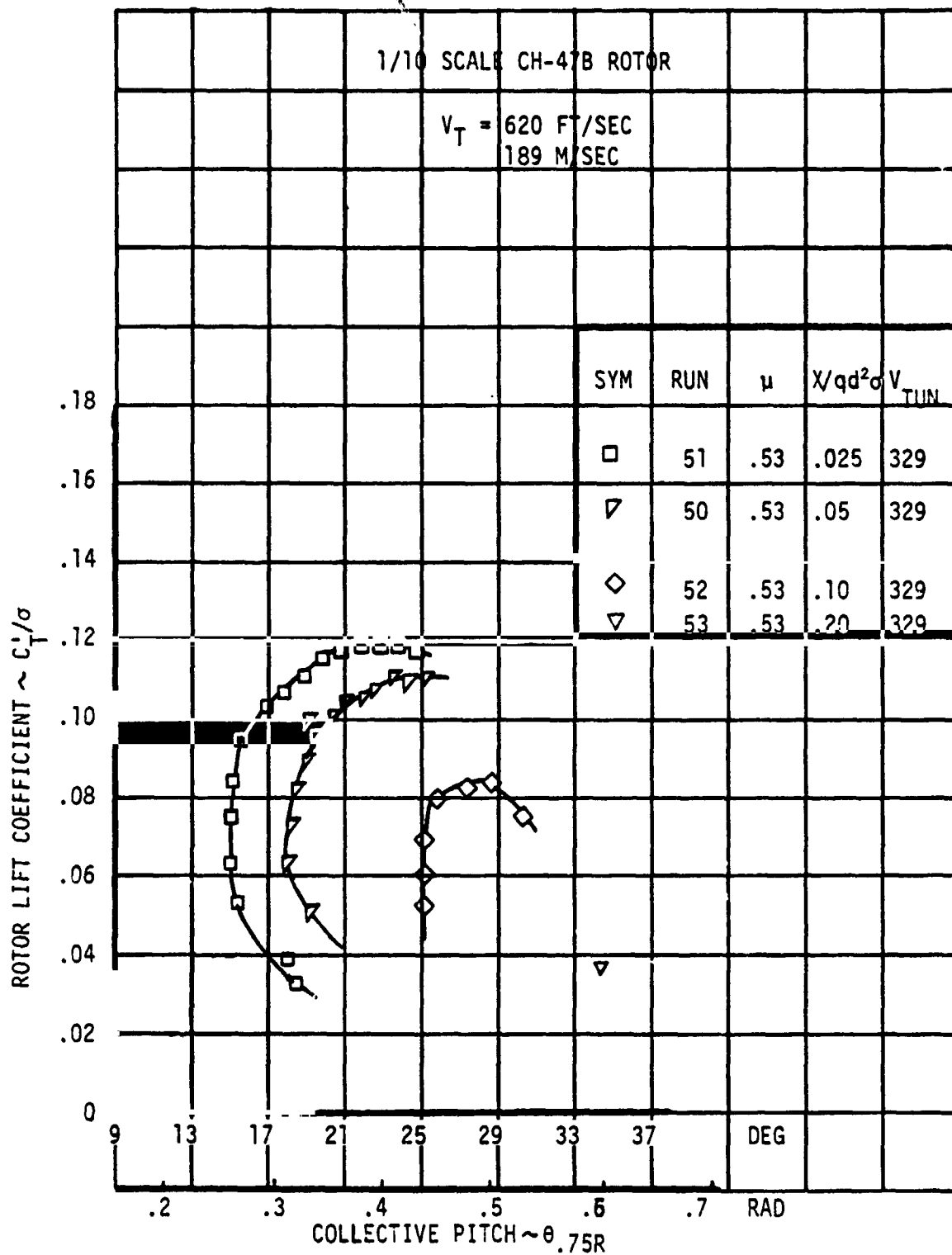


FIGURE 1.2 LIFT LIMIT DEFINED BY AERODYNAMIC CAPABILITY

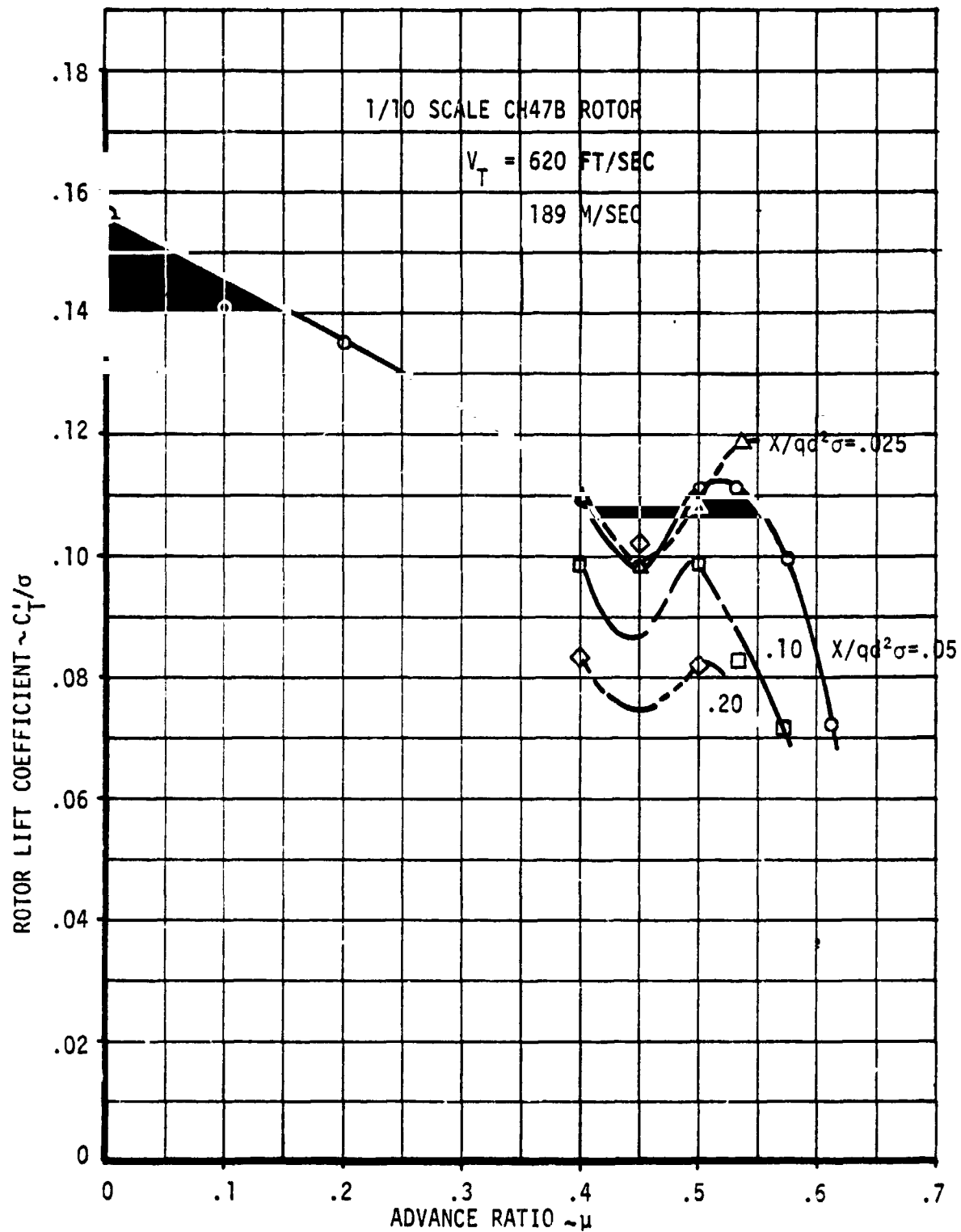


FIGURE 1.3 EFFECT OF PROPULSIVE FORCE REQUIREMENTS ON MAXIMUM LIFT LIMIT

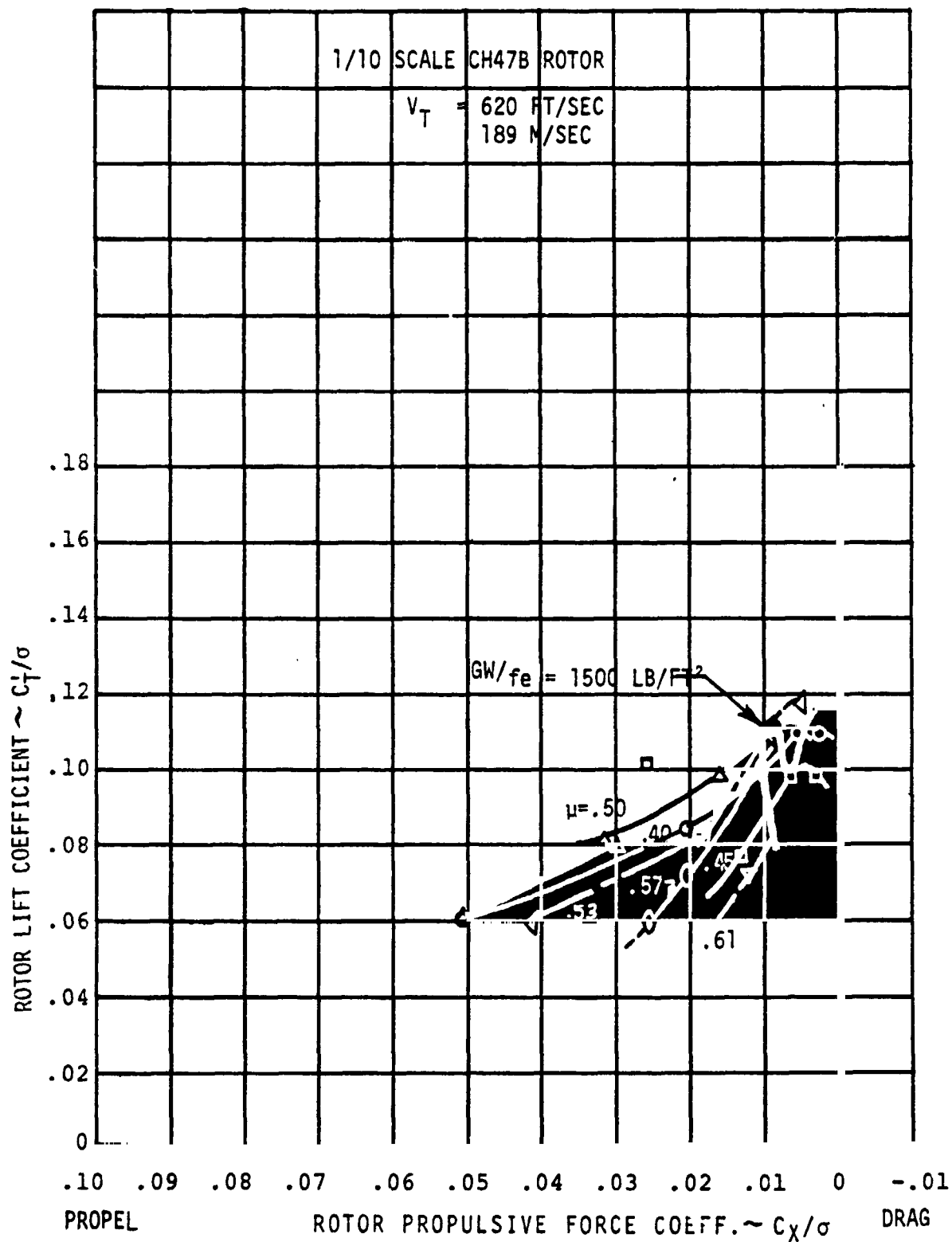


FIGURE 1.4 LIFT-PROPULSIVE FORCE LIMIT

ORIGINAL PAGE IS
OF POOR QUALITY

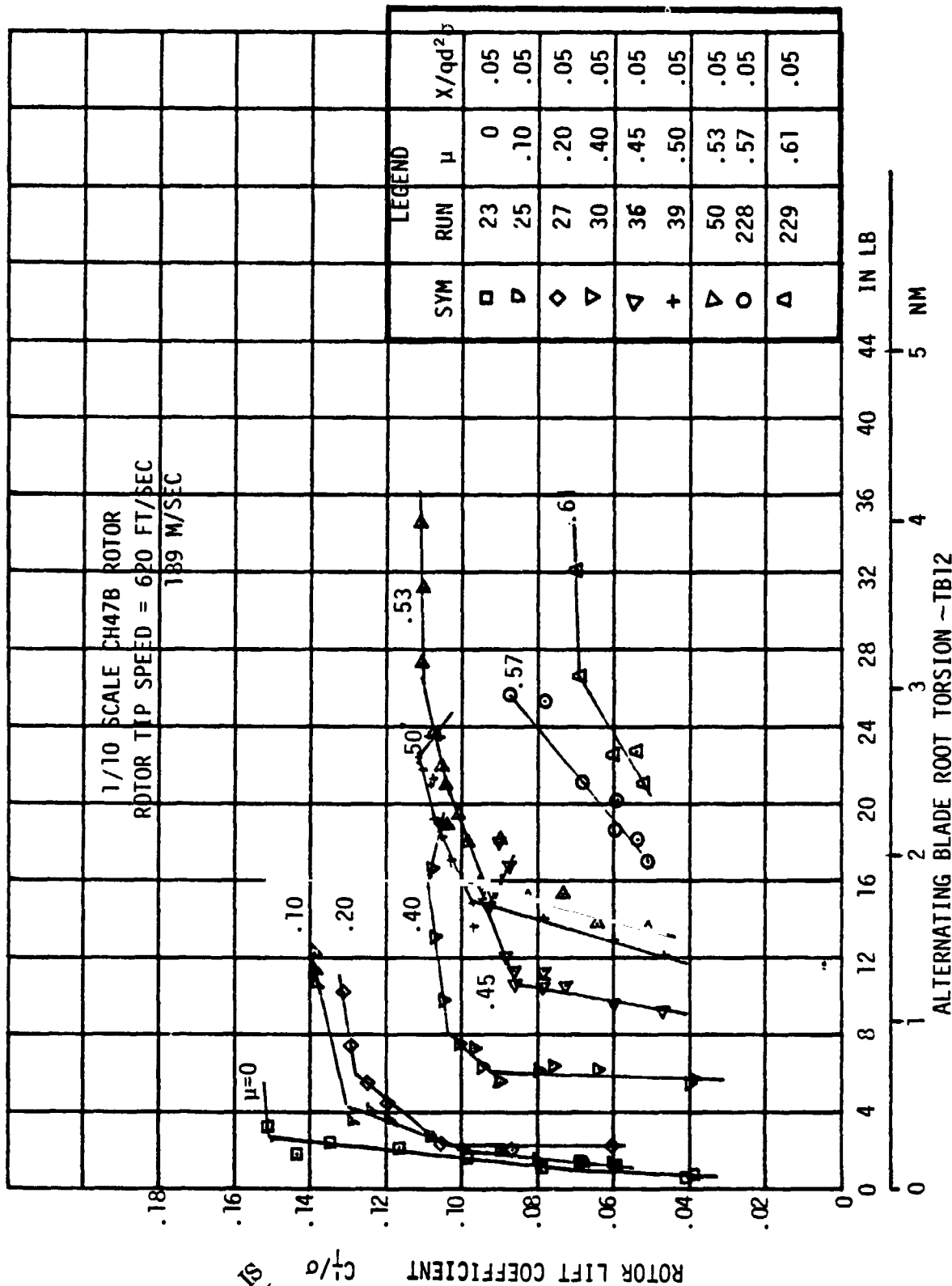


FIGURE 1.5 SUMMARY OF ALTERNATING BLADE ROOT TORSION LOAD GROWTH AS LIFT LIMIT IS APPROACHED

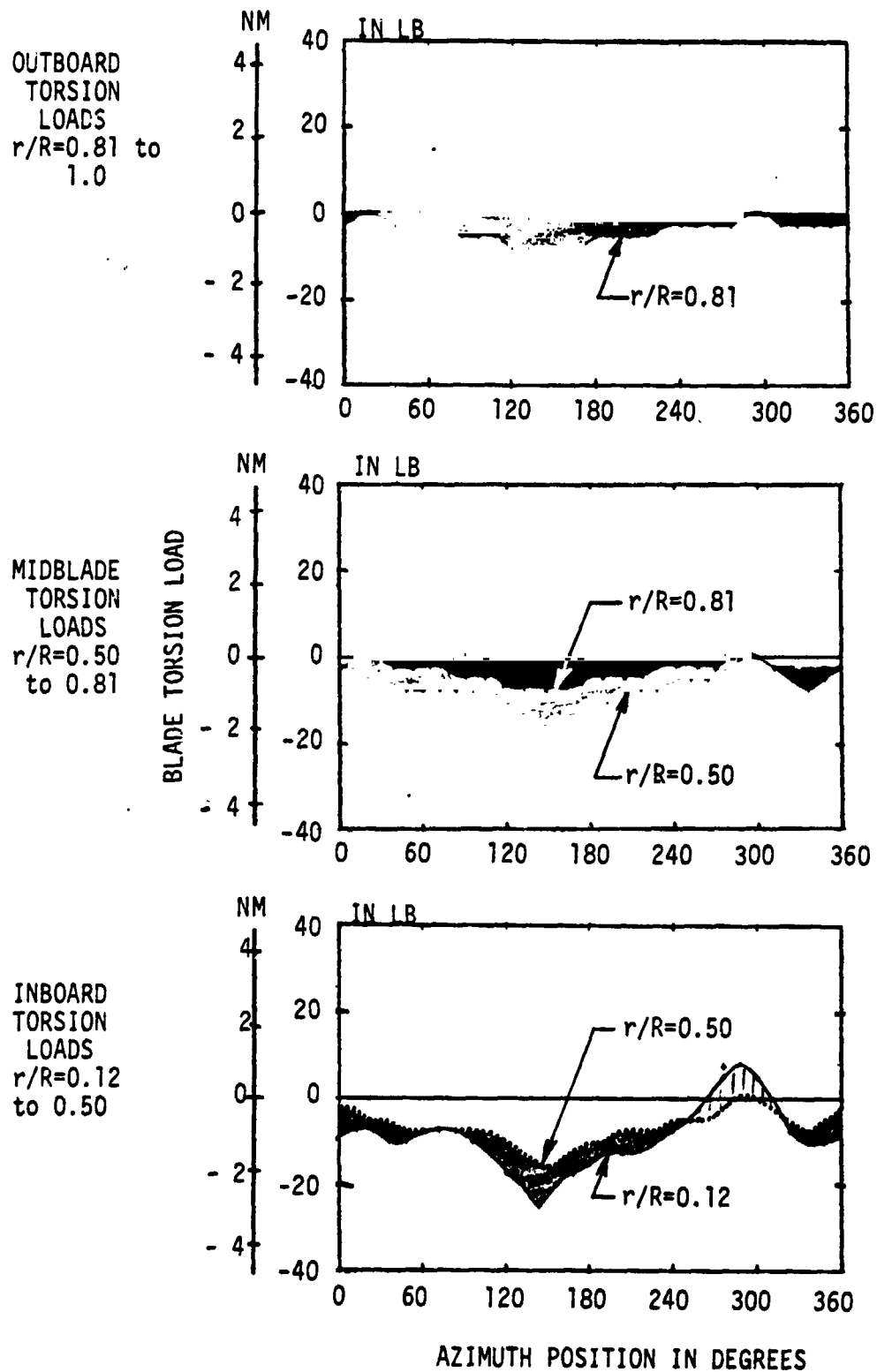


FIGURE 1.6 RADIAL AND AZIMUTHAL DISTRIBUTION OF BLADE TORSION LOADS,
 $\mu = 0.50$ $C_T/\sigma = 0.0894$, $X/qd^2\sigma = 0.05$

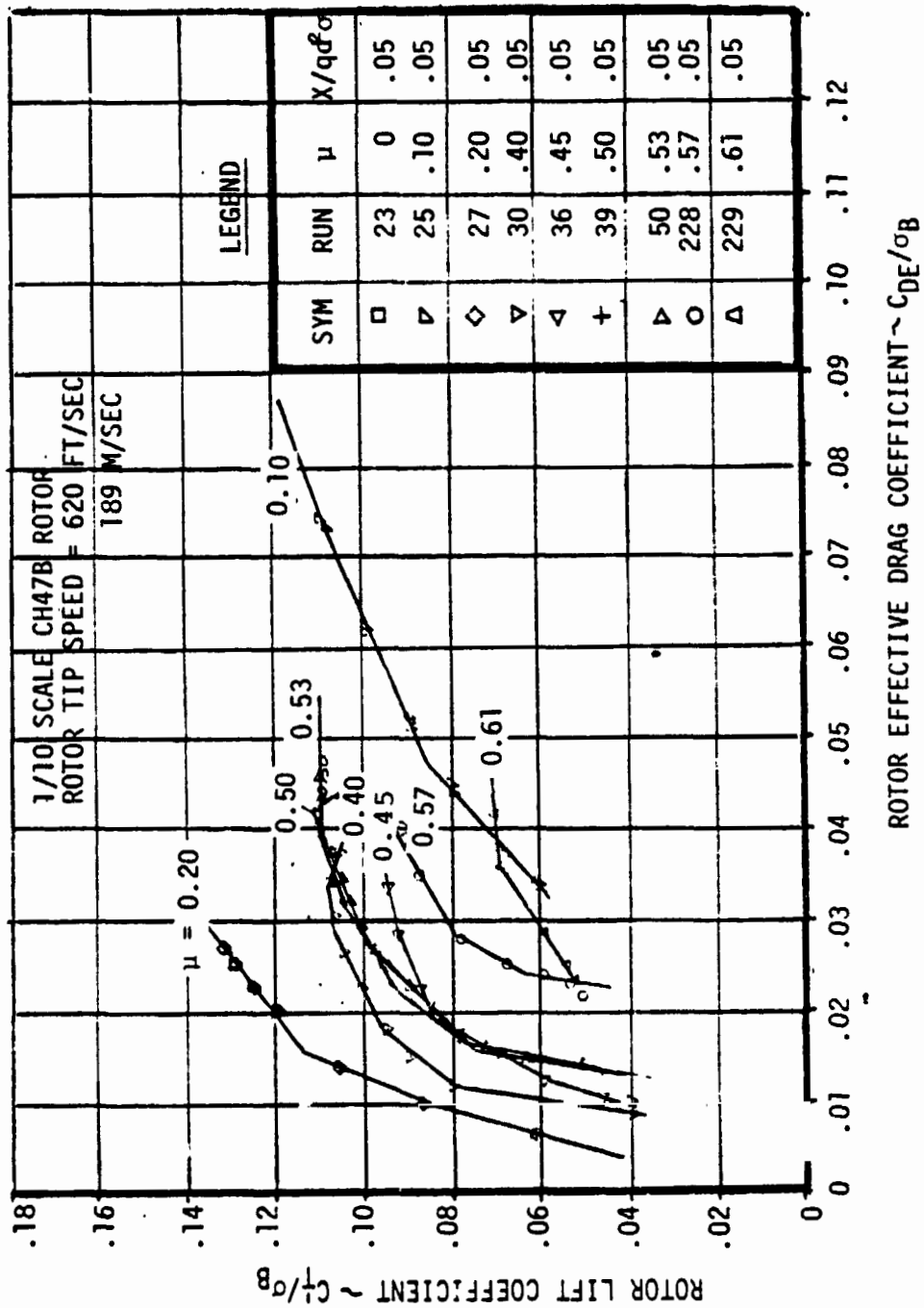


FIGURE 1.7 ROTOR EFFECTIVE DRAG FOR PERFORMANCE SUMMARY $V_T = 620$ FT/SEC

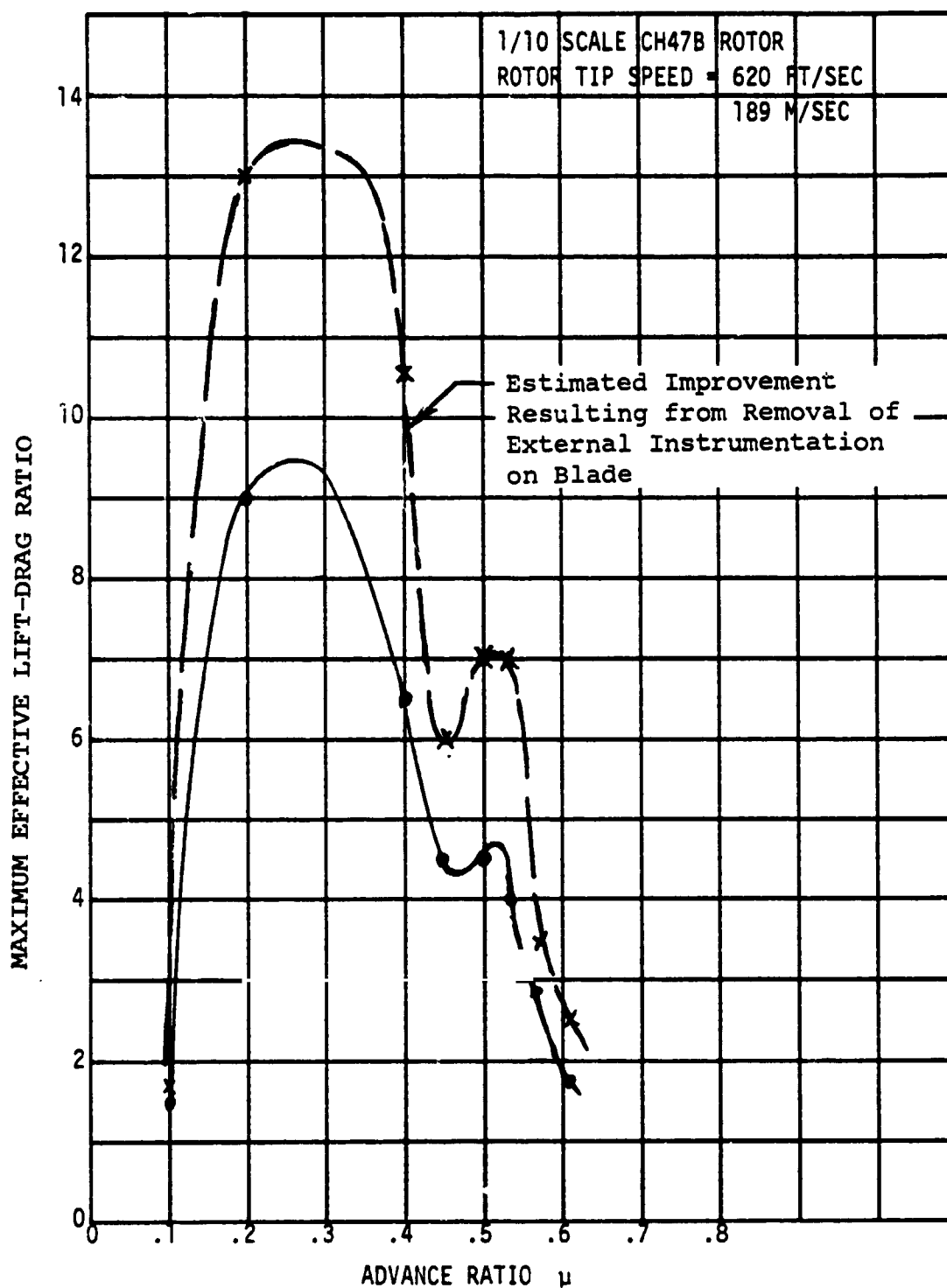


FIGURE 1.8 SUMMARY OF MAXIMUM EFFECTIVE LIFT-DRAG RATIO

1/10 SCALE CH-47B ROTOR

$V_T = 620 \text{ FT/SEC}$

$= 189 \text{ M/SEC}$

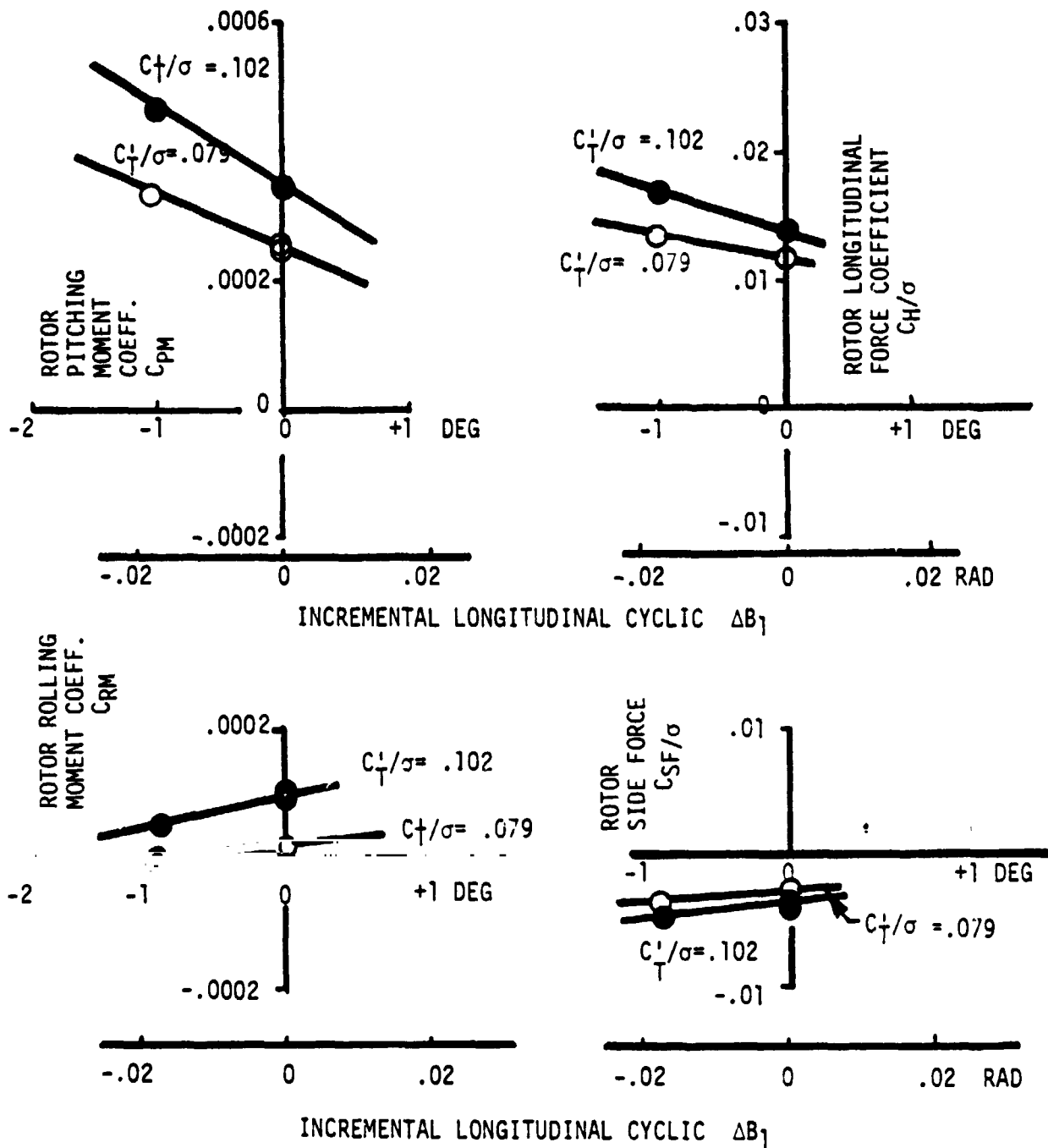


FIGURE 1.9 EFFECT OF STALL PROXIMITY ON LONGITUDINAL CONTROL POWER
ROTOR MOMENTS & INPLANE FORCES AT $\mu = 0.53$; $X/qd^2\sigma = 0.05$

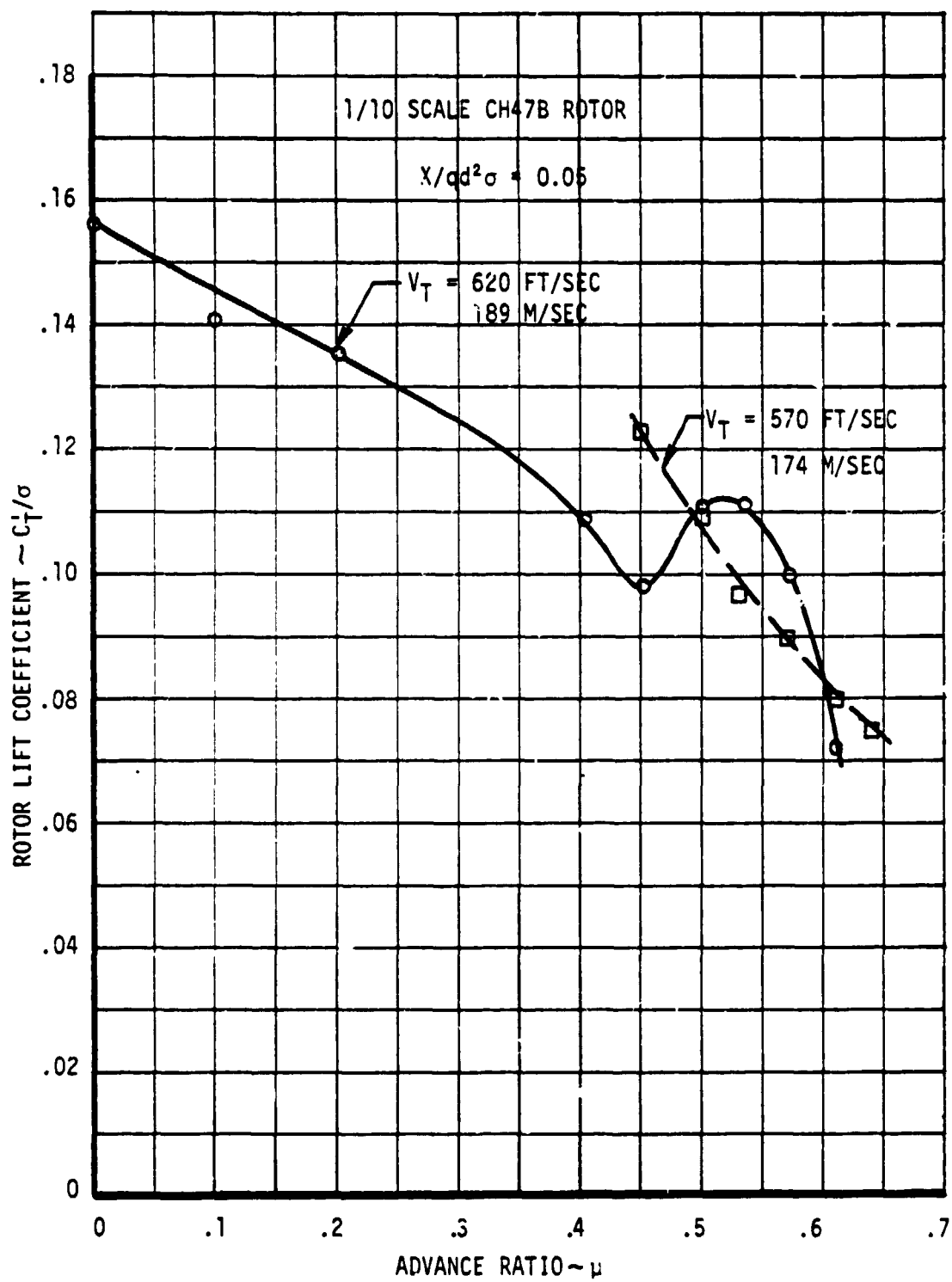


FIGURE 1.10 EFFECT OF ROTOR SPEED ON MAXIMUM LIFT LIMIT

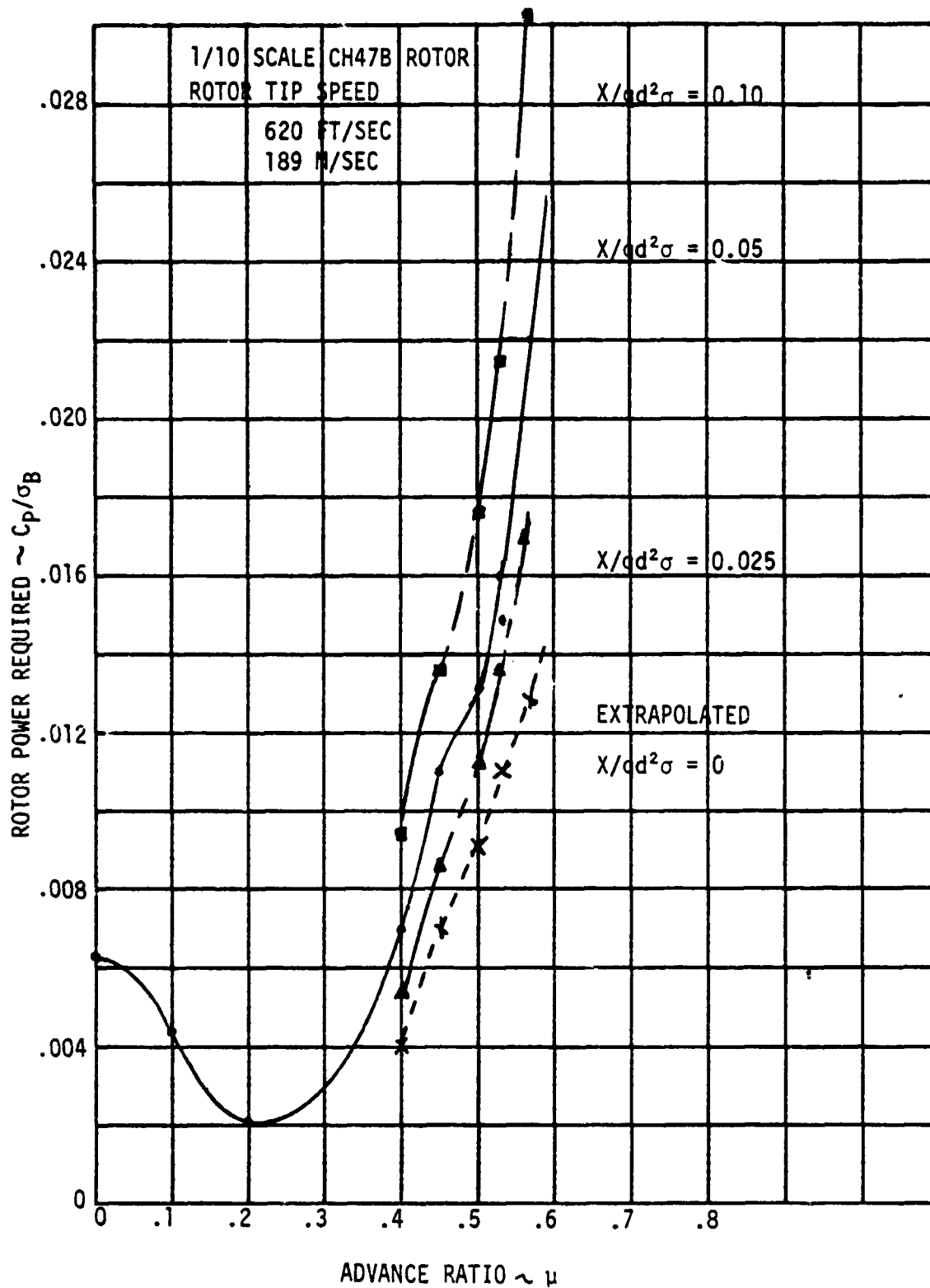


FIGURE 1.11 EFFECT OF PROPULSIVE REQUIREMENT ON MODEL CONFIGURATION PERFORMANCE, $C_T/\sigma = 0.08$

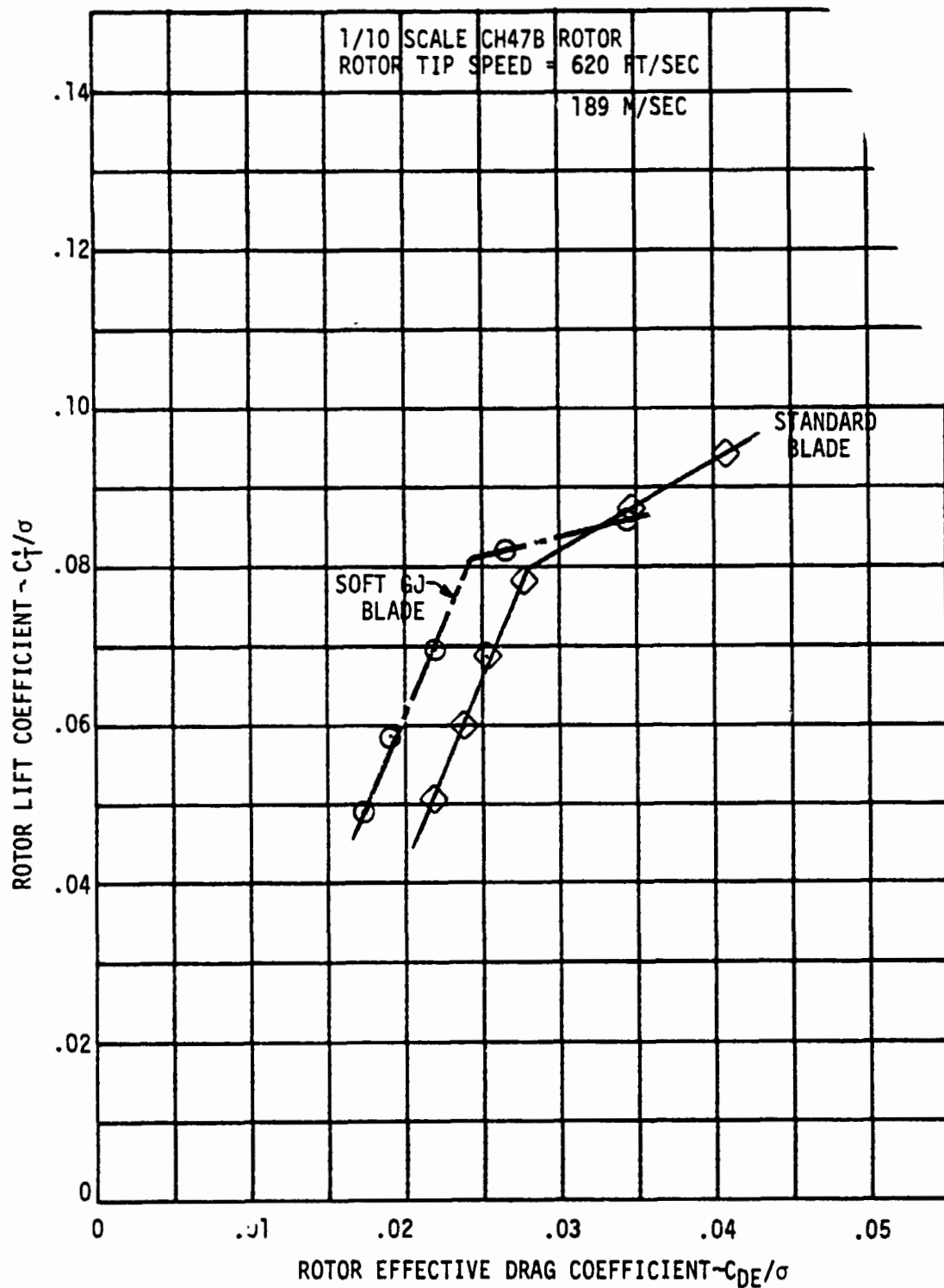


FIGURE 1.12 EFFECT OF TORSIONAL STIFFNESS ON ROTOR EFFECTIVE DRAG $\mu = 0.57$ $X/qd^2\sigma = 0.05$

2.0 INTRODUCTION

In the development of current helicopters, during the 1960's, investigations were conducted to explore the growth potential of conventional rotors. Analytical studies performed at the time and substantiated by a minimum amount of test data, established generalized rotor performance. These results indicated rotor operation beyond an advance ratio of 0.5 at typical design lift levels in the propelling mode was not recommended. As more rotor testing was accomplished at higher lift levels and higher speeds, the theory was modified and substantiated with the test data. The operational boundaries of the rotor were expanded and detailed study of these boundaries indicated that they were a result of blade stall. The continued study of blade stall has resulted in the development of a more complete aeroelastic representation of the rotor system and an increased understanding of the aerodynamic and aeroelastic response of the blade when it encounters stall.

With this better understanding of the rotor system, an analysis of the limitations of the rotor defined by stall for the 200 to 300 knot speed regime was performed. The analysis indicated that lift was increased without any serious degradation in performance but at high levels of lift the methodology would not iterate to a converged blade motion and trimmed rotor solution. These results implied a rotor potential existed and exploratory wind tunnel testing was performed in 1974 to verify it. A minimum

amount of test data was obtained at reduced tip speed operation at high advance ratios without severe limitations to lift or blade loads produced by stall. These results indicated a more detailed examination of the high speed potential of the conventional rotor was required and has led to the test program summarized in this report.

3.0 MODEL DESCRIPTION AND INSTRUMENTATION

3.1 Test Stand

The Single Rotor Helicopter Model is designed as a fully integrated system, containing necessary power plants, controls and data measuring transducers to simulate any desired configuration of conventional helicopter or isolated rotor. Figure 3.1 shows the arrangement of the motors, transmissions, controls, balances and air supply systems. The main rotor drive consists of a package of three (3) Tech. Development Air Motors, developing a total of 400 shp from dried compressed air at up to 350 psi and mass flow up to 6 lb/sec. The three motors drive the main rotor through a 9 to 1 reduction gearbox and bevel set, from which a maximum of 1600 rpm and minimum of 80 rpm is available. Additional gears are available to provide higher rotor rpm's for testing smaller diameter rotors. The rotor and controls are mounted on a six component total loads balance. Fairings enclose the controls and balance so that the loads measured by the balance are produced by the hub and blades only. The model's shaft angle, collective and cyclic are remotely controlled. The operational range of the shaft angle is from 45 degrees forward to 10 degrees aft.

3.2 Model Details

The testing was performed with a CH-47B/C type rotor which has a V23010-1.58 section from root to tip and a linear twist of -7.0

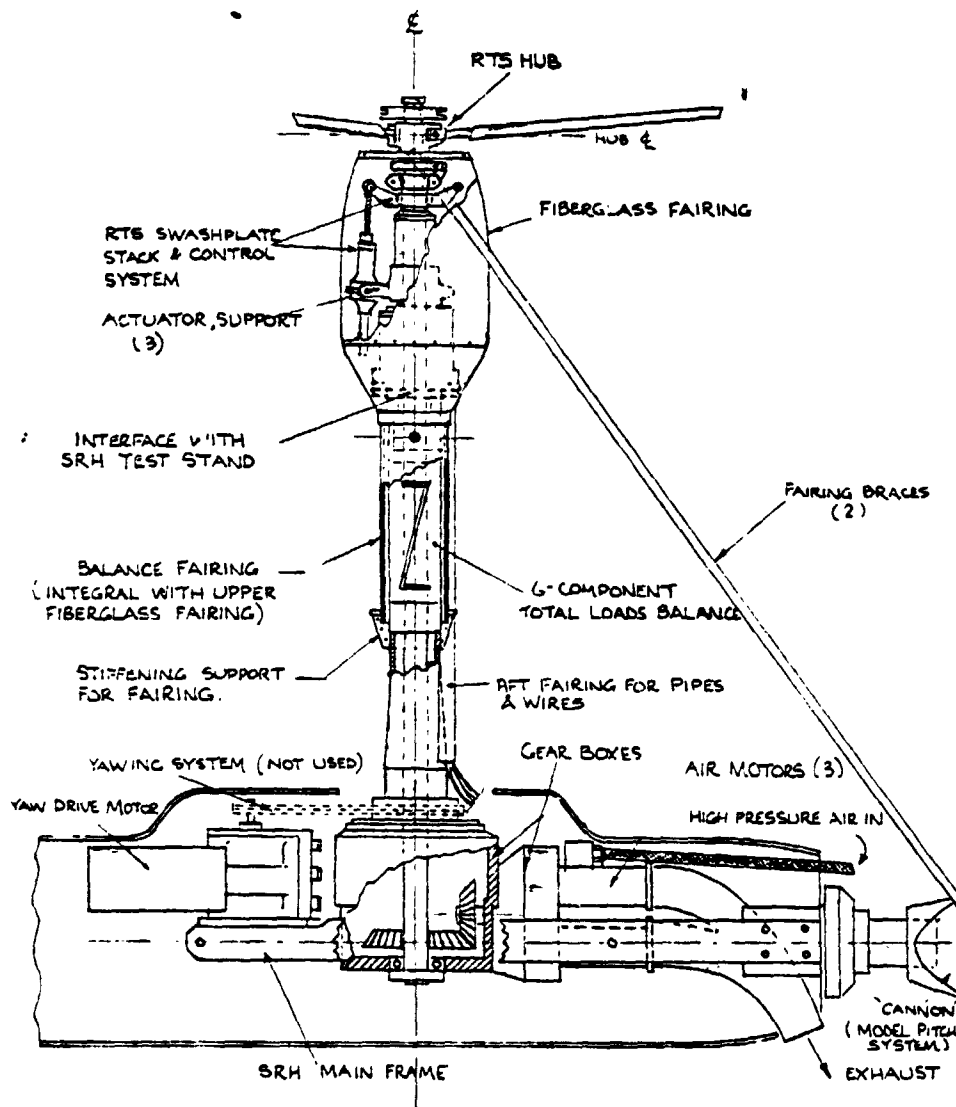


FIGURE 3.1 SRH ROTOR TEST STAND WITH RTS HUB AND STACK

degrees (actual blade thickness is 10.2%). The rotor hub has roller bearings for pitch and flap motion and elastomeric bearings for lead-lag motion. The blade physical properties are summarized in Table 3.1. The construction of the blades, as shown in Figure 3.2 is a single lay-up, molded type utilizing several types of fiberglass for skin and spar in conjunction with a balsa wood spar mandrel and a balsa wood trailing-edge box. A 0.05 inch diameter tantalum rod is incorporated in the leading edge as a balance weight. This type of molded construction results in accurate tolerance; within +0.0015, -0.0 inches over the leading edge, and within +0.003 and -0.0 inches overall. Blade natural frequency spectra for the blades derived from test data obtained from operation at various rpm's is presented in Figure 3.3.

TABLE 3.1
SUMMARY OF ROTOR BLADE PHYSICAL PROPERTIES

Airfoil Section	V23010-1.58 (t/c = .102)
Rotor I.D. Number	= S.N. 122, 123, 124, 101, 104, 105, 106
Radius	= 0.9017 m (2.9583 FT)
Chord	= 0.0583 m (0.1913 FT)
Flap Hinge Offset	= 0.0538 m (2.12 IN.)
Pitch Axis Location	= 0.0146 m (0.5738 IN.) 25% CHORD
Blade Attachment	= 0.0545 m (2.145 IN.)
Blade Twist	= -0.1222 rad (-7.0 degrees) LINEAR
Disc Area	= 2.554 m ² (27.4938 FT ²)
Number of Blades	= 3
Flap Inertia	= 0.0433 kgm ² (0.0319 slug-FT ²)
Weight Moment	= 0.0713 kgm (0.516 FT-LB)
Lock Number	= 6.7
Solidity	= .06175

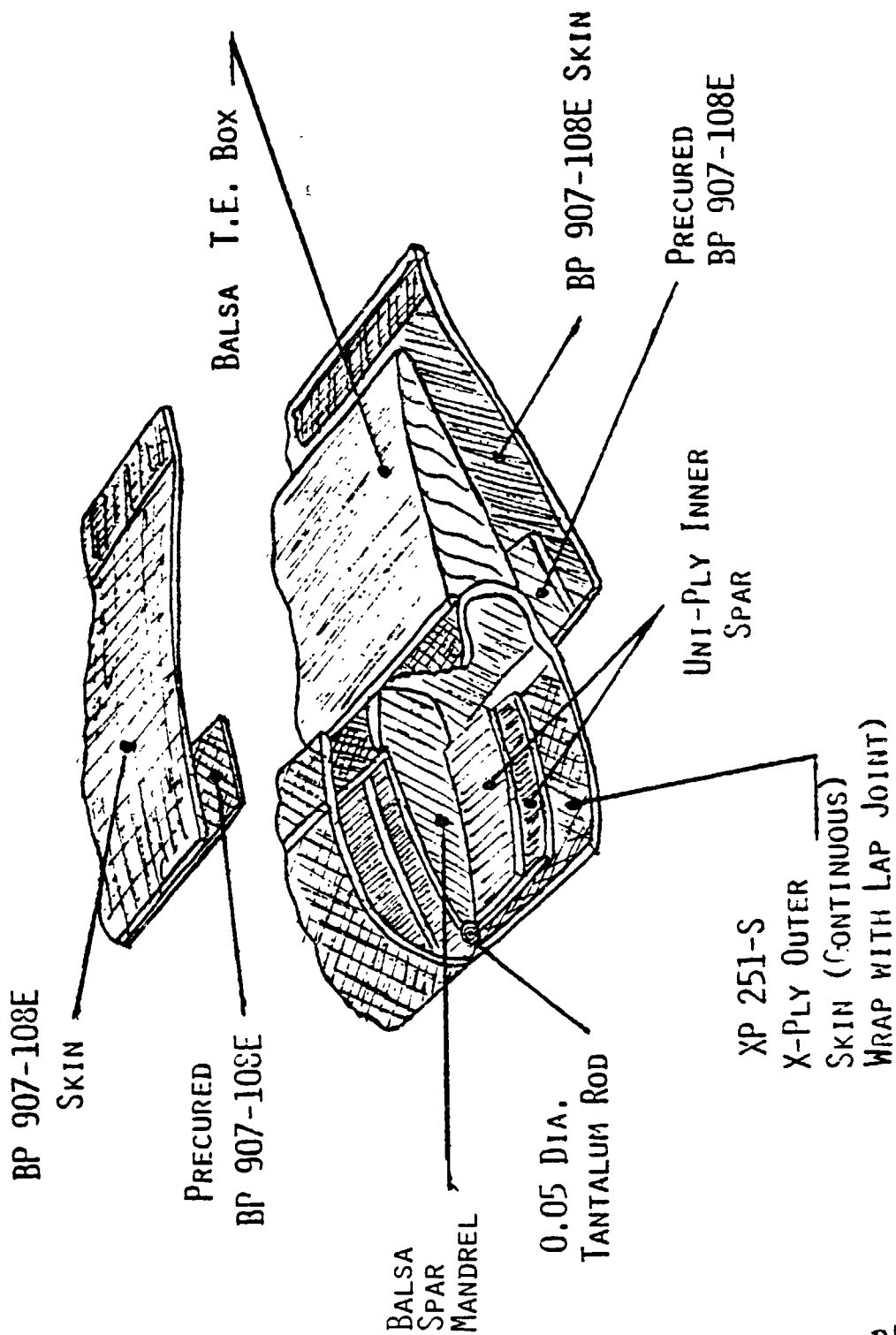


FIGURE 3.2 BLADE CONSTRUCTION

ORIGINAL PAGE IS
OF POOR QUALITY

3.3 Instrumentation

The major areas of instrumentation are the total loads balance, controls and the blade. Measurements recorded from each are discussed below and other instrumentation items installed for this test are also described in the following paragraphs.

Total Loads Balance

The total loads balance (BV-6054) is integral with the vertical strut. This balance measures six components of force and moment. The output signal is conditioned and then processed for weight tares and balance interactions in the computer to provide forces and coefficients.

Control Instrumentation

Rotor control positions of collective, longitudinal and lateral cyclic are instrumented to record the magnitude of the input controls. The collective and cyclic capability of the control system is presented in Figure 3.4 as longitudinal cyclic variation with collective at fixed levels of lateral cyclic. The root end of the blade is instrumented to provide the continuous measurement of blade pitch and blade flapping.

Rotor Blade Instrumentation

Three blades are fully instrumented (S/N 105, 106, 123), as indicated in Figure 3.5, with the following strain gages:

Flap bending - $r/R = .118, .222, .477, .778$

Chord bending - $r/R = .118, .522$

Blade torsion - $r/R = .118, .200, .500, .800$

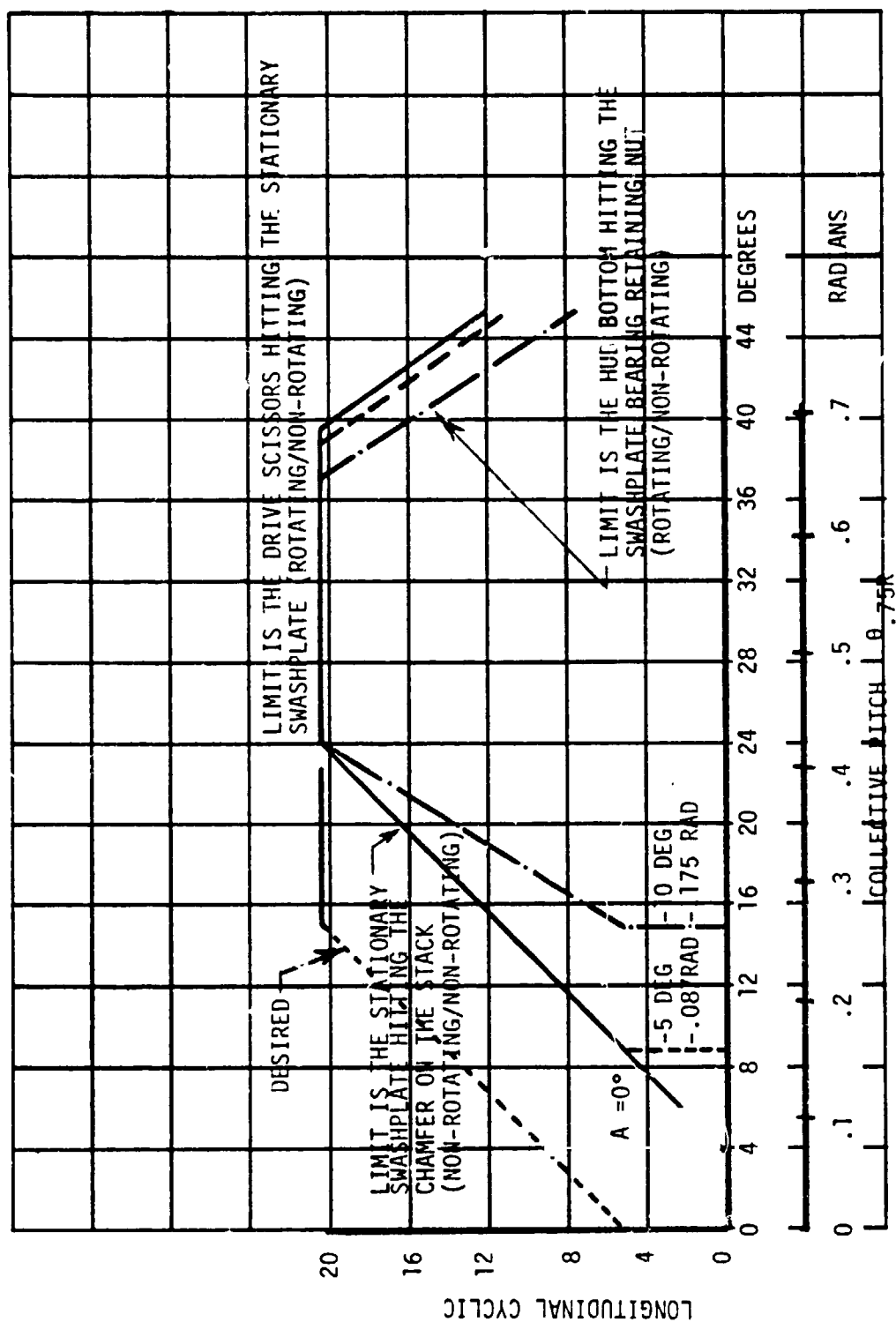


FIGURE 3.4 LONGITUDINAL AND LATERAL CYCLIC ENVELOPE AS INFLUENCED BY COLLECTIVE

Two other blades are partially instrumented with the root end safety of flight gages and the mid-span flap and chord bending gages.

Additional Instrumentation

Several temperature probes are installed in the gearbox, drive system bearings of the main rotor and the swashplate to enable the respective temperatures to be monitored during the test. Lubricating oil flow rates were also monitored.

4.0 DATA REDUCTION

The wind tunnel test of a rotor requires the measurement of net rotor forces and moments, rotor control positions and blade loads almost simultaneously. To achieve this, the data is sensed, multiplexed, processed then stored on magnetic tape and/or printed. The flow diagram of the wind tunnel data system used to accomplish this for the lift-propulsive force test is shown in Figure 4.1. Signals from the model and tunnel itself were routed as illustrated to an IBM 1800 computer for processing and data reduction. Computed results in standard engineering units and/or coefficient format were tabulated by a line printer and selected variables were plotted by the X-Y plotters. Final data was stored on magnetic tape for additional processing when necessary.

A control panel digital display of nine channels of processed data was available for setting up model test conditions or for monitoring purposes during the testing. Dynamic data of six quantities was continuously displayed on oscilloscopes to provide assistance in preventing model balance or rotor structural limits from being exceeded.

A data reduction program developed for Model VR096Q enabled the electrical signals to be transformed and the various tunnel parameters to be printed out on-line. In addition to these items, the maximum and minimum values, mean value and alternating component

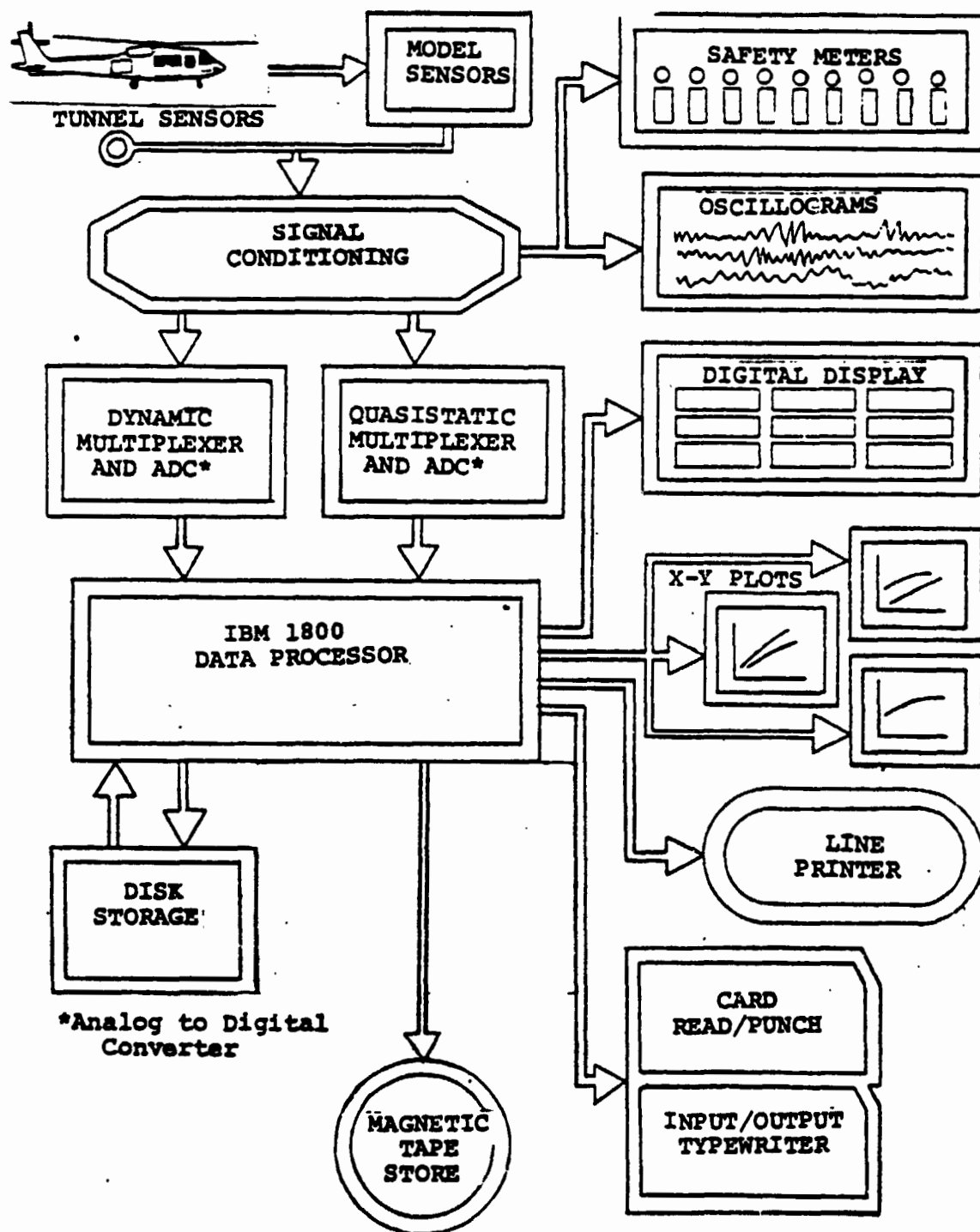


Figure 4.1. Data Acquisition System

of each selected blade load measurement were calculated and tabulated on-line. Root flap bending, chord bending and torsion loads, as well as, root flapping angle were harmonically analyzed on-line up through the first nine harmonics with the results being listed along with the other data. Subsequent to actual testing, reconstituted wave forms were developed from the dynamic data on the magnetic tapes.

At each test point, measurements are taken for computing and tabulating on-line the quantities listed. The listed balance forces and moments were consistent with the sign convention illustrated in Figure 4.2.

a) Tunnel and Model Parameters

Air density,	slugs/ft ³
Freestream dynamic pressure, q	lb/ft ²
Tunnel velocity (corrected), V	ft/sec
Tunnel static temperature, T _s	°F
Rotor advance ratio, $\mu' = \frac{V}{\Omega R}$	
Rotor collective angle, $\theta_{.75}$	deg
Rotor lateral cyclic angle, A _{1c}	deg
Rotor longitudinal cyclic angle, B _{1c}	deg
Rotor RPM	
Rotor shaft angle, α_s	deg
Rotor flappling angle, β	deg
Rotor lag angle, ζ	deg

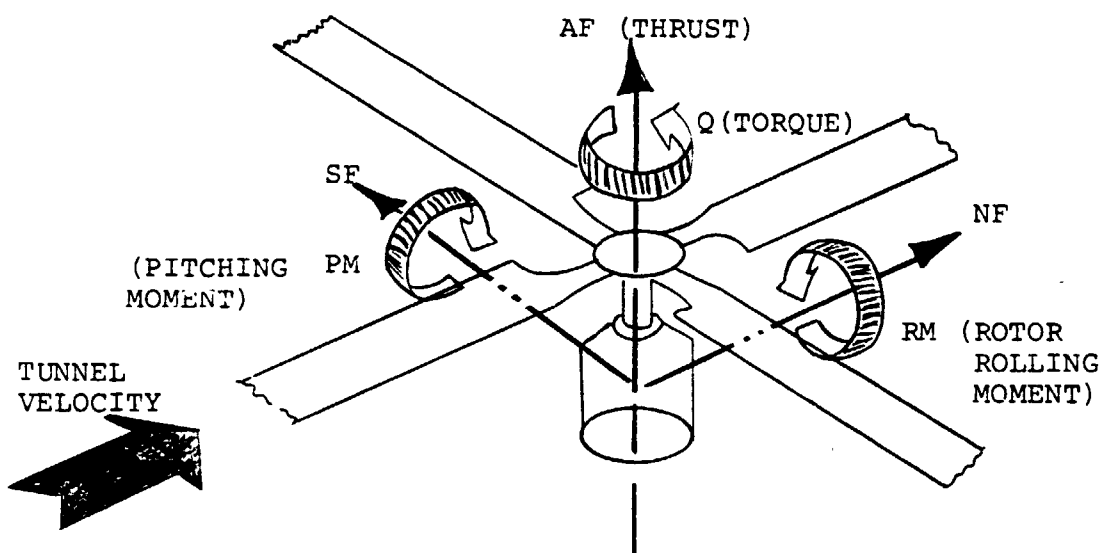


Figure 4.2. Model Force and Moment Convention

b) Total Loads Balance and Instrumented Shaft

Axial force (thrust), T	lb
Normal force, NF	lb
Side force, SF	lb
Pitching moment, PM	ft-lb
Yawing moment, YM	ft-lb
Shaft torque, Q	ft-lb

Forces and moments from balances were printed out on-line in engineering units in three successive forms: first, as forces and moments with the wind off zeros removed, balance interaction corrections applied and the weight tares removed.

Corrected main rotor balance forces and moments were reoriented into a standard aircraft convention system and transferred on-line to the hub center so that moments could be evaluated in the plane of the rotor. The transfer distance along the shaft axis from the balance center to the hub is 2.192 feet., The resolved shaft axis system hub forces and moments are noted in the following list along with their sign convention.

Main Rotor Hub Forces/Moments (Shaft Axis)

Thrust, T (positive: up)	lb
H force (positive: aft)	lb
Side force (positive: to the right)	lb
Hub pitching moment (positive: nose up)	ft-lb
Hub rolling moment (positive: advancing tip down)	ft-lb
Yawing moment (Q_f , friction torque)	ft-lb

Since the actual hub generated forces and moments were included in the rotor characteristics, it is necessary to establish hub tares and subtract them from the main rotor balance measurements. The hub tares were obtained from rotor-off runs conducted with the rotor shanks rotating at the normal operating speed. The rotor is then corrected for these tares and represents the second form of the rotor performance printout.

The third form of rotor data is presented on the printout in coefficient form. The rotor data is reduced on-line into coefficient form in the shaft axis system per the following terminology. Hub pitching moment, hub rolling moment and side force are retained in their more meaningful dimensional form.

$$\text{Main rotor thrust coefficient, } C_T/\sigma = \frac{T}{\rho (\Omega R)^2 A \sigma}$$

(where σ is the rotor solidity)

$$\text{Main rotor power coefficient, } C_P/\sigma = \frac{Q}{\rho (\Omega R)^2 A R \sigma}$$

Main rotor data is also reduced on-line into the following engineering units and non-dimensional forms in the wind axis system. Hub side force components are included when the model is yawed.

$$D_e = \frac{\pi RPM}{30V} (Q - Q_f) - X$$

Lift to equivalent drag ratio, L/D_e

$$\text{Rotor lift coefficient, } C_{Tl}/\sigma = \frac{L}{\rho (\Omega R)^2 A \sigma}$$

$$\text{Propulsive force coefficient, } \frac{X}{q d^2 \sigma} \quad \text{or} \quad \bar{x}/\sigma$$

5.0 TEST PROGRAM

The wind tunnel program for this lift and propulsive force limit test explores the high-speed regime to define the capabilities and limitations of the conventional rotor. Details of the test objectives, test procedures and operating conditions are described in the following sections along with the run log.

5.1 Test Objectives

The overall program objective was to define the cruise performance and determine if there were any limitations to lift and propulsive force. Test data obtained was to assist in the verification of the theoretical rotor analysis in the high-speed regime.

The general purpose of the test as defined above was divided into distinct tasks or objectives. These objectives are listed here in the order of importance to the overall program purpose:

1. Determine the maximum lift and propulsive force obtainable from an articulated rotor for advance ratios of 0.4 to 0.67.
2. Establish the blade load growth as the lift approaches the limit.
3. Obtain cruise rotor performance for advance ratios of 0.4 to 0.67.

4. Determine the sensitivity of the rotor forces and moments to rotor control inputs as the lift limit is approached.
5. Define the effect of advancing tip Mach number on these limits.
6. Determine the blade flapping response to a step input in cyclic as the lift limit is approached.

5.2 Test Procedures

Prior to performing any data runs, hub tares were measured at each of the test conditions. For these tare runs, the hub was rotating at the correct rpm and pitch sweeps were made at each dynamic pressure. This data was removed from the rotor data during reduction to provide the aerodynamic characteristics of just the rotor blades.

The blades were then installed and a series of runs made for track and balancing. This was done to eliminate the one per rev unbalance resulting from one blade being instrumented while the other two were not, and also to provide final adjustment to the pitch links to have all blades flying in track. Following this, a forward flight run was made at a fixed rotor lift coefficient and various rotor speeds to verify the model resonance points and insure the selected test rotor speeds were resonance free.

Two types of testing with rotor blades on were performed to achieve the objectives presented in Section 4.1: basic performance testing and rotor control power testing. The first, basic performance

testing, was accomplished by setting the rotor speed and tunnel speed to achieve the required advance ratio and advancing tip Mach number. At these conditions, a sweep in rotor lift coefficient was made at a fixed rotor propulsive force coefficient by increasing shaft angle and collective. At each shaft position, the collective was adjusted to provide the required propulsive force and the rotor blade flapping was reduced to a minimum with longitudinal and lateral cyclic. The rotor lift was increased until a limit is reached in blade loads or the rotor lift reached a maximum. A sensitivity to longitudinal cyclic was made to define the trade-off in rotor performance with blade flapping and hub moment.

The definition of a propulsive force limit was accomplished at a fixed rotor lift level. Shaft angle was decreased and the collective increased to maintain the desired lift level. Rotor blade flapping was reduced to a minimum with longitudinal and lateral cyclic. The propulsive force was increased until limited by blade loads, stall flutter or no further increase in propulsive force was achieved. This procedure was repeated at each lift level selected.

Rotor control testing consisted of excursions in longitudinal and lateral cyclic about the trimmed operating condition in the performance testing. Control power data from longitudinal cyclic and lateral cyclic variations were made only at 90 percent and 70 percent of the maximum rotor lift coefficient (C_T^1/σ). Control power characteristics were obtained at these two levels and provide insight into the amount of degradation in control that results at the maximum lift limit.

5.3 Test Operating Conditions

The basic tip speed utilized in the testing performed was 620 ft/sec. Additional testing was performed at tip speeds of 572 ft/sec and 665 ft/sec to define the effects of an advancing tip Mach number on the lift and propulsive force limits. These rotor tip speeds were selected to provide an increment in Mach number of 0.05.

Tunnel speeds up to 225 knots were achieved and result in a maximum advance ratio (μ) of 0.61 for the basic tip speed of 620 ft/sec. Advance ratios of 0.64 and 0.53 were achieved for the alternate tip speeds tested. A summary of the conditions tested is presented in Figure 5.1.

5.4 Run Log

A detail list of runs accomplished is presented in Table 5.1. For each run, the rotor tip speed advance ratio, rotor lift coefficient, propulsive force coefficient and tunnel speed are listed along with comments defining the purpose of each run.

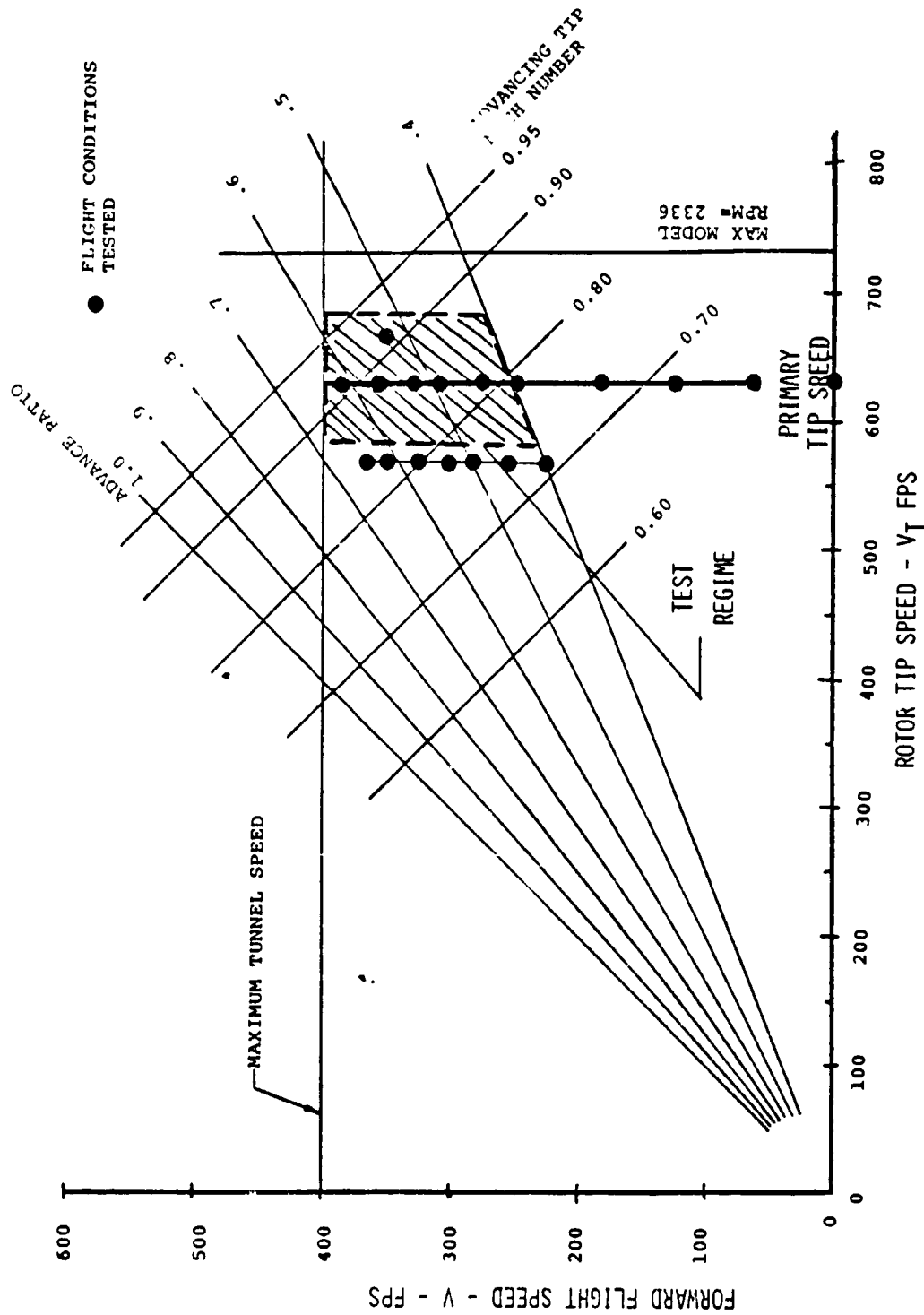


FIGURE 5.1 SUMMARY OF TEST OPERATING CONDITIONS

TABLE 5.1 RUN LOG

TYPE OF TESTING	RUN NO.	ROTOR TIP SPEED V_T	ADVANCE RATIO μ	ROTOR LIFT COEFF. C_L/σ	ROTOR PROPULSIVE FORCE COEFF $X/qd^2\sigma$	TUNNEL SPEED V	COMMENTS
BASELINE ROTOR CHARACTERISTICS	21	Range	0	.06	0	0	Blade Frequency Check
LIFT LIMIT AND CONTROL POWER TESTING	22 23 24	620 FPS	0	Range	- - -	0 0 0	Hover Performance and Lift Limits
	25 27 28 29 30	620 FPS	.10 .20 .20 .30 .40	Range	.05	62 FPS 124 FPS 124 FPS 186 FPS 248 FPS	Cruise Performance and Lift Limits at Baseline Rotor Tip Speed, Control Power Testing at 90% and 70% C_L/σ Max
	32 33 34	620 FPS	.40	Range	.01 .10 .20	248 FPS	
	35 36 37 38	620 FPS	.45	Range	.01 .05 .10 .20	279 FPS	
	39 40 41 42	620 FPS	.50	Range	.05 .025 .10 .20	310 FPS	
	50 51 52 53	620 FPS	.53	Range	.05 .025 .10 .20	329 FPS	
	54	620 FPS	.57	Range	.05	353 FPS	Control System Problem Destroyed the Blades
	55	Range	.30	.06	.05	For μ	Blade Frequency Check
	56 57	620 FPS	.57	Range	.05 .025	353 FPS	New set of blades torsional stiffness approx. 50% of standard blades and twist approx. 10.4° (an increase of 35%) burned out swashplate bearing.
	END OF PART 1						

TABLE 5.1 RUN LOG (continued)

TYPE OF TESTING	RUN NO.	ROTOR TIP SPEED V_T	ADVANCE RATIO μ	ROTOR LIFT COEFF. C_L/σ	ROTOR PROPULSIVE FORCE COEFF $X/qd^2\sigma$	TUNNEL SPEED V	COMMENTS
BASILINE ROTOR CHARACTERISTICS	219	Range			C	For μ	Blade Frequency Check
CHECK AND VERIFICATION RUNS	221 222 224 225 226 227	620 FPS	.53 .50 .50 .45	Range	.05 .05 .05 .05 .05	328 310 FPS 310 FPS 279 FPS	These runs were made to verify that the rotor performance on Part 1 and Part 2 were consistent and did not include any model fouling
LIFT LIMIT TESTING	228 245 246 249	620 FPS	.57	Range	.05 .025 .025 .10	353 FPS	Cruise performance and lift limits at baseline rotor tip speed
	229 248	620 FPS	.61	Range	.05 .075	378 FPS	
	250 251 252 253	570 FPS	.40 .45 .50 .53	Range	.05	228 FPS 256 FPS 285 FPS 302 FPS	Cruise performance and lift limits at reduced rotor tip speed to define effect of advancing tip Mach number
	256 255 254 257 258 259 260	570 FPS	.40 .45 .50 .53 .57 .61 .64	Range	.05	228 FPS 256 FPS 285 FPS 302 FPS 325 FPS 348 FPS 368 FPS	
PROPULSIVE FORCE LIMIT TESTING	230 231	620 FPS	.40	.06 .09	Range	248 FPS	Cruise performance and propulsive force limits at baseline tip speed
	243 244	620 FPS	.45	.06 .076	Range	279 FPS	
	232 233 234 235	620 FPS	.50	.06 .06 .08 .08	Range	311 FPS	

TABLE 5.1 RUN LOG (continued)

TYPE OF TESTING	RUN NO.	ROTOR TIP SPEED V_T	ADVANCE RATIO μ	ROTOR LIFT COEFF. C_L/σ	ROTOR PROPULSIVE FORCE COEFF. $X/qd^2\sigma$	TUNNEL SPEED V	COMMENTS
PROPULSIVE FORCE LIMIT TESTING	269 270 271 272	620 FPS	.50	.05	Range	311 FPS	Cruise performance and propulsive force limits at baseline tip speed
	268 240 266 241 242 257	620 FPS	.53	.05 .06 .08 .09 .09 .10	Range	328 FPS	
	254 265	620 FPS	.53	.05 .07	Range	328 FPS	
	236 237	620 FPS	.57	.06 .076	Range	353 FPS	
	239 238	620 FPS	.61	.04 .055	Range	378 FPS	
	276 277	665 FPS	.53	.06 .08	Range	352 FPS	Cruise performance and propulsive force limits at increased tip speed
	273 274	620 FPS	Range	.08	.05	For μ	Testing to represent a speed sweep for a specific configuration
END OF PART 2							

ORIGINAL PAGE IS
OF POOR QUALITY

6.0 TEST DATA OPERATION

As defined in Section 5, the overall program objective was to define the performance characteristics of a conventional helicopter rotor in high speed forward flight. Six specific test objectives were presented in Section 5.3, in order of priority, and will be discussed in the following sections. Additional areas of test data analysis are included that examine the rotor operation in and out of stall, summarize the model performance and indicate the importance of drag cleanup, correlate theory and test data and show the impact of reduced torsional stiffness.

For the testing and data analysis, the primary rotor tip speed is 620 ft/sec (189 m/sec) and a propulsive requirement defined in coefficient form is $X/qd^2\sigma = 0.05$ which is representative of an advanced helicopter level of drag cleanup. Variation in propulsive force and rotor tip speed are examined to show the impact on the basic trends defined.

6.1 Lift and Propulsive Force Limits

Test Objective 1: Determine the maximum lift and propulsive force obtainable from an articulated rotor for advance ratios of 0.4 to 0.67.

As defined in Section 5.2, a sweep in rotor lift was made at a fixed rotor propulsive force coefficient. The rotor lift was increased until a limit defined by aerodynamic capability, blade loads or control capability was reached. Since collective pitch defined the rotor lift and shaft angle of attack controlled the rotor propulsive force, the variation of rotor lift with collective pitch was used to establish an aerodynamic limitation on lift. Figure 6.1.1 presents a typical variation of rotor lift coefficient (C_T/σ) with collective pitch ($\theta, 75R$) at an advance ratio (μ) of 0.53 for three levels of propulsive force coefficient ($X/qd^2\sigma$) of 0.025, 0.05 and 0.10. At the lower level of rotor lift coefficient, approximately 0.05, small changes in collective pitch were required to change rotor lift but large changes in shaft angle of attack were necessary. Beyond C_T/σ of 0.08 the sensitivity of rotor lift with collective pitch decreased and smaller changes were required in shaft angle of attack. As shown in Figure 6.1.1 there is a point where further increases in collective pitch produces either no change or a decrease in rotor lift coefficient, indicating the lift is limited by the aerodynamic capability of this model rotor system.

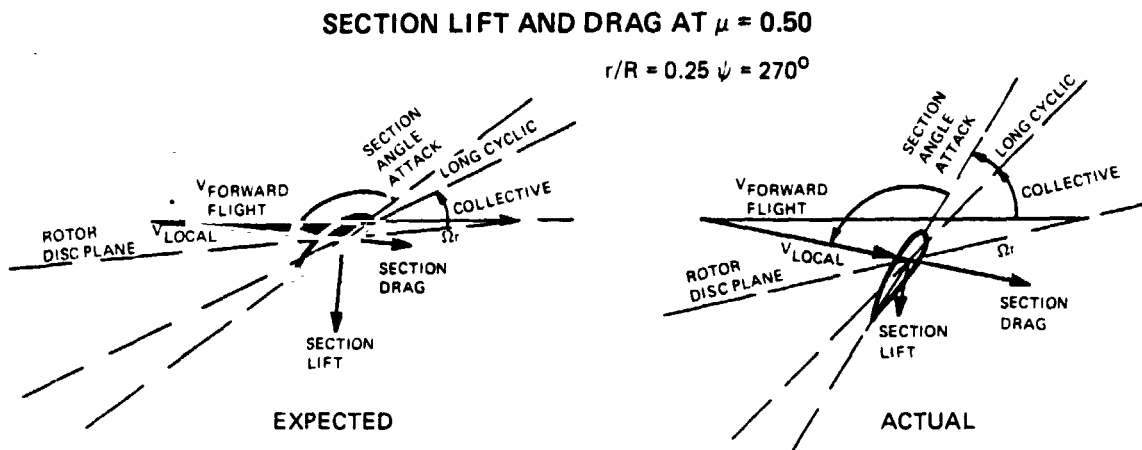
Having demonstrated an aerodynamic limit in lift, it is necessary to examine the blade loads to insure that a load limit has not been reached or exceeded. The most critical load is alternating blade root torsion, therefore, the corresponding variation of alternating blade root torsion load with rotor lift coefficient must be monitored at the same time to insure that the limit of 50 in.lb. was not exceeded. Figure 6.1.2 presents this variation but the maximum load indicated was approximately 60 percent of the limit. Since the lift was not limited by loads and we reached an aerodynamic limitation there was obviously no control system limitation for this case. There were only a few cases where longitudinal and lateral cyclic capability limited the testing and there were no limitations imposed on the testing by blade loads.

A summary of the rotor lift limit for the basic propulsive force coefficient of 0.05 is presented in Figure 6.1.3 from hover ($\mu = 0.0$) to 225 knots ($\mu = 0.61$). The lift limit shown at $\mu = 0.0$ was defined by the maximum collective pitch attainable with the normal length pitch links. For the high speed testing a set of long pitch links were used but no hover data was obtained with them. The trend of lift limit with advance ratio is approximately linear up to a $\mu = 0.35$, beyond this value the lift decreases rapidly to a C_T/σ of 0.098 at $\mu = 0.45$. From $\mu = 0.45$ to 0.50 the lift limit rises rapidly and levels off at a value of $C_T/\sigma = 0.112$ out to $\mu = 0.53$. After this advance ratio the lift limit drops to C_T/σ of 0.072 at 225 knots ($\mu = 0.61$). The

decrease in lift limit with increasing advance ratio appears to be a result of the decrease in section $C_{l_{max}}$ with decreasing Mach number as occurs on the outboard retreating blade. Also the decrease in local velocity on the outboard section of the retreating blade defines lower dynamic pressure and the blade area outside of the reverse flow region becomes smaller causing the lift capability to fall off. To maintain minimum hub moments requires reducing the lift on the advancing blade, thereby, further reducing the lift capability of the rotor.

The reversal in the lift limit trend beyond advance ratio of 0.45 appears to be caused by a change in the type of stall and the region on the rotor disc where it occurs. It is also influenced by the increased area and dynamic pressure in the reverse flow but further data analysis and theoretical predictions are required to adequately define the reason for the resulting trend. A possible rationalization is offered here which is based on a small amount of predicted data obtained during the correlation and an estimation of what is happening as the advance ratio changes. As the advance ratio increases the local velocity and hence the dynamic pressure on the blade becomes greater in reverse flow and the blade area in reverse flow becomes greater producing larger lift and drag at each blade section. With the high shaft angles, collectives and longitudinal cyclic the resulting section angle of attack is significantly less than would be expected. This could result in the local lift and drag combining to produce less negative rotor lift and provide the increase in maximum

rotor lift between an advance ratio of 0.50 and 0.53 as shown below.



Also the reverse flow region is reduced significantly by the increased shaft angle, thereby producing a smaller degradation at high advance ratio than anticipated. Beyond an advance ratio of 0.53 the dynamic pressure and working blade area continue to increase in reverse flow. There is also a change in angle of attack produced by the increase in collective and longitudinal cyclic with advance ratio. The combined change in angle of attack dynamic pressure and blade area in reverse flow could result in both lift and drag acting in a direction that reduces lift, or the drag produces a significantly large component of negative rotor lift and offsets the positive contribution of local lift.

To provide some insight into the stall impact on the lift and the change in characteristics with advance ratio, an examination of the flap bending and torsion loads in Figures 6.2.15 through 6.2.22 were combined to provide a qualitative assessment of the

lift distribution radially and azimuthally. Figure 6.1.4 presents the lift distribution at an advance ratio of 0.20 for a moderate rotor lift coefficient of 0.1238 and at the lift limit of 0.1333. At $C_T'/\sigma = 0.1238$, the lift is produced inboard on the retreating side of the rotor and outboard on the forward portion of the rotor. There is a region of negative lift outboard in the first quadrant. As the rotor lift is increased to the limit, the lift distribution changes to that in the lower portion of the figure. The increase in lift is generated on the outboard portion of the rotor disc in the third and fourth quadrants. The increase in lift on the retreating side of the disc is accompanied by an increase in lift on the outboard end of the advancing blade. The high levels of lift shown in Figure 6.1.4 correspond to the regions of the rotor that have high nose down torsional loads representative of stall in Figure 6.2.15 as discussed in Section 6.2. Figure 6.1.5 presents a set of lift distributions for an advance ratio of 0.50. The upper part of the figure presents the radial and azimuthal distribution for a moderate level of lift, $C_T'/\sigma = 0.0894$. Lift on the inboard portion of the blade is high all the way around the azimuth except in part of the fourth and first quadrant where there is very little lift. This is where there is a slight nose up torsional load shown in Figure 6.2.17. Lift is produced outboard on the forward portion of the rotor disc. The outboard portion of the rotor in the fourth quadrant appears to be producing a moderate amount of negative lift. As the lift

is increased up toward the limit, the lift is increased in the inboard forward portion of the rotor and on the outboard aft portion of the rotor. The amount of negative lift generated on the inboard portion of the rotor appears to increase as indicated by the torsion and flap bending loads. On the outboard region of the rotor that had negative lift becomes smaller. Although qualitative, the lift distributions indicated would produce blade deflections that were representative of those observed visually during the testing.

As shown in Figure 6.1.1 the effect of propulsive force on the lift limit was also defined by the testing at advance ratios of 0.40 and above. A summary of the lift limit at propulsive force coefficients ($X/qd^2\sigma$) of 0.025, 0.10 and 0.20 is presented in Figure 6.1.6 and compared with the basic lift limit shown in Figure 6.1.3. Reducing the $X/qd^2\sigma$ to 0.025 resulted in no change between $\mu = 0.40$ and 0.50 but there was an increase in lift limit (C'_T/σ) of 0.008 at an advance ratio of 0.53. Increasing $X/qd^2\sigma$ from 0.05 to 0.10 resulted in a decrease in lift limit (C'_T/σ) of 0.01 between $\mu = 0.40$ to 0.50 and the decrement in lift limit (C'_T/σ) increases to 0.03 beyond an advance ratio of 0.50. Similar changes were established when the propulsive force coefficient was increased from 0.10 to 0.20.

To define the propulsive force limit, a sweep in propulsive force coefficient was made at a fixed level of rotor lift coefficient. As discussed previously in Section 5.2, the propulsive force was

increased until a limit was defined by aerodynamic capability, blade loads or control capability was reached. The variation of propulsive force coefficient with collective pitch was used for determining if there was an aerodynamic limit to propulsive force. Figure 6.1.7 presents this variation for an advance ratio of 0.40 and as indicated, the testing was limited at a level 9 to 10 times greater than the basic propulsive force by a physical limitation of the model - the lag stops. The lead-lag motion was not large (less than 2 degrees) but the steady lag was large at these high levels of propulsive force, thus causing the blade to bang on the lag stops. An increase in steady lag is demonstrated by an increase in rotor power or torque. Figure 6.1.8 presents the variation of rotor power coefficient with propulsive force coefficient and at the limits defined by the lag stops, the rotor power coefficients have increased by a factor of 4 over the power at the basic propulsive force. This increase represents a significant increase in steady lag. At all the advance ratios tested the maximum propulsive force obtained was limited in the same manner.

Propulsive force limits were obtained at two levels of lift at each advance ratio: 80 percent of the maximum lift and 60 percent of the maximum lift for a propulsive force coefficient of 0.05.

A summary of the propulsive force at the lag stop limits is shown in Figure 6.1.9 as an envelope of rotor lift and rotor propulsive coefficients that the model rotor can operate within. The lowest propulsive force capability demonstrated was at an advance ratio of 0.61 but this corresponds to a level of $X/qd^2\sigma$ of 0.105.

The lift limits that were defined in Figure 6.1.6 can also be presented as an operational envelope of rotor lift and rotor propulsive force coefficient. This has been done in Figure 6.1.10 and the restriction imposed by an advance ratio of 0.45 is almost as severe as operating at an advance ratio of 0.61. Further study of all the data at an advance ratio of 0.45 is required to determine the cause of reduced capability.

The maximum lift obtained at specific level of propulsive force or the maximum propulsive force obtained at fixed levels of rotor lift combine to establish a restriction on the operational capability of the model rotor system. This in essence is the combination of Figures 6.1.10 and 6.1.9 into an overall operational envelope and is presented in Figure 6.1.11.

Superimposed on Figure 6.1.11 is an equivalent flat plate drag area loading $GW/fe = 1500 \text{ lb/ft}^2$, a drag level representative of an advanced helicopter. This established the flight envelope for the model rotor system and specifies that the rotor can operate at a rotor lift coefficient $C_L'/\sigma = 0.10$ up to an advance ratio of 0.57 or 210 knots. Flight at an advance ratio of 0.61 or 225 knots can be achieved when operating at a $C_L'/\sigma = 0.08$. This answers the repeatedly asked question - can the conventional rotor operate at useful lift levels in high speed forward flight without auxiliary lift or auxiliary propulsion? - with a firm YES.

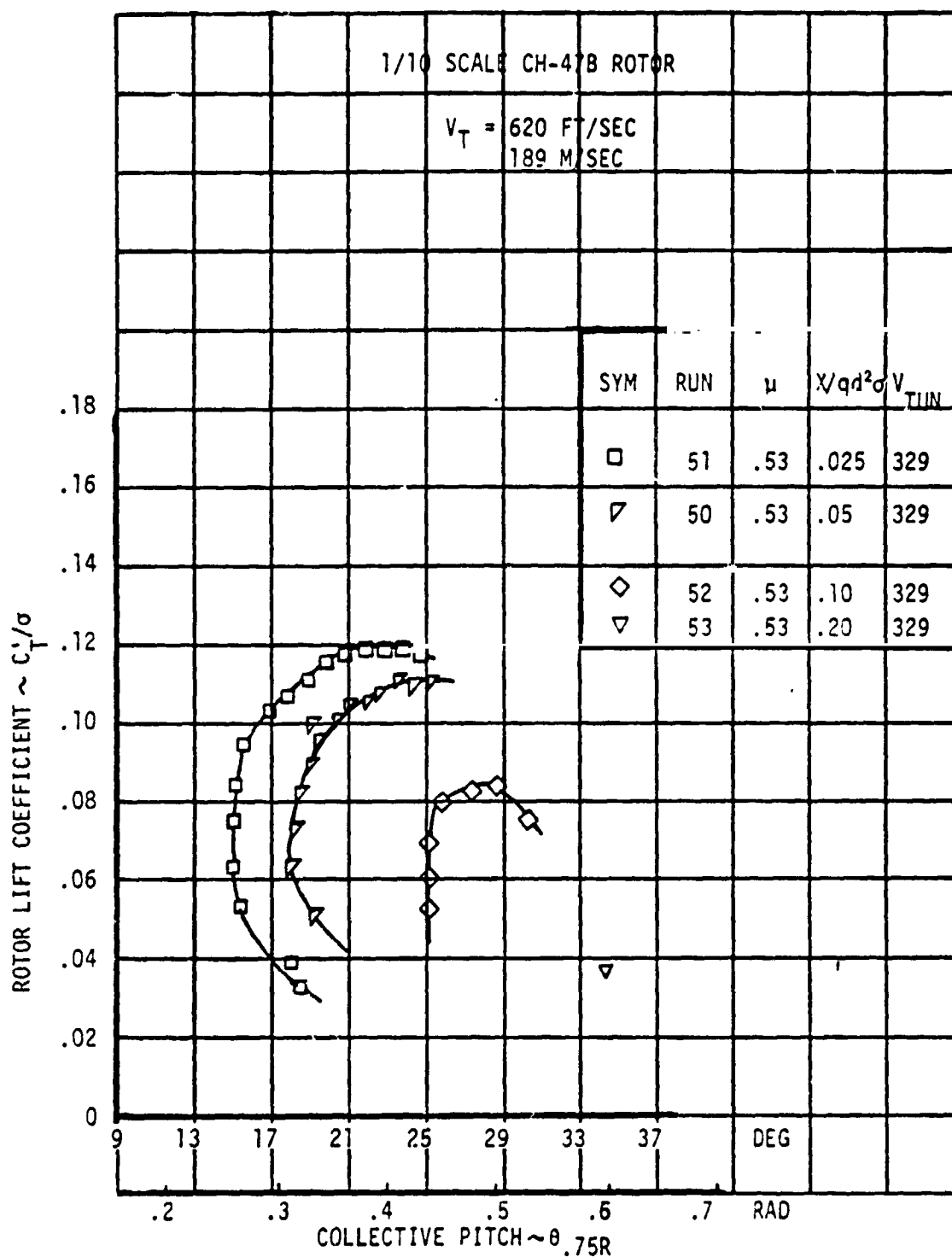


FIGURE 6.1.1 LIFT LIMIT DEFINED BY AERODYNAMIC CAPABILITY

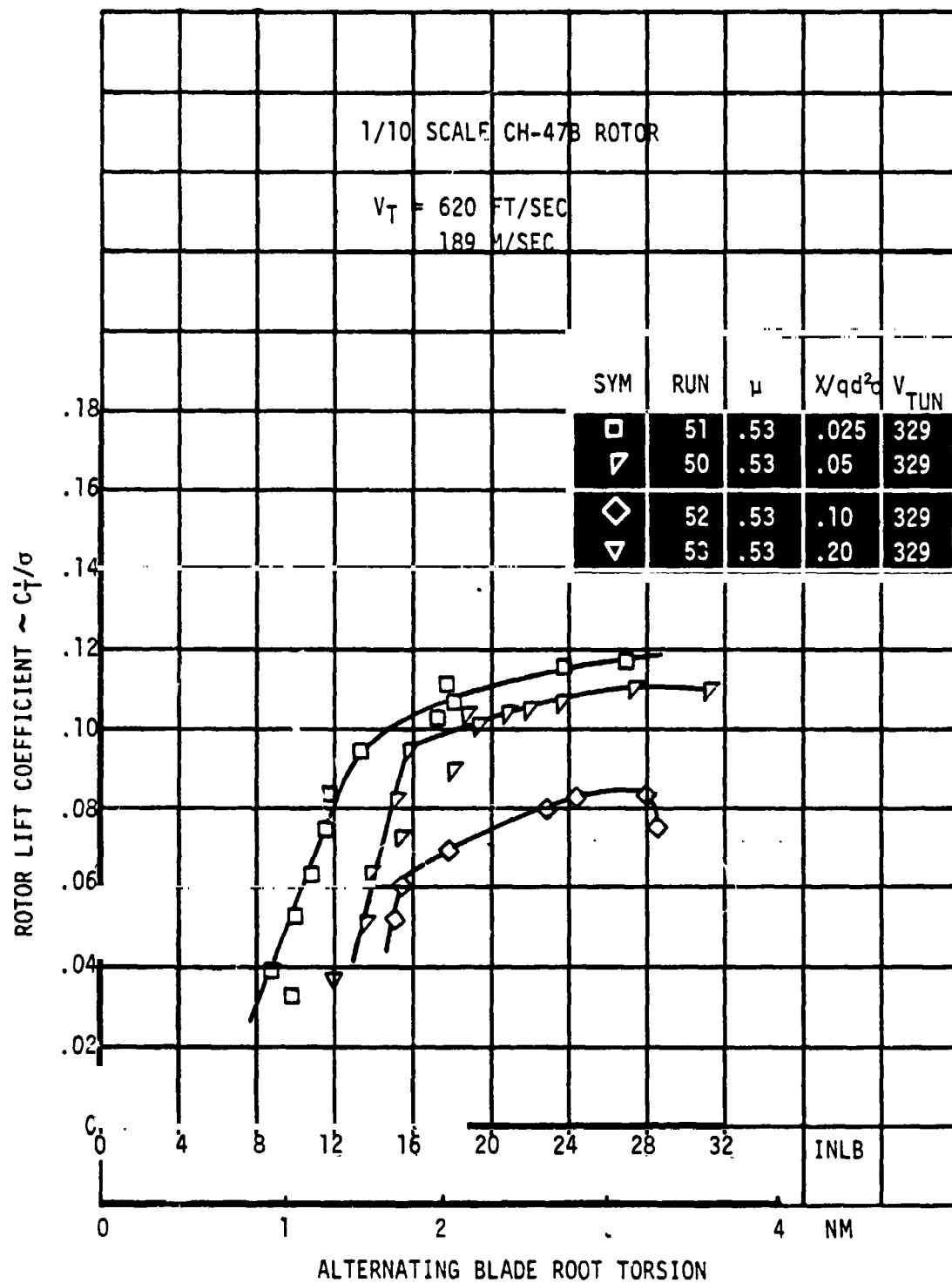


FIGURE 6.1.2 LIFT LIMIT NOT DEFINED BY BLADE LOADS

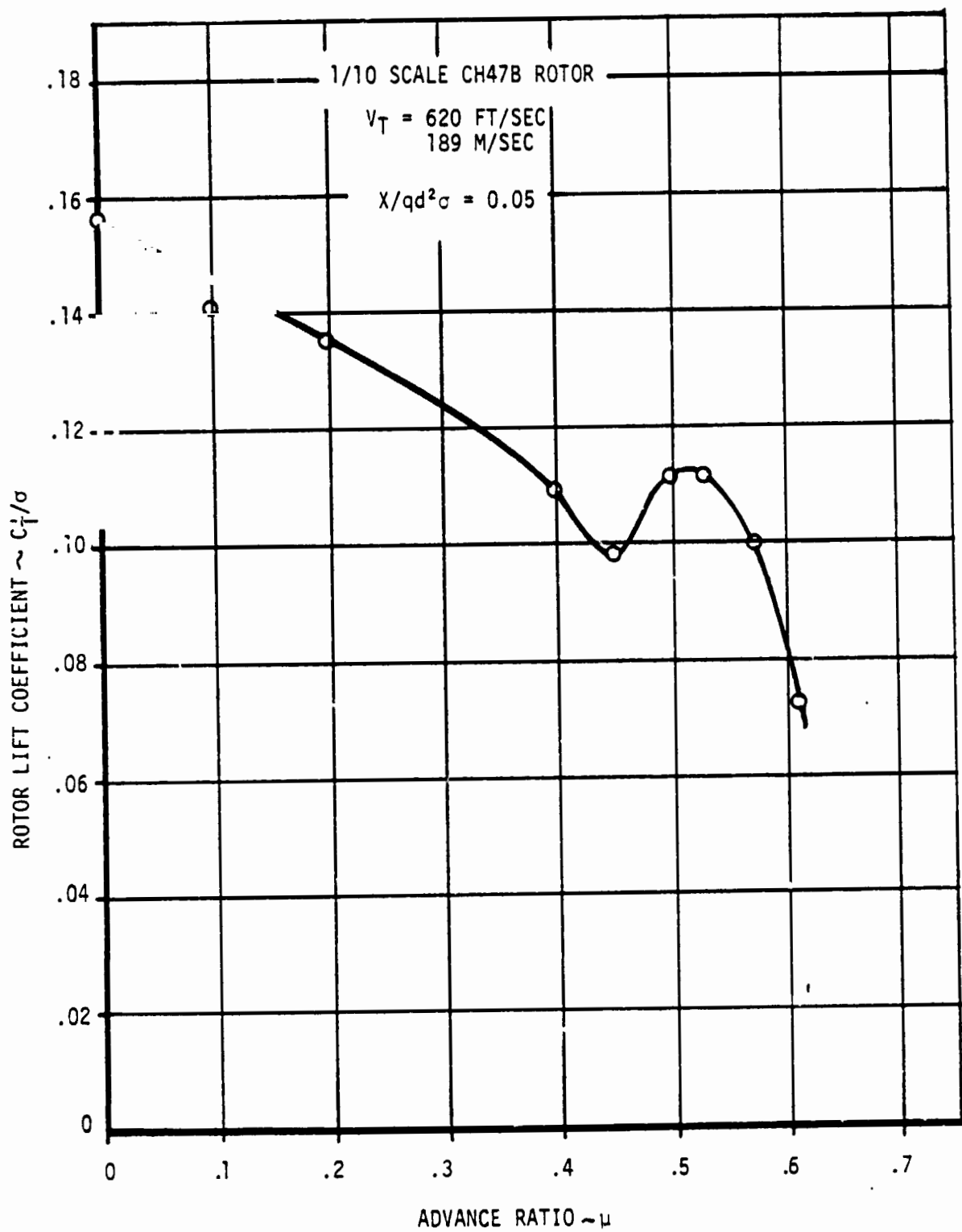


FIGURE 6.1.3 MAXIMUM LIFT LIMIT

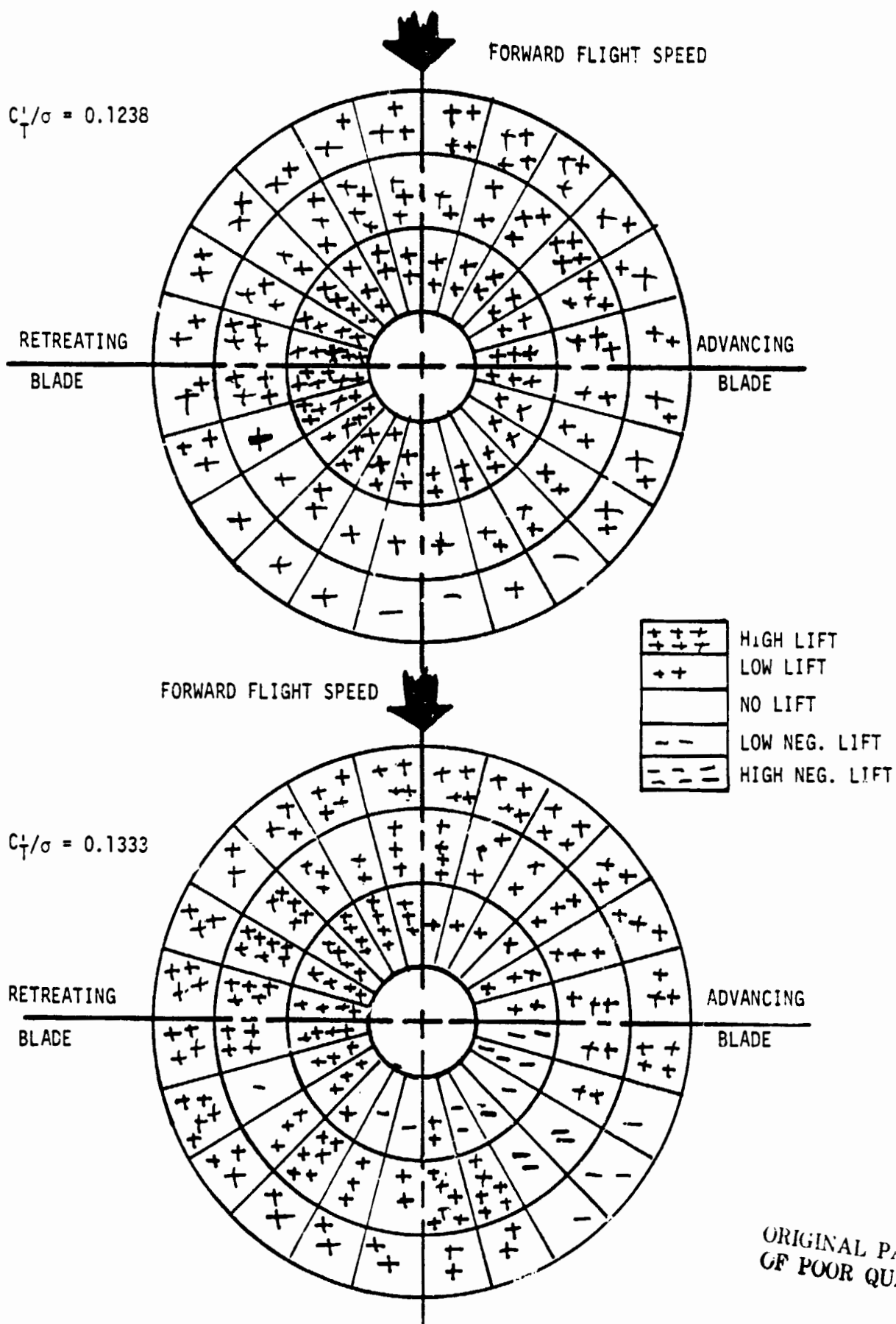


FIGURE 6.1.4 LIFT DISTRIBUTION ESTIMATED FROM TORSION LOADS
 AT $\mu = 0.20$ AND $X/qd^2\sigma = 0.05$

ORIGINAL PAGE IS
 OF POOR QUALITY

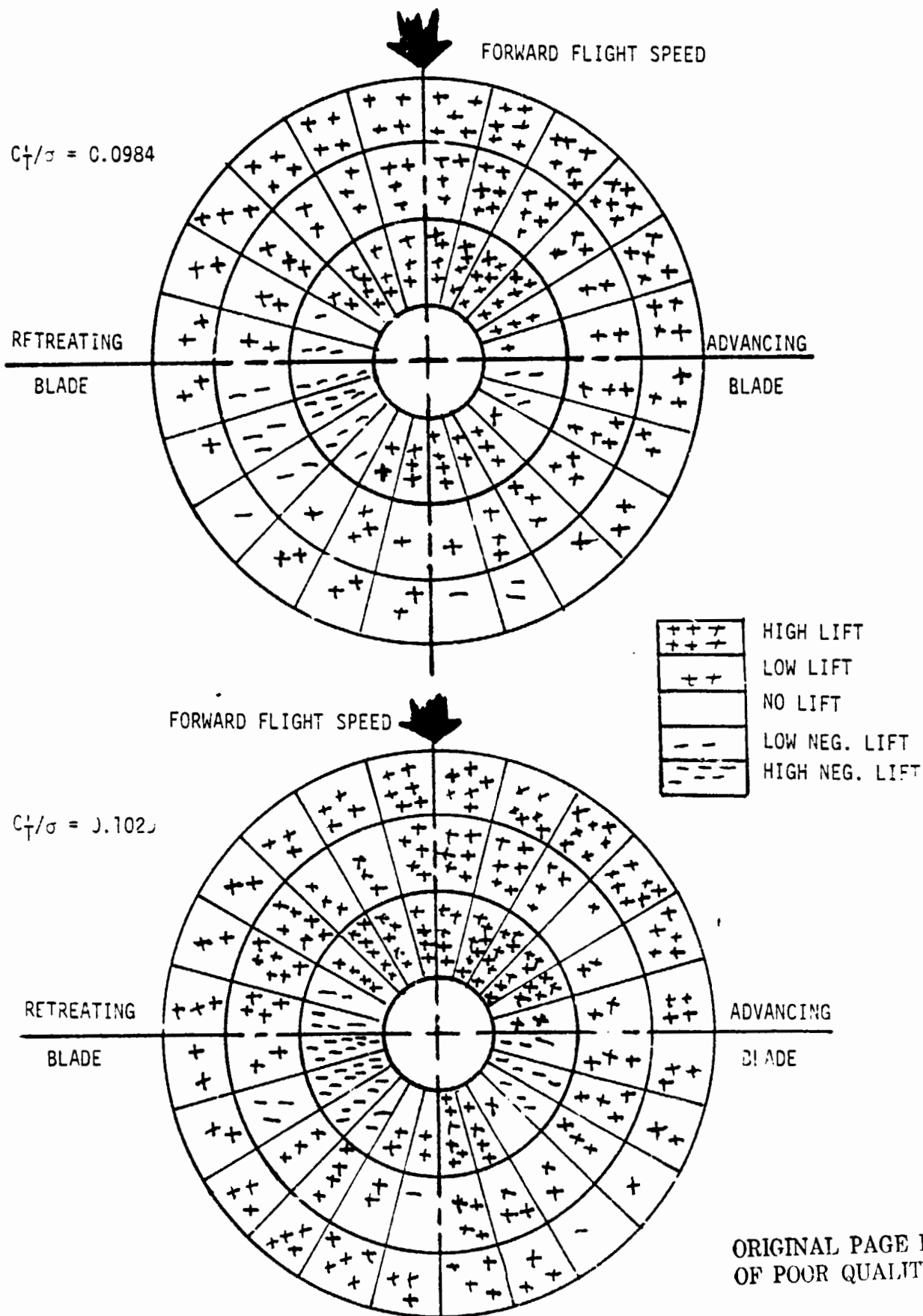


FIGURE 6.1.5 LIFT DISTRIBUTION ESTIMATED FROM TORSION LOADS AT
 $\mu = 0.50$ AND $X/qd^2\sigma = 0.05$

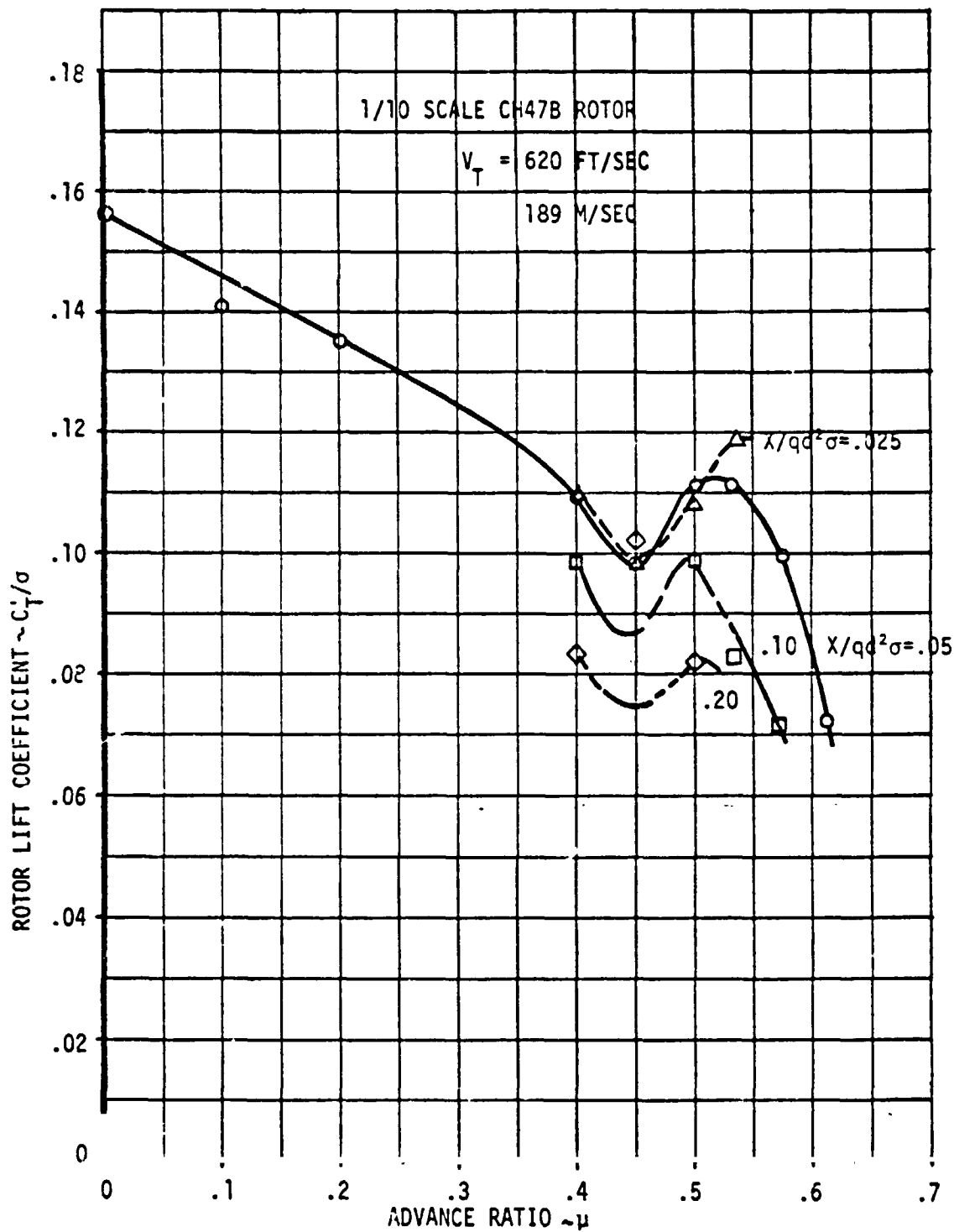


FIGURE 6.1.6 EFFECT OF PROPULSIVE FORCE REQUIREMENTS ON MAXIMUM LIFT LIMIT

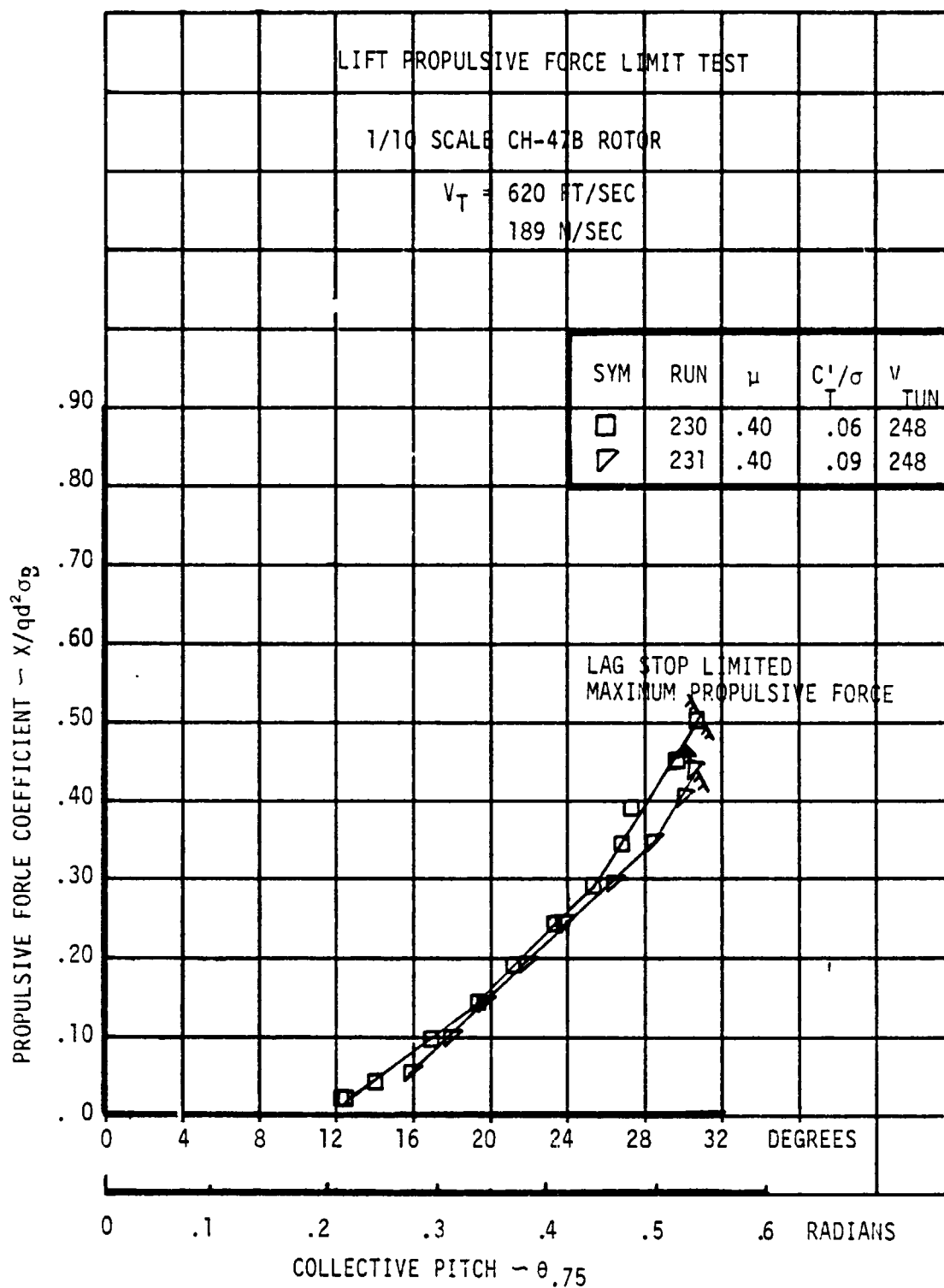


FIGURE 6.1.7 PROPULSIVE FORCE LIMIT NOT DEFINED BY STALL

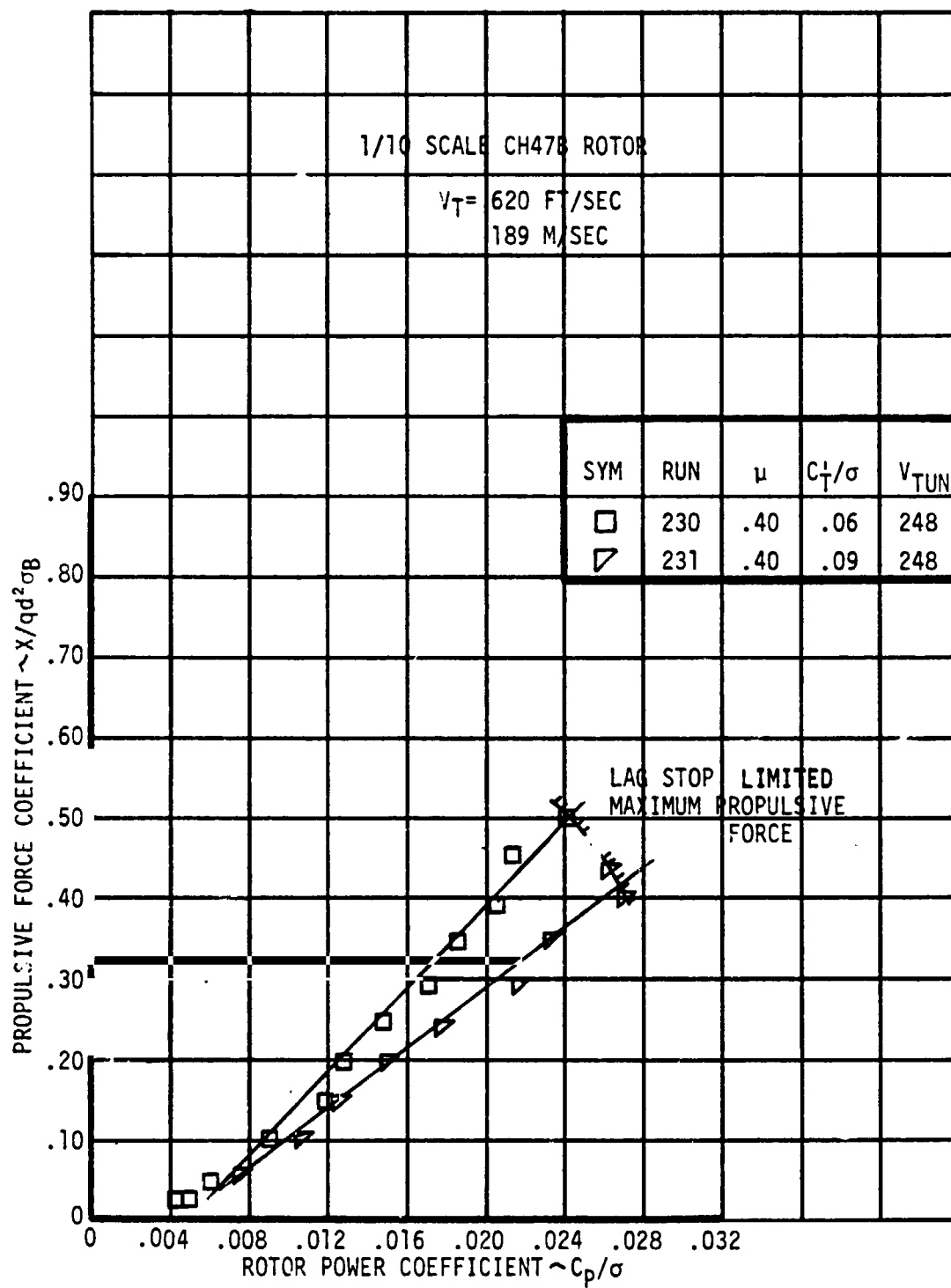


FIGURE 6.1.8 PROPULSIVE FORCE LIMIT NOT DEFINED BY AERODYNAMICS

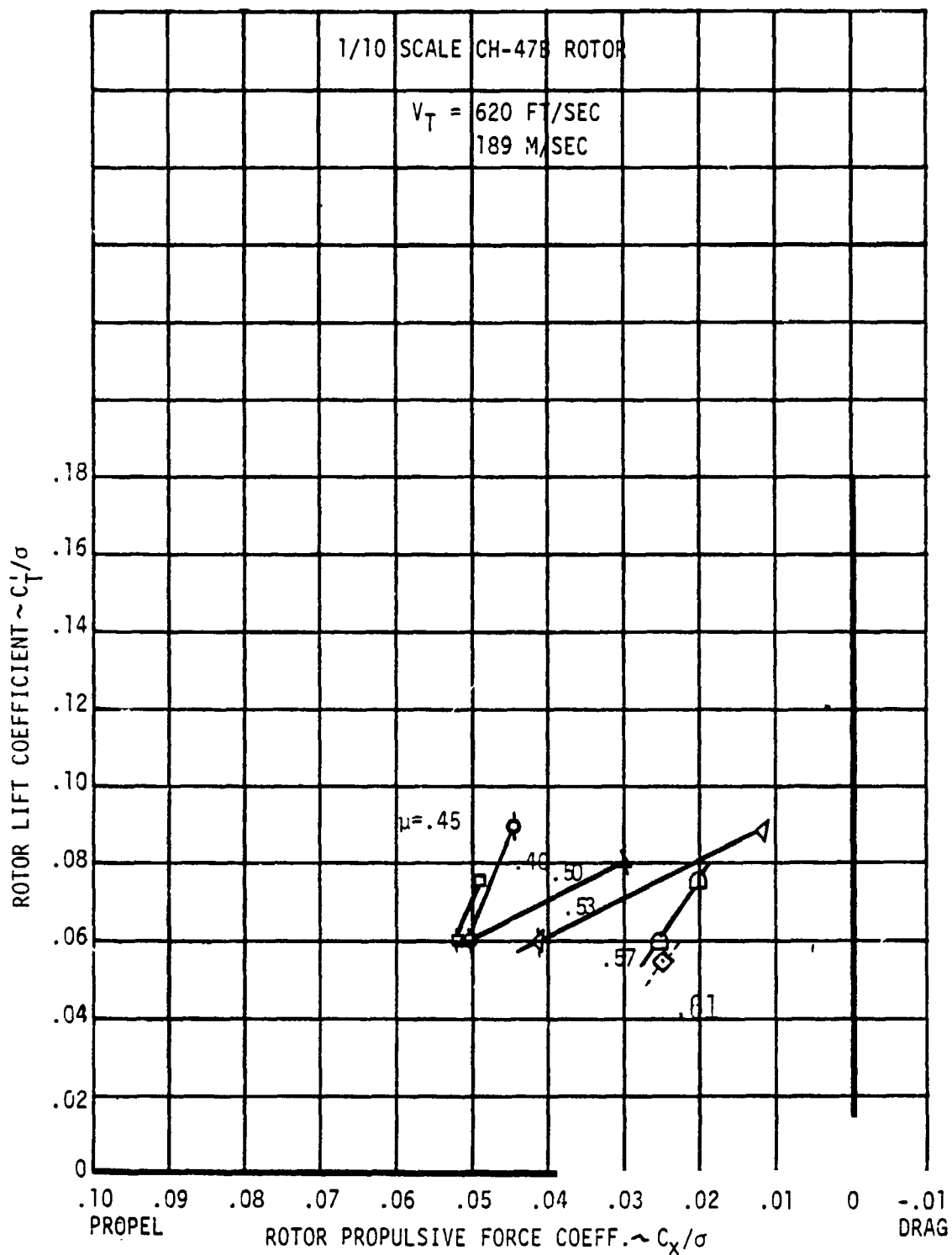
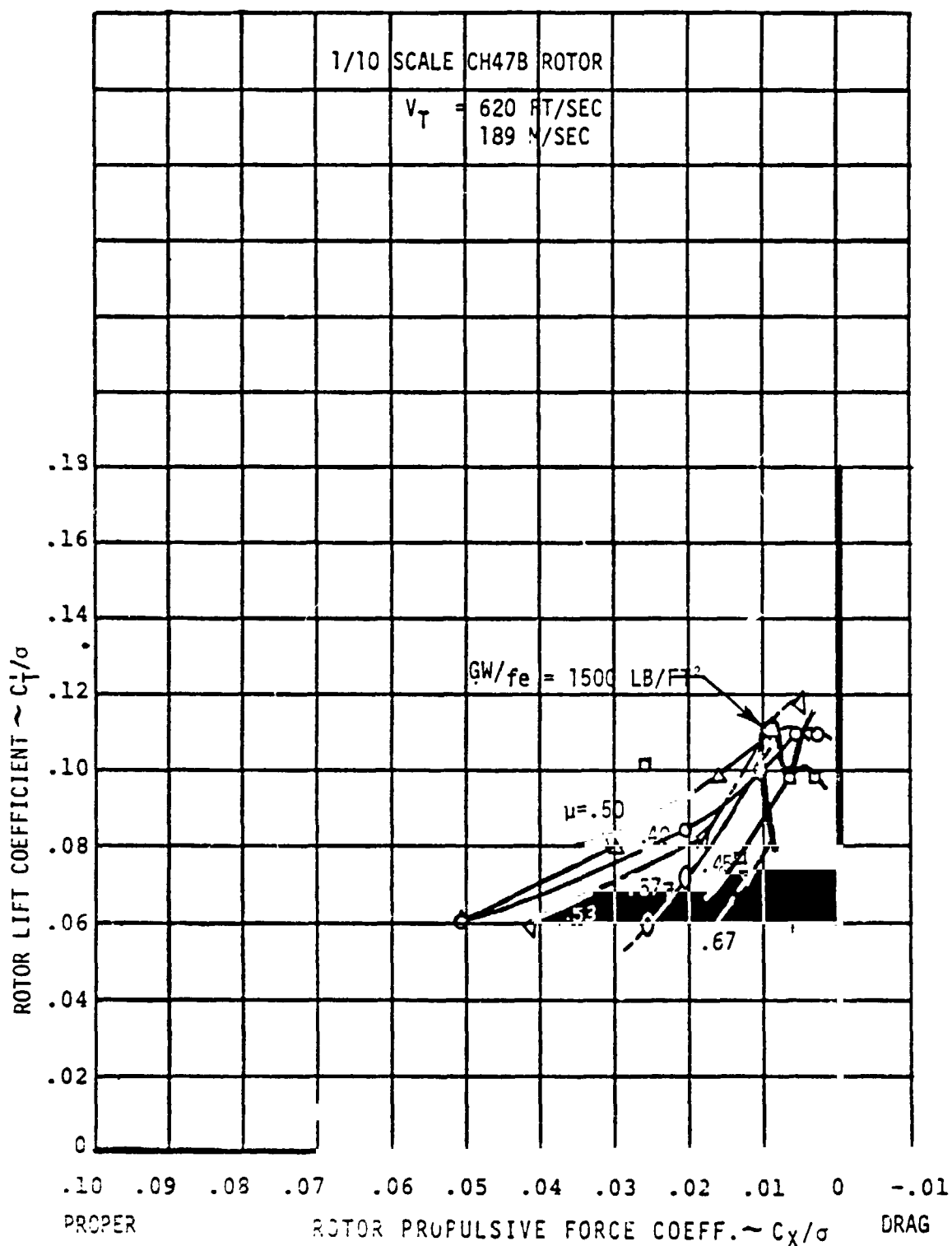


Figure 6.1. MAXIMUM PROPULSIVE FORCE LIMIT ACHIEVED DURING TESTING
LIMIT DEFINED BY LAG STOP





6.1.11

DRIVE FORCE LIMIT

6.2 Blade Load Growth Approaching Limits

Test Objective 2: Establish the blade load growth as the lift approaches the limit

Before discussing the load characteristics, it is necessary to establish the blade frequency trends with RPM to insure that there are no critical resonances at the operating conditions. The frequency spectrum for the model rotor blade, as shown in Figure 6.2.1, was obtained from an RPM sweep at an advance ratio of 0.20 and a rotor lift coefficient of 0.10. The first torsion mode and six per rev coalesce at 2100 RPM and the third flap mode and seven per rev also coalesce at 2100 RPM, but normal operation at the basic tip speed of 620 ft/sec is at 2005 RPM. This is sufficiently removed from the resonances to avoid severe load amplification. At the alternate tip speed of 570 ft/sec, a rotor speed of 1840 RPM, there is a coalescence of the second chord mode with the eight per rev but this is not a critical resonance condition.

The loads of torsion, flap and chord bending were measured at ten locations on the blade as described in Section 3.3, presented in Appendix A and summarized in Figures 6.2.2 through 6.2.4. Of these loads, torsion was the load to be monitored most critically since it indicates the presence of stall and had the smallest margin with the anticipated loads. A summary of the alternating blade root torsion loads are presented in Figure 6.2.2

for a propulsive force coefficient ($X/qd^2\sigma$) of 0.05 at advance ratios of 0.0 to 0.61. The general trend exhibited a very slight increase in loads with rotor lift coefficients up to C_T^1/σ of approximately 0.09 and advance ratios of 0.50. At higher lift levels the growth in alternating root torsion significantly increase. There is a second change in the slope, becoming almost asymptotic, indicating a trend normally associated with stall and the lift limit. The growth in alternating flap and chord bending loads with rotor lift coefficient, as shown in Figures 6.2.3 and 6.2.4, were similar to the trends exhibited by torsion; i.e., as the maximum lift limit is approached, the loads increase rapidly.

The alternating torsion load presented in Figure 6.2.2 is at the blade root and is the integrated sum of the radial and azimuthal distribution of the alternating torsion loads. An examination of the radial distribution of the torsion load will provide some insight as to where the major portion of the alternating load is developed and the impact of approaching the lift limit has on this distribution. Figure 6.2.5 presents the radial distribution of alternating torsion loads for four levels of rotor lift ($C_T^1/\sigma = 0.0597, 0.0984, 0.1348$ and 0.1511) in hover ($\mu = 0.0$). The lowest three values of rotor lift show that major portion of the load is developed by the outboard half of the blade (r/R 0.50 to 1.00) and there is only a slight increase to the point where the blade ends ($r/R=0.20$). The growth in load with

increasing lift is very gradual but for the lift limit, shown in the upper part of the figure, there is an increase in load occurring outboard on the blade. Similar trends are exhibited for an advance ratio of 0.20 as shown in Figure 6.2.6 but the magnitude increases. At an advance ratio of 0.40, a typical load variation is shown for the outboard 20 percent of blade ($r/R = 0.80$ to 1.00) in Figure 6.2.7. The distinct difference in the distribution at $\mu = 0.4$ with that at $\mu = 0.20$ or 0.0 is demonstrated by the uniform increase in the alternating torsion load from the outboard station, $r/R = 0.80$ to the point where the blade ends $r/R = 0.20$. This may result from the direct trade in section pitching moment coefficient with section dynamic pressure. Figure 6.2.8 presents the radial distribution for an advance ratio of 0.50. Trends for the outboard half of the blade were similar to that shown for $\mu = 0.40$ with an increase in magnitude. The load growth between $r/R = 0.50$ to 0.20 is twice as great as that presented for $r/R = 0.80$ to 0.50 which appears to be the impact of the increased forward speed on the inboard portion of the blade either on the advancing or retreating blade. Figure 6.2.9 presents the data for an advance ratio of 0.57 and the trends shown are similar to those for $\mu = 0.50$.

To better understand the load growth with lift, the blade root torsion waveforms have been superimposed on the alternating root torsion loads of Figure 6.2.2 for the same advance ratios of Figures 6.2.5 to 6.2.9. Figure 6.2.10 presents the loads and

wave forms at four levels of rotor lift for hover ($\mu = 0.0$). The root torsion wave form is relatively uniform up to a rotor lift coefficient (C_T/σ) of 0.135. At $C_T/\sigma = 0.151$ there is a slight oscillation in the load on the retreating side of the rotor disc at a frequency of approximately 6/rev. The blade will respond at the torsional natural frequency if it is disturbed by a torsional load. The rotor encounters stall on the retreating blade, developing large nose down pitching moments once per rev; therefore, the blade will respond at the first torsional natural frequency - six per rev, as shown on the top wave form. Figure 6.2.11 presents similar data for an advance ratio of 0.20. Between $C_T/\sigma = 0.10$ and 0.125 there is a modest increase in torsion loads and the wave form presented for the rotor lift coefficient of 0.12 indicates an increase in nose down torsion load at a rotor azimuth of 270° . This is indicating a slight amount of stall on the retreating blade. For the top wave form, at the lift limit, there is a greater amount of nose down torsion load and the load is oscillating at the torsion frequency, 6/rev, on the retreating side of the rotor disc. At an advance ratio of 0.40 the torsion wave form of Figure 6.2.12 shows less nose down load at a rotor azimuth of 300 degrees even at low rotor lift ($C_T/\sigma = 0.06$). This is indicative of the blade operating at negative section angles of attack. When the rotor lift coefficient reaches 0.094 the change in nose down torsion load is very sharp indicating the possibility of negative stall. At the lift limit, $C_T/\sigma = 0.107$, there is a large nose down

torsion load at 240 degrees rotor azimuth, indicating conventional tip stall, and a sharp decrease in nose down load at 300 degrees rotor azimuth possibly reflecting more negative stall.

As the advance ratio is increased to 0.50, the blade torsion load becomes even positive at 300 degrees of rotor azimuth for rotor lift coefficients as low as 0.060, as established in Figure 6.2.13. As C_T'/σ is increased to 0.095 the magnitude of the root torsion load at a rotor azimuth of 300 degrees becomes more positive while the load at an azimuth angle (ψ) of 150 degrees becomes more negative. At the rotor lift limit ($C_T'/\sigma = 0.11$) the positive load at $\psi = 300$ degrees becomes more positive while there has developed an apparent region of stall near a rotor azimuth of 150 degrees and 240 degrees. For an advance ratio of 0.57 the alternating blade root torsion load and also the wave forms are presented in Figure 6.2.14. There is a large nose up load even at a low rotor lift coefficient of 0.060 and is significantly greater than that shown in Figure 6.2.13 for an advance ratio of 0.50. As the lift is increased to 0.087 there is the apparent stall region, defined by the two peaks in nose down load at a rotor azimuth of 150 degrees and 240 degrees. The load at 300 degrees rotor azimuth becomes a significant large nose up load.

The discussion has presented the radial distribution of the alternating load measured around the azimuth or the azimuthal distribution of the alternating blade root torsion load. In an effort

to combine both these discussions, the azimuthal variation of the outboard portion of the blade ($r/R=0.81$ to 1.00), mid blade ($r/R=0.50$ to 0.81) and the inboard portion of the blade ($r/R=0.12$ to 0.50) will be shown for selected lift levels at two advance ratios from the data just discussed. At an advance ratio of 0.20 the alternating root torsion loads of Figure 6.2.2 grow gradually with lift up to $C_T'/\sigma = 0.105$ then there is an increase in torsion load sensitivity with lift. Figure 6.2.15 will examine the region for a lift level of $C_T'/\sigma = 0.1238$ showing the three incremental torsional load variations around the azimuth. There is a uniform level of torsional load from 30 degrees to 270 degrees rotor azimuth with a slight increase between 140 degrees to 180 degrees and 270 degrees to 300 degrees. A very low level of torsion load is evident between 300 degrees to 30 degrees. The torsion load is almost constant around the azimuth for the mid portion of the blade. At the bottom of the figure the inboard torsion loads indicate an increase between 210 degrees and 330 degrees with a maximum at 270 degrees. This indicates that conventional stall is occurring in the region of the rotor with the greatest amount occurring at 270 degrees. From the blade midspan to the edge of the reverse flow region, the section angle of attack increases rapidly to 90 degrees. Where the angle is greater than that of stall, there is a large nose down section pitching moment coefficients but the dynamic pressure is low on the inboard portion of the blade, thereby producing a moderate increase in the torsion load.

Referring back to Figure 6.2.2 as the rotor lift is increased above $C_T/\sigma = 0.129$ the alternating load increases very rapidly, becoming almost asymptotic. It is necessary to determine the cause of this rapid increase in loads and how it is different from the load growth caused by the inboard conventional stall. Figure 6.2.16 presents the three azimuthal distributions for the lift limit $C_T/\sigma = 0.1333$. The outboard torsion load distribution is approximately uniform from 90 degrees all the way around to 30 degrees azimuth with an increase near 290 degrees possibly caused by stall. Between 30 degrees to 90 degrees the moment increased to a slightly positive value, usually the result of operating at negative angles of attack which would be expected with the lateral hub moments trimmed to zero. The mid blade distribution is approximately uniform between 40 degrees and 210 degrees but the remainder of the wave form shows three distinct peaks in the torsion load. The frequency of these nose down load growths is 6/rev which is the torsional natural frequency definitely establishing stall. The inboard wave form indicates a slight increase in the torsion load at 270 degrees, 315 degrees and 20 degrees azimuth which are the same regions where stall was exhibited on the mid blade trace and is possibly a carry-over of stall to the inboard portion of the blade. Therefore, the increase in the load sensitivity with lift is a result of stall shifting out to the mid and outboard portions of the blade.

Referring back to Figure 6.2.2 the alternating torsion load growth at an advance ratio of 0.50 shows a moderate sensitivity up to a lift level of $C_T'/\sigma = 0.095$ and beyond that level there is a sharp increase in the sensitivity. Are these load growth trends caused by stall occurring on the same areas of the blade? Figure 6.2.17 shows the three incremental torsional load variations comparable to those of Figure 6.2.15 but for a $C_T'/\sigma = 0.0894$ at $\mu = 0.50$. The outboard load variation shows a similar trend with a slight increase in magnitude. For the mid blade variation there is a significant increase in nose down load at 150 degrees azimuth typical of stall while at 300 degrees azimuth the load becomes slightly positive indicative of operation at negative section angle of attack. In the inboard portion of the blade there is an increase in nose down load at 150 degrees azimuth representing stall. At 300 degrees azimuth there is a large increase in nose up load indicating negative stall and operation at extremely large negative angles of attack. There is a decrease in torsion load to zero between 60 and 90 degrees on the inboard portion of the blade indicating operation at negative section angles of attack.

For operation beyond $C_T'/\sigma = 0.095$ is there a change in the stall characteristics, similar to that discussed for $\mu = 0.20$? Figure 6.2.18 presents the three incremental azimuthal variations in the torsion load at $C_T'/\sigma = 0.1029$ and $\mu = 0.50$. The outboard load torsional wave form shows operation at negative angle of attack between 30 degrees and 70 degrees with increased torsion load from 260 degrees to 300 degrees azimuth. Stall is exhibited in

6-2

the mid blade wave form by increased nose down loads at 240 degrees, 310 degrees and 20 degrees azimuth. The inboard portion indicates conventional stall at 150 degrees and 210 degrees while there is a very large increase in nose up torsion load at 300 degrees rotor azimuth. Again, the change in torsional load sensitivity at high levels of rotor lift results from a significant amount of conventional stall on the mid blade and inboard portion of the blade. The sensitivity for high levels of lift at an advance ratio of 0.50 is less than at 0.20 and appears to be the influence of the large negative stall on the inboard portion of the blade.

Similar characteristics can be generated with the flap bending loads which will indicate the regions of the rotor that are producing high lift and help confirm the regions where the rotor is encountering stall. Figures 6.2.19 to 6.2.22 present mid span and root flap bending wave forms and also an indication of the incremental outboard ($r/R=0.48$ to 1.00) and inboard ($r/R=0.12$ to 0.48) lift distribution around the azimuth. At a rotor lift coefficient of 0.1238 and an advance ratio of 0.20, there is a region of negative flap bending load between 90 degrees and 150 degrees azimuth for the outboard blade region as shown in Figure 6.2.19. For the inboard portion of the blade there is a region of very high flap bending loads between 60 degrees and 150 degrees and slightly reduced load level from 150 degrees to

270 degrees azimuth. The high estimated lift on the inboard portion of the blade drops very rapidly after 270 degrees, indicative of the stall demonstrated by the torsion loads. The estimated lift or inboard flap bending load is higher between 60 degrees and 150 degrees than on the retreating blade, yet there is no stall indicated by the torsion loads. This is a result of the lift on the outboard portion of the blade and is not as uniform as assumed in the estimation of the contribution of the outboard loads to inboard loads. Figure 6.2.20 is for a rotor lift coefficient of 0.1333 and indicates high lift levels near 240 degrees, 300 degrees and 30 degrees suggesting the presence of stall on the inboard blade as indicated in Figure 6.2.16. The outboard lift level is higher between 180 degrees and 330 degrees azimuth indicating a possible cause for stall for this outboard section of the blade ($r/R=0.48$ to 1.00).

At the higher advance ratio of 0.50 the outboard flap bending load is negative between 90 degrees and 210 degrees rotor azimuth as shown by Figure 6.2.21 at a $C'_T/\sigma = 0.0894$. For the inboard portion of the blade the estimated high level of lift between 90 degrees and 180 degrees could produce the conventional stall indicated in Figure 6.2.17. The zero estimated lift at 270 degrees supports the positive torsion loads associated with negative stall. Figure 6.2.22 presents the flap bending loads and estimated lift for an advance ratio of 0.50 and a rotor lift

coefficient of 0.1029. The increase in lift on the outboard portion of the blade between 210 degrees and 330 degrees provide support to the mid blade stall indicated in Figure 6.2.18. The very high lift between 120 degrees and 240 degrees azimuth supports the conventional stall on the inboard blade while the negative lift or download occurring between 240 degrees and 270 degrees verifies the operation at large negative angles of attack and the negative stall defined in Figure 6.2.18 for the inboard section of the blade. This estimated lift distribution data in addition to the torsion data of Figures 6.2.15 through 6.2.18 provided the basis for the qualitative lift distributions presented in Section 6.1.

To summarize the results there is an inboard stall that produces a moderate increase load sensitivity with lift and a mid blade plus outboard stall that results in the almost asymptotic variation of loads with lift coefficient for low advance ratios. For the high advance ratios there is an inboard stall that has a higher sensitivity with lift than the low advance ratios have. For rotor lift levels near the lift limit there is a decrease in sensitivity to rotor lift for the higher advance ratio. This is a result of operating at negative section angles of attack, negative lift between 240 degrees and 270 degrees azimuth and positive section pitching moments alleviating the load growth with rotor lift. Addition analysis of the loads data in conjunction

with performance data must be accomplished. This data must be compared with predictions to substantiate the theory and help in developing an understanding of rotor operation in the high speed regime.

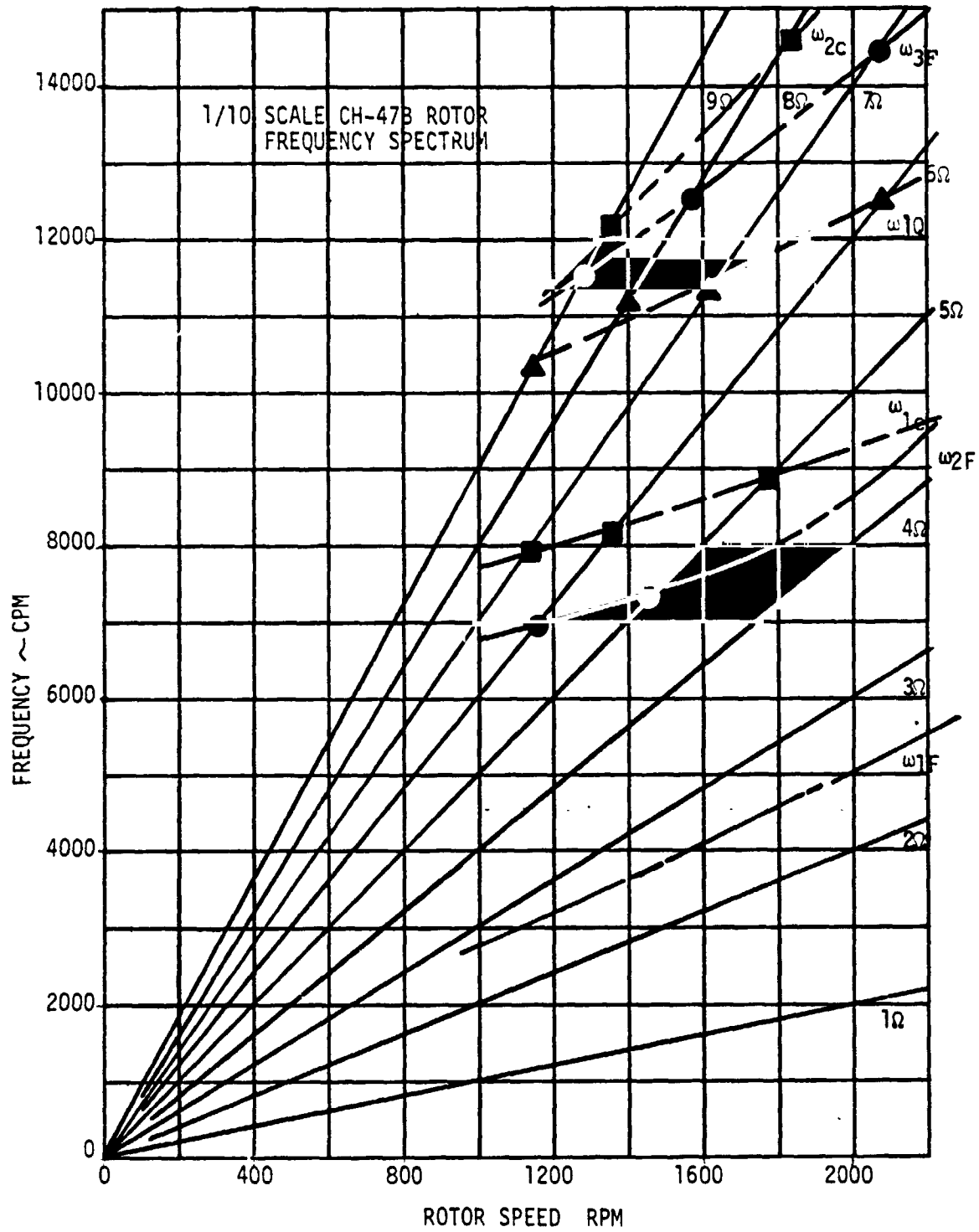


FIGURE 6.2.1 FREQUENCY SPECTRUM FOR 1/10 SCALE CH-47B ROTOR

ORIGINAL PAGE IS
OF POOR QUALITY

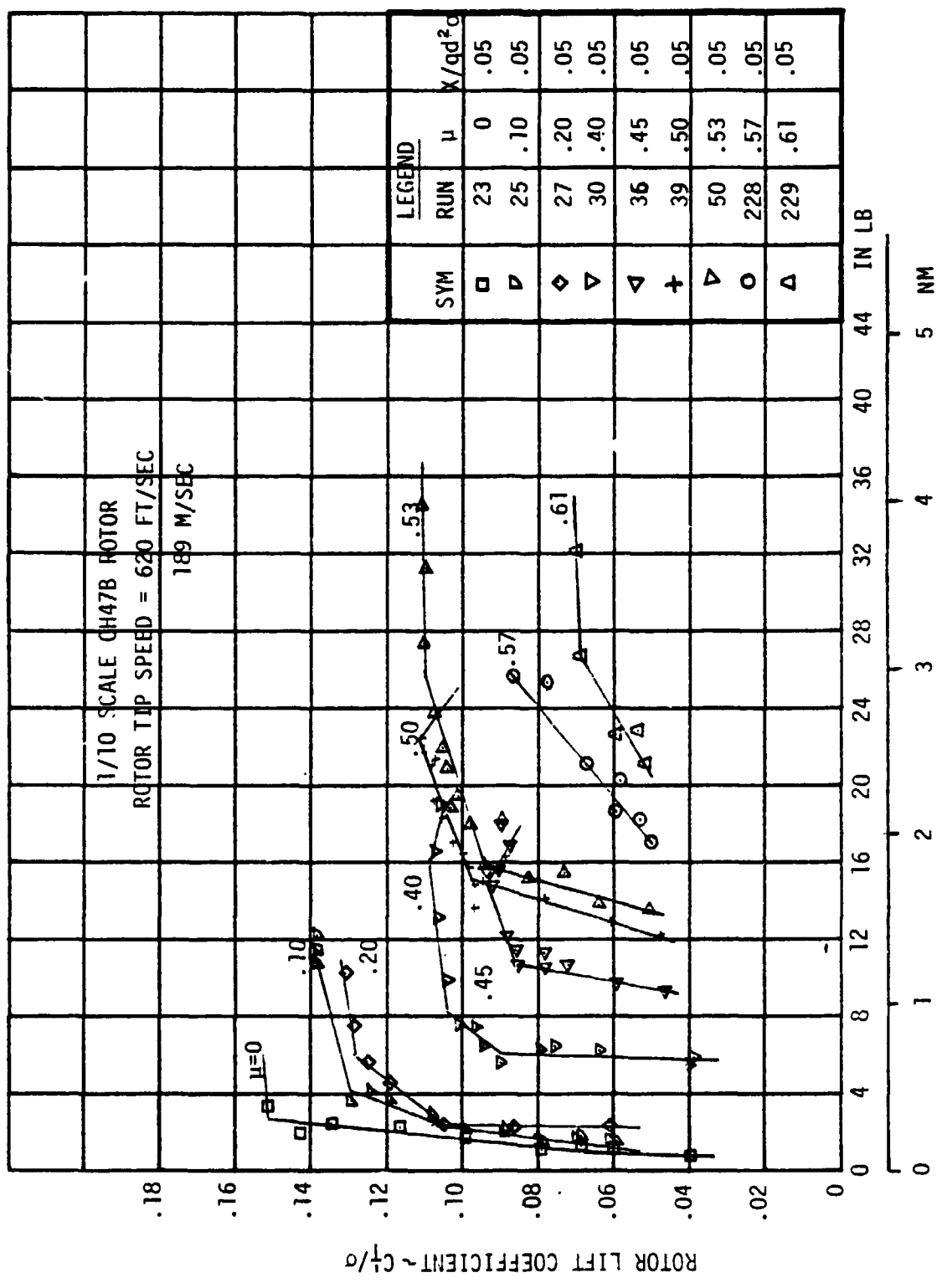


FIGURE 6.2.2 SUMMARY OF ALTERNATING BLADE ROOT TORSION ~TB12
ALTERNATING BLADE ROOT TORSION ~TB12

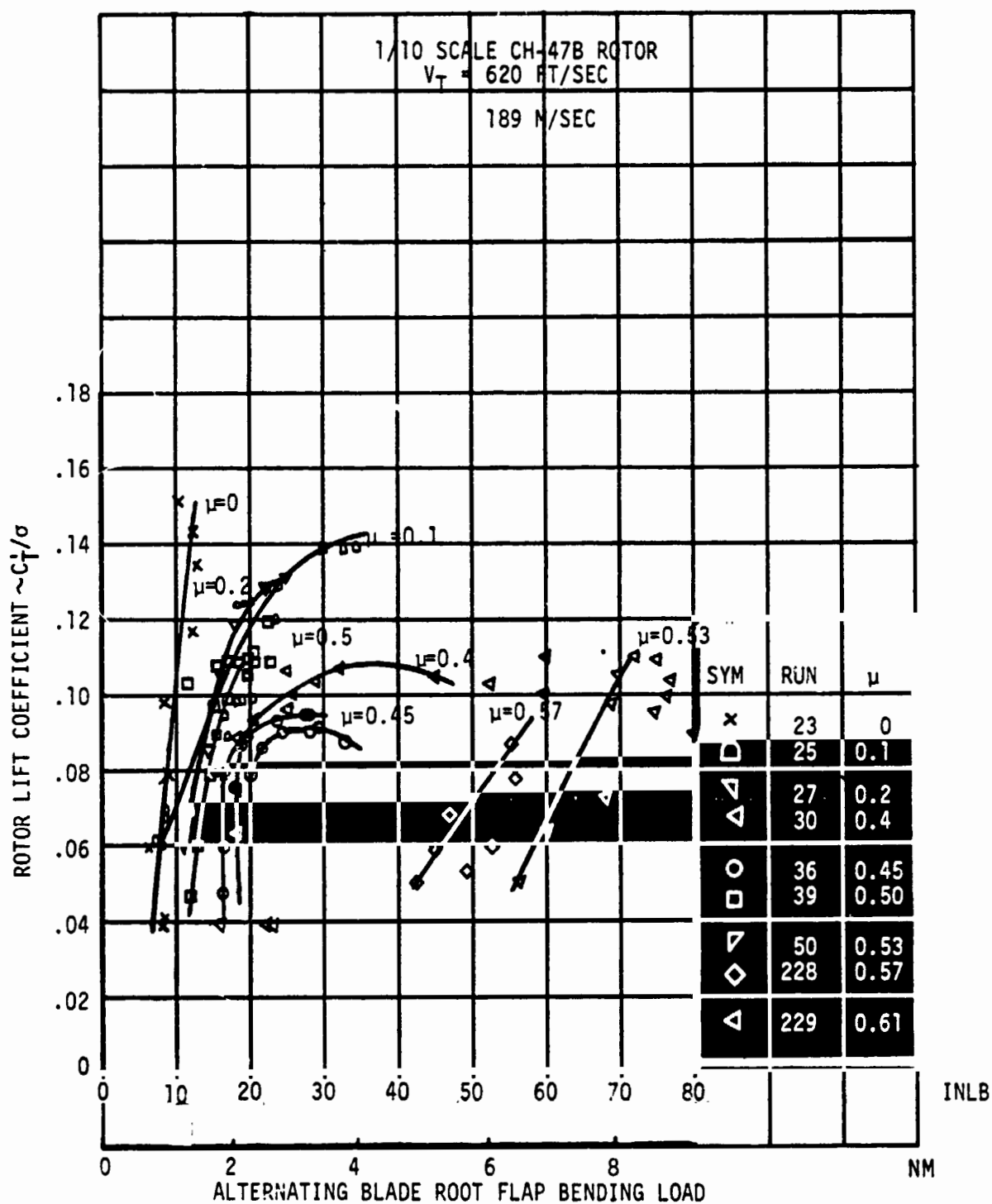


FIGURE 6.2.3 SUMMARY OF ALTERNATING BLADE ROOT FLAP BENDING LOADS

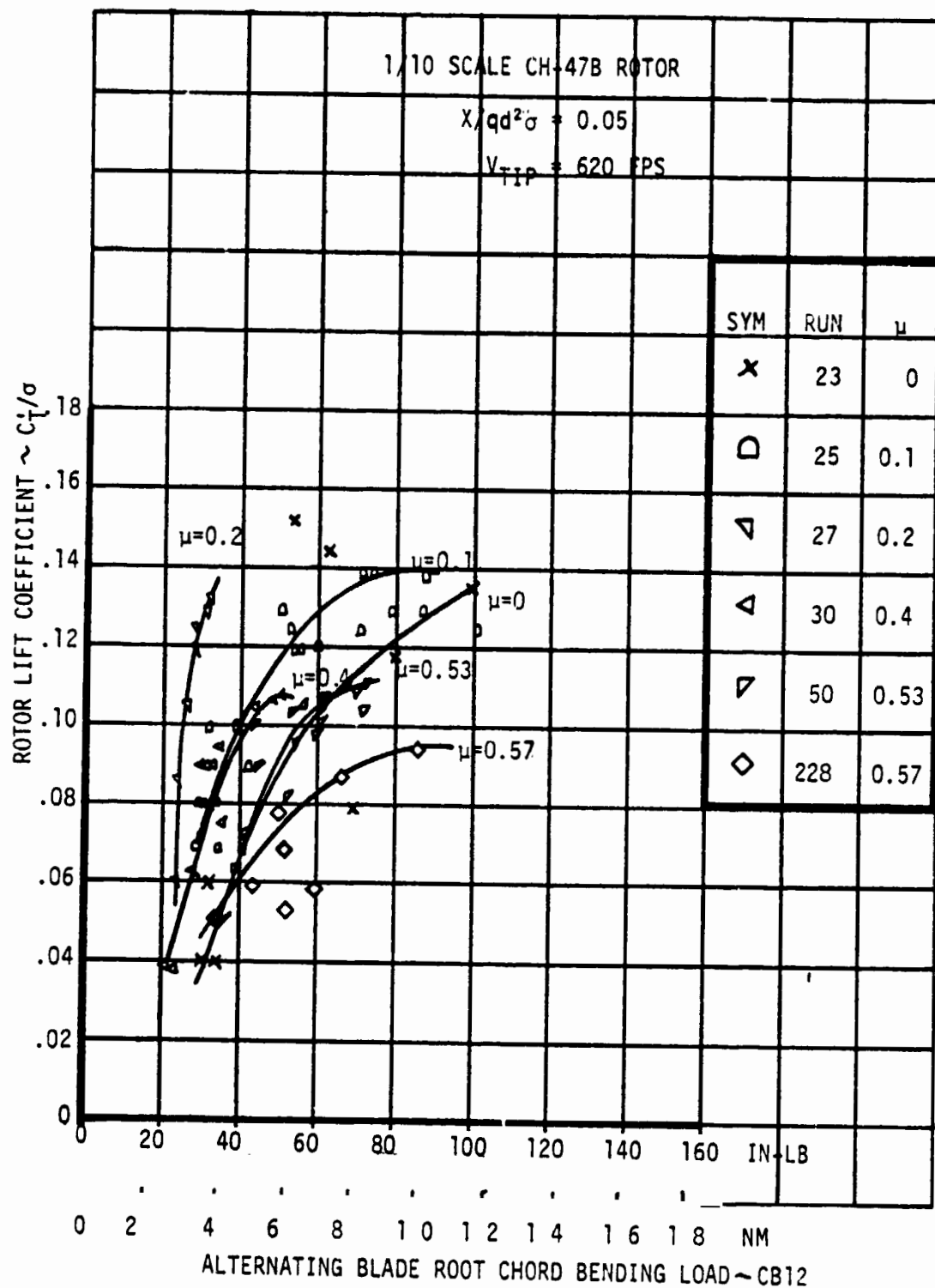


FIGURE 6.2.4 SUMMARY OF ALTERNATING ROOT CHORD BENDING LOADS

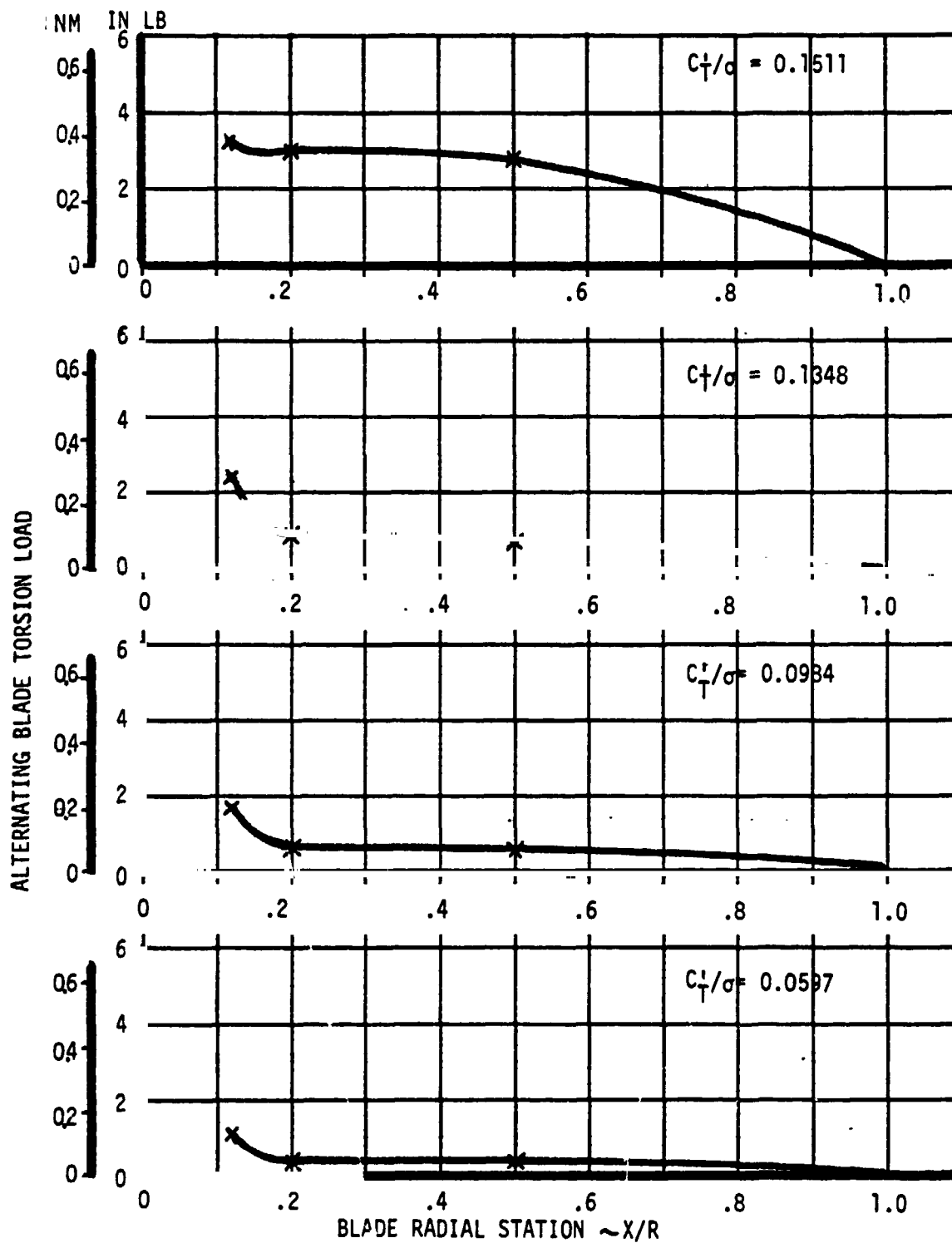


FIGURE 6.2.5 EFFECT OF ROTOR LIFT ON RADIAL DISTRIBUTION OF BLADE TORSION LOAD AT $\mu = 0$

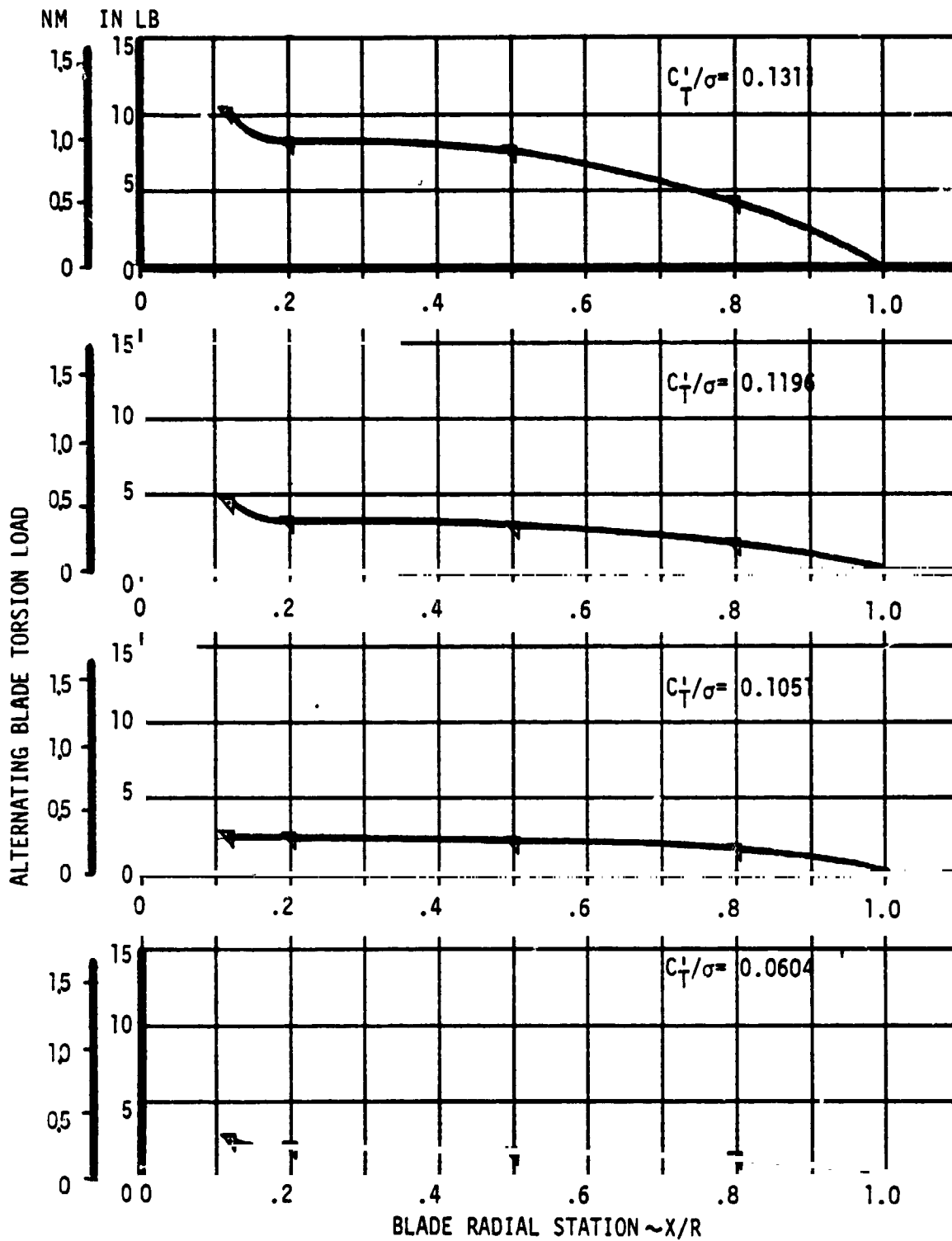


FIGURE 6.2.6 EFFECT OF ROTOR LIFT ON RADIAL DISTRIBUTION OF BLADE TORSION LOAD AT $\mu = 0.20$; $X/qd^2\sigma = 0.05$

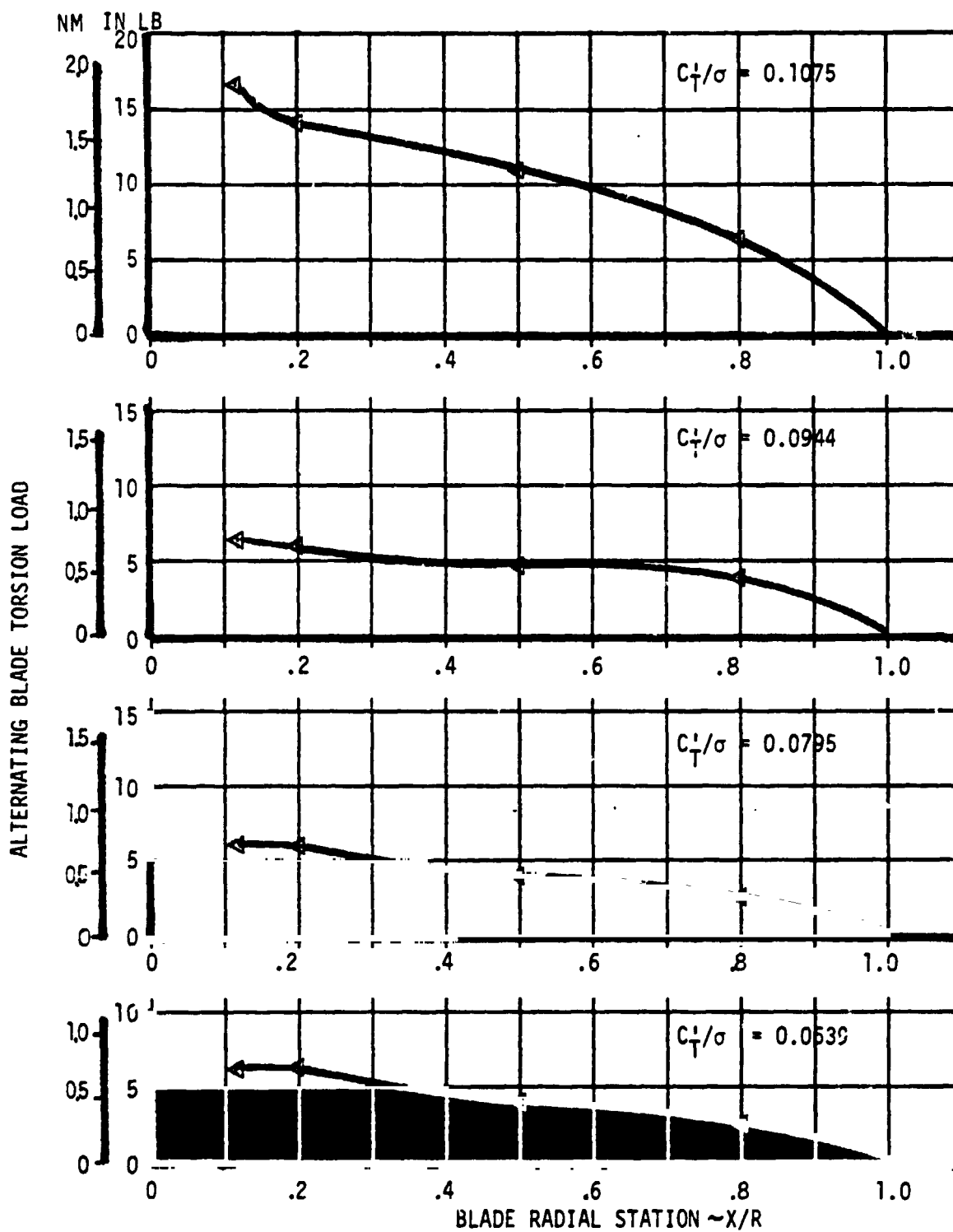


FIGURE 6.2.7 EFFECT OF ROTOR LIFT ON RADIAL DISTRIBUTION OF BLADE TORSION LOAD AT $\mu = 0.40$; $X/qd^2\sigma = 0.05$

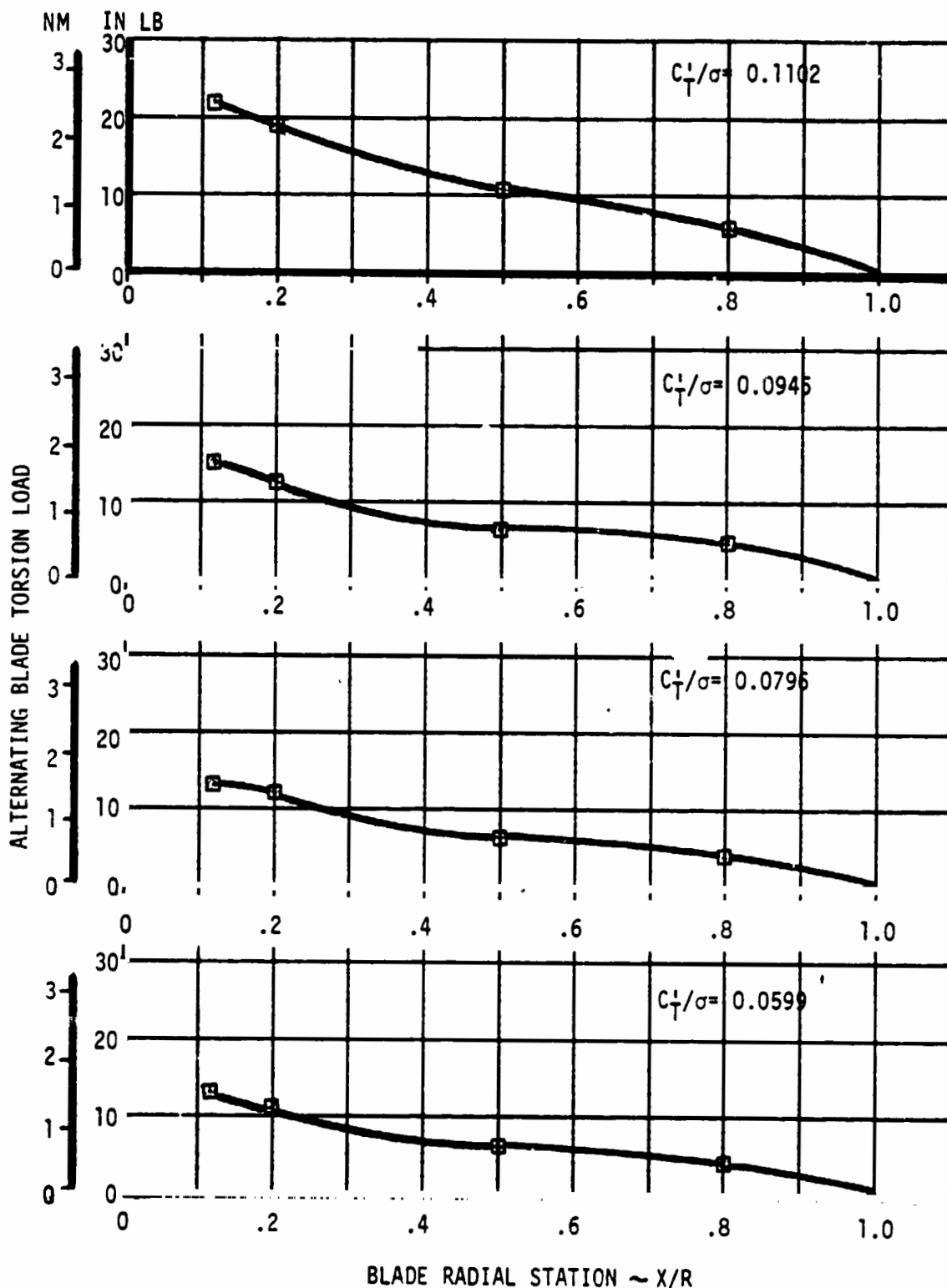


FIGURE 6.2.8 EFFECT OF ROTOR LIFT ON RADIAL DISTRIBUTION OF BLADE TORSION LOAD AT $\mu=0.50$; $X/qd^2\sigma = 0.05$

ORIGINAL PAGE IS
OF POOR QUALITY

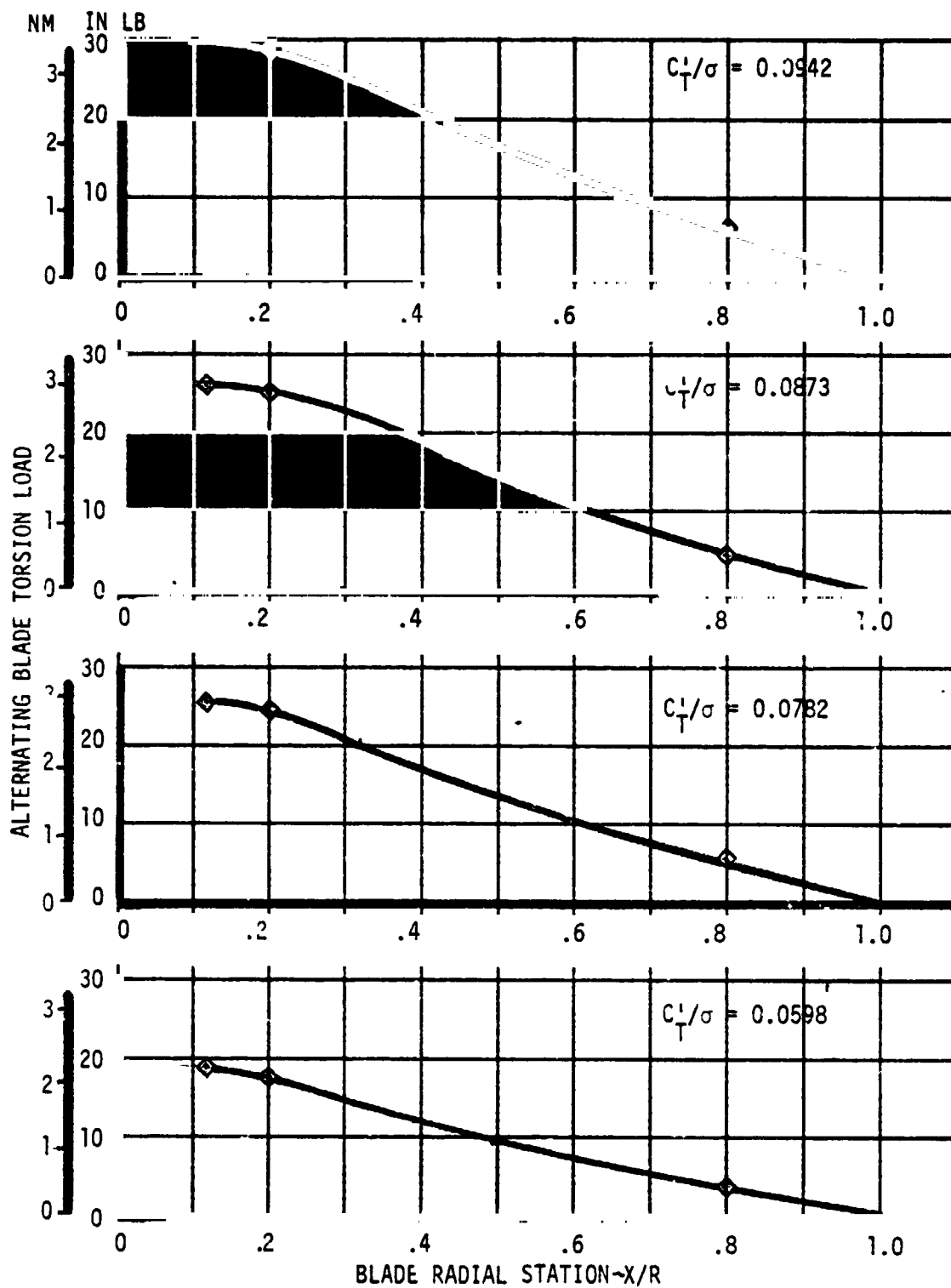


FIGURE 6.2.9 EFFECT OF ROTOR LIFT ON RADIAL DISTRIBUTION OF BLADE TORSION LOAD AT $\mu = 0.57$; $X/qd^2\sigma = 0.05$

1/10 SCALE CH47B ROTOR

$\mu = 0.0$
 $V_T = 620 \text{ FT/SEC}$
 189 M/SEC

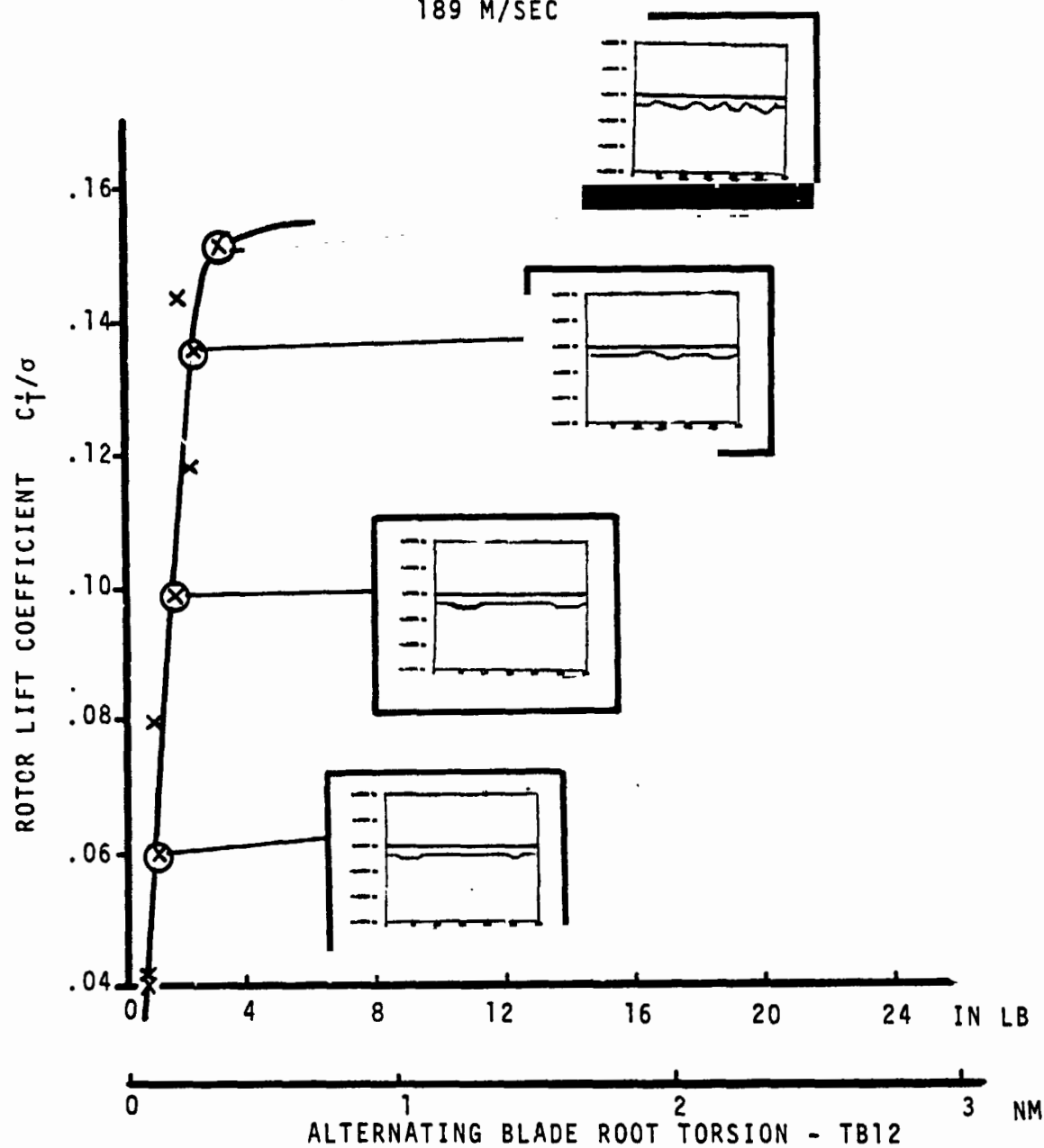


FIGURE 6.2.10 EFFECT OF APPROACHING THE LIFT LIMIT ON THE BLADE TORSION LOAD AT $\mu = 0$

1/10 SCALE CH47B ROTOR

$\mu = 0.20$

$X/qd^2\sigma = 0.05$

$V_{TIP} = 620 \text{ FT/SEC}$

189 M/SEC

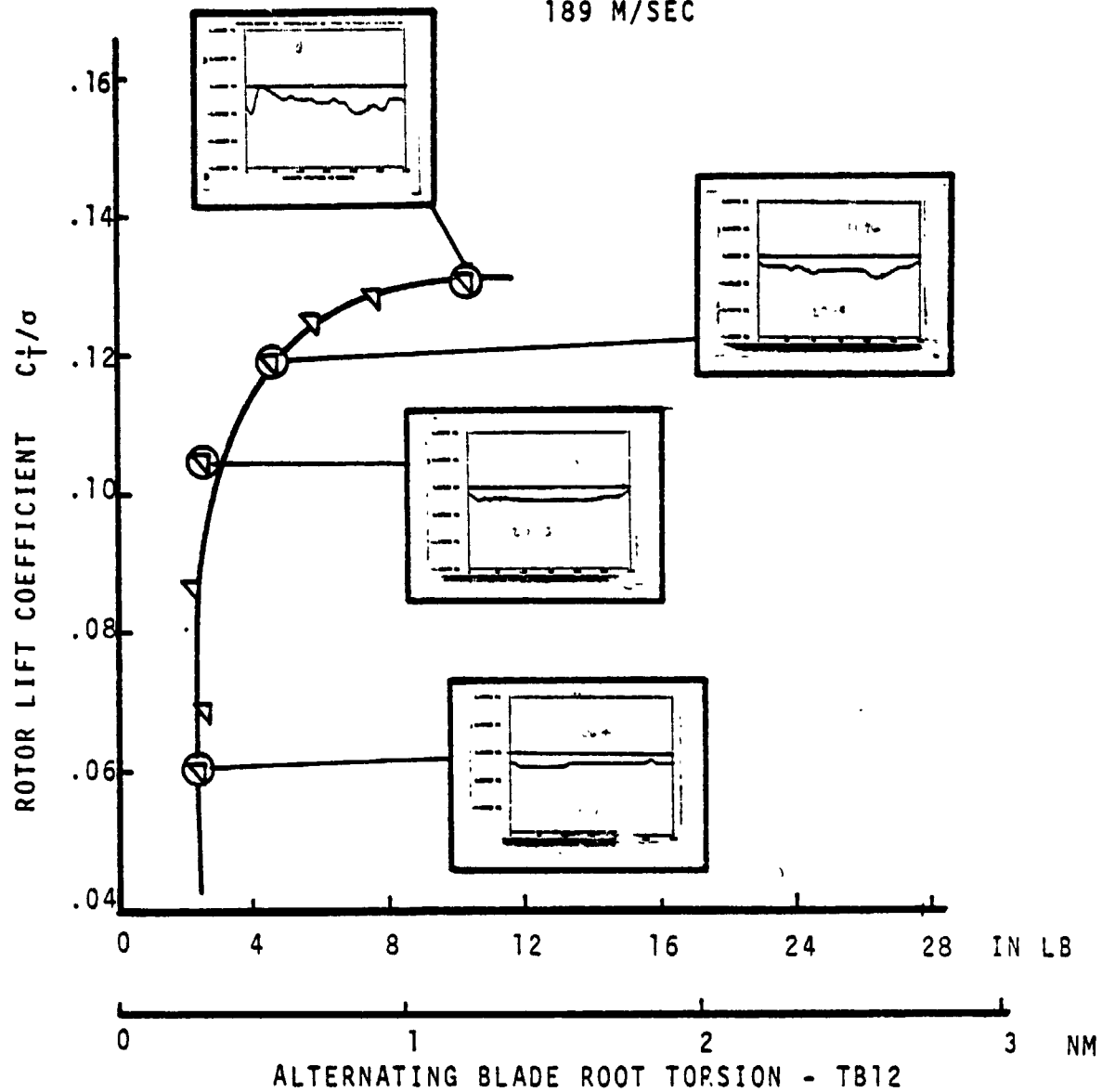


FIGURE 6.2.11 EFFECT OF APPROACHING THE LIFT LIMIT ON THE BLADE TORSION LOAD AT $\mu = 0.2$

1/10 SCALE CH47B ROTOR
 $\mu = 0.40$

$V_T = 620 \text{ FT/SEC}$
 189 M/SEC

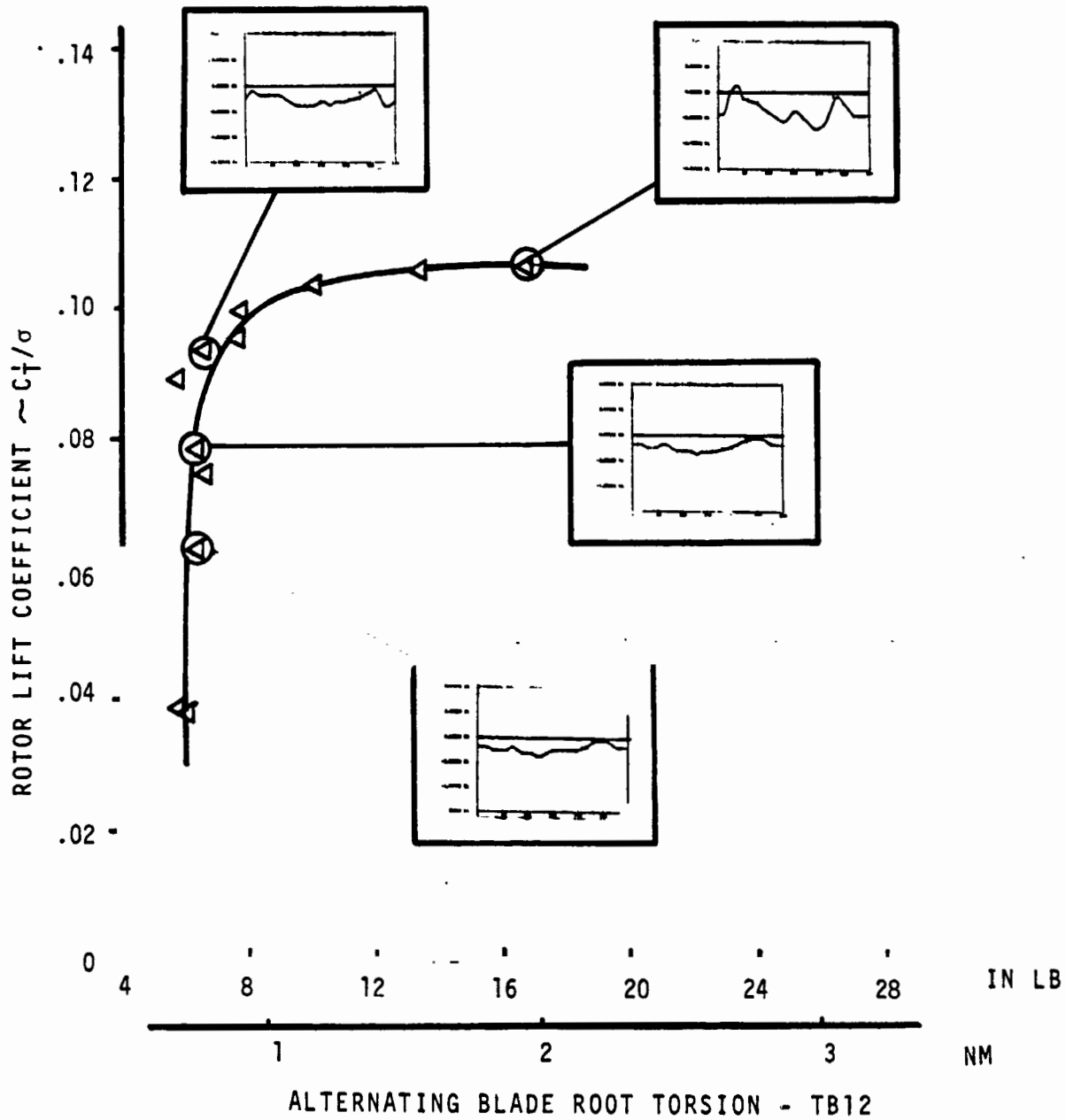


FIGURE 6.2.12 EFFECT OF APPROACHING LIFT LIMIT ON THE
 BLADE TORSION LOAD AT $\mu = 0.40$

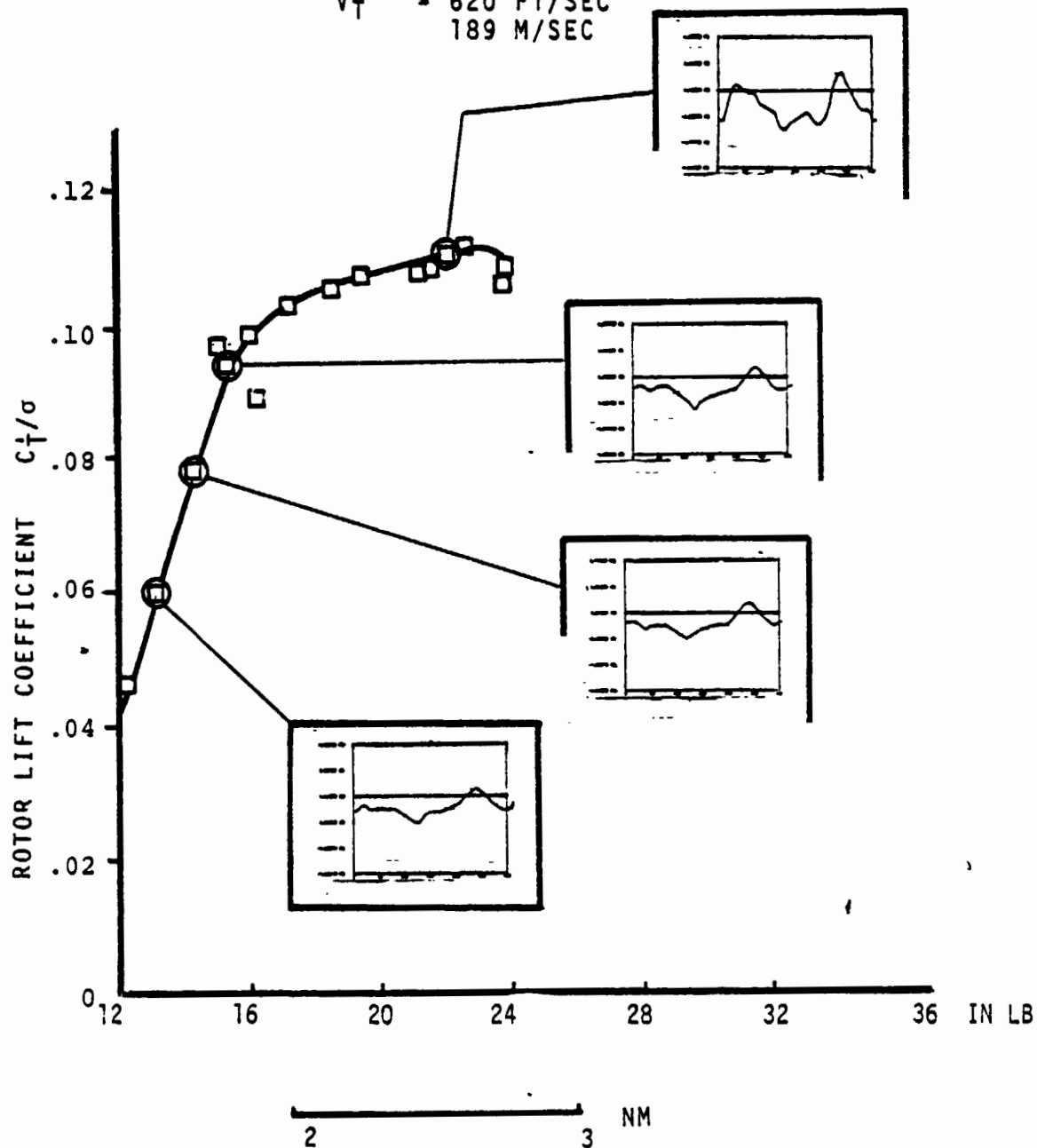
1/10 SCALE CH47B ROTOR

$$\mu = 0.50$$

$$X/qd^2\sigma = 0.05$$

$$V_T = 620 \text{ FT/SEC}$$

$$189 \text{ M/SEC}$$



ALTERNATING BLADE ROOT TORSION - TB12

FIGURE 6.2.13 EFFECT OF APPROACHING THE LIFT LIMIT ON THE BLADE TORSION LOAD AT $\mu = 0.50$

1/10 SCALE CH47B ROTOR
 $\mu=0.57$

$V_T = 620 \text{ FT/SEC}$
 189 M/SEC

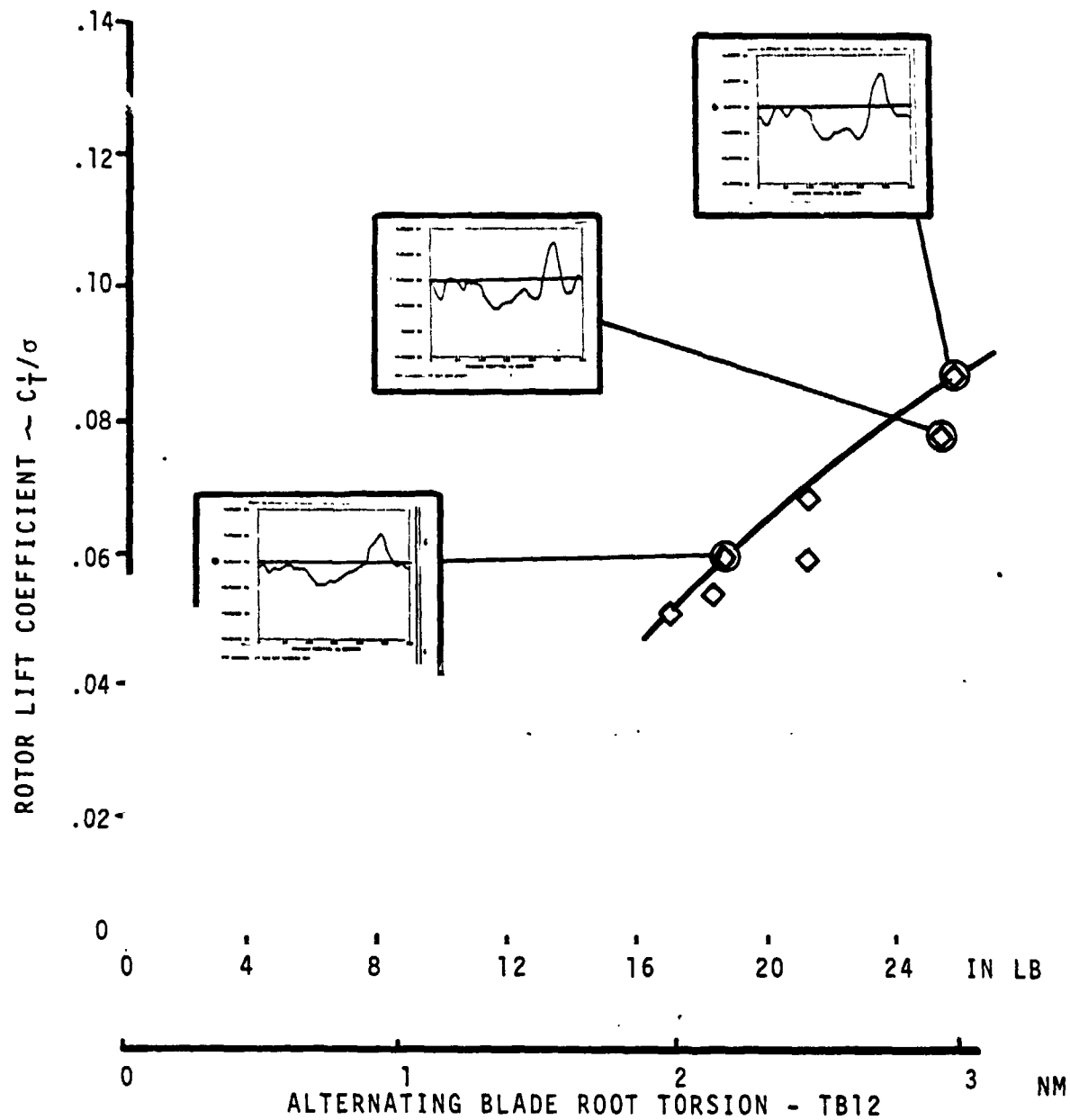
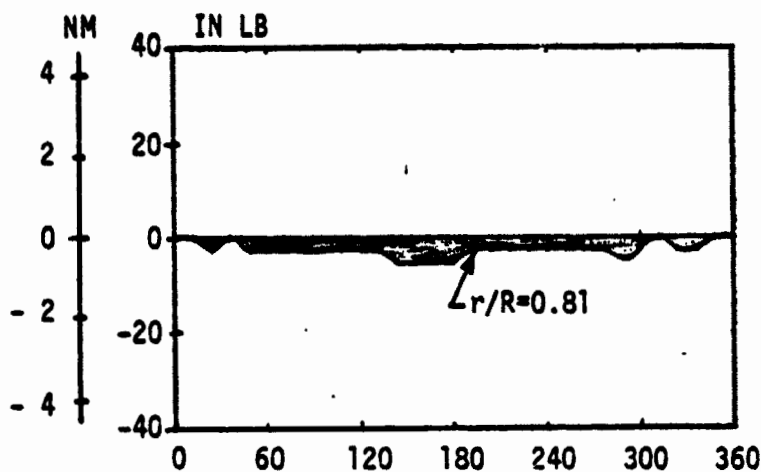
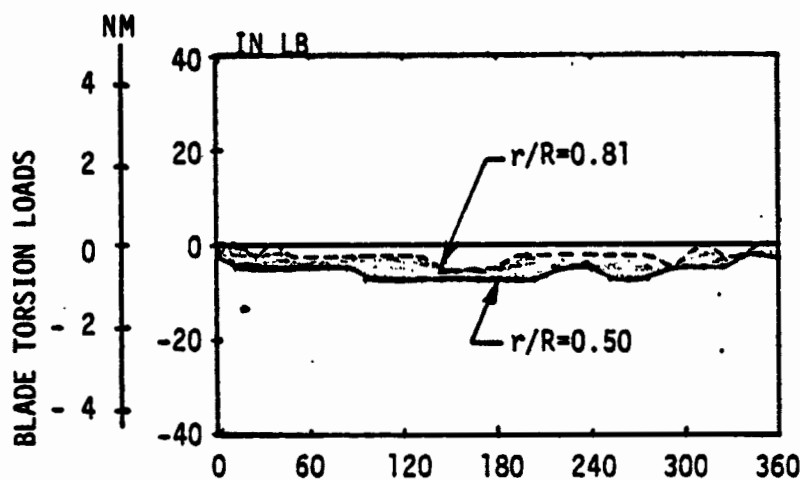


FIGURE 6.2.14 EFFECT OF APPROACHING THE LIFT LIMIT ON THE
 BLADE TORSION LOAD AT $\mu = 0.57$

OUTBOARD
TORSION
LOADS
 $r/R=0.81$ to
1.0



MID BLADE
TORSION
LOADS
 $r/R = 0.50$
to 0.81



INBOARD
TORSION
LOADS
 $r/R=0.50$
to 0.12

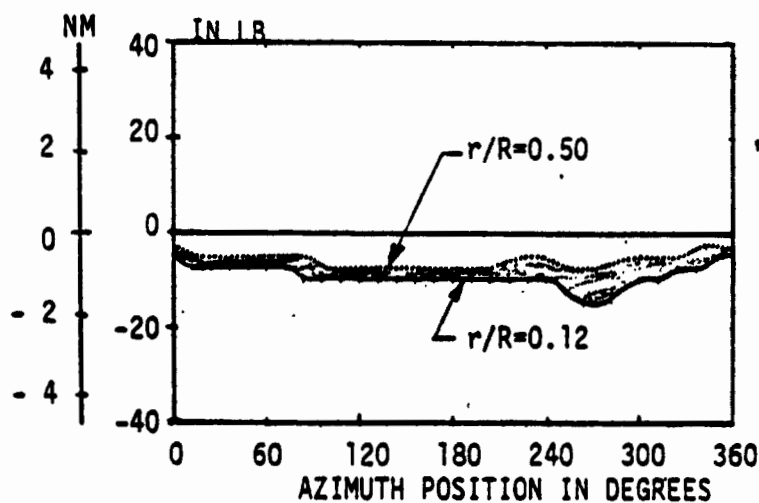
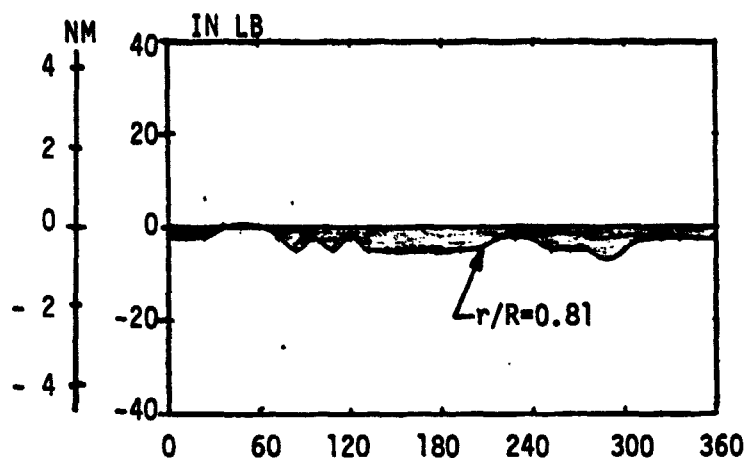
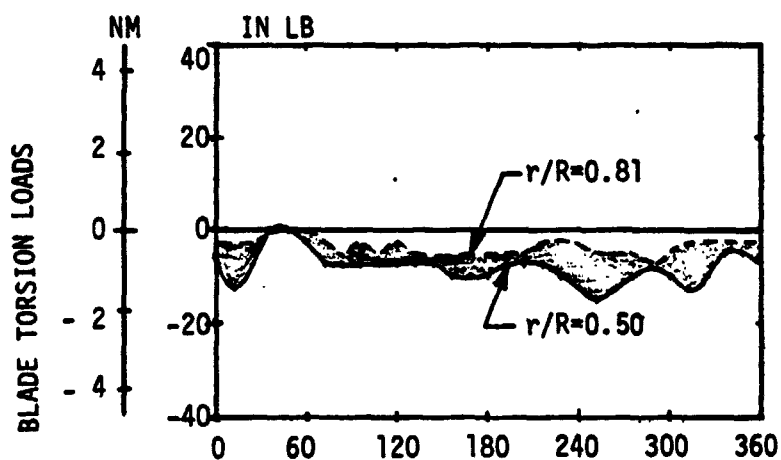


FIGURE 6.2.15 RADIAL AND AZIMUTHAL DISTRIBUTION OF BLADE TORSION LOADS,
 $\mu = 0.20$, $C_T/\sigma = 0.1238$, $X/qd^2\sigma = 0.05$

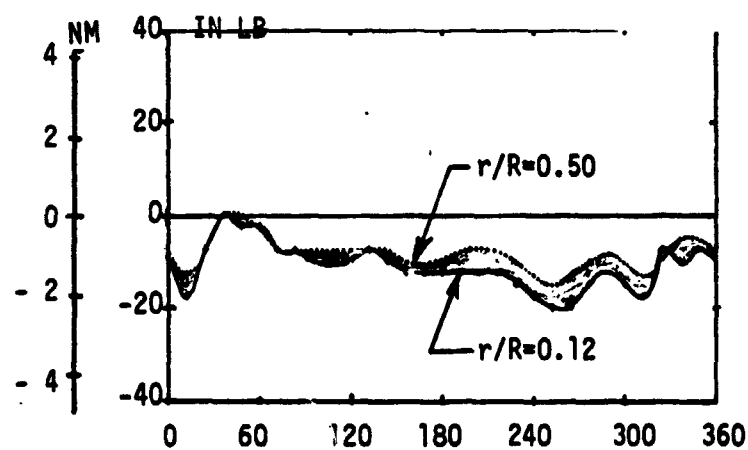
OUTBOARD
TORSION
LOADS
 $r/R=0.81$
to 1.0



MID BLADE
TORSION
LOADS
 $r/R=0.50$
to 0.81



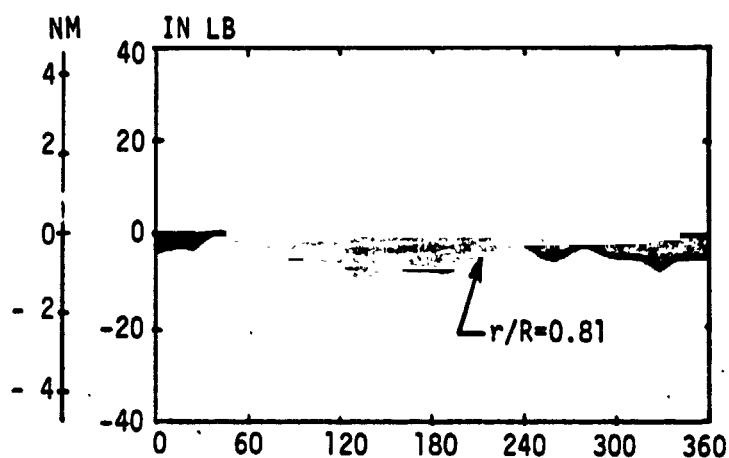
INBOARD
TORSION
LOADS
 $r/R=0.12$ to
0.50



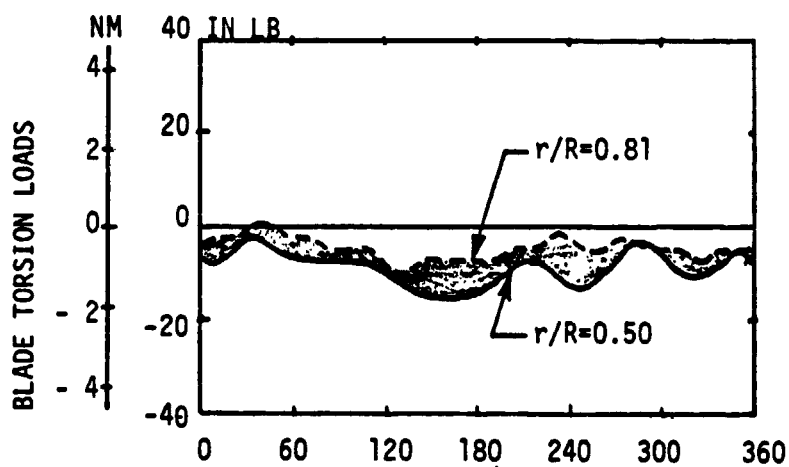
AZIMUTH POSITION IN DEGREES

FIGURE 6.2.16 RADIAL AND AZIMUTHAL DISTRIBUTION OF BLADE TORSION LOADS,
 $\mu = 0.20$, $C_T/\sigma = 0.1333$, $X/qd^2\sigma = 0.05$

OUTBOARD
TORSION
LOADS
 $r/R=0.81$
to 1.0



MID BLADE
TORSION
LOADS
 $r/R=0.50$
to 0.81



INBOARD
TORSION
LOADS
 $r/R=0.12$
to 0.50

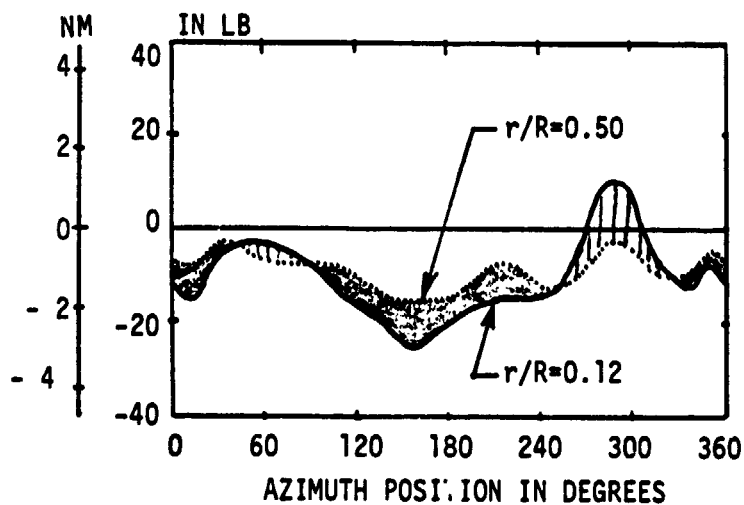
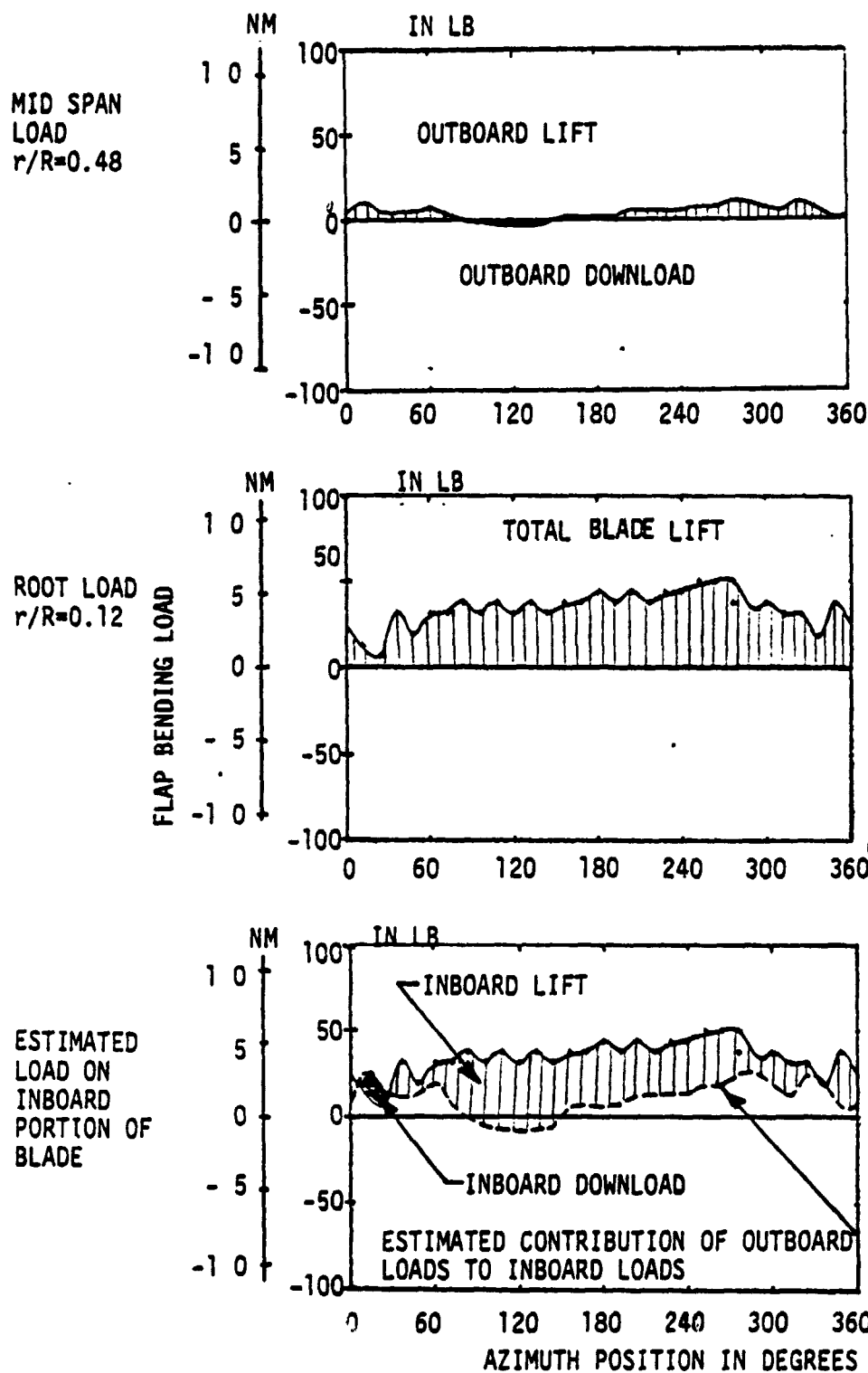


FIGURE 6.2.18 RADIAL AND AZIMUTHAL DISTRIBUTION OF BLADE TORSION LOADS,
 $\mu = 0.50$ $C_T/\sigma = 0.1029$ $X/qd^2\sigma = 0.05$



ORIGINAL PAGE IS
OF POOR QUALITY

FIGURE 6.2.19 AZIMUTHAL VARIATION IN FLAP BENDING LOAD AND ESTIMATION OF MAJOR AREAS OF ROTOR LIFT $\mu = 0.20$, $C_l/\sigma = 0.1238$, $X/qd^2\sigma = 0.05$

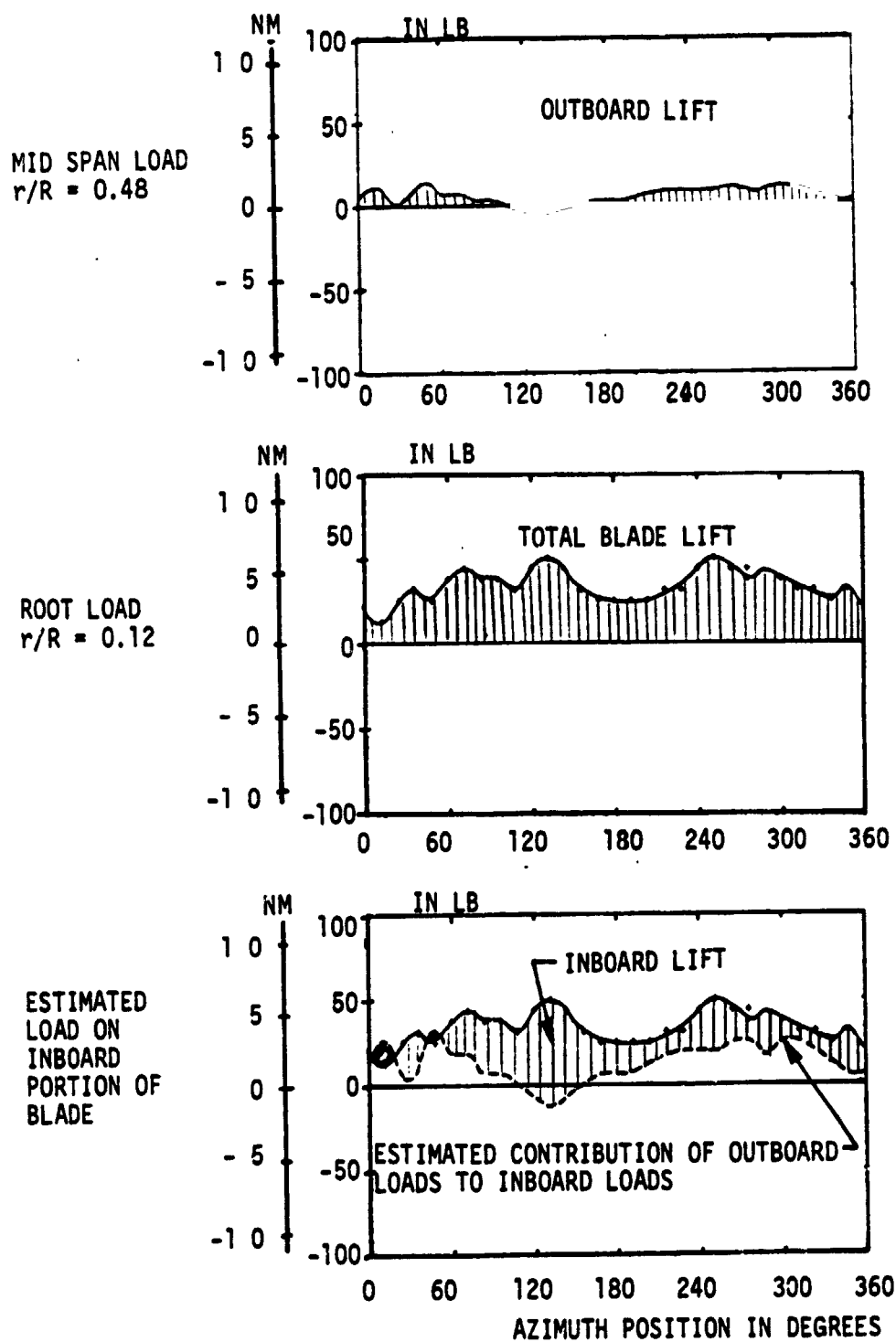


FIGURE 6.2.20 AZIMUTHAL VARIATION IN FLAP BENDING LOAD AND ESTIMATION OF MAJOR AREAS OF ROTOR LIFT $\mu = 0.20$, $C_T/\sigma = 0.133$, $X/qd^2\sigma = 0.05$

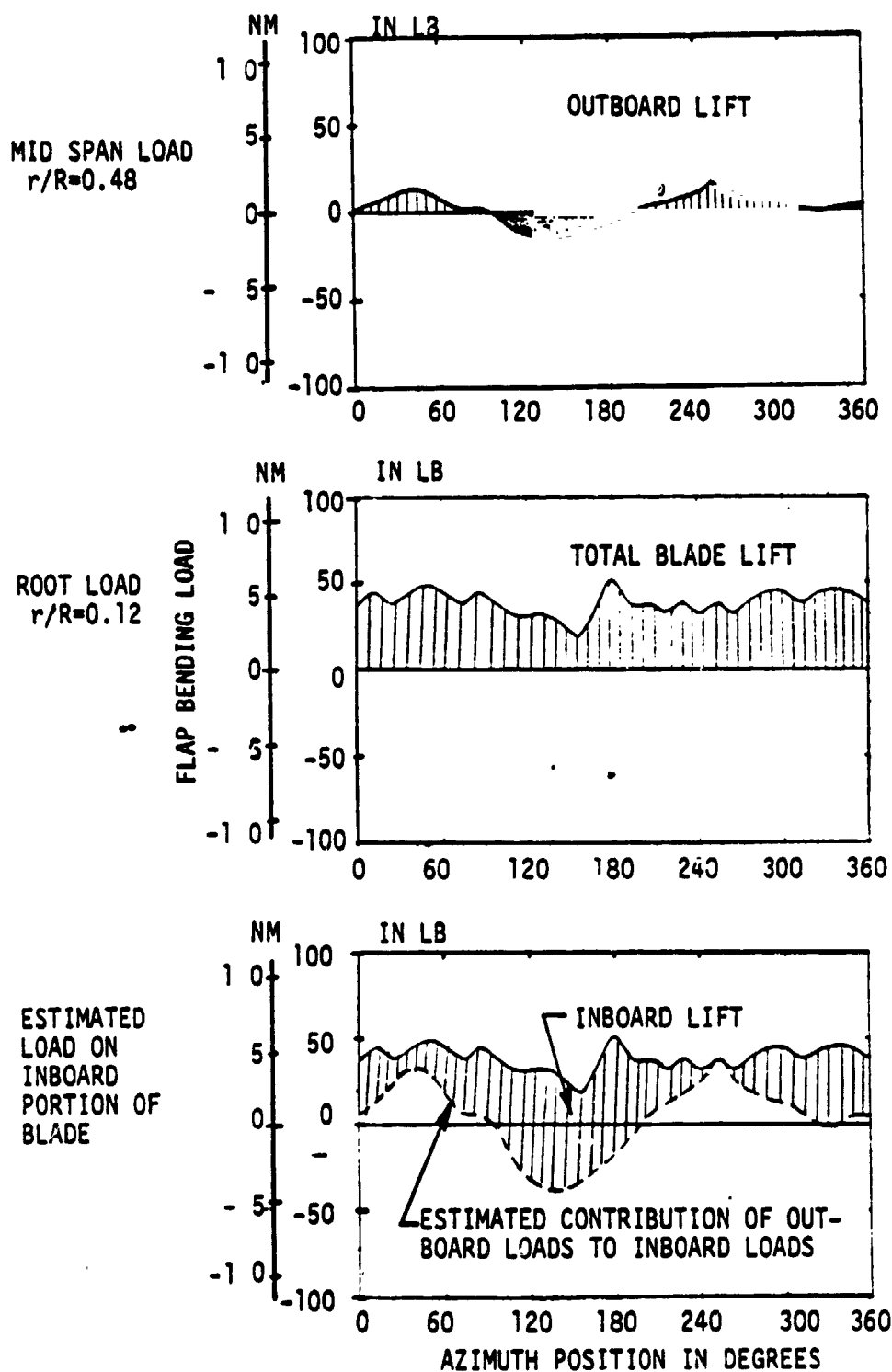


FIGURE 6.2.21 AZIMUTHAL VARIATION IN FLAP BENDING LOAD AND ESTIMATION OF MAJOR AREAS OF ROTOR LIFT $\mu = 0.50$, $C_l/\sigma = 0.0894$, $X/qd^2\sigma = 0.05$

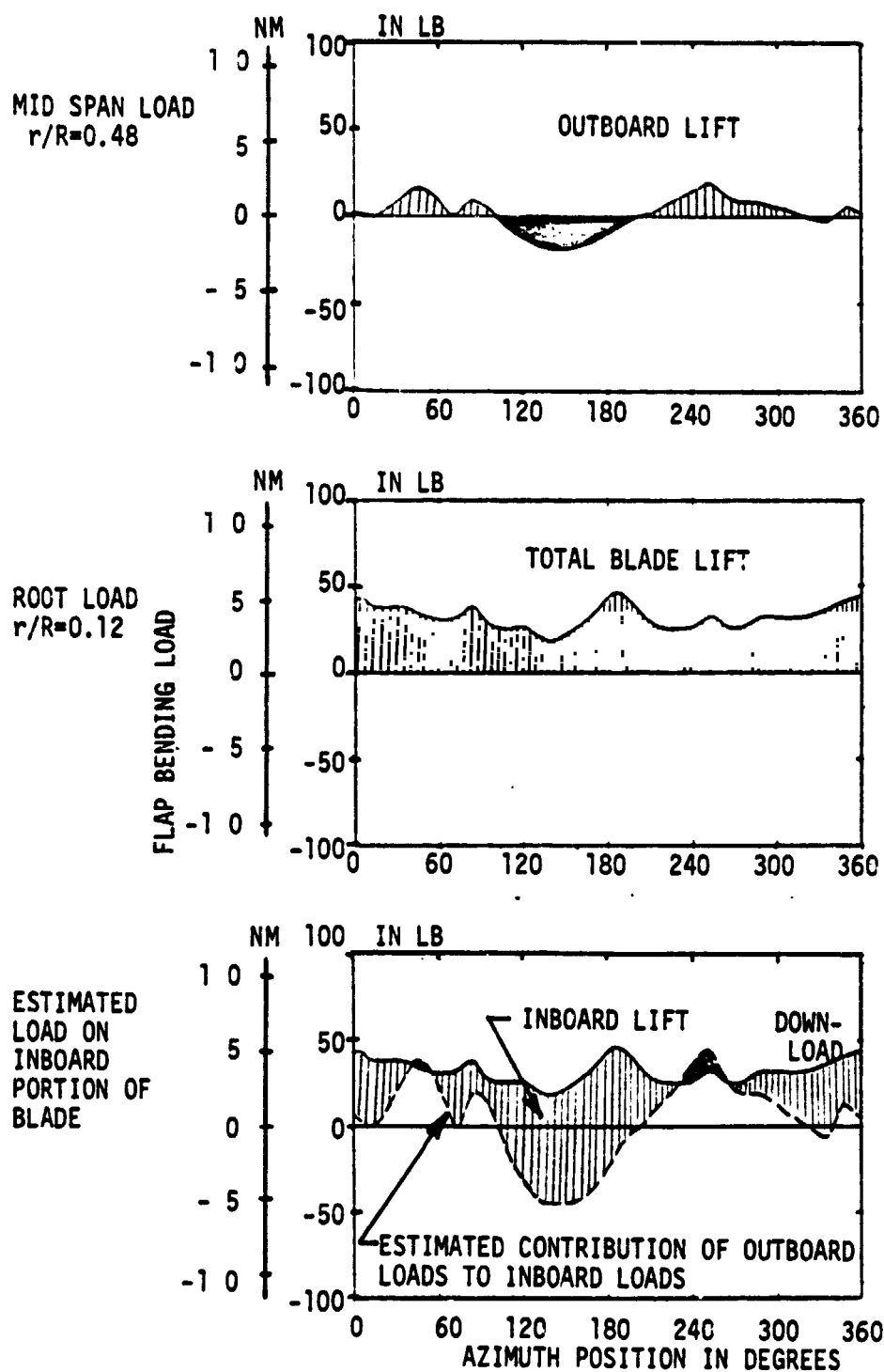


FIGURE 6.2.22 AZIMUTHAL VARIATION IN FLAP BENDING LOAD AND ESTIMATION OF MAJOR AREAS OF ROTOR LIFT - $\mu = 0.50$, $C_l/\sigma = 0.1029$
 $X/qd^2\sigma = 0.05$

6.3 Cruise Rotor Performance

Test Objective 3: Obtain cruise rotor performance for advance ratios of 0.40 to 0.67.

Testing was performed at the primary tip speed of 620 ft/sec (189 m/sec) and a propulsive force requirement defined in coefficient form by $X/qd^2\sigma = 0.05$ which is representative of an advanced helicopter level of drag cleanup. This testing was performed to define the lift limit as described in Section 6.1 with a sweep in rotor lift at a fixed level of propulsive force coefficient. By testing in this manner, performance data was obtained from lift levels as low as C_T/σ of 0.04 up to the limit defined in Figure 6.1.3. This data is representative of steady level cruise performance for the 1/10 scale CH47B rotor. All of the data obtained is included in Appendix A and summarized in Appendix F but only a portion of the data will be presented here and discussed.

Figures 6.3.1 through 6.3.7 present the summary of the rotor performance and the control positions associated with this performance. The variation of rotor power coefficient with rotor lift coefficient is presented in Figure 6.3.1, from hover to an advance ratio of 0.61. Rotor power reduces from hover to a minimum at an advance ratio of 0.20. As advance ratio increases to 0.4 there is a gradual increase in power, and as the advance ratio increases to 0.57 and again to 0.61 the increase in power becomes significantly larger.

Figure 6.3.2 presents the performance data in terms of the rotor effective drag coefficient (C_{D_e}/σ) variation with rotor lift. There is a large improvement in rotor effective drag from an advance ratio of 0.10 to 0.20. A slight increase in effective drag coefficient is shown as the advance ratio is increased to $\mu = 0.40$. For advance ratios of 0.45, 0.50 and 0.53 the effective drag level is slightly increased over an advance ratio of 0.40 and they are all approximately the same. Increasing the advance ratio to 0.57 and then to 0.61 increases the effective drag reaching a level that is equal to that of an advance ratio of $\mu = 0.10$. The general trend evident for each of the advance ratios is that the effective drag starts to increase significantly at lift levels well below the lift limit, but in the lift level that is incurring inboard stall.

Rotor lift to effective drag ratio is a measure of cruise efficiency. The slope to any point on Figure 6.3.2 provides the L/D_E and the position of each advance ratio on this figure indicates their efficiency relative to each other. Maximum L/D_E indicated is 9.0 for an advance ratio of 0.20, decreases to 6.5 for $\mu = 0.40$ and then down to 1.8 at $\mu = 0.61$. A summary of the maximum rotor L/D_E is presented in Figure 6.3.3 indicating a peak value of 9.5 at $\mu = 0.28$. The trend from $\mu = 0.40$ to 0.61 resembles the lift limit trend showing a dip at an advance ratio of 0.45 and a lower peak of 4.5 at $\mu = 0.52$.

The strain gages and wire bundles for the torsion, flap and chord bending loads were mounted externally on the blade. This produces lumps and spanwise surface irregularities that increase the basic drag of the airfoil section. From testing performed under the HLH program, data was obtained to define increments in section drag coefficient (ΔC_D) for instrumentation and wire bundles. For the instrumentation arrangement on the blades used in the Lift-Propulsive Force Limit test the increment in section drag coefficient was $\Delta C_D = 0.020$. Utilizing this ΔC_D , an estimate of the change in rotor effective drag coefficient was made and the associated impact on the maximum effective lift-drag ratio. This was added to Figure 6.3.3 and indicates that the peak in maximum L/D_E increases to approximately 13.5 at $\mu = 0.28$. The second peak in L/D_E increases to 7.0 at an advance ratio of 0.52.

No estimates have been made at present to scale this data up to full scale. Since the characteristics resemble the lift limit and are significantly influenced by stall, there would be changes in the magnitude of maximum effective lift to drag ratio. The most significant changes are expected in the operational regime above $\mu = 0.50$ where the rotor stall severely limiting the model characteristics as indicated in Figure 6.3.3. This scaling up must be performed to establish the full potential of the conventional rotor.

The rotor shaft angle of attack, collective pitch, longitudinal

cyclic and lateral cyclic that correspond to the performance summary of Figure 6.3.1 are presented in Figures 6.3.4 through Figure 6.3.7. The other aspect of rotor performance is the capability of the rotor to accelerate from one steady state cruise condition to another and/or carry external loads. Performance data that addresses this was obtained during the propulsive force testing. At fixed levels of lift, the propulsive force was increased until a model physical limit was reached. This data is presented in Appendix B of Volume 2 and Figures 6.3.8 through Figure 6.3.10 are selected to present the performance data obtained at three advance ratios. Figure 6.3.8 shows the variation in rotor power coefficient with the increasing propulsive force requirements at $\mu = 0.40$. The two data trends are for 80 percent and 60 percent of the maximum lift limit when $X/qd^2\sigma = 0.05$. The resulting trends are linear with a slight decrease in slope as the lift is increased. A linear variation indicates a fixed effectiveness of the rotor for converting power to propulsive force and is defined as rotor propulsive efficiency (η_P). A rotor propulsive efficiency of 100% is the ideal conversion of power to propulsive force.

$$\eta_P = \frac{\Delta(X)}{\Delta(P/V)}$$

$$\text{Ideal } \eta_P = 100\%$$

$$\frac{\Delta P}{V} = \Delta X$$

The dashed line in Figures 6.3.8 through Figure 6.3.10 presents this ideal conversion and is labeled 100 percent Rotor Propulsive Efficiency. A decrease in slope indicates the deviation from the 100%. For the rotor lift coefficient of 0.06 the slope is .91 of the ideal; therefore, the propulsive efficiency (η_p) is 91 percent. At the higher lift level $C_T/\sigma = .09$ the propulsive efficiency decreases to 77 percent. This is the impact of the root stall discussed in Sections 6.1 and 6.2. Figure 6.3.9 presents similar data for an advance ratio of 0.50. The propulsive efficiency is 88 percent at $C_T/\sigma = 0.06$ and 84 percent at $C_T/\sigma = 0.08$. At the highest advance ratio, $\mu = 0.61$ presented in Figure 6.3.10, the propulsive efficiency is 100 percent for both levels of lift. To show the change in η_p for these three advance ratios and to integrate the data obtained from the remainder of the propulsive force testing a summary trend with μ was developed. Figure 6.3.11 presents this trend showing η_p decreasing to a minimum of 85 percent at $\mu = 0.48$ and increasing to 100 percent at $\mu = 0.61$. This indicates that at its poorest capability the rotor is as good as a propeller operating very near maximum efficiency.

A performance summary and corresponding control positions are presented for a rotor tip speed of 570 ft/sec (174 M/sec) in Figures 6.3.12 through Figures 6.3.18. No detail discussion is included here but the general level of performance is similar at the lower lift levels. More detail comparison should be made to

understand the differences in performance resulting at the higher levels of lift and at $\mu = 0.53$ and 0.57 . These differences are also reflected in the lift limits that are discussed in Section 6.5.

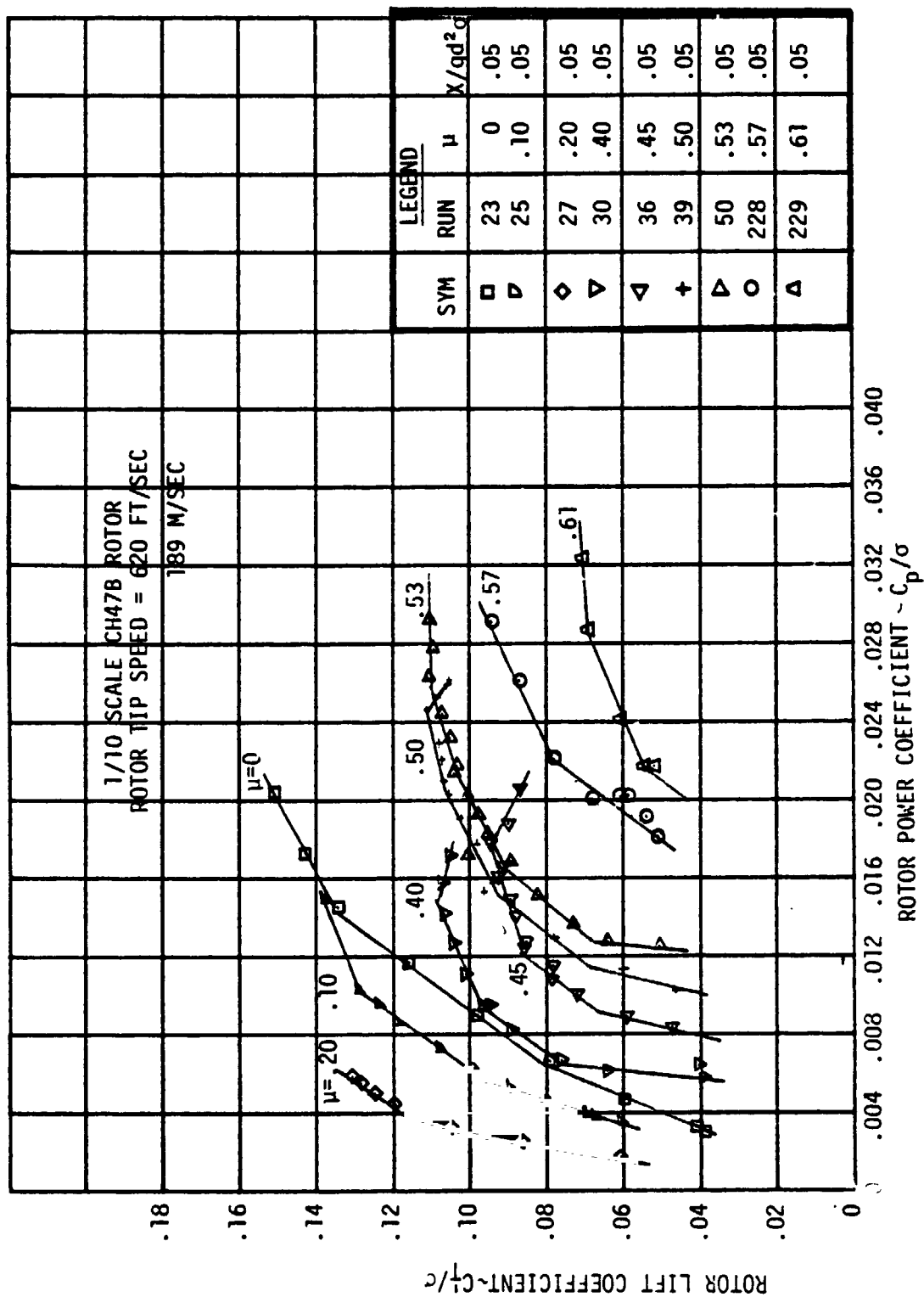


FIGURE 6.3.1 ROTOR PERFORMANCE SUMMARY AT $V_T = 620$ FT/SEC

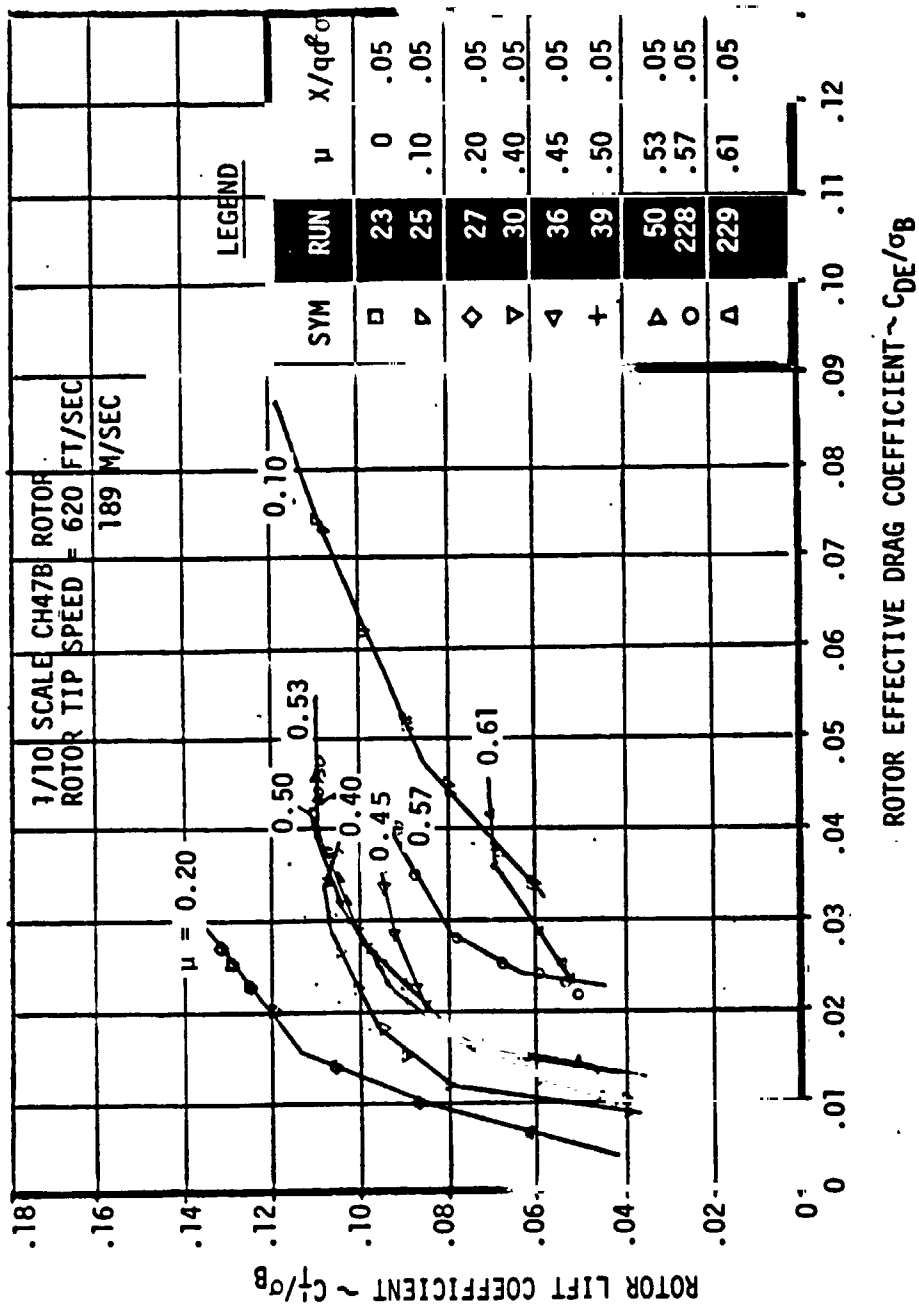


FIGURE 6.3.2 ROTOR EFFECTIVE DRAG FOR PERFORMANCE SUMMARY $V_T = 620$ FT/SEC

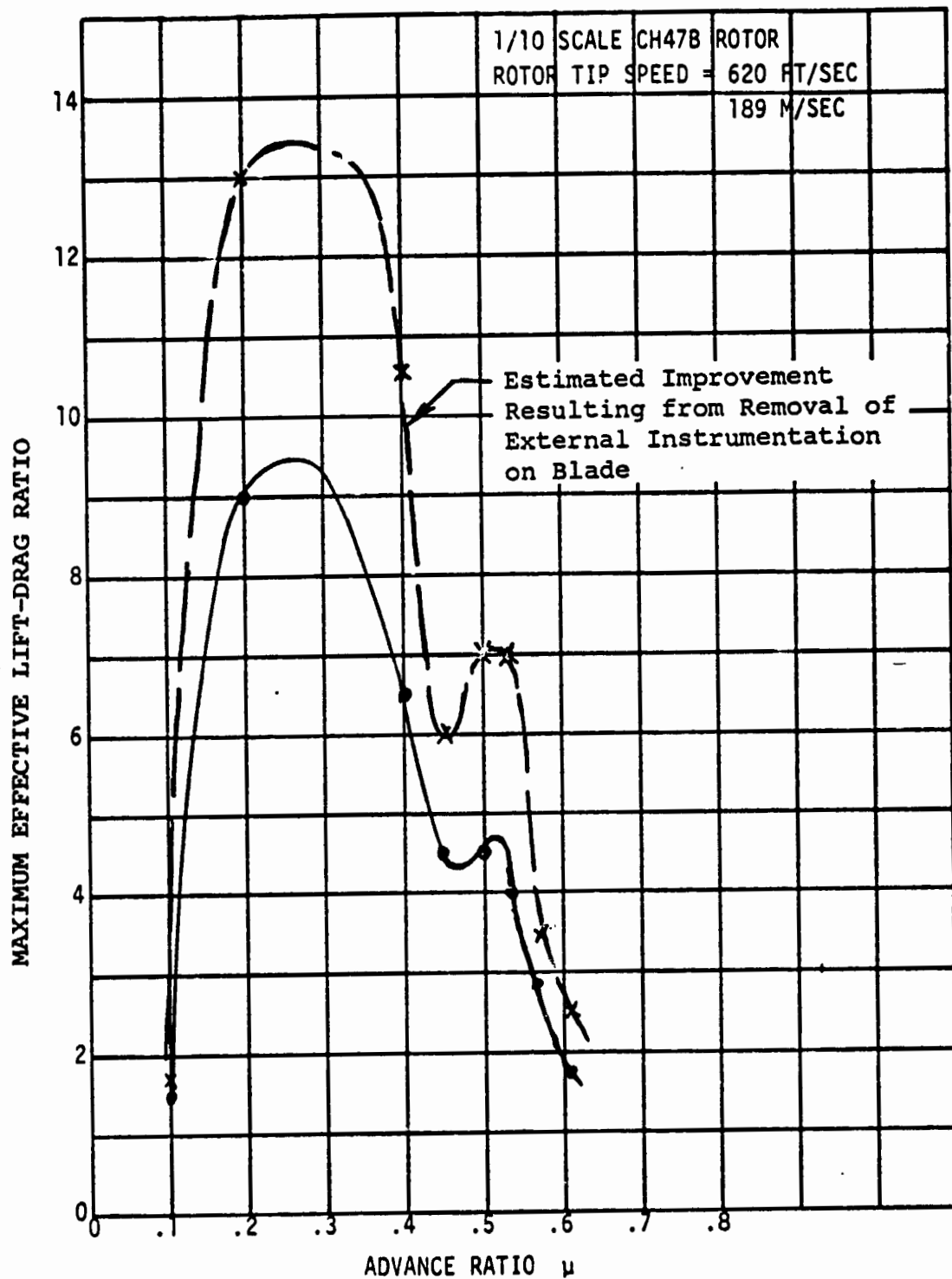


FIGURE 6.3.3 SUMMARY OF MAXIMUM EFFECTIVE LIFT-DRAG RATIO

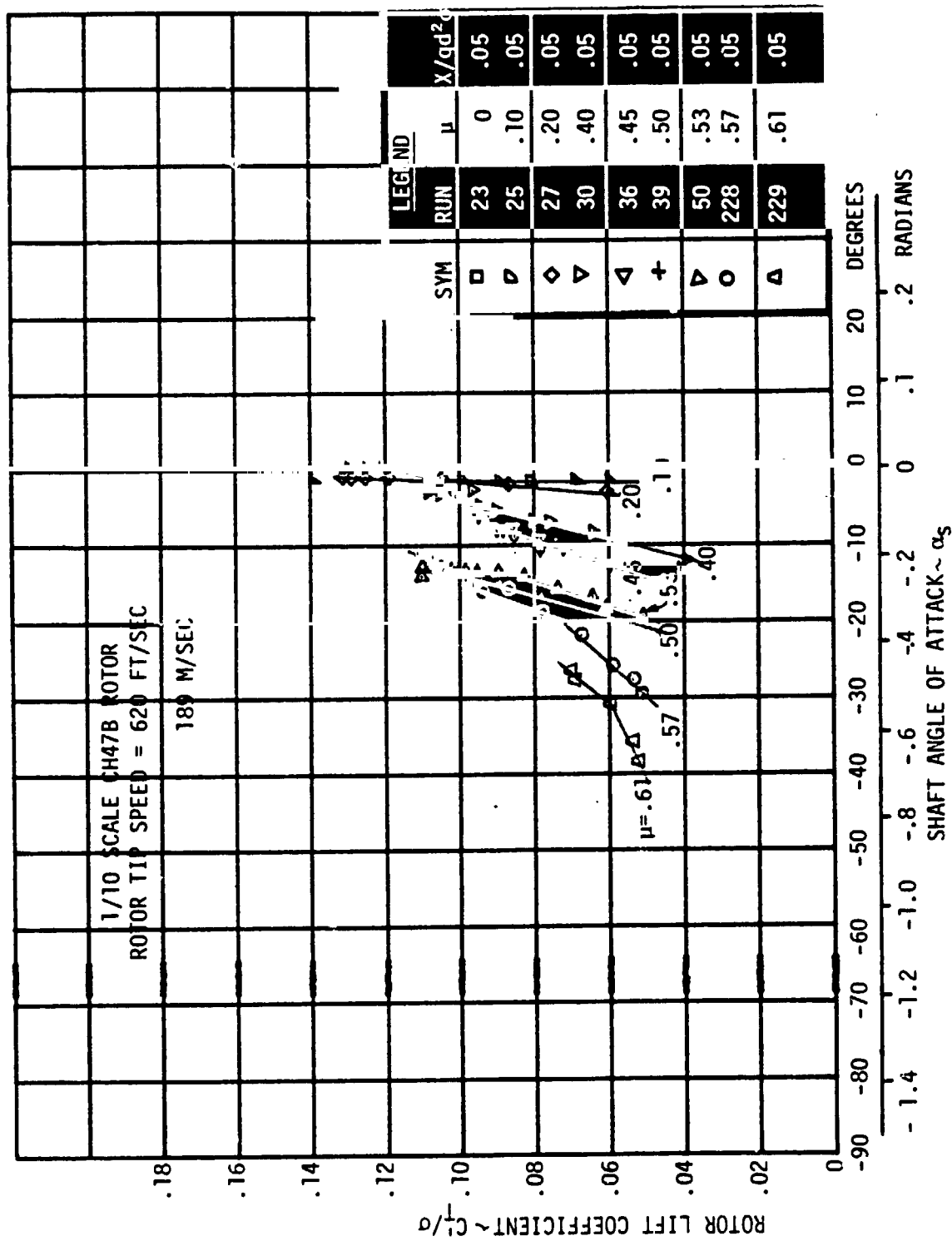


FIGURE 6.3.4 SHAFT ANGLE OF ATTACK FOR PERFORMANCE SUMMARY $V_T = 620$ FT/SEC

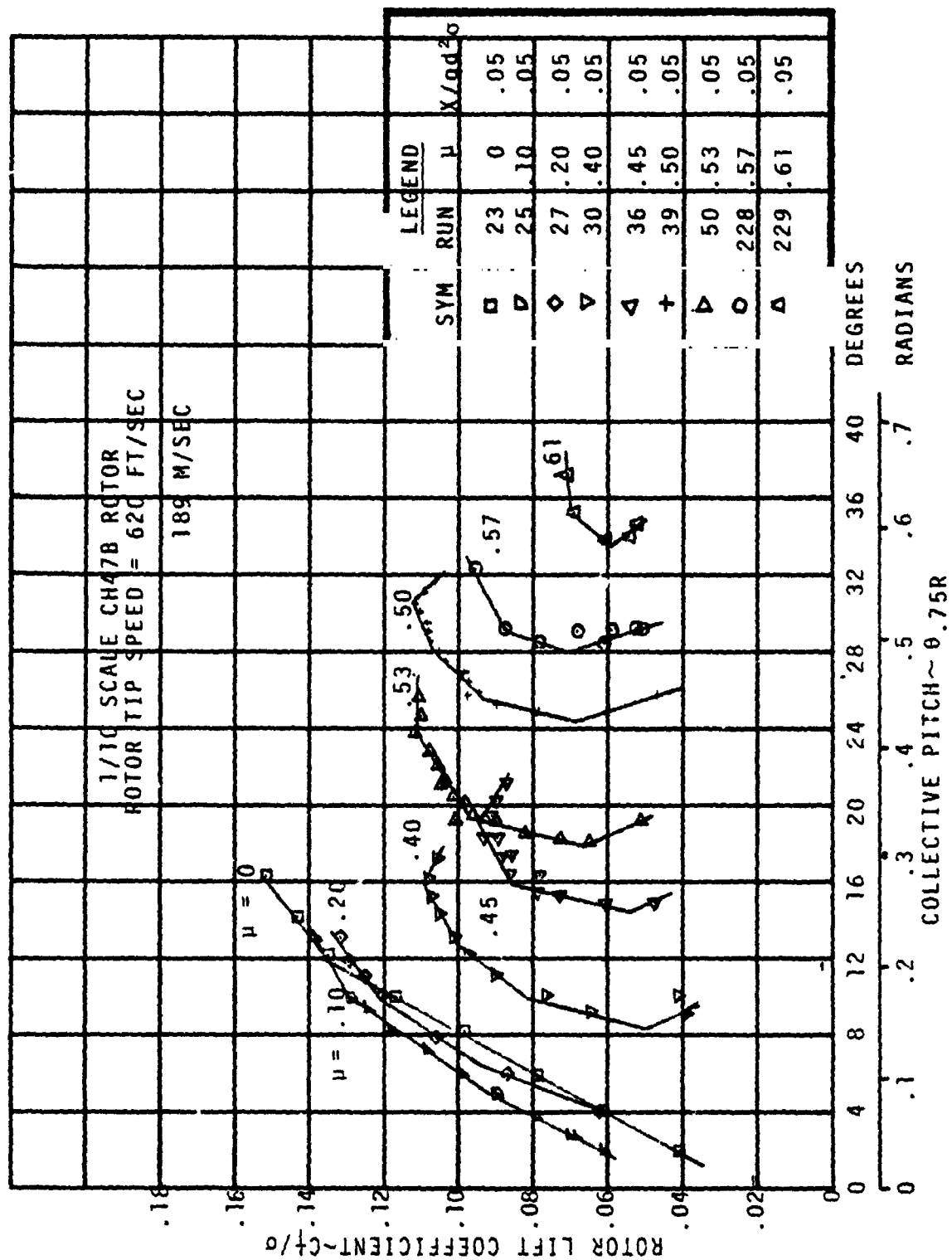


FIGURE 6.3.5 COLLECTIVE PITCH FOR PERFORMANCE SUMMARY $V_T = 620$ FT/SEC

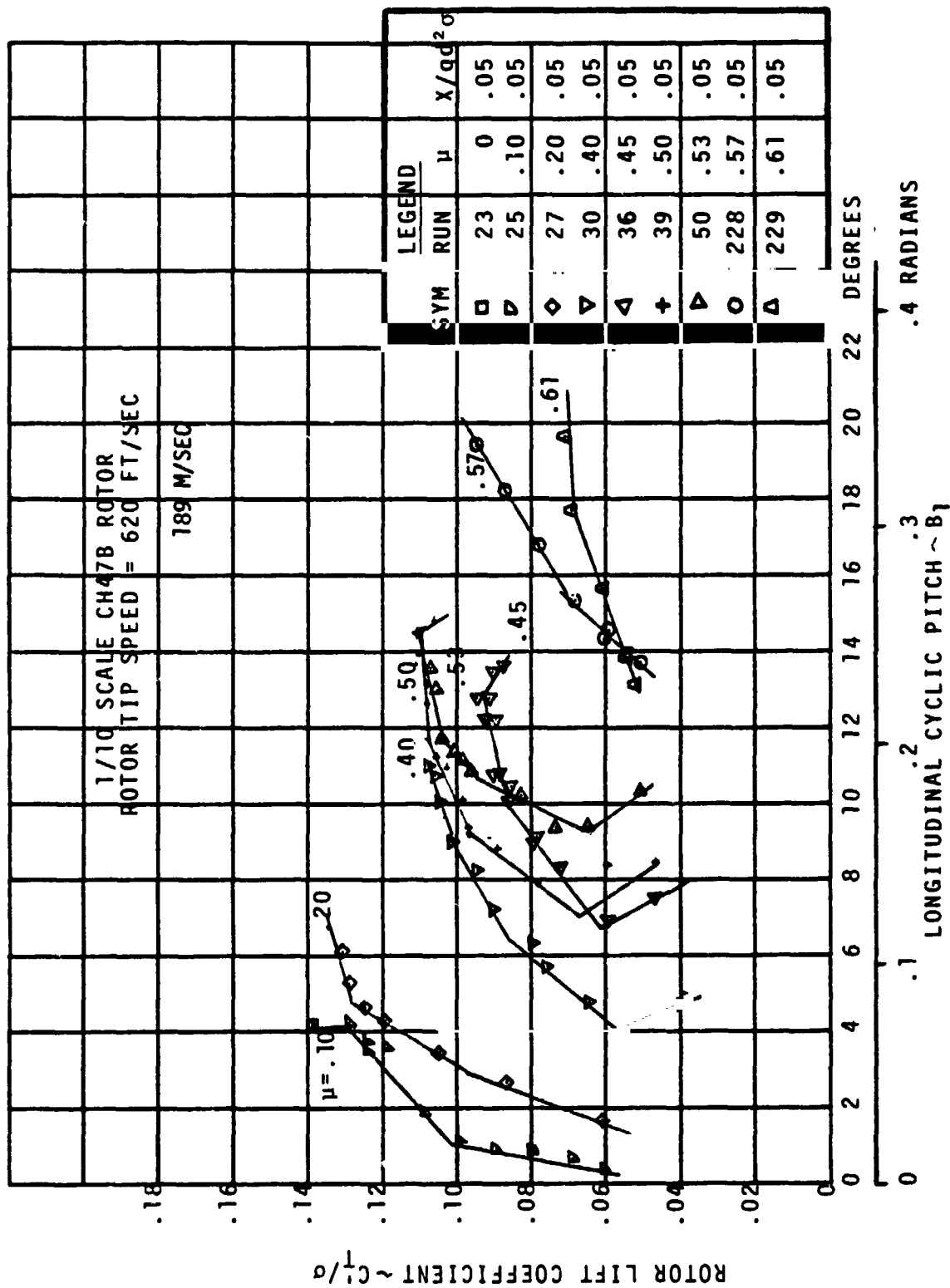


FIGURE 5.3.6 LONGITUDINAL CYCLIC PITCH FOR PERFORMANCE SUMMARY $V_T = 620$ FT/SEC

ORIGINAL PAGE IS
OF POOR QUALITY

121

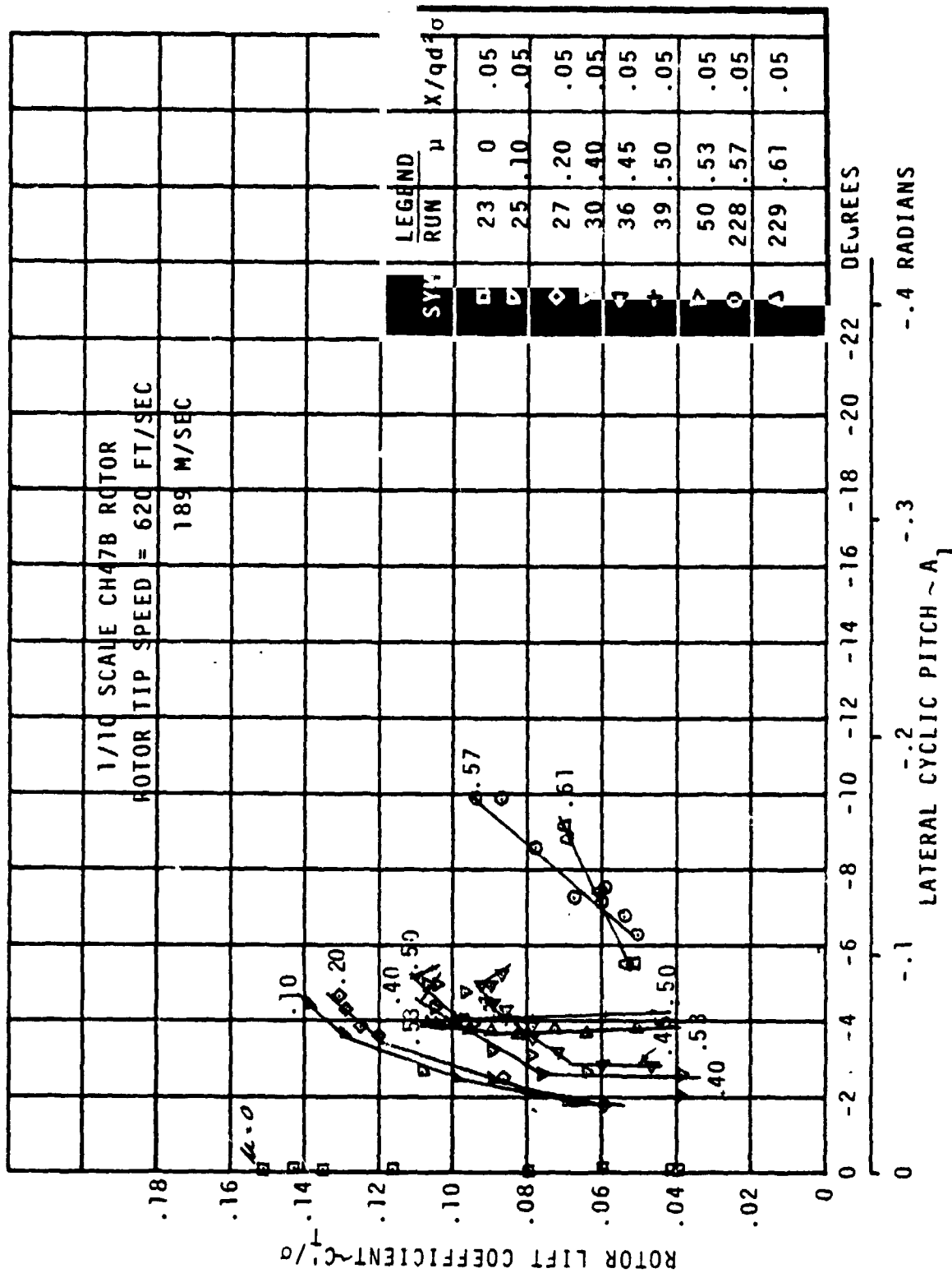


FIGURE 6.3.7 LATERAL CYCLIC PITCH FOR PERFORMANCE SUMMARY $V_T = 620$ FT/SEC

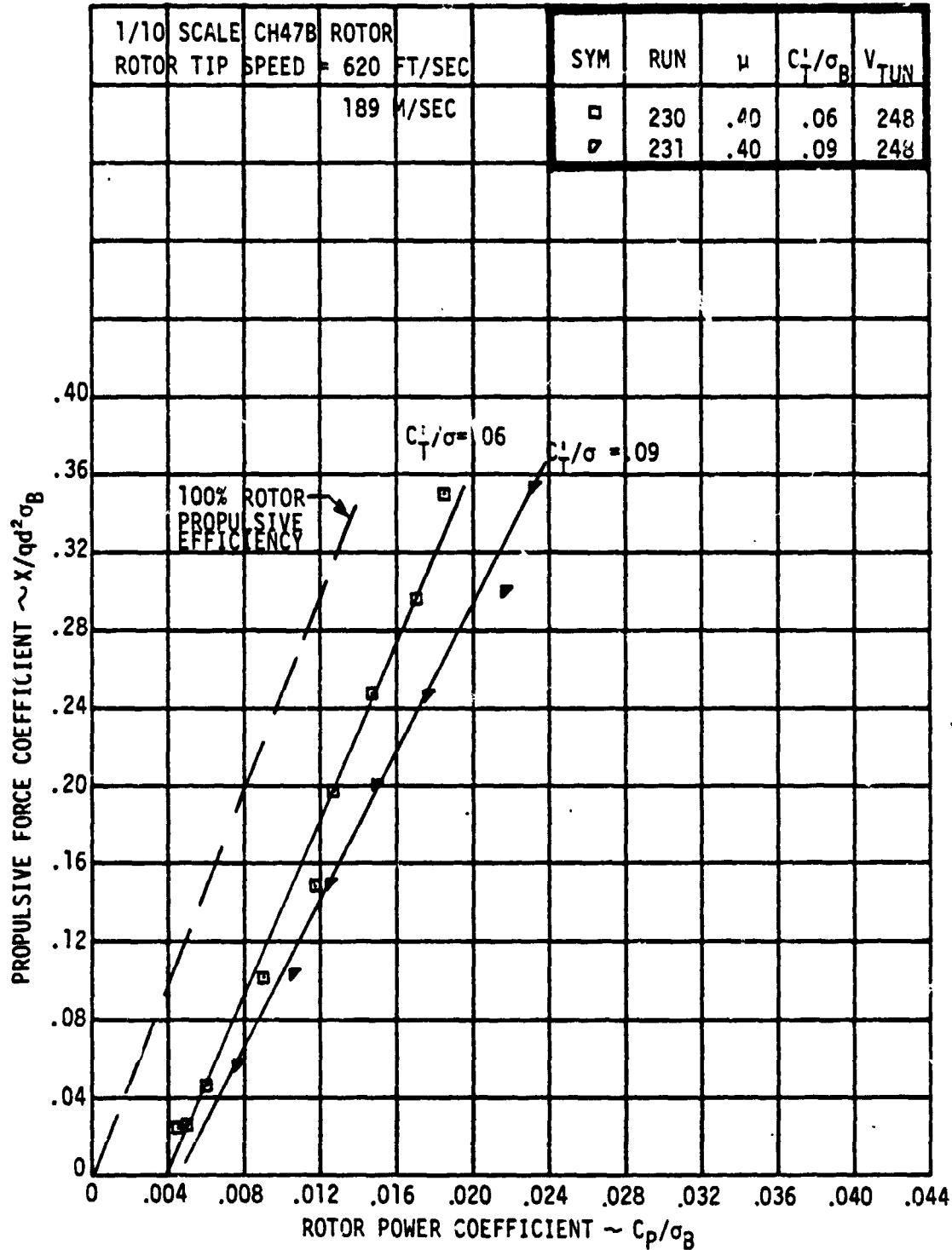


FIGURE 6.3.8 EFFECT OF PROPULSIVE FORCE ON ROTOR POWER REQUIRED
AT CONSTANT LIFT, $\mu = 0.40$

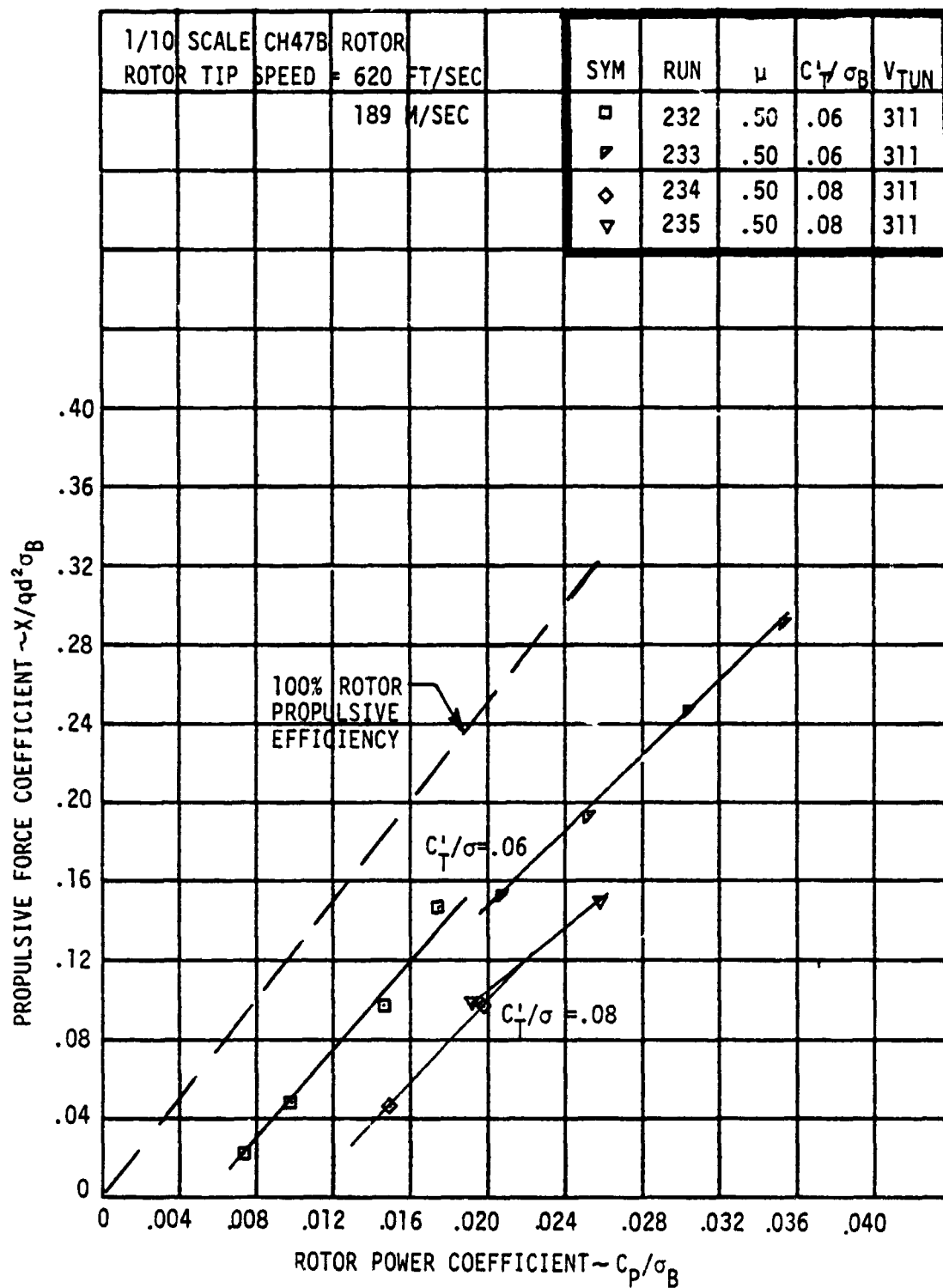


FIGURE 6.3.9 EFFECT OF PROPULSIVE FORCE ON ROTOR POWER
REQUIRED AT CONSTANT LIFT, $\mu = 0.50$

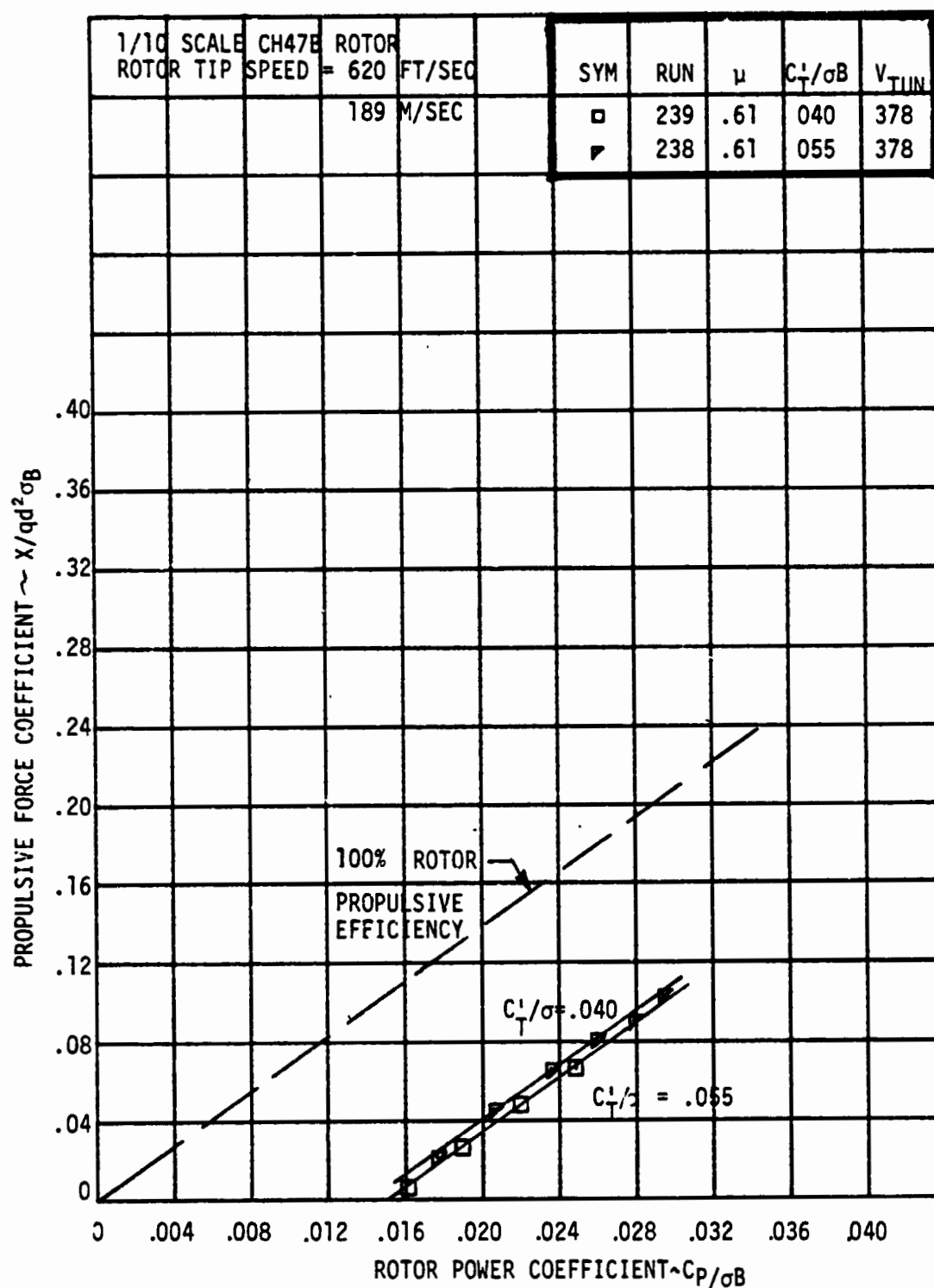


FIGURE 6.3.10 EFFECT OF PROPULSIVE FORCE ON ROTOR POWER REQUIRED AT CONSTANT LIFT, $\mu = 0.61$

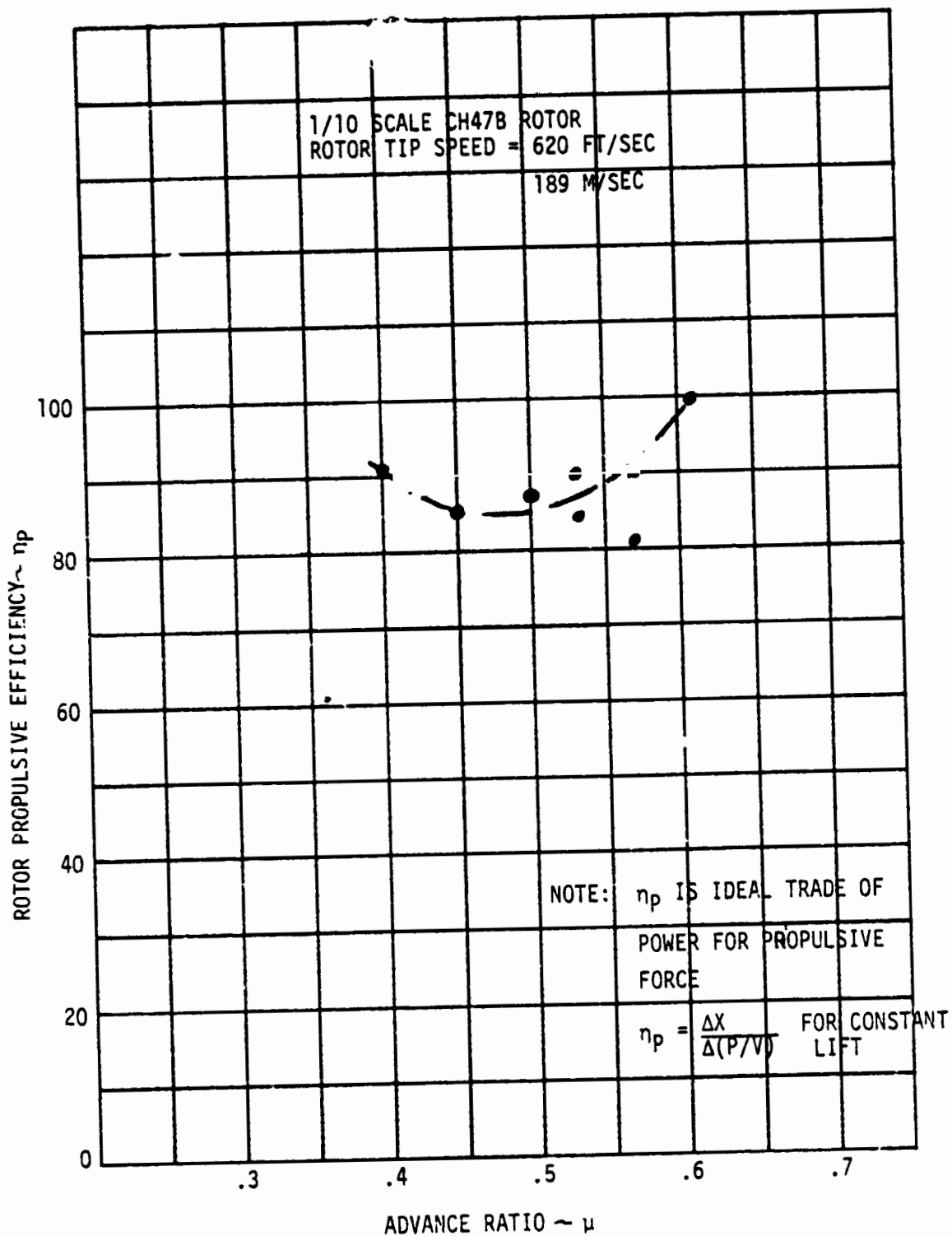


FIGURE 6.3.11 SUMMARY OF ROTOR PROPULSIVE EFFICIENCY

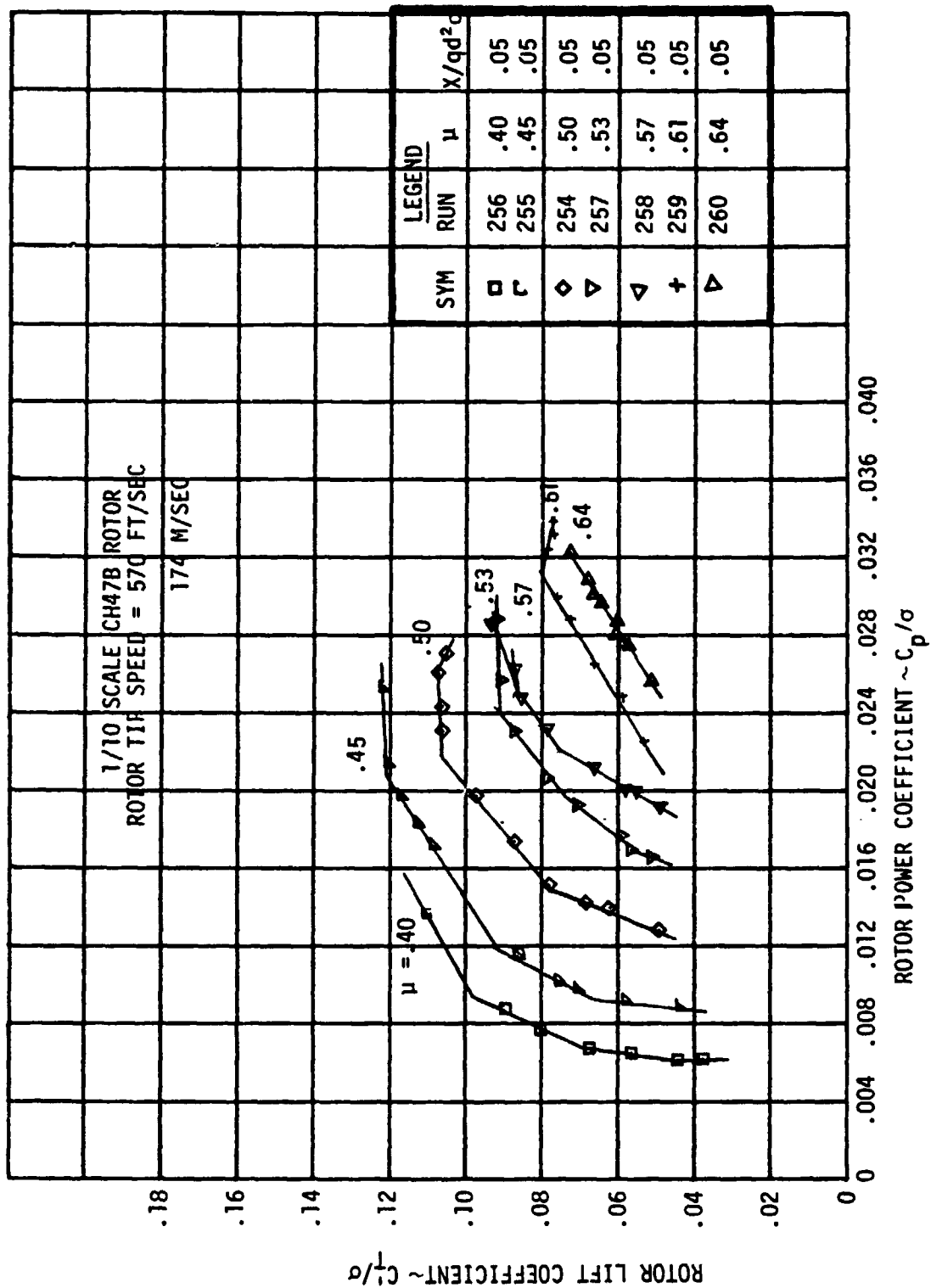


FIGURE 6.3.12 ROTOR PERFORMANCE SUMMARY AT $V_T = 570$ FT/SEC

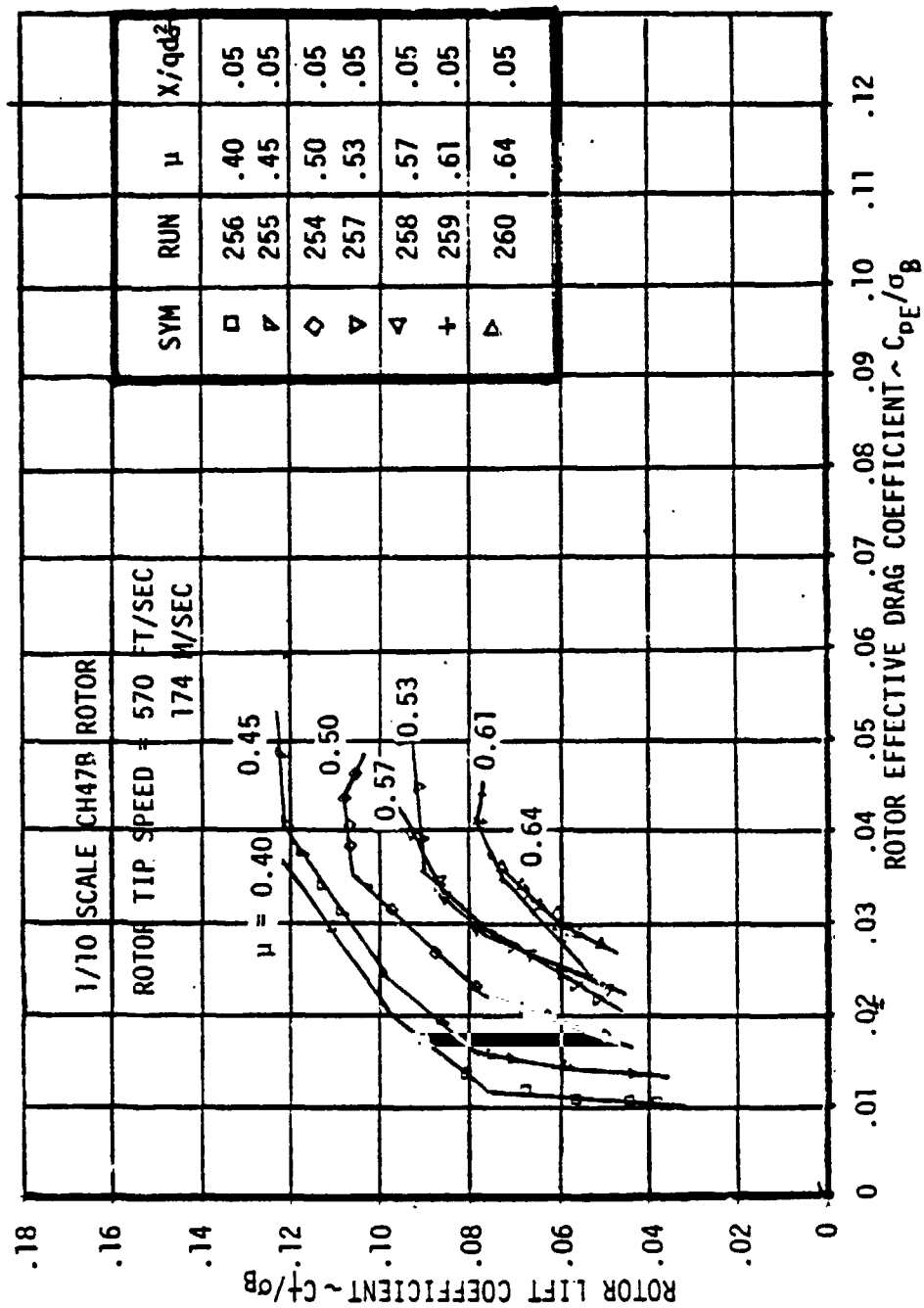


FIGURE 6.3.13 ROTOR EFFECTIVE DRAG FOR PERFORMANCE SUMMARY $V_T = 570$ FT/SEC

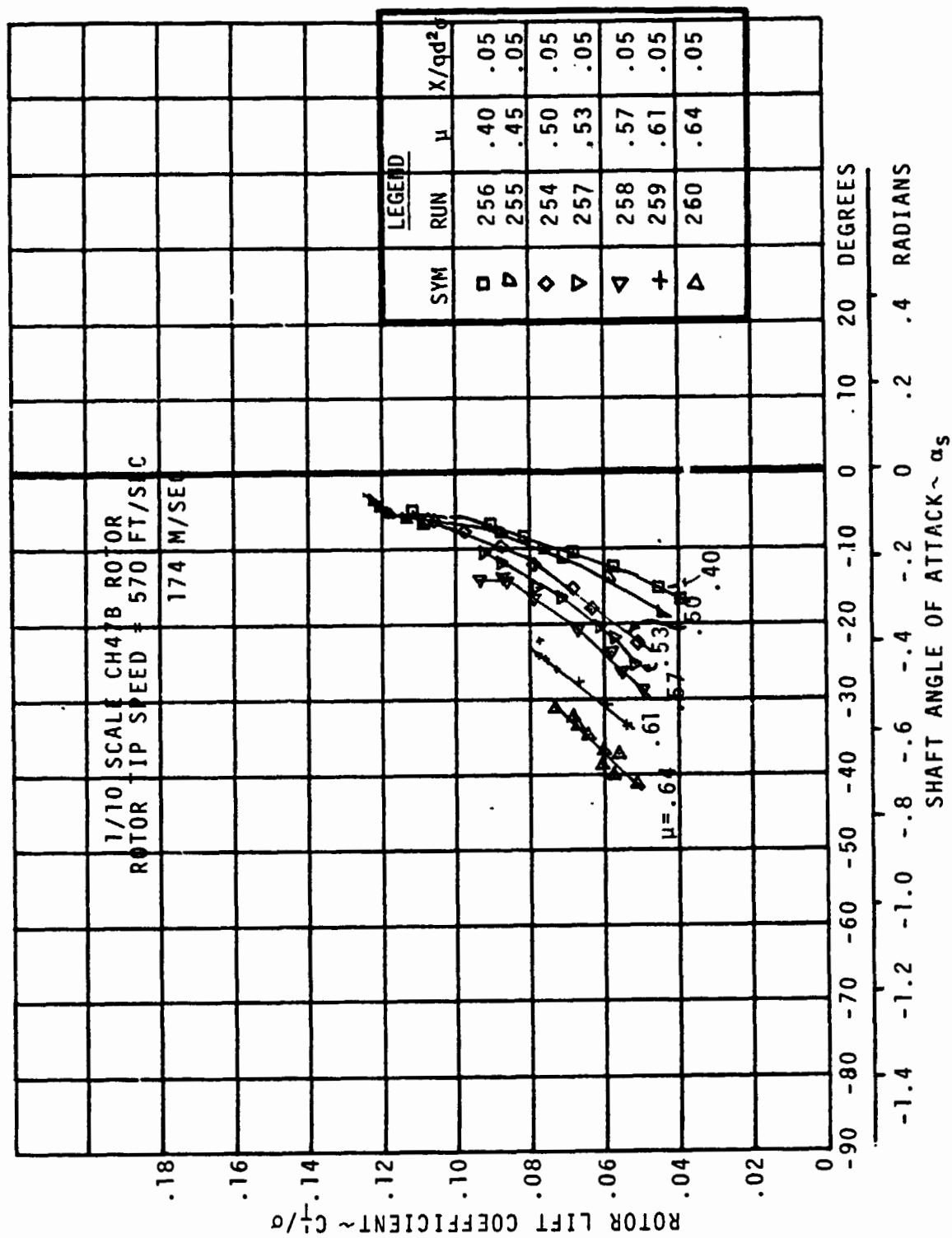


FIGURE 6.3.14 SHAFT ANGLE OF ATTACK FOR PERFORMANCE SUMMARY $V_T = 570$ FT/SEC

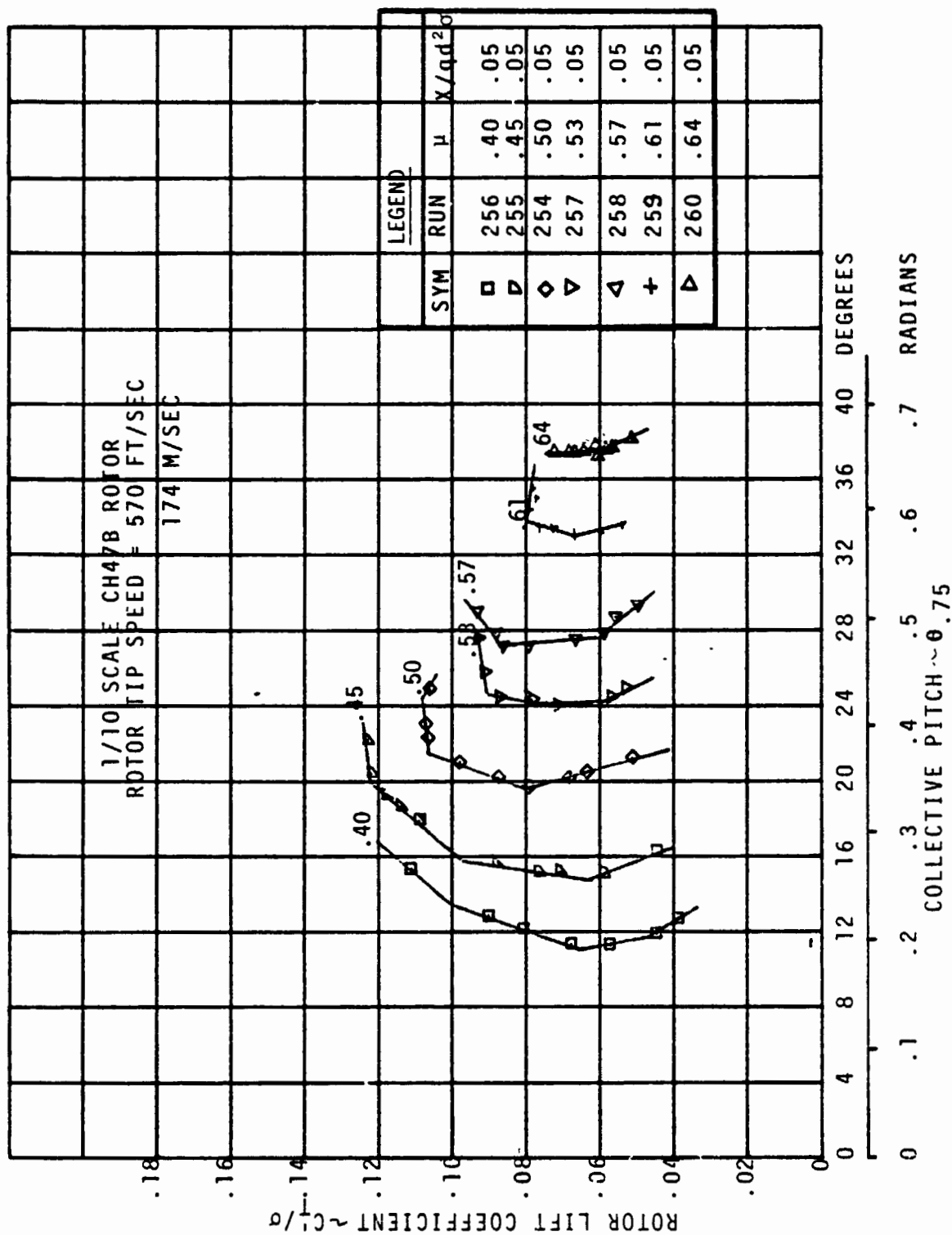


FIGURE 6.3.15 COLLECTIVE PITCH FOR PERFORMANCE SUMMARY $V_T = 570$ FT/SEC

ORIGINAL PAGE IS
 OF POOR QUALITY

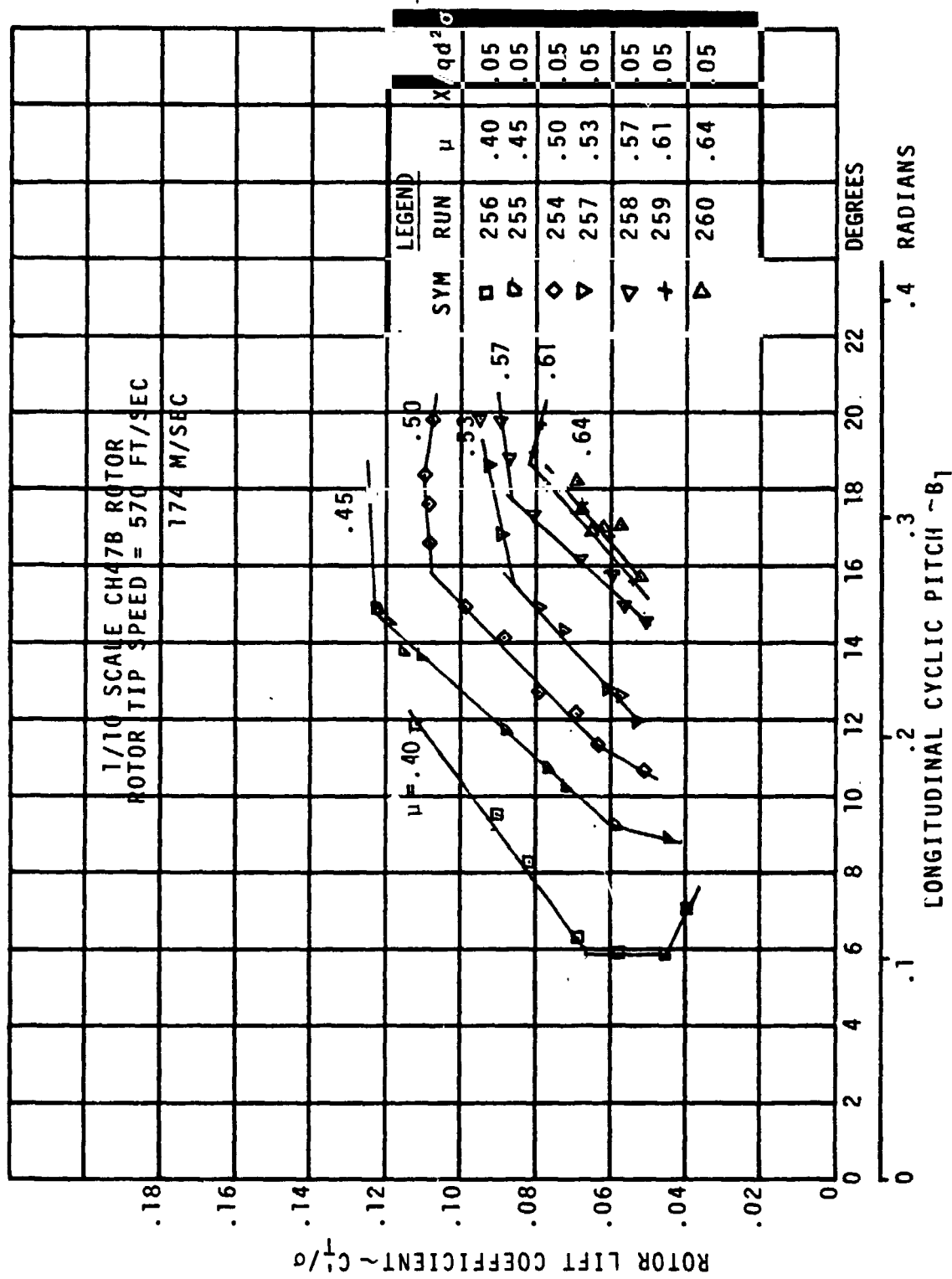


FIGURE 6.3.16 LONGITUDINAL CYCLIC PITCH FOR PERFORMANCE SUMMARY $V_T = 570$ FT/SEC

ORIGINAL PAGE IS
OF POOR QUALITY

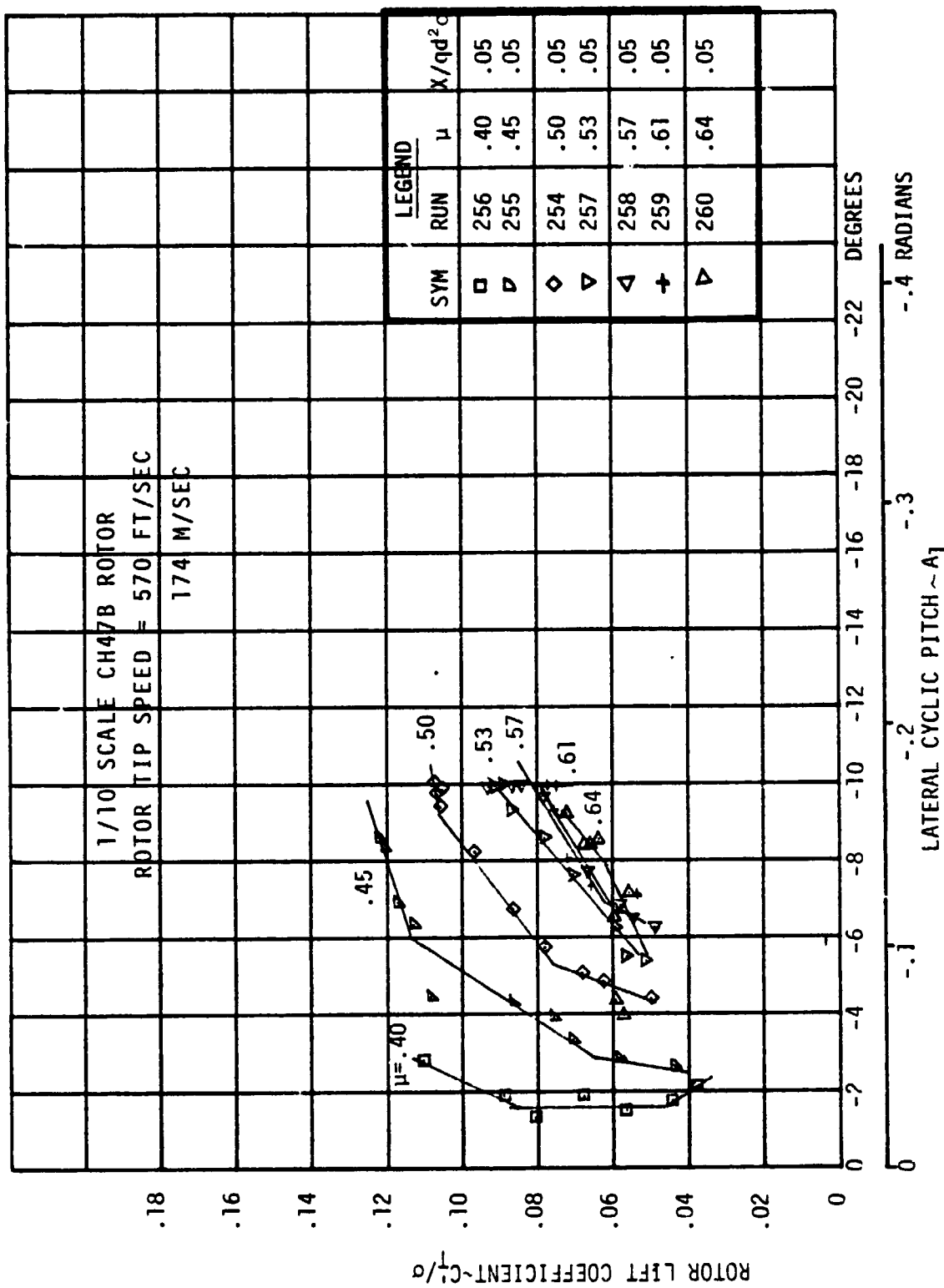


FIGURE 6.3.17 LATERAL CYCLIC PITCH FOR PERFORMANCE SUMMARY $V_T = 570$ FT/SEC

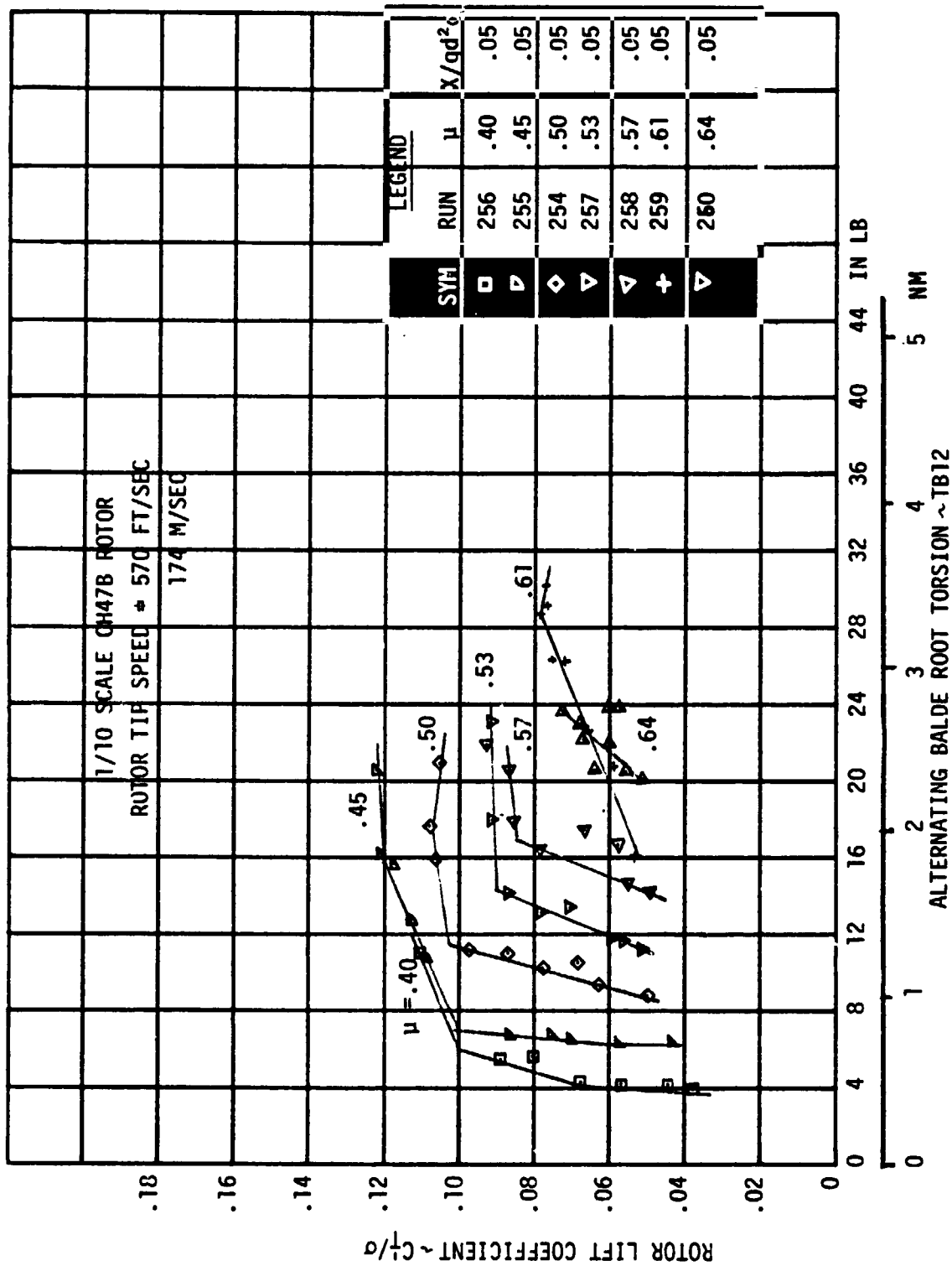


FIGURE 6.3.18 ALTERNATING BLADE ROOT TORSION LOADS FOR PERFORMANCE
 SUMMARY AT $V_T = 570$ FT/SEC

6.4 Rotor Control Power in Proximity of Stall

Test Objective 4: Determine the sensitivity of the rotor forces and moments to rotor control inputs as the lift limit is approached.

During the testing to determine the maximum lift limits, perturbations in longitudinal and lateral cyclic were made from the trimmed operating conditions. This was accomplished at 90 percent and 70 percent of the maximum lift to determine if there was any decrease in the incremental forces and moments generated. The basic test data is presented in Appendix C in Volume 3. From that data three advance ratios have been selected for discussion here: low speed regime, $\mu = 0.20$; mid speed regime, $\mu = 0.40$; high speed regime, $\mu = 0.53$.

For the low speed regime, $\mu = 0.20$, the longitudinal control power is presented in Figure 6.4.1 for $C_T/\sigma = 0.090$ and 0.123 . Rotor pitching moment and longitudinal force sensitivities are presented in the upper portion of the figure and indicate no significant change produced when operating near the lift limit. On the bottom of the figure, the cross coupling in rotor rolling moment and side force also show no effect of operating near the lift limit. Lateral control power is presented in Figure 6.4.2, showing the sensitivity of rotor rolling moment and side force to lateral cyclic. There is no change in the rolling moment and only a slight change in the side force sensitivity to lateral cyclic. The cross coupling terms of rotor pitching moment and

longitudinal force indicate no change in sensitivity when operating near the lift limit. Rotor thrust and power variations with longitudinal or lateral cyclic are unaffected as the rotor lift is increased from 70 percent to 90 percent of the lift limit at an advance ratio of 0.20, as indicated in Figure 6.4.3.

For an advance ratio of 0.40, the sensitivity of rotor hub moments and inplane forces to longitudinal cyclic are presented in Figure 6.4.4 and to lateral cyclic in Figure 6.4.5. There is no change in any of the sensitivities as a result of operating near stall. The impact of longitudinal or lateral cyclic on rotor thrust and power is presented in Figure 6.4.6 and indicates no change results from operating at the higher lift level.

When increasing the operating speed up to an advance ratio of 0.53 the sensitivity of rotor pitching moment and longitudinal force are slightly increased when operating near the lift limit as shown in Figure 6.4.7. The sensitivities become slightly greater in the cross coupling terms of rotor rolling moment and side force when operating near stall. The lateral control characteristics of Figure 6.4.8 are less affected by operation near stall than the longitudinal control characteristics. At $\mu = 0.53$ there was no effect on the thrust or power sensitivities to longitudinal or lateral cyclic. The conclusion drawn from these data trends is that there is a negligible effect on the control power resulting from operation at 90 percent of the lift limit at all speeds up to an advance ratio of 0.53.

1/10 SCALE CH47B ROTOR

$V_T = 620 \text{ FT/SEC}$

189 M/SEC

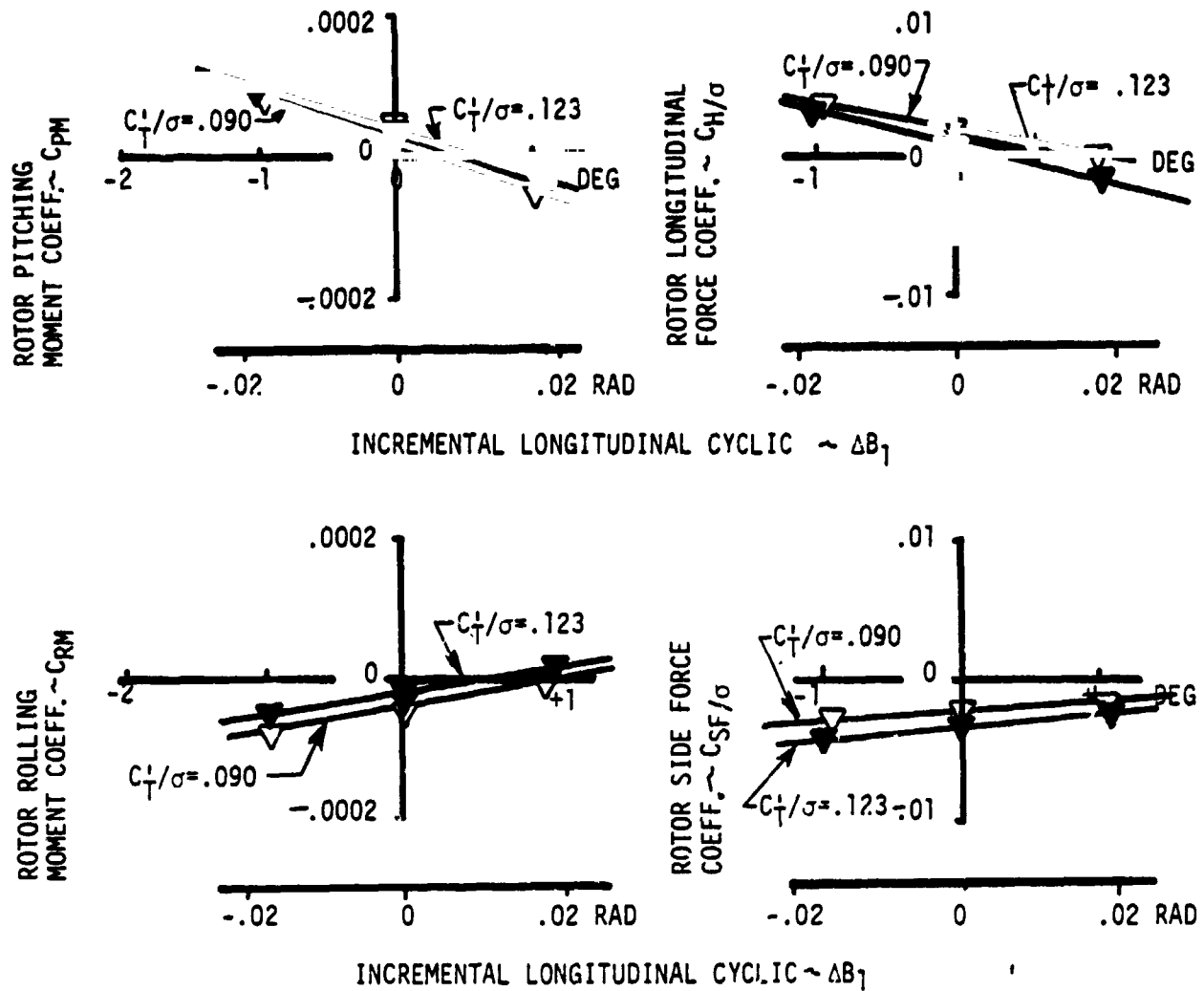


FIGURE 6.4.1 EFFECT OF STALL PROXIMITY ON LONGITUDINAL CONTROL POWER - ROTOR MOMENTS & INPLANE FORCES AT $\mu = 0.20$, $X/qd^2\sigma = 0.05$

1/10 SCALE CH47B ROTOR

$V_T = 620 \text{ FT/SEC}$

189 M/SEC

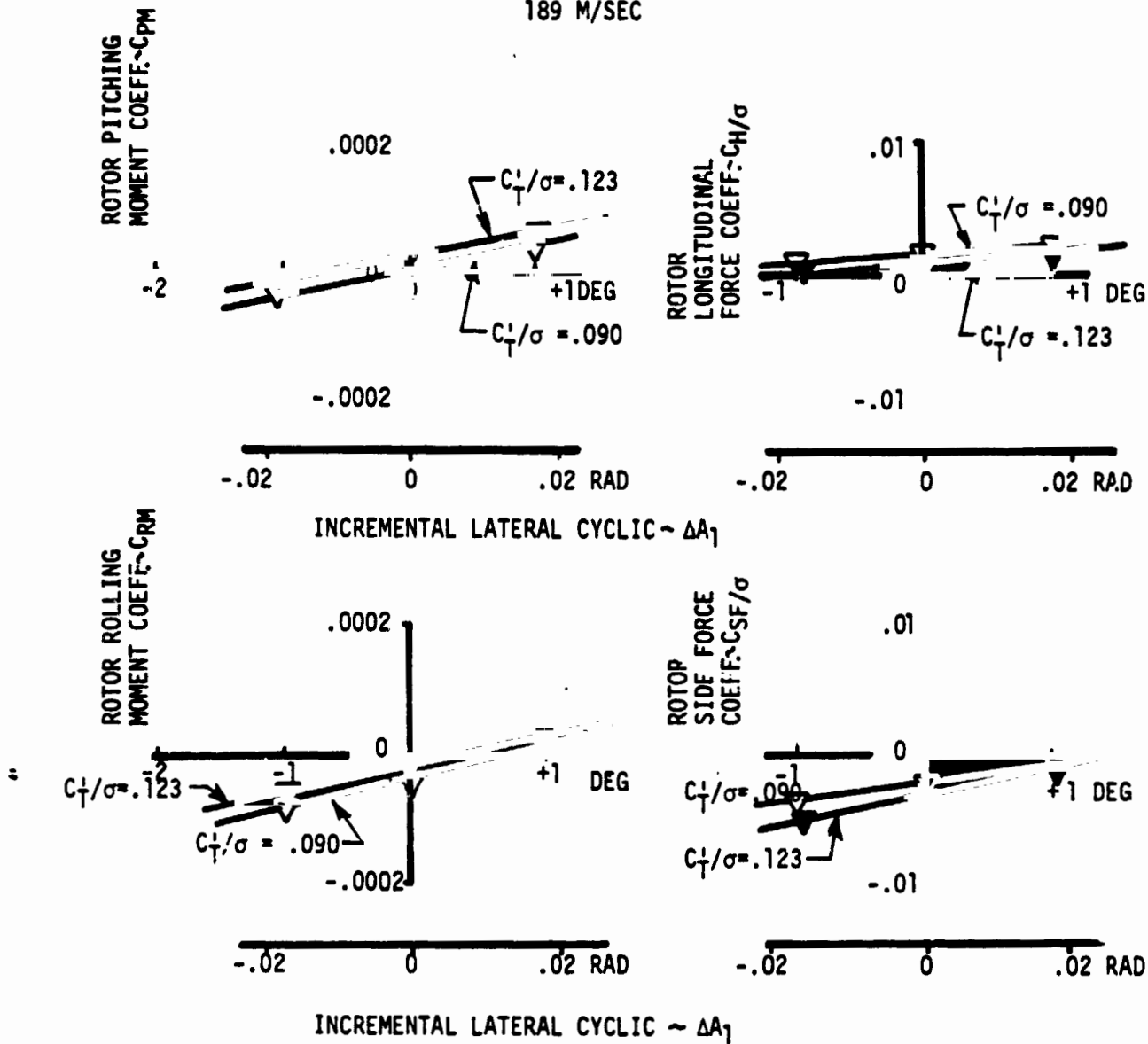


FIGURE 6.4.2 EFFECT OF STALL PROXIMITY ON LATERAL CONTROL POWER - ROTOR MOMENTS & INPLANE FORCES AT $\mu=0.20$, $X/qd^2\sigma = 0.05$

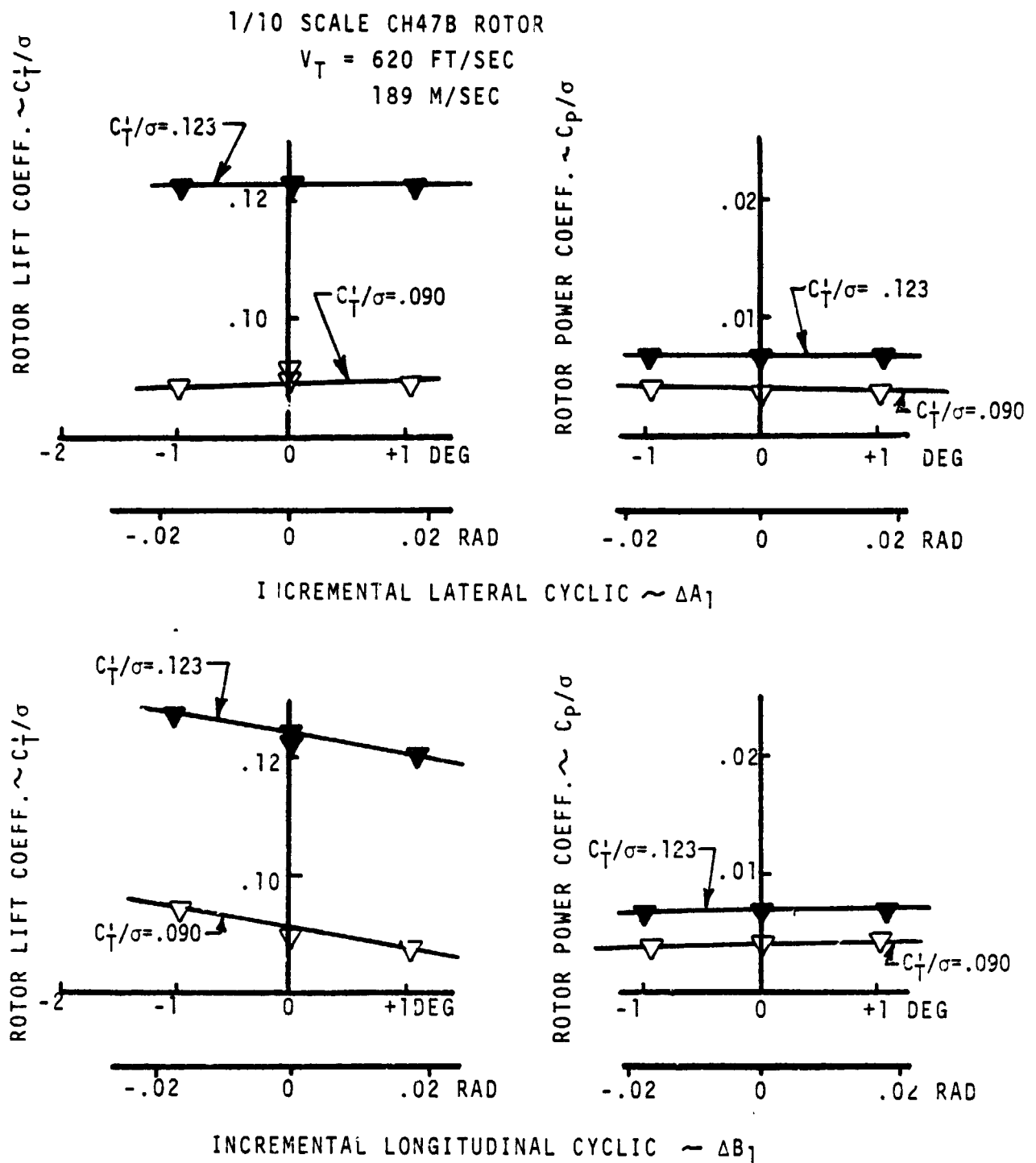


FIGURE 6.4.3 EFFECT OF STALL PROXIMITY ON ROTOR CONTROL POWER -
 ROTOR LIFT & POWER VARIATION AT $\mu=0.20$, $X/qd^2\sigma = 0.05$

1/10 SCALE CH47B ROTOR

$V_T = 620 \text{ FT/SEC}$

189 M/SEC

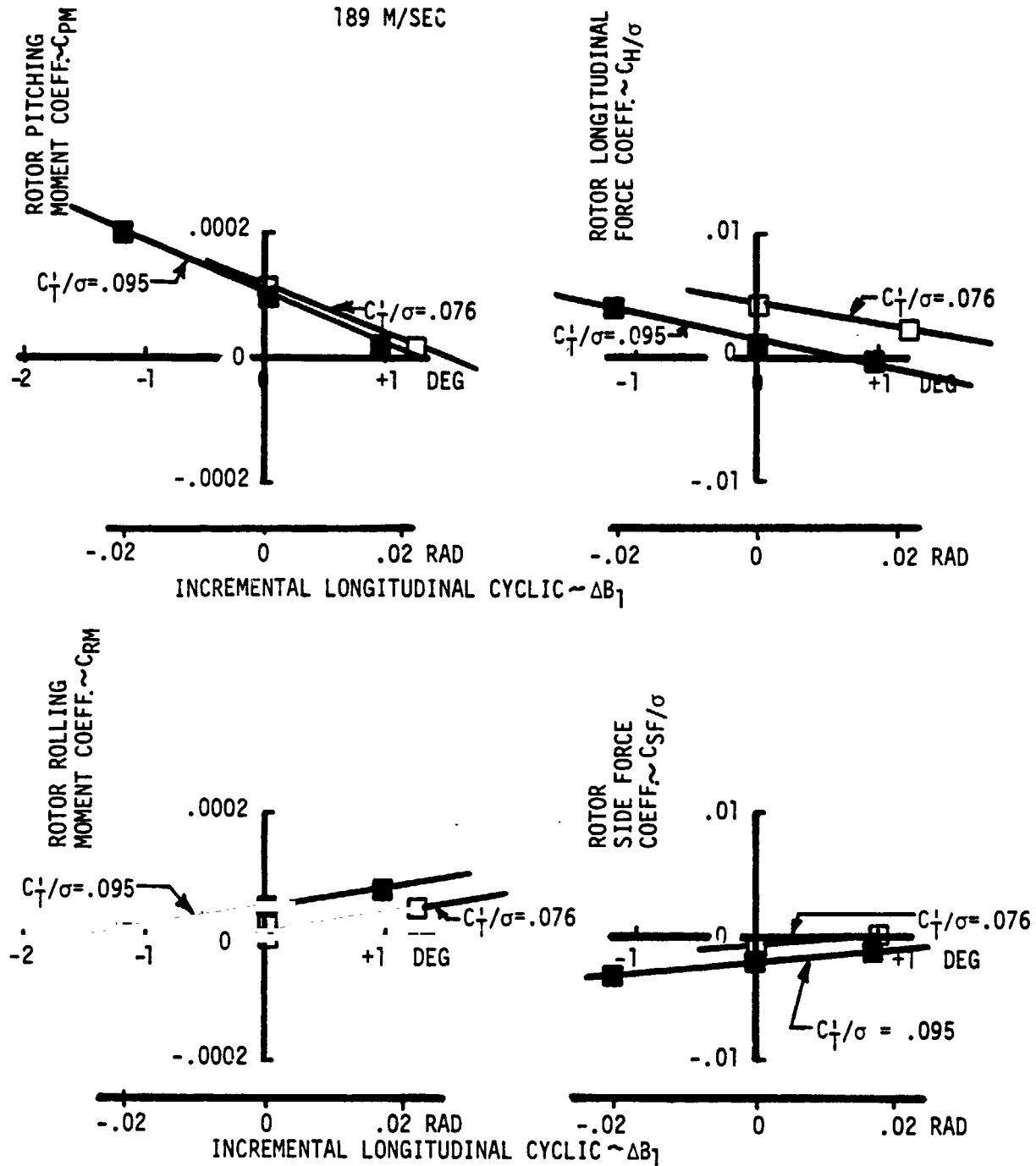


FIGURE 6.4.4 EFFECT OF STALL PROXIMITY ON LONGITUDINAL CONTROL POWER - ROTOR MOMENTS & INPLANE FORCES AT $\mu=0.40$ X/qd² $\sigma = 0.05$

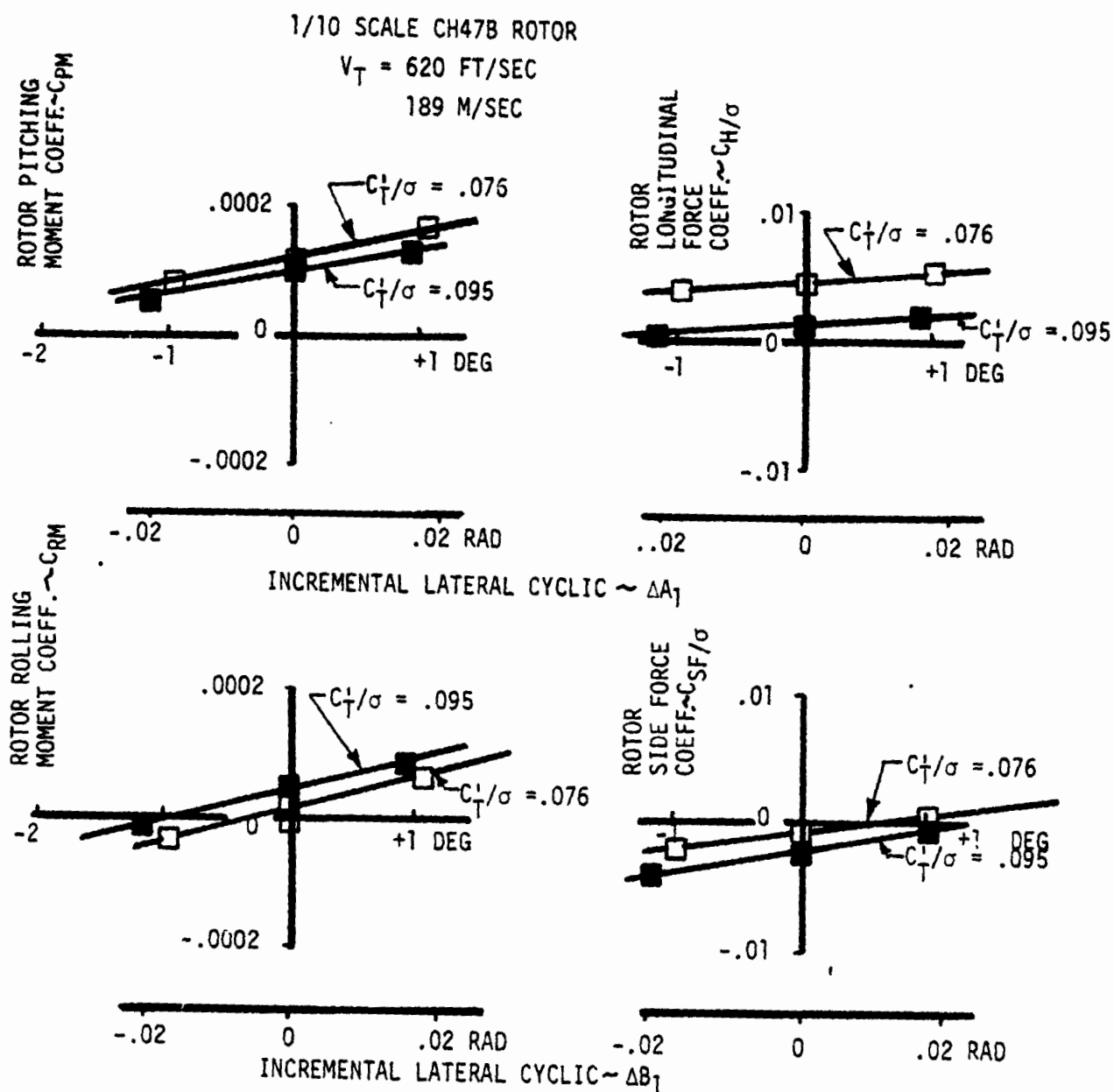


FIGURE 6.4.5 EFFECT OF STALL PROXIMITY ON LATERAL CONTROL POWER -
 ROTOR MOMENTS & INPLANE FORCES AT $\mu = 0.40$ X $q/d^2\sigma = 0.05$

1/10 SCALE CH47B ROTOR

$V_T = 620 \text{ FT/SEC}$

189 M/SEC

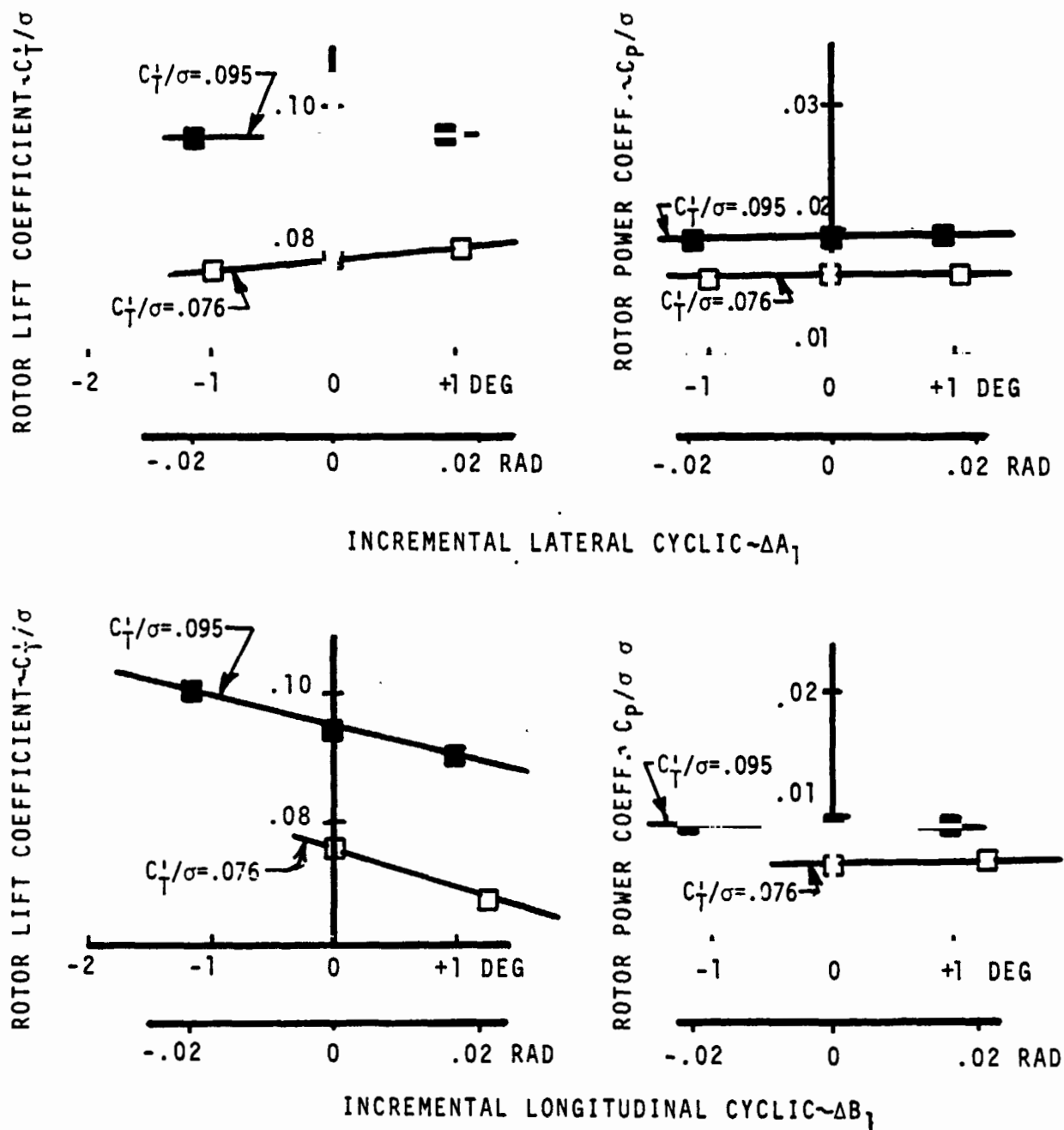


FIGURE 6.4.6 EFFECT OF STALL PROXIMITY ON ROTOR CONTROL POWER - ROTOR LIFT & POWER AT $\mu=0.40$, $X/qd^2\sigma = 0.05$

1/10 SCALE CH-47B ROTOR
 $V_T = 620 \text{ FT/SEC}$
 $= 189 \text{ M/SEC}$

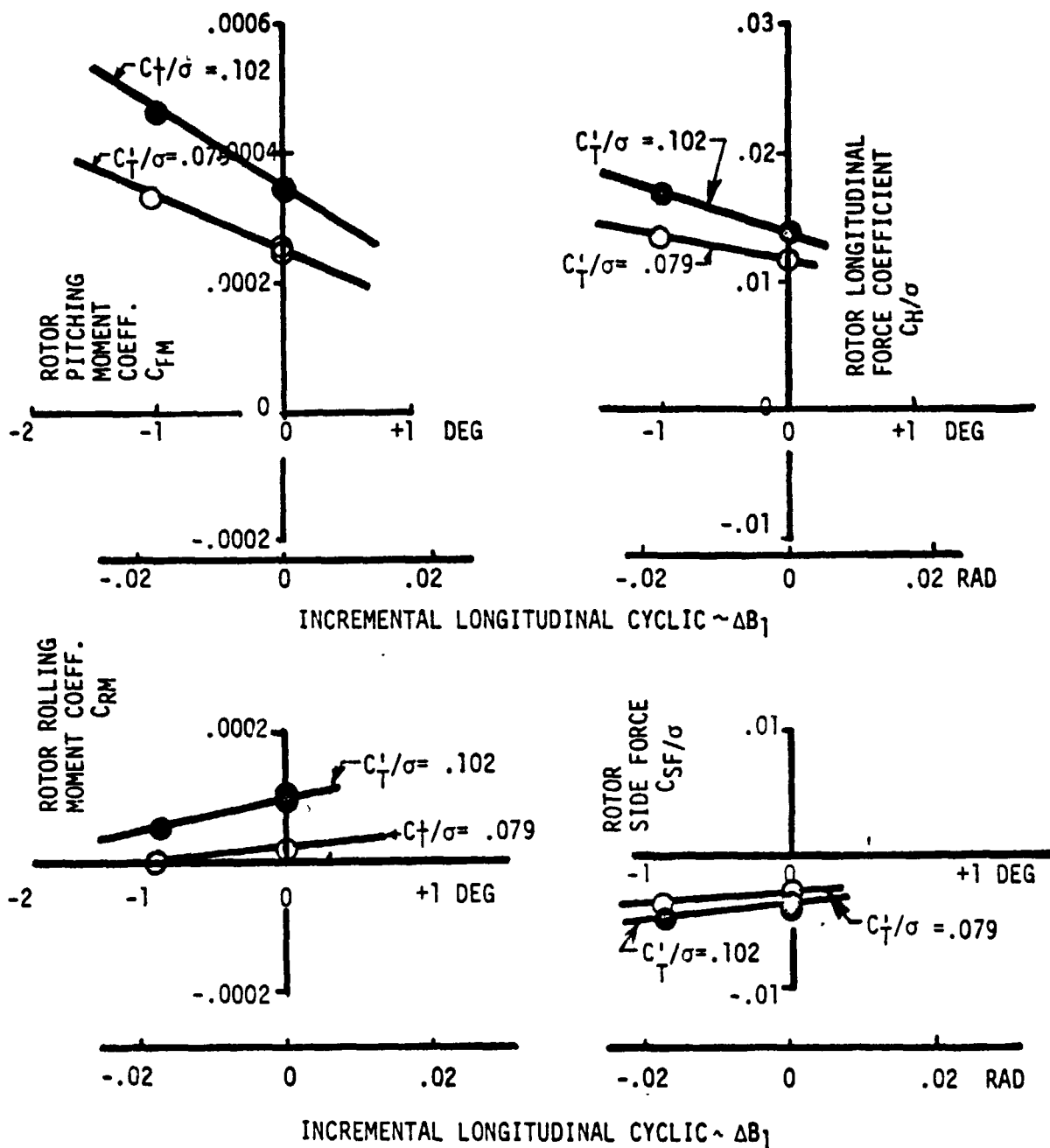


FIGURE 6.4.7 EFFECT OF STALL PROXIMITY ON LONGITUDINAL CONTROL POWER
 ROTOR MOMENTS & INPLANE FORCES AT $\mu = 0.53$; $X/qd^2\sigma = 0.05$

ORIGINAL PAGE IS
 OF POOR QUALITY

1/10 SCALE CH47B ROTOR
 $V_T = 620 \text{ FT/SEC}$
 189 M/SEC

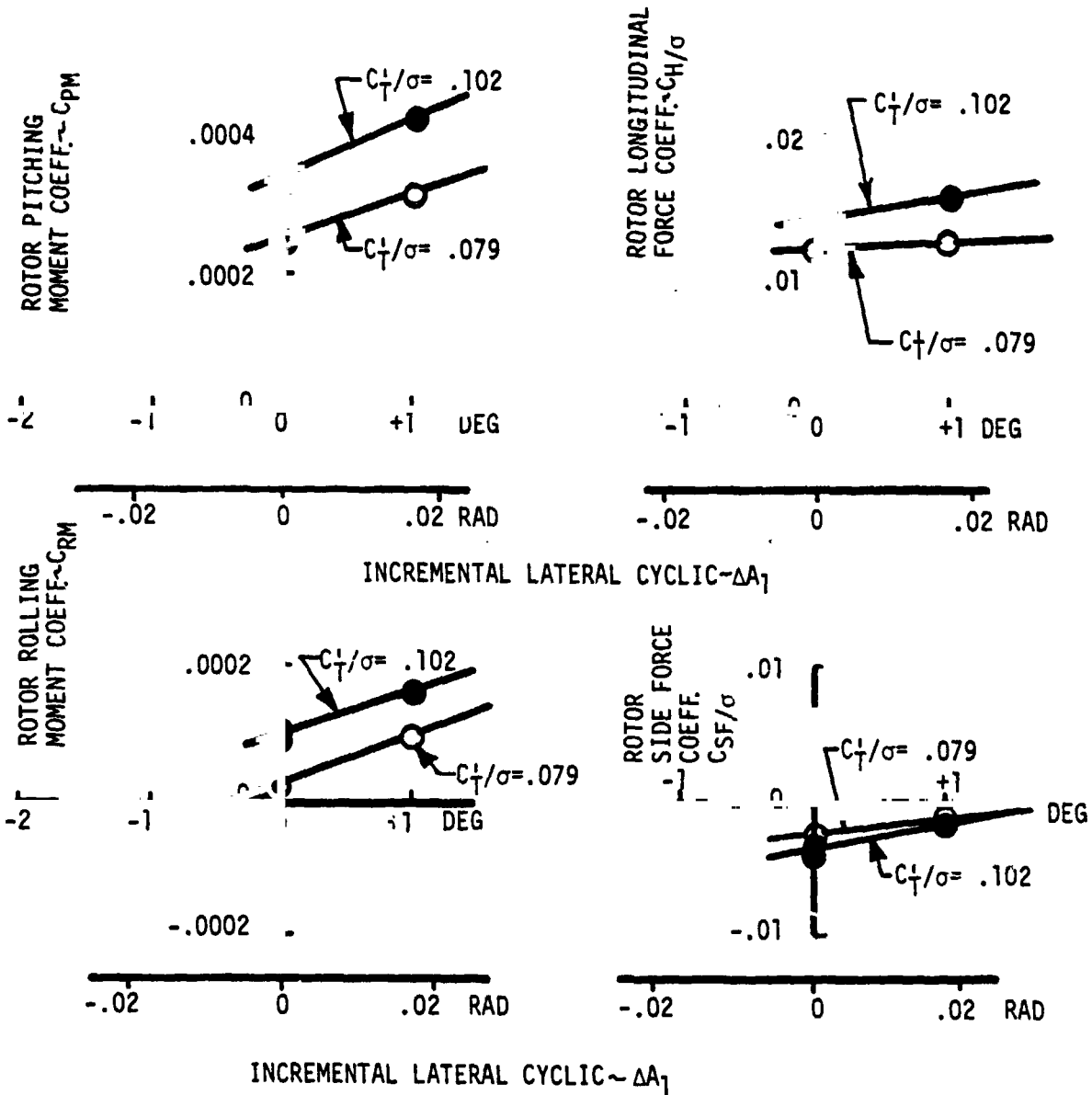


FIGURE 6.4.8 EFFECT OF STALL PROXIMITY ON LATERAL CONTROL POWER-ROTOR MOMENTS & INPLANE FORCES AT $\mu = 0.53$, $X/qd^2\sigma = 0.05$

1/10 SCALE CH47B ROTOR

$V_T = 620 \text{ FT/SEC}$

189 M/SEC

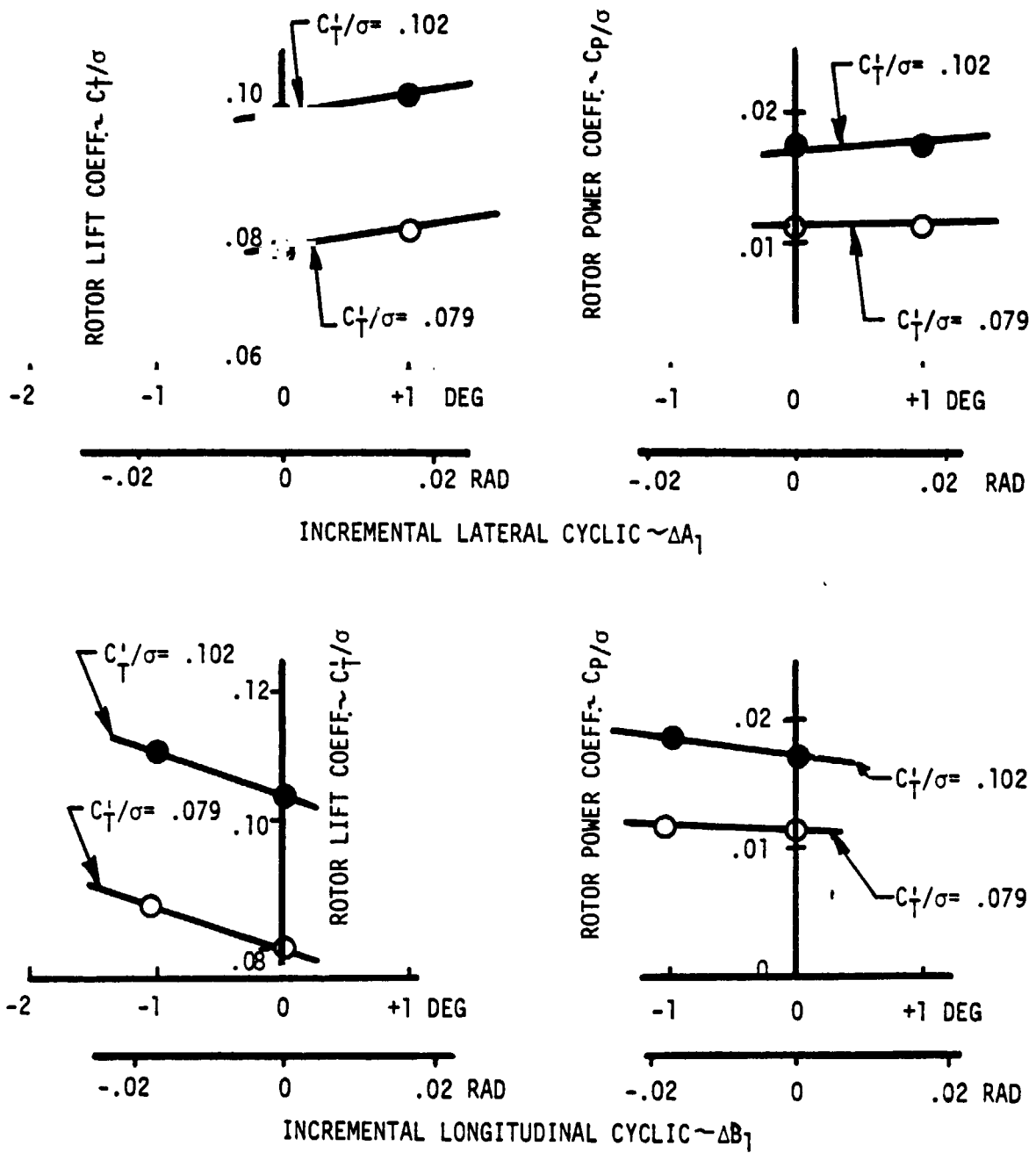


FIGURE 6.4.9 EFFECT OF STALL PROXIMITY ON ROTOR CONTROL POWER-ROTOR LIFT & POWER AT $\mu = 0.53$, $X/qd^2\sigma = 0.05$

6.5 Advancing Tip Mach Number Effects on the Lift Limit

Test Objective 5: Define the effect of advancing tip Mach number on the lift and propulsive force limits.

The lift and propulsive force limitations defined and presented up to this point have been for the basic tip speed of 620 ft/sec. Since the lift limit is a result of stall, and stall of an airfoil is significantly influenced by Mach number, it led to the obvious question what is the influence of advancing tip Mach number on the lift limits of a rotor? To determine this effect, a nominal increment of 0.05 in Mach number was selected which required reducing the rotor tip speed to approximately 570 ft/sec. The lift limit testing was performed in the same manner as described in Section 6.1 and a summary of the performance data obtained in the process of defining the lift limit for 570 ft/sec at a propulsive force coefficient of 0.05 has been shown in Figures 6.3.12 through 6. 3.18.

A summary of the lift limit variation with advance ratio for 570 ft/sec is shown in Figure 6.5.1, with a dashed line, and shows a continuous decrease in the limit from an advance ratio of 0.45 to 0.64. To show the relative change in the limits resulting from this 0.05 change in Mach number, the lift limit of Figure 6.1.3 is superimposed on Figure 6.5.1. The most significant difference in the limit is the distinct change in shape. For the lower tip speed there is no dip in lift limit at an advance

ratio of 0.45 increasing to a maximum between 0.50 and 0.53. The result is a lower lift limit between advance ratios of 0.50 and 0.60 by approximately $\Delta C_T^1/\sigma = 0.01$, but beyond $\mu = 0.60$, the lower tip speed has a definite advantage with the more shallow rate of change in lift limit with advance ratio.

The difference in the limits between the low tip speed and the high tip speed data between $\mu = 0.50$ and 0.60 appears consistent with the trend of section characteristics: as the section Mach number is reduced from 0.40 toward zero the maximum section lift coefficient reduces. It could also result from the lower dynamic pressure decreasing the beneficial effects of the reverse flow region. At advance ratios below 0.50 and above 0.60 the trend reverses and is contrary to expected results. A possible reason for the higher lift limit with the lower tip speed could be the result of operating at a higher effective stiffness since the torsional natural frequency ratio is approximately 6.5 whereas the torsional natural frequency ratio is approximately 6.1 for the higher tip speed. This would reduce the amount of elastic wind up of the blade and could change the lift distribution in a favorable manner providing some stall alleviation. Further analysis is required to fully understand and establish the reason for the results produced.

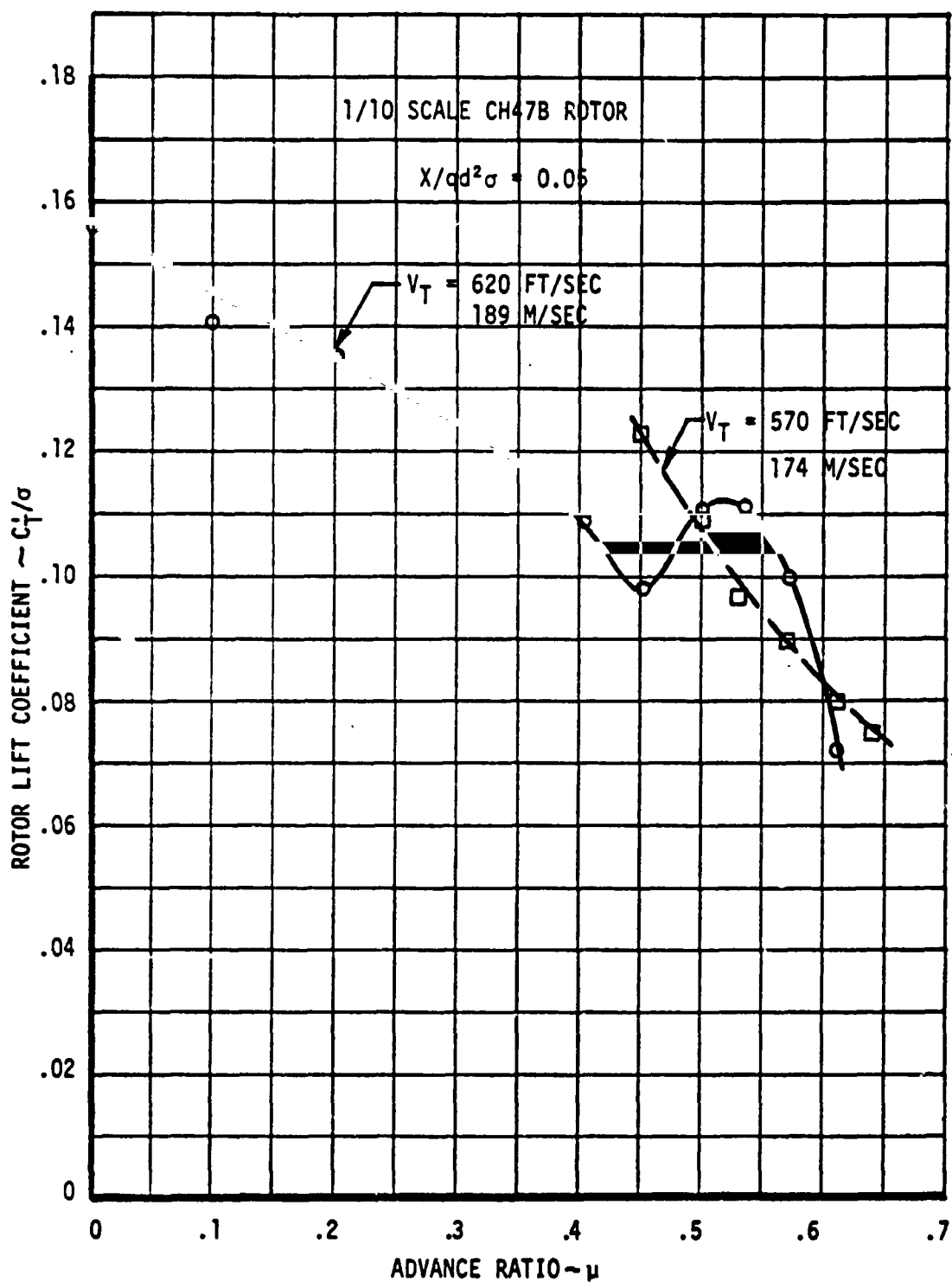


FIGURE 6.5.1 EFFECT OF ROTOR SPEED ON MAXIMUM LIFT LIMIT

6.6 Blade Flapping Response

Test Objective 6: Determine the blade flapping response to a step input in cyclic as the lift limit is approached.

The last section of the wind tunnel test was set aside for the higher risk testing: defining the blade flapping response to a step input to cyclic at the lift limit. An instrumentation failure prevented measuring blade flapping response during this portion of the testing. Although a quantitative answer was not achieved a qualitative one was provided each time the rotor hub moments were trimmed to zero. The hydraulic control system had very rapid response and any input command to the collective or cyclic controls resulted in a step input. Visual observation of the rotor indicated that the blade flapping was highly damped since the rotor stabilized very rapidly without any rotor wobble.

6.7 Rotor Operation in Stall

The test program was accomplished in two different periods in the wind tunnel. This was the result of a model control system problem requiring extensive repairs to the model. Upon re-entering the tunnel, a number of check runs were scheduled to compare data obtained with the repaired model and new blades with data already obtained. During an early run at an advance ratio of 0.53, the rotor power and loads data were significantly higher than the previous data. The control positions were also very different, so an effort was made to obtain the desired rotor lift and propulsive at control settings that were closer to those obtained previously. This was done without shutting down the tunnel or the model. During the second half of the run the performance and loads data obtained for the same rotor lift and propulsive force were very close to the data from the earlier testing but distinctly different from the first half of the run. The resulting performance is presented in Figure 6.7.1 indicating a difference of 0.004 in C_p/σ at the lower lift levels. The maximum lift that was achieved was different by a $\Delta C_{T1}/\sigma = 0.01$. Figure 6.7.2 presents the variation of Rotor Propulsive Force coefficient, Rotor Power coefficient and Rotor Effective Drag coefficient with Rotor Lift Coefficient indicating that there was negligible difference in the rotor propulsive force coefficient. The effective rotor lift to drag ratio, uncorrected for the blade instrumentation, decreases from 3.7 to 2.7.

Rotor controls position and shaft angle are presented in Figure 6.7.3 indicating that the better level of performance has a lower rotor shaft angle of attack and collective. The longitudinal and lateral cyclic are also lower. Examining the alternating blade loads presented in 6.7.4 establishes that there is a slightly lower outboard torsion but the flap and chord bending are significantly lower for the better level of performance.

To assist in the definition of the differences shown, a comparison was made in the outboard torsion (TB 80) wave forms, in Figure 6.7.5. The lift level is approximately 0.098 and the upper wave form is that obtained from data with the highest C_p/σ . The lower wave form is that associated with the better performance. The upper wave form has three distinct load peaks in the last half of the rotor cyclic indicative of rotor stall response at 6/rev, while the lower wave is just starting to show an increase in nose download at $\psi = 270$ degrees. Figure 6.7.6 presents the flap bending wave forms in the same order and the upper wave form is responding at the third flap frequency of 7/rev. Figure 6.7.7 presents the chord wave forms in the same format with the upper curve responding at the first chord frequency of 4.5/rev. Each of these upper wave forms indicate response at the natural frequency for each mode of bending and establishing that the rotor is operating in stall.

These results were shown at a high value of rotor lift coefficient ($C_T^1/\sigma = 0.098$). Figure 6.7.8 defines the sensitivity to lift of the outboard alternating torsion loads with and without stall.

At four selected levels of lift, wave forms are superimposed on the figure. For the lower alternating load level the large nose down load representative of stall is becoming evident only at the highest lift. The wave forms associated with the higher alternating load curve have the six per rev high nose down loads at all lift levels indicating the presence of stall at all lift levels.

A cursory evaluation of other test data runs indicate similar trends but further analysis work is required to determine the differences in the rotor lift distribution and loads distribution.

Stall impacts the maximum lift attainable and a survey through the data from Appendix A provided the data for the lift limit with severe stall that is shown by the dashed line in Figure 6.7.9.

Superimposed on this figure is the lift limit presented in Figure 6.1.3 indicating with severe stall results in a decrease in lift limit by $\Delta C_T^1/\sigma = .006$.

The impact of stall on the lift limit variation with advance ratio has been established as well as the effects on rotor power and loads at one advance ratio. To define the magnitude of the power penalty trend with advance ratio would be demonstrated most effectively in the form of a power required curve with and without stall. A typical configuration was defined by a rotor lift

coefficient (C_l/σ) of 0.08 and a propulsive force coefficient ($X/qd^2\sigma$) of 0.05 to be used for the demonstration of the stall effects. Carefully selecting data from every lift limit and propulsive force limit test run, the power required for the typical model configuration is developed in Figure 6.7.10. In the high speed regime the power penalty, shown by the upper line, is approximately 30 percent greater than the baseline power required.

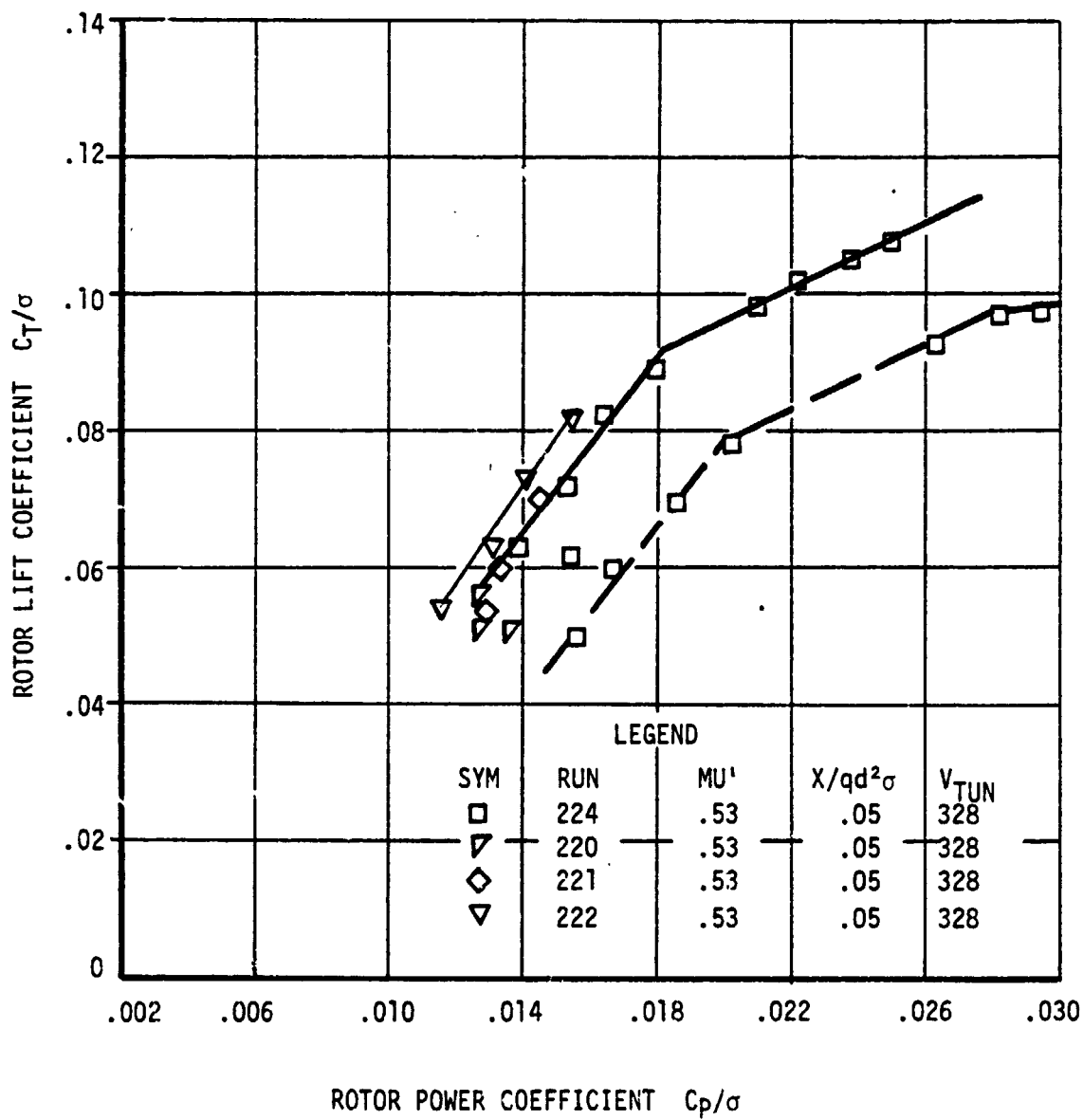


FIGURE 6.7.1 ROTOR PERFORMANCE WITH AND WITHOUT TIP STALL
FOR SAME LIFT AND PROPULSIVE FORCE

ORIGINAL PAGE IS
OF POOR QUALITY

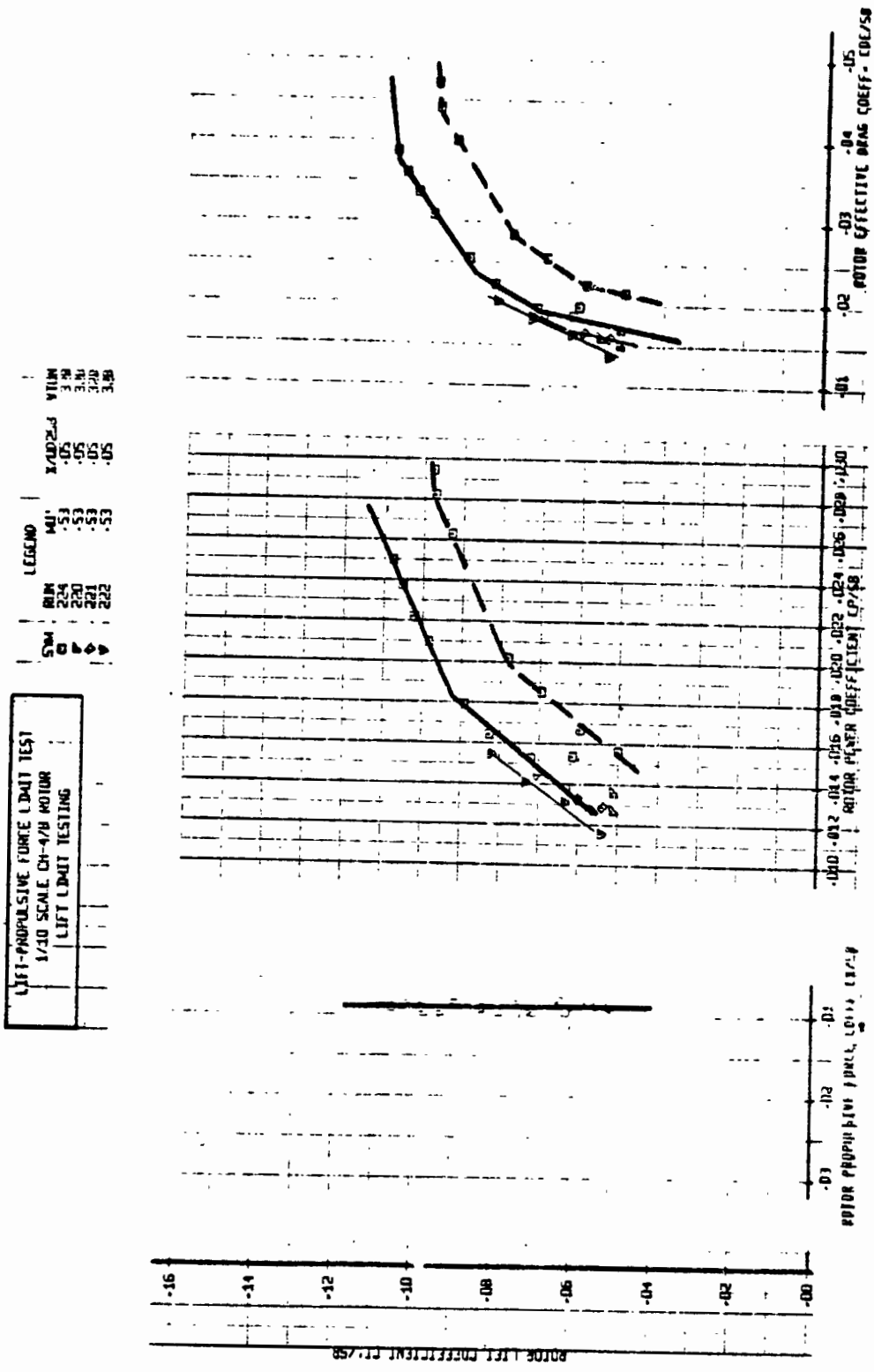


Figure 6.7.2 Rotor Operation With and Without Tip Stall for Same Lift and Propulsive Force

LIFT-PROPULSIVE FORCE LIMIT TEST			
1/10 SCALE CH-47B ROTOR			
LIFT LIMIT TESTING			
5.04	LEGEND	W/D0.258	V/DUN
0	5.3	0.5	3.28
0	5.3	0.5	3.28
0	5.3	0.5	3.28
0	5.3	0.5	3.28

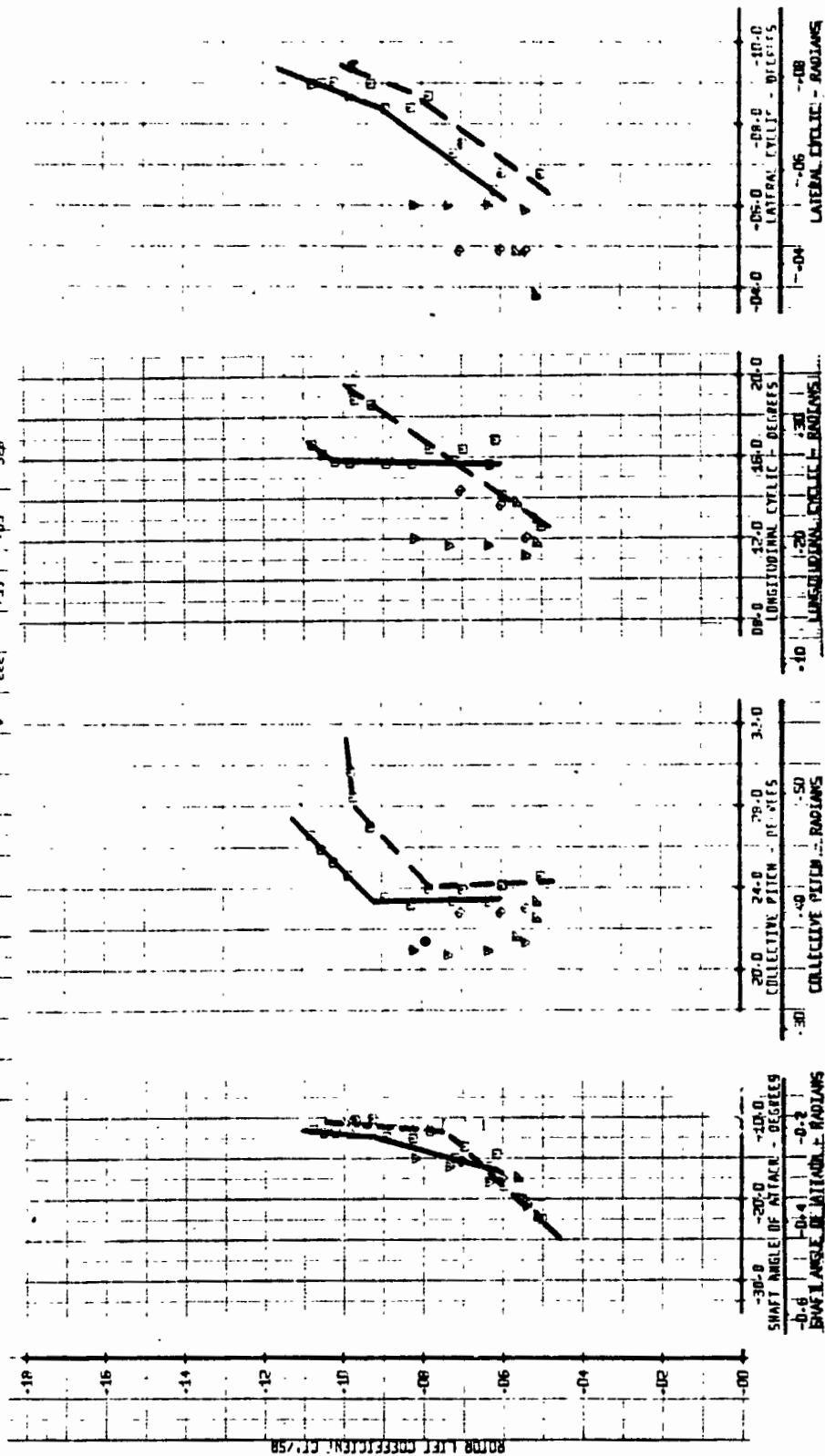


Figure 6.7.3 Rotor Attitude and Control Positions for Operation With and Without Tip Stall for Same Lift and Propulsive Force

LIFT-PROPULSIVE FORCE LIMIT TEST
1/10 SCALE CH-47B ROTOR
LIFT LIMIT TESTING

LEGEND	SYM	AL	1/10 SCALE	VTOL
224	□	.53	.05	330
220	△	.53	.05	330
221	▽	.53	.05	330
222	▽	.53	.05	330

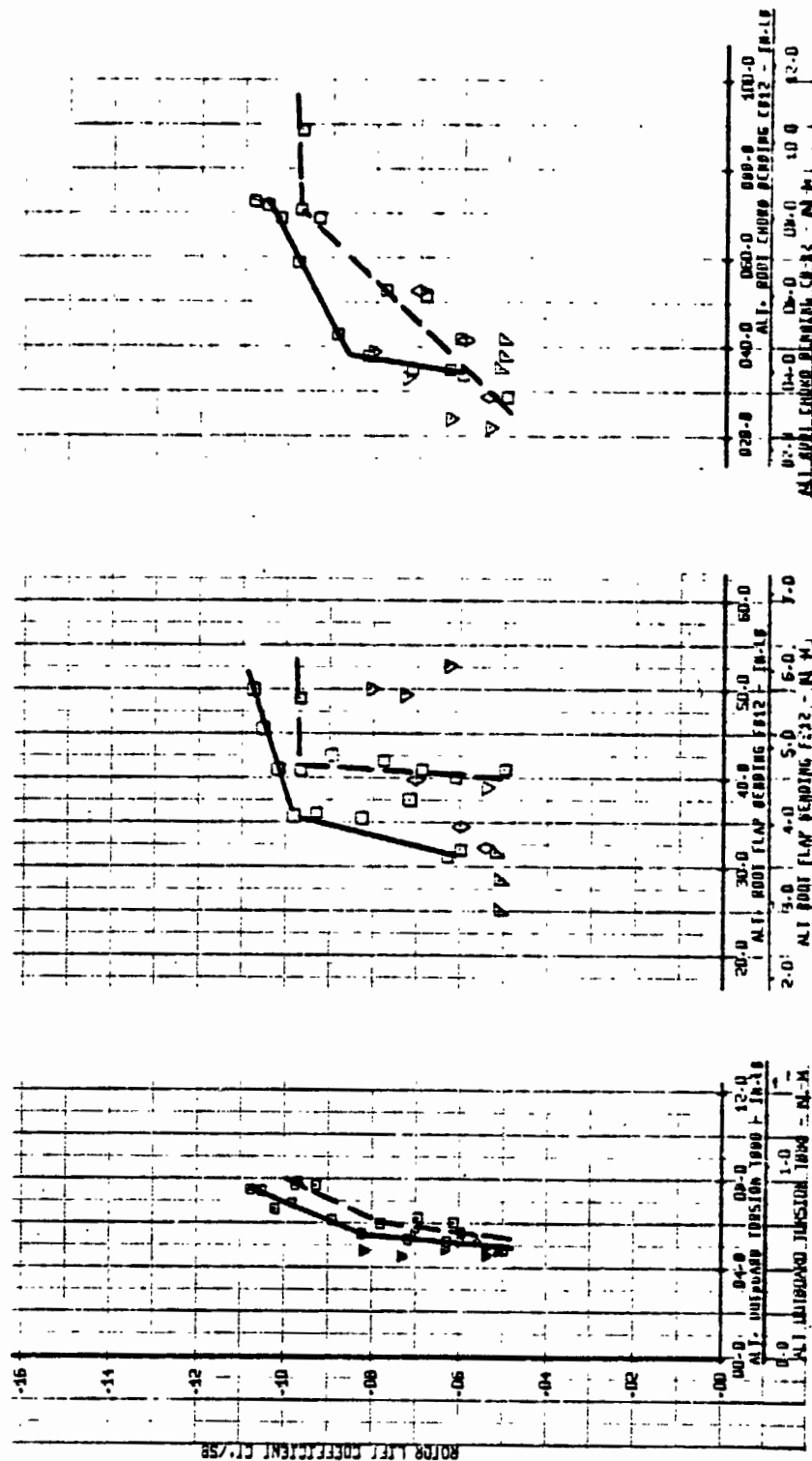


Figure 6.7.4 Alternating Blade Loads for Operating With and Without Tip Stall for Same Lift and Propulsive Force

OUTBOARD BLADE TORSION LOAD TB 80

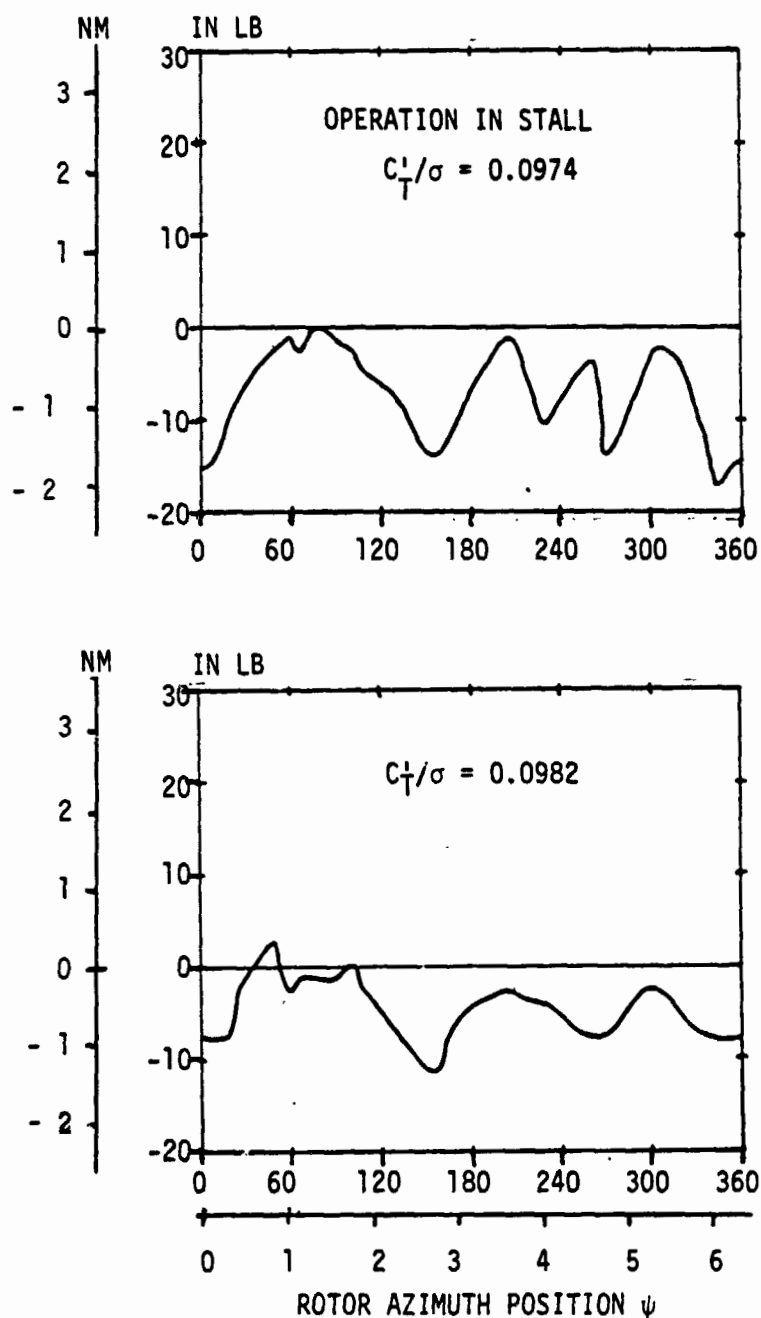


FIGURE 6.7.5 COMPARISON OF OUTBOARD TORSION LOAD WAVE FORM FOR OPERATION IN AND OUT OF STALL $\mu = 0.53$ $X/qd^2\sigma = 0.05$

BLADE ROOT FLAP BENDING LOAD FBI2

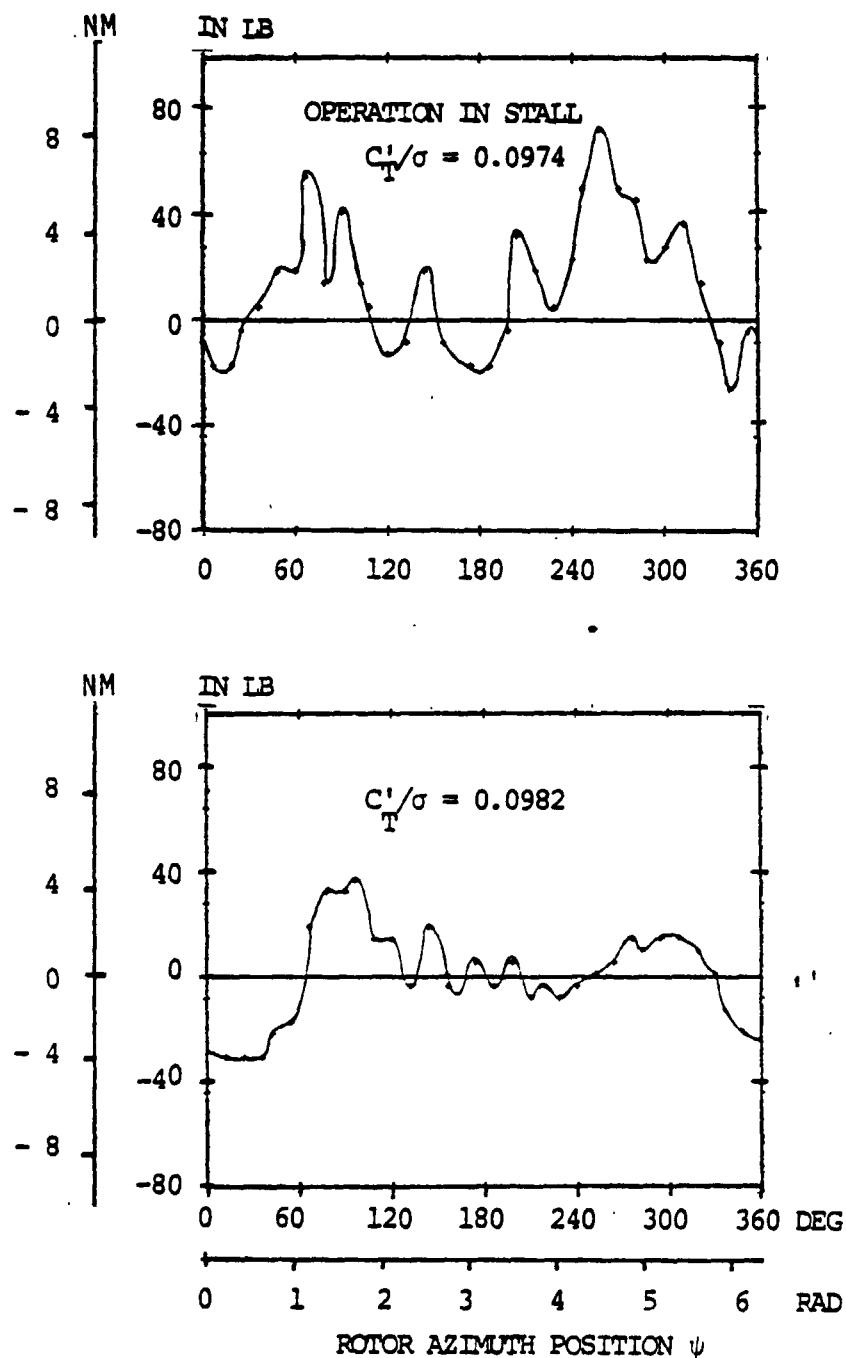


FIGURE 6.7.6 COMPARISON OF FLAP BENDING LOAD WAVE FORM FOR
OPERATION IN AND OUT OF STALL $\mu = 0.53$ $X/qd^2\sigma = 0.05$

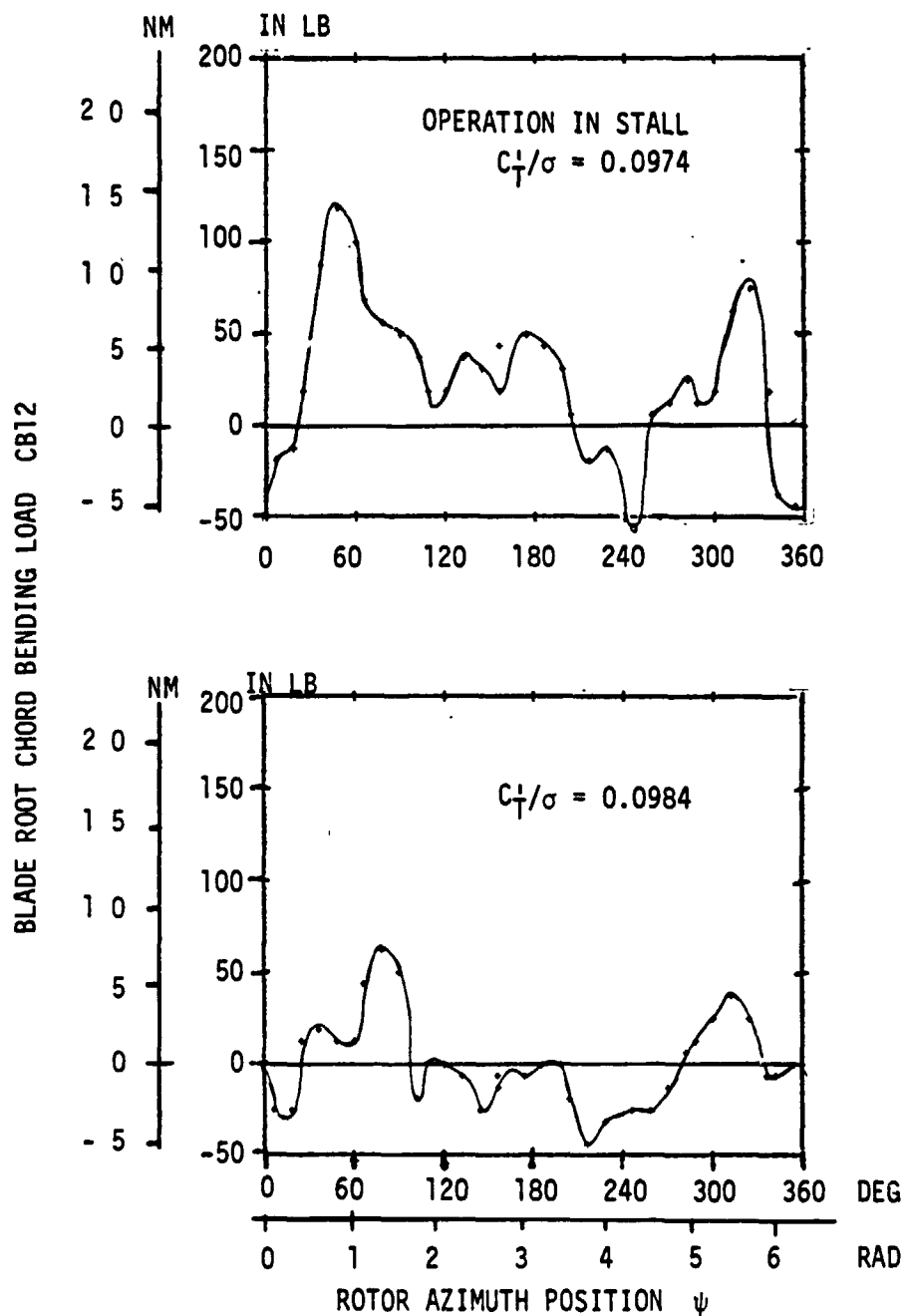


FIGURE 6.7.7 COMPARISON OF CHORD BENDING LOAD WAVE FORM FOR
OPERATION IN AND OUT OF STALL $\mu = 0.53$ $X/qd^2\sigma = 0.05$

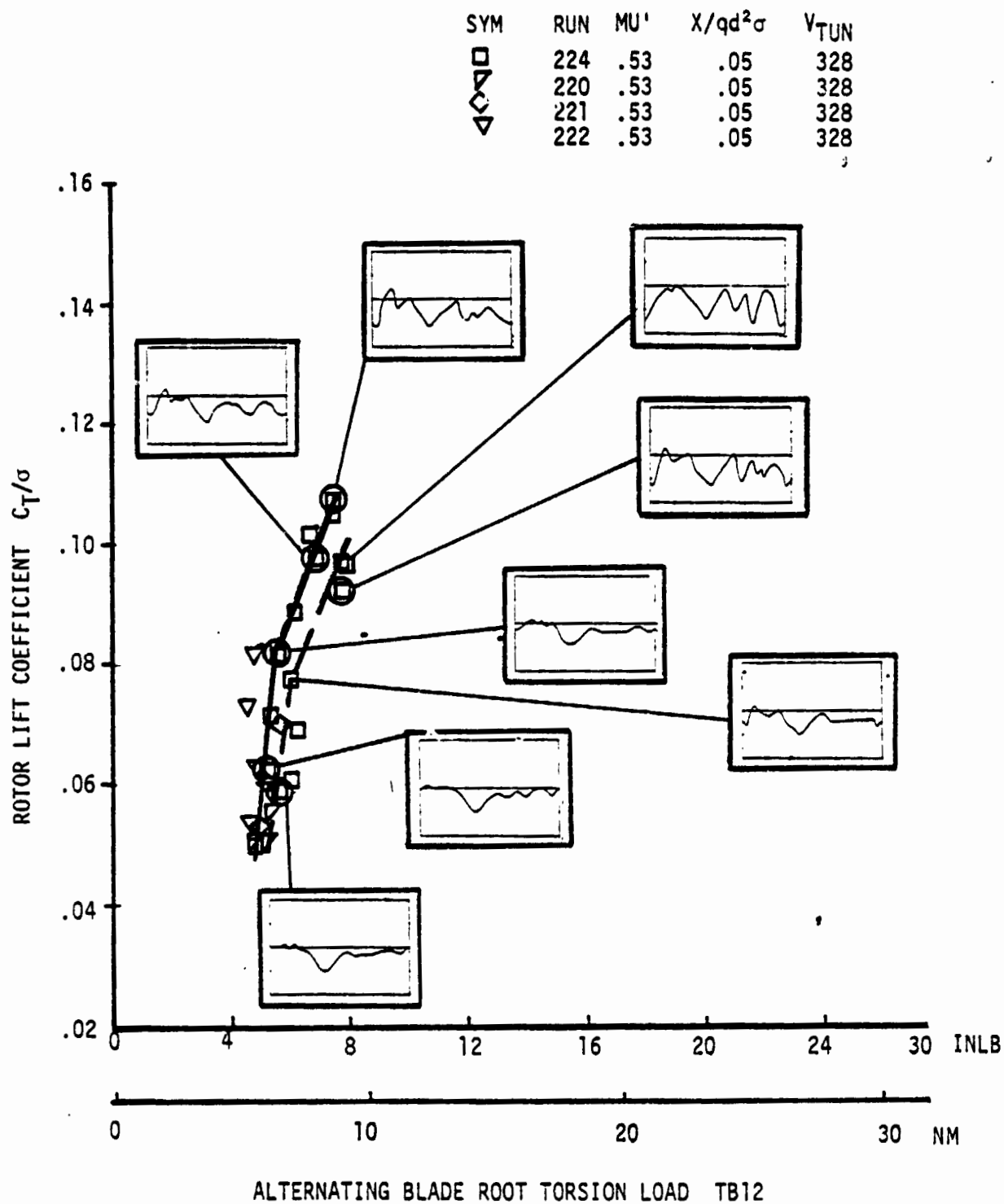


FIGURE 6.7.8 ALTERNATING BLADE ROOT TORSION LOADS WITH AND WITHOUT TIP STALL FOR SAME LIFT AND PROPULSIVE FORCE

ORIGINAL PAGE IS
OF POOR QUALITY

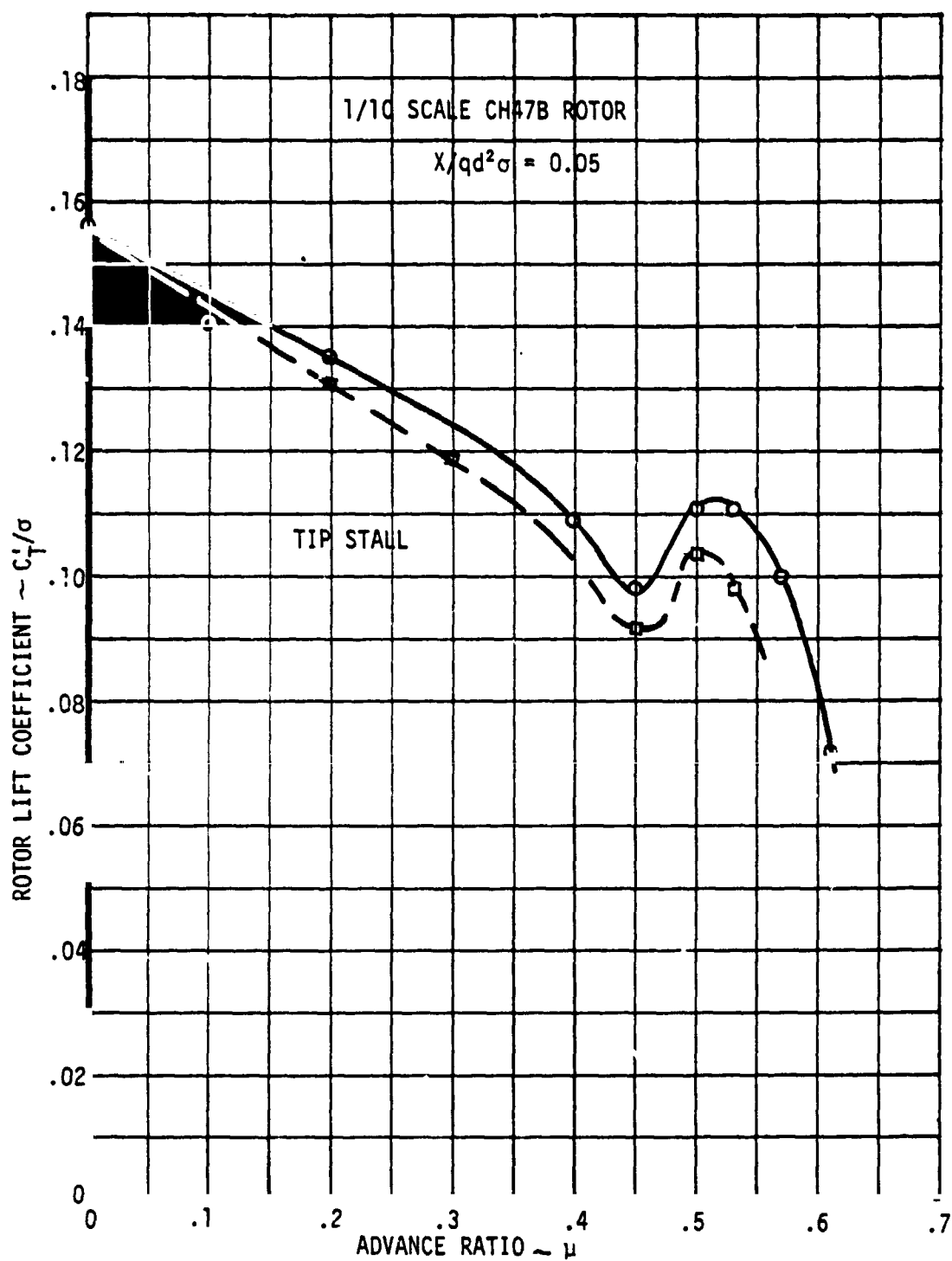


FIGURE 6.7.9 TIP STALL EFFECTS ON MAXIMUM LIFT LIMIT

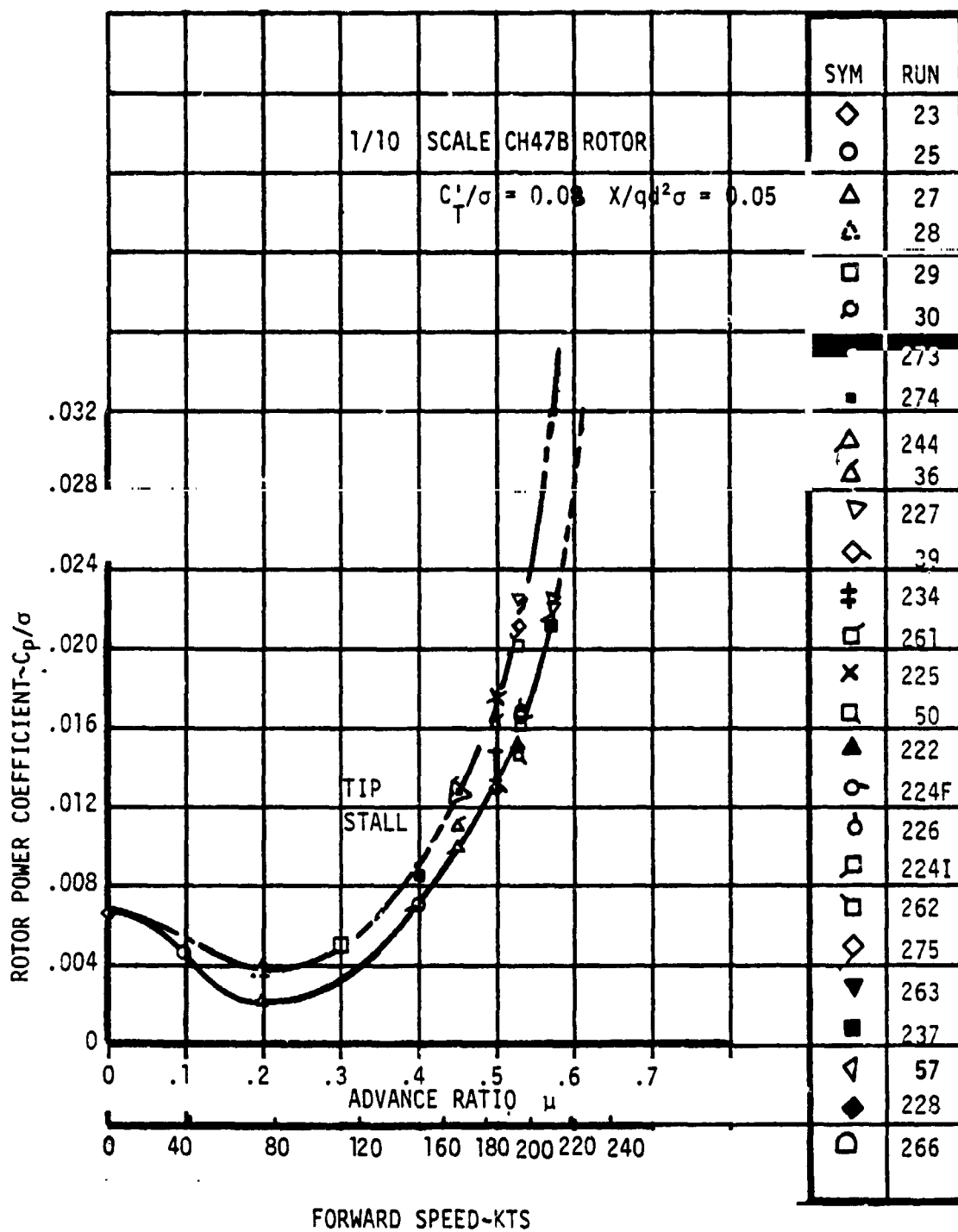


FIGURE 6.7.10 MODEL CONFIGURATION ROTOR POWER REQUIRED

6.8 Model Configuration Performance

The data presentations up to this point in the discussion has addressed maximum lift, maximum propulsive force or maximum effective lift to drag ratio; always defining the limit to the capability of the rotor system. It is equally important to define the capability for a fixed lift and propulsive force requirement to provide visibility on the characteristics of this rotor system. This would simulate the rotor under normal operation, not just the limits, and be representative of a model configuration. The definition of this configuration was as follows:

- o Reduced drag levels, representative of an advanced helicopter ($X/qd^2\sigma = 0.05$)
- o Normal operating lift ($C_T/\sigma = 0.08$), reduced from the full scale value of $C_T/\sigma = 0.10$ to allow for reduced capability resulting from Reynolds number
- o Normal operating tip speed 620 ft/sec

The performance for this configuration is presented in Figure 6.8.1 in terms of the rotor power coefficient variation with advance ratio. This is representative of the typical power required curve going from hover to high speed forward flight. Minimum power required occurs at $\mu = 0.20$, typical of a lighter condition with a power required 30 percent of the hover value. High speed cruise at an advance ratio of 0.57 has a power required four times greater than hover power. The performance shown here is for the model with all the external blade load instrumentation included.

To get an appreciation for the level of performance that is shown in Figure 6.8.1, the effective rotor lift to drag ratio was calculated and presented in Figure 6.8.2. A maximum L/D_E of 9.7 is achieved at an advance ratio of 0.28 which drops down and levels off at 4.5 between $\mu = 0.45$ to 0.53 and finally decreasing to 3.4 at $\mu = 0.57$. An estimate is made to correct for the external strain gages and wire bundles degrading the model rotor performance. This is presented by the dashed line in Figure 6.8.2 showing a maximum L/D_E of 13.5, reducing to approximately 6.5 between $\mu = 0.45$ and 0.53. At the highest speed tested for this lift level, $\mu = 0.57$, the effective rotor lift to drag ratio is approximately 4.5. No estimate has been made of the equivalent full scale performance. The lift limit and performance would be significantly affected by the increased maximum section lift characteristics of full scale, eliminating much of the stall influence inherent in the high speed model test data.

Figure 6.8.3 presents the rotor shaft angle of attack and rotor control positions associated with the performance characteristics of Figures 6.8.1 and 6.8.2.

Alternating blade root torsion loads consistent with the performance data just discussed, are presented in Figure 6.8.4. There is a gradual rise in loads up to an advance ratio of 0.35 where the load sensitivity with advance ratio becomes much greater. Beyond $\mu = 0.53$ the torsion load growth becomes almost asymptotic.

This trend in load resembles the load growth with lift at a fixed advance ratio:

- o Slight rise in alternating torsion loads up to the level where root stall occurs
- o Moderate increase in torsion loads in region influenced by root stall up to the level where the stall region expands to the outboard portion of the blade
- o Large increase in torsion loads resulting from both inboard and outboard stall

The discussion of the inboard and outboard stall mentioned here is discussed in depth in Sections 6.1 and 6.2. The influence of full scale airfoil section data would move the regions of inboard and outboard stall to a higher advance ratios and also result in a lower load growth with advance ratio between $\mu = 0.35$ and 0.53 .

These characteristics have been presented for a propulsive force level representing a judicious drag cleanup consistent with an advanced helicopter. What is the impact of not carrying out the drag clean up and what is the ultimate capability? Figure 6.8.5 presents typical power required performance in coefficient form for various propulsive force requirements. The solid line is for a propulsive force coefficient $X/qd^2\sigma$ of 0.05 which was presented in Figure 6.8.1. A propulsive force coefficient of 0.10

is representative of the drag levels of current helicopters. By incorporating the drag clean up from $X/qd^2\sigma = 0.10$ to 0.05 reduces the power required by 25 to 30 percent. This can have a sizeable impact on a vehicle, if a significantly smaller engine, transmission and drive train are required. The effect also results in a lighter hub, blades and control system. The combined weight savings from reduced power and reduced empty weight of the vehicle combine to provide a significant saving in fuel. With the cost of fuel increasing dramatically and energy conservation being carefully considered in the development of the next generation helicopter, drag reduction and cleanup becomes a very high priority effort.

Testing was performed for a propulsive force coefficient of 0.025 . This data is included here to indicate the impact of an additional 50 percent reduction from the advanced helicopter level. These three propulsive force levels provide the means of extrapolating to the ultimate capability-zero drag. Earlier in the discussion it was indicated that the drag reduction associated with the advanced helicopter ($X/qd^2\sigma = 0.05$) provided a 25 to 30 percent reduction in overall power required. This in itself is a significant improvement but when considering that it takes the configuration half way to the ultimate goal this adds a greater emphasis to the accomplishment of drag reduction.

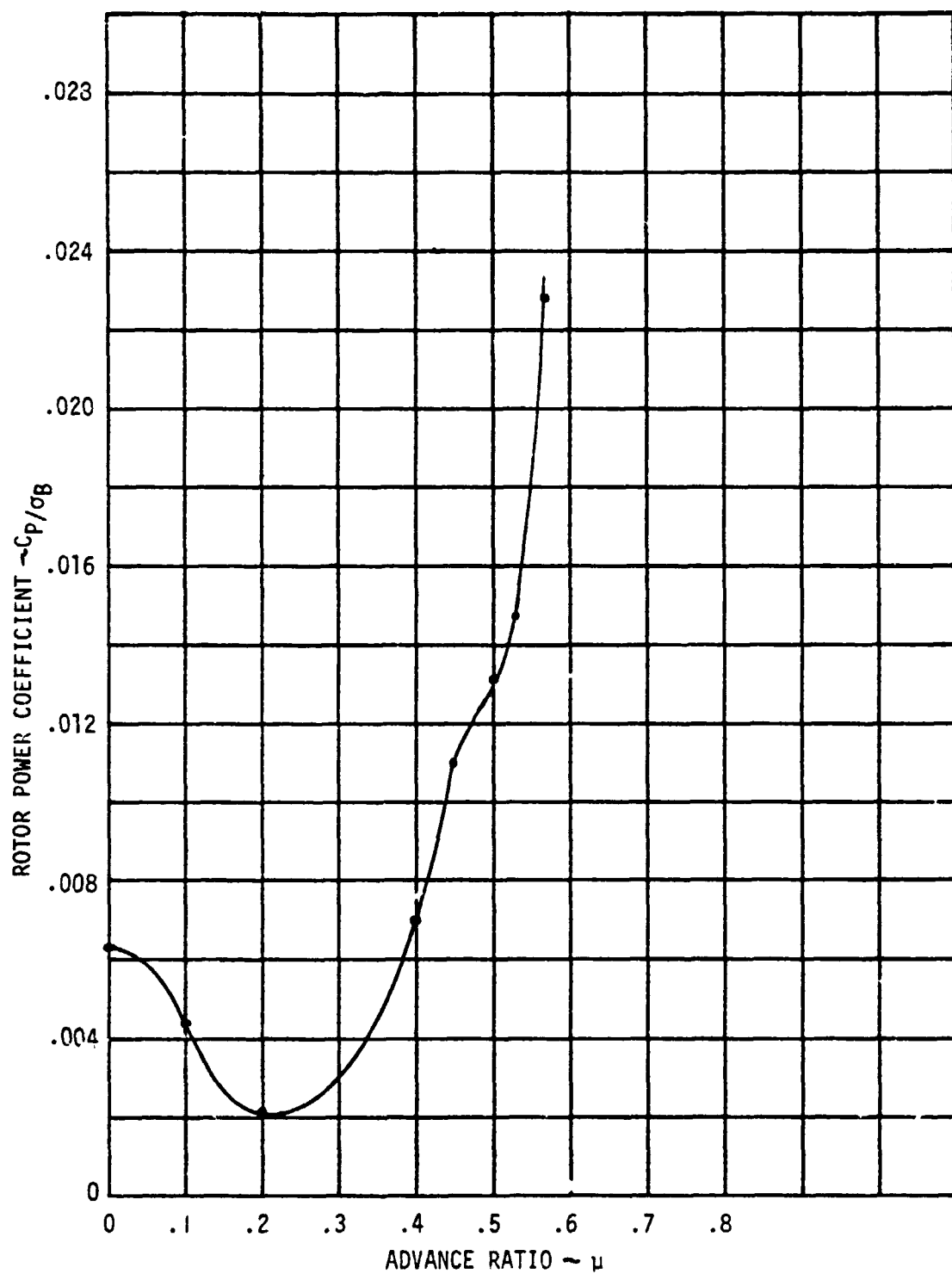


FIGURE 6.8.1 MODEL CONFIGURATION PERFORMANCE $C_T'/\sigma = 0.08$,
 $X/qd^2\sigma = 0.05$

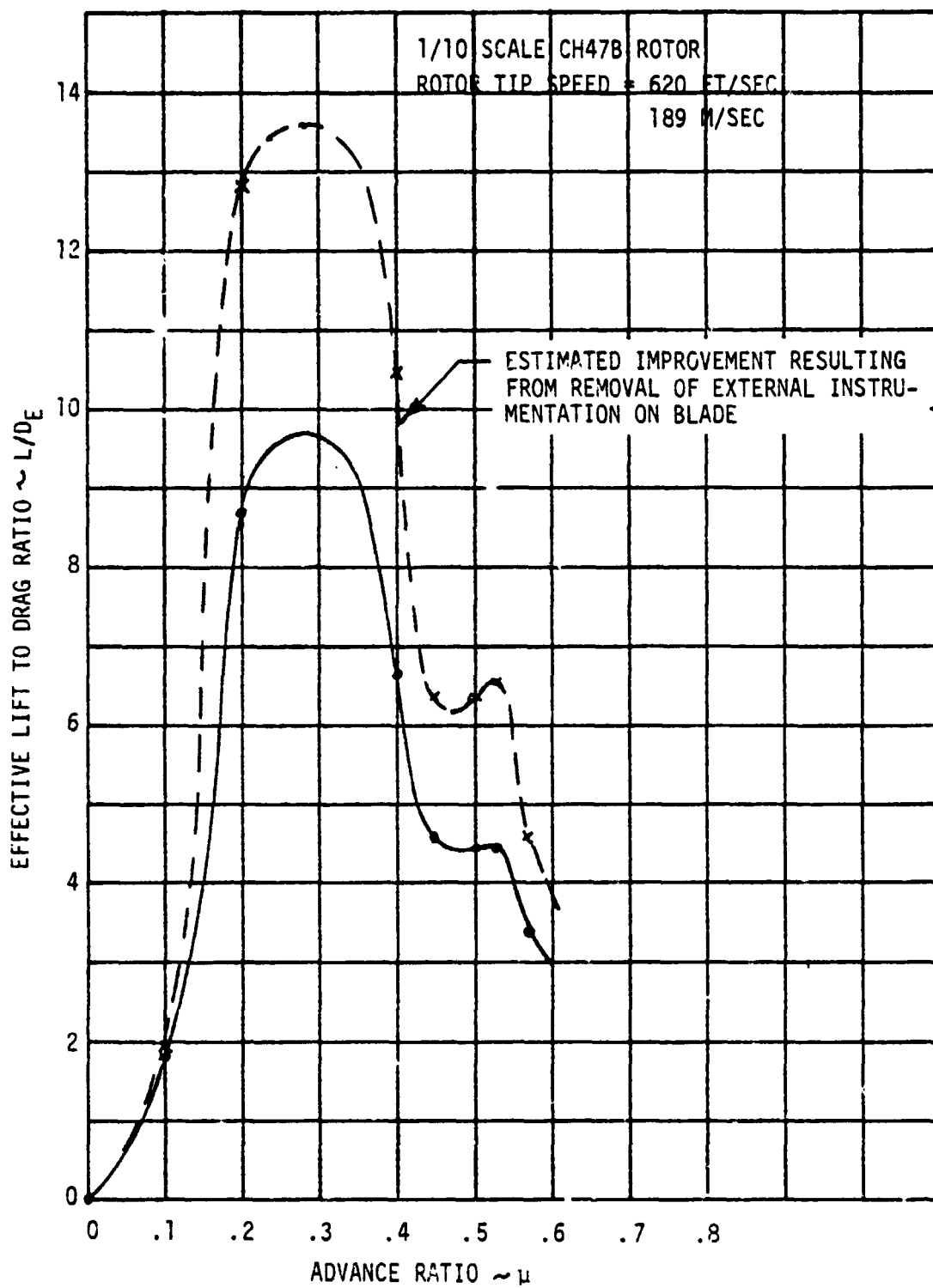


FIGURE 6.8.2 MODEL CONFIGURATION EFFECTIVE LIFT TO DRAG RATIO
 $C_T/\sigma = 0.08$; $X/qd^2\sigma = 0.05$

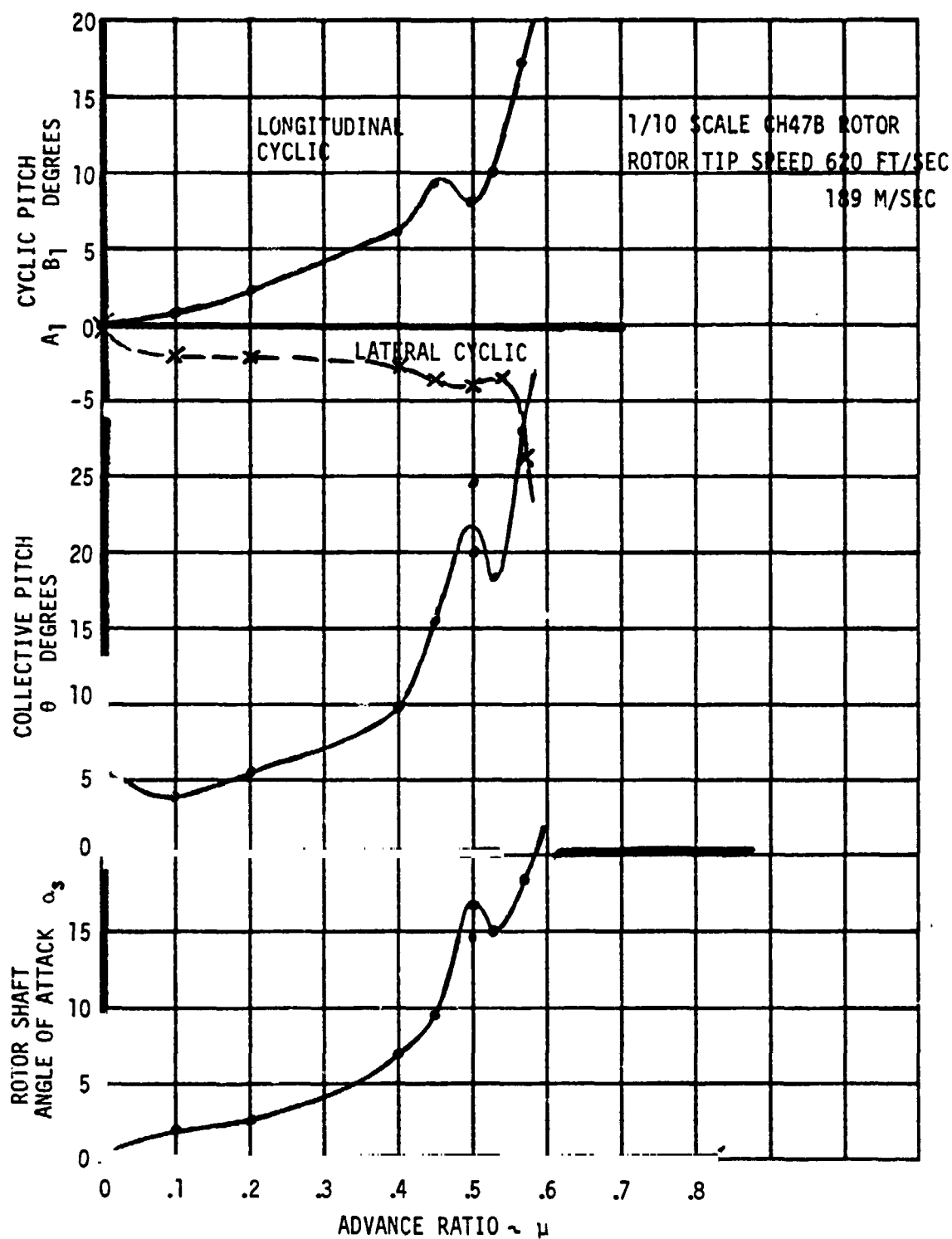


FIGURE 6.8.3 SHAFT ANGLE OF ATTACK AND CONTROL POSITIONS ASSOCIATED WITH MODEL CONFIGURATION PERFORMANCE $C_T/\sigma = 0.08$, $X/qd^2\sigma = 0.05$

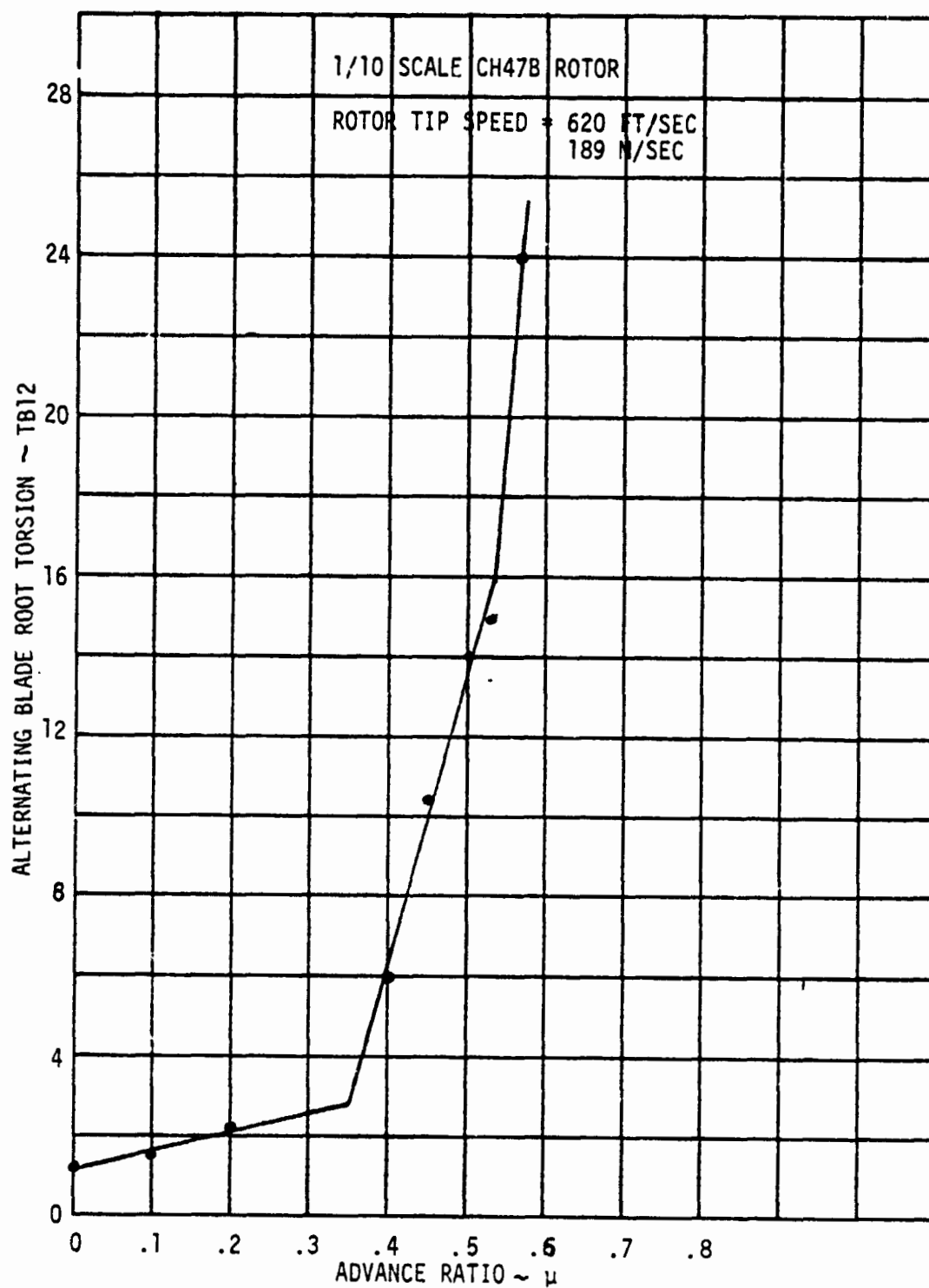


FIGURE 6.8.4 ALTERNATING BLADE ROOT TORSION LOADS FOR MODEL CONFIGURATION $C_T/\sigma = 0.08$, $X/qd^2\sigma = 0.05$

ORIGINAL PAGE IS
 OF POOR QUALITY

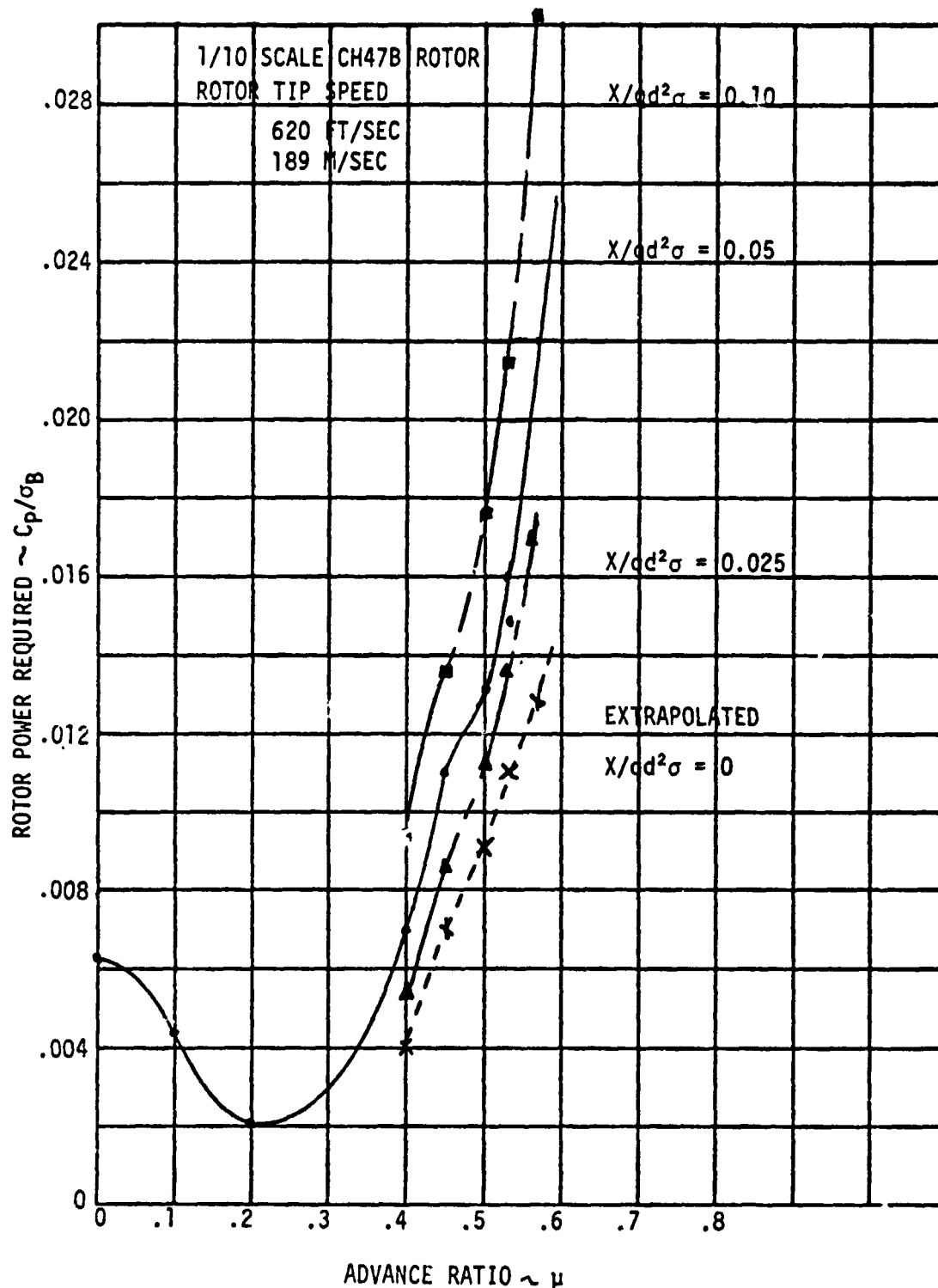


FIGURE 6.8.5 EFFECT OF PROPULSIVE REQUIREMENT ON MODEL CONFIGURATION PERFORMANCE, $C_T/\sigma = 0.08$

6.9 Correlation of Theory with Test Data

Wind tunnel model testing provides a means of defining the capability of a rotor system as well as determining the limits imposed on the operational flight envelope. Baseline data is obtained to guide the near term development of the rotor and this data also serves in the substantiation of the theoretical prediction methods over wider speed ranges or higher lift capabilities. Extending the substantiation of the methods to greater operating envelopes is required to provide an increased understanding of the rotor system. This improved methodology permits an efficient and effective development of the next generation rotor system that can achieve improved performance, lower loads and greater reliability. This test was no exception, it is in fact the type of test that can greatly advance the development of the technology prediction methods. The first step is to correlate the existing programs with the test data, determine where the differences exist, define the cause of the differences and then upgrade the methodology.

Three types of correlation have been performed in this test program.

- o Rotor performance predicted with a rapid preliminary design performance program
- o Rotor controls predicted with a helicopter trim program
- o Torsional loads predicted with a sophisticated aeroelastic rotor loads program

The rotor performance prediction program, SRIBR, was used in the first correlation effort to determine its adequacy. SRIBR is a rapid prediction method used primarily for preliminary design studies of various rotor configurations since it has numerous options and has a computational time of 10 to 15 seconds of machine time. SRIBR is a strip-theory analysis with an assumed tip loss and an induced velocity calculated as a function of the local loading to approximate the nonuniform downwash. The equations are written in the tip-path-plane which eliminates the requirement for iterating on blade flapping and the airfoil characteristics are approximated with a series of equations.

Since SRIBR, the rapid performance prediction program used in preliminary design, was substantiated at speeds of 250 knots to 350 knots for the eight foot diameter Reverse Velocity Rotor model, it could provide a useful analysis tool for use in the study of rotors but it was necessary to substantiate it at lower speeds. Testing of the high speed regime was accomplished in this wind tunnel program and provided model performance data of a conventional rotor at speeds up to 225 knots. A comparison of the predictions obtained from SRIBR was made with test data obtained at 110 knots, an advance ratio of 0.3, and at 195 knots, an advance ratio of 0.53. The results of these comparisons are shown in Figure 6.9.1 and indicate good correlation in this speed range, also. This prediction technique will serve useful in follow-on activities in the development of an advanced rotor concept.

The continued study of the conventional rotor experimental and theoretical data has provided additional understanding of the conventional rotor capabilities and characteristics at speeds of 150 to 250 knots. As part of this study, an examination of the requirements of the control system for flight in the high speed regime was made. Preliminary results are presented in Figure 6.9.2 showing the predicted collective pitch and longitudinal cyclic requirements for a full scale High Advance Ratio Propulsive rotor. Superimposed on this figure are the collective pitch and longitudinal cyclic obtained from the test data of Appendix A operating at the same lift/propulsive force requirements and flight speeds. The model data when compared to the full scale predictions indicate reasonable agreement.

For the prediction of torsional loads, C-60, the Aeroelastic Rotor Analysis is used since it normally provides the best prediction of the alternating loads.

The aeroelastic rotor analysis calculates rotor blade flapwise, chordwise and torsional deflections and loads as well as rotor performance, control system forces and vibratory hub loads. The analysis addresses a rotor in steady state flight with blades of arbitrary planform, twist and radial variation in airfoil section.

The analysis considers coupled flapwise-torsion deflections and uncoupled chordwise deflections of the rotor blades. The blade is represented by twenty (20) lumped masses, interconnected in series of elastic elements. Boundary conditions for either articulated or hingeless rotors are applied and the solution obtained by expanding the variables in a ten harmonic Fourier series.

Airload calculations include the effects of airfoil section geometry, compressibility, stall, 3-dimensional flow, unsteady aerodynamics and non-uniform inflow. Static airfoil tables are used to account for compressibility, static stall and airfoil shape. The unsteady aerodynamic loads are calculated by modifying the static loads resulting from the airfoil tables to include Theodorsen's shed wake function, dynamic stall effects based on oscillating airfoil data and yawed flow across the blade.

The non-uniform inflow calculations are based on a tip and root vortex trailed from each blade. Through an iterative technique, each trailed vortex is made compatible with the calculated blade lift distribution, and the lift distribution is compatible with the non-uniform downwash field. The vortex wake is assumed to be rigid and drift relative to the hub with a constant resultant velocity composed of thrust induced uniform downwash and the aircraft airspeed.

Since alternating blade root torsion load was monitored during the test as the best indicator of stall, it was selected as the load to be used in the correlation. To provide the best insight into the adequacy of this loads methodology, the prediction of the azimuthal variation in the torsional load at the blade midspan and root was made. Figure 6.9.3 presents the prediction of the midspan torsion wave form. The location of the stall load peaks occurring at rotor azimuth angles (ψ) of 280, 345 and 50 degrees are accurate but the correlation of the magnitude at each peak is only fair. There is a large nose download occurring at 150 and 240 degrees rotor azimuth typical of rotor stall which the analysis does not predict at all. The reason for this difference must be investigated further. Figure 6.9.4 presents the comparison of the predicted blade root torsion wave form with test data. The prediction of the azimuth for the nose up loads peaks as accurate but the magnitude is significantly different. Prediction of the large nose down peaks at $\psi = 165$ and 240 degrees was not accomplished. To determine the adequacy of the prediction of the loads predicted on the inboard portion of the blade, it is necessary to correct the predicted root torsion wave form for the inadequacy of the midspan prediction. This was accomplished in Figure 6.9.5 and the shape and magnitude between 15 to 140 degrees agrees moderately well but the level is low. Between $\psi = 180$ through 360 the agreement in the azimuthal location is good but the predicted magnitude is extremely low at 280 degrees. Further analysis must be performed to understand the cause for these differences.

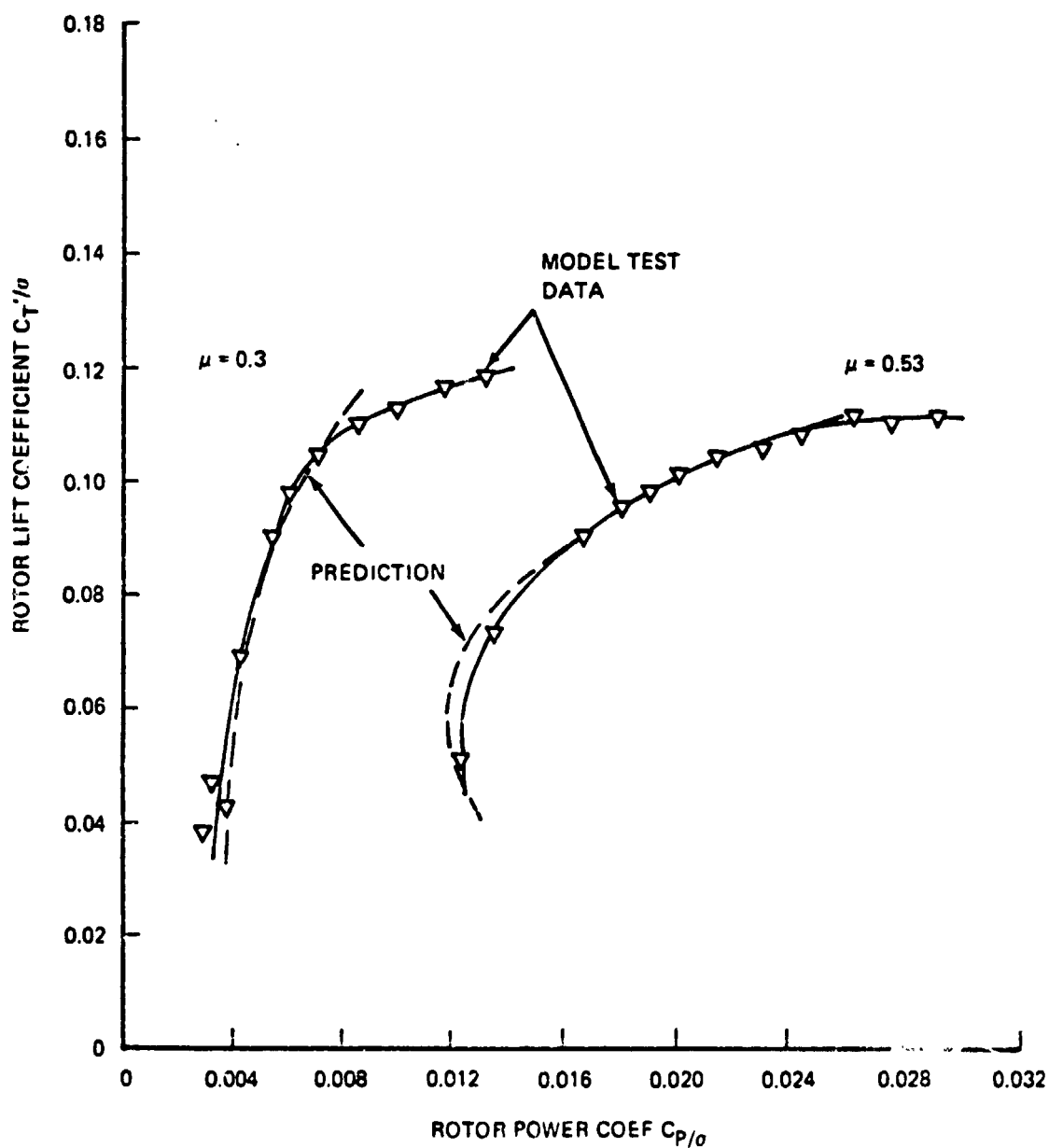


FIGURE 6.9.1 COMPARISON OF PREDICTED ROTOR PERFORMANCE WITH TEST DATA FOR CONVENTIONAL ROTOR USING SRIBR PROGRAM

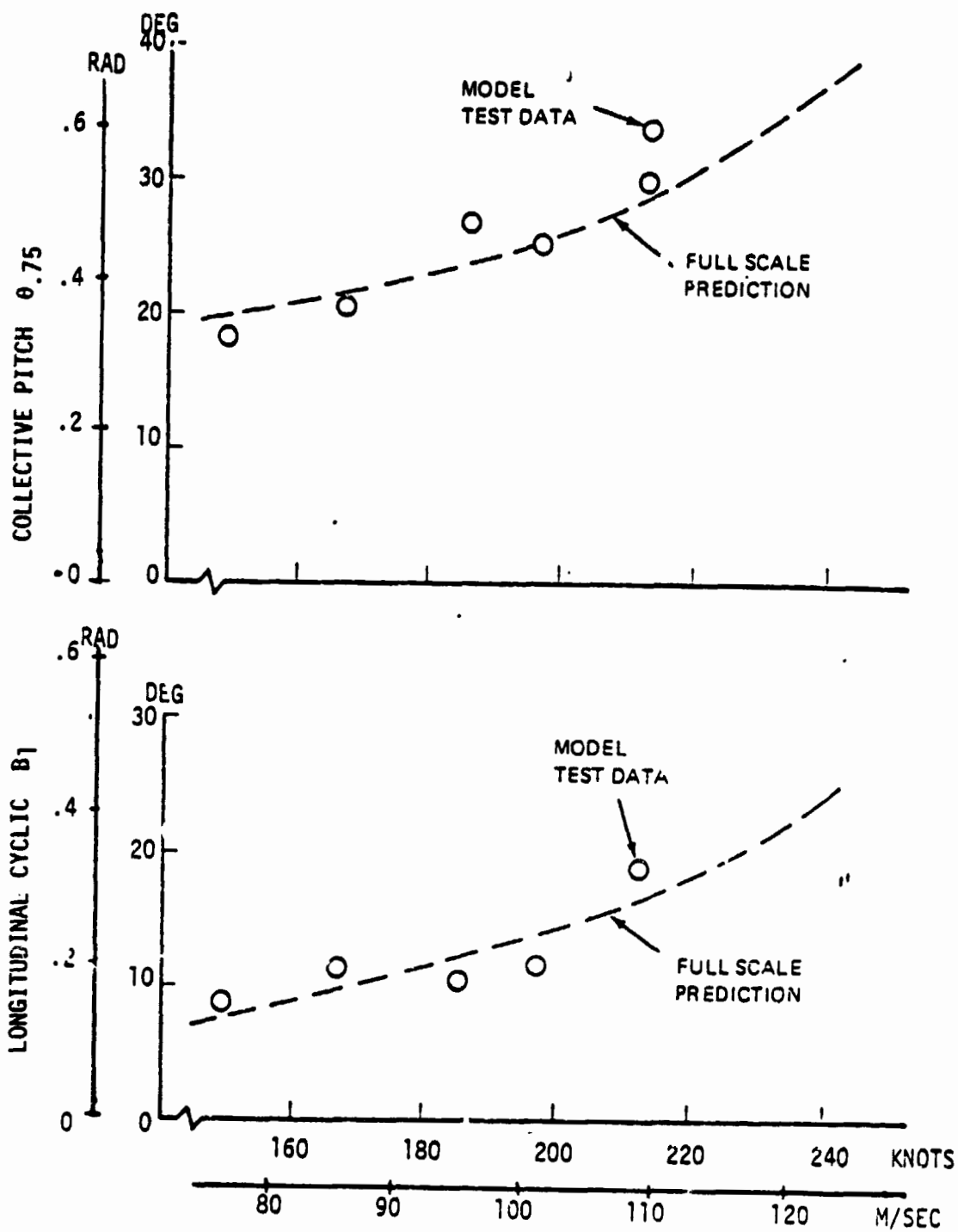


FIGURE 6.9.2 COMPARISON OF FULL SCALE ROTOR CONTROL POSITION PREDICTION WITH MODEL TEST DATA

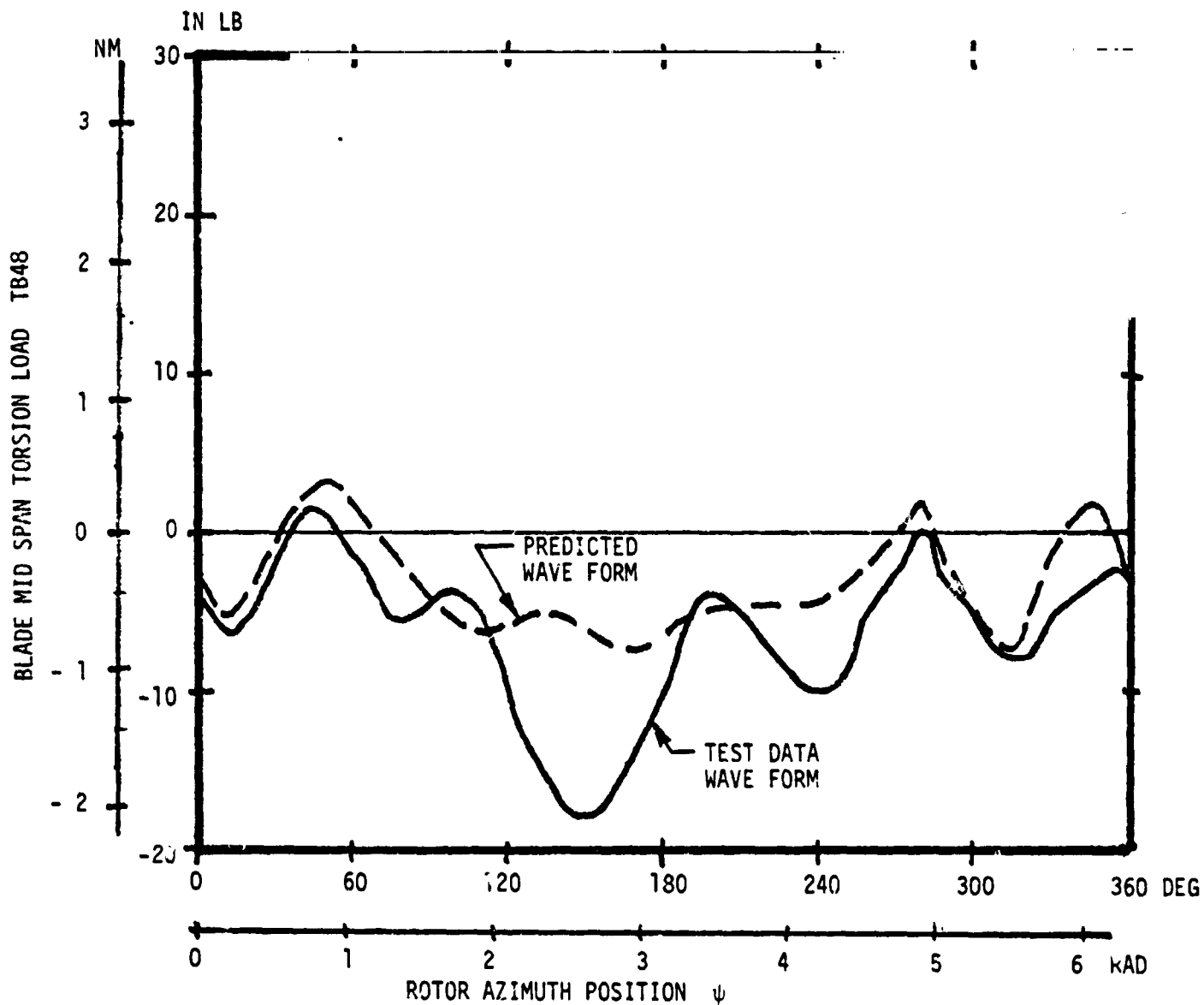


FIGURE 6.9.3 COMPARISON OF MID SPAN TORSION PREDICTION WITH
TEST DATA $\mu = .53$; $C_T/\sigma = 0.08$; $X/qd^2\sigma = 0.05$

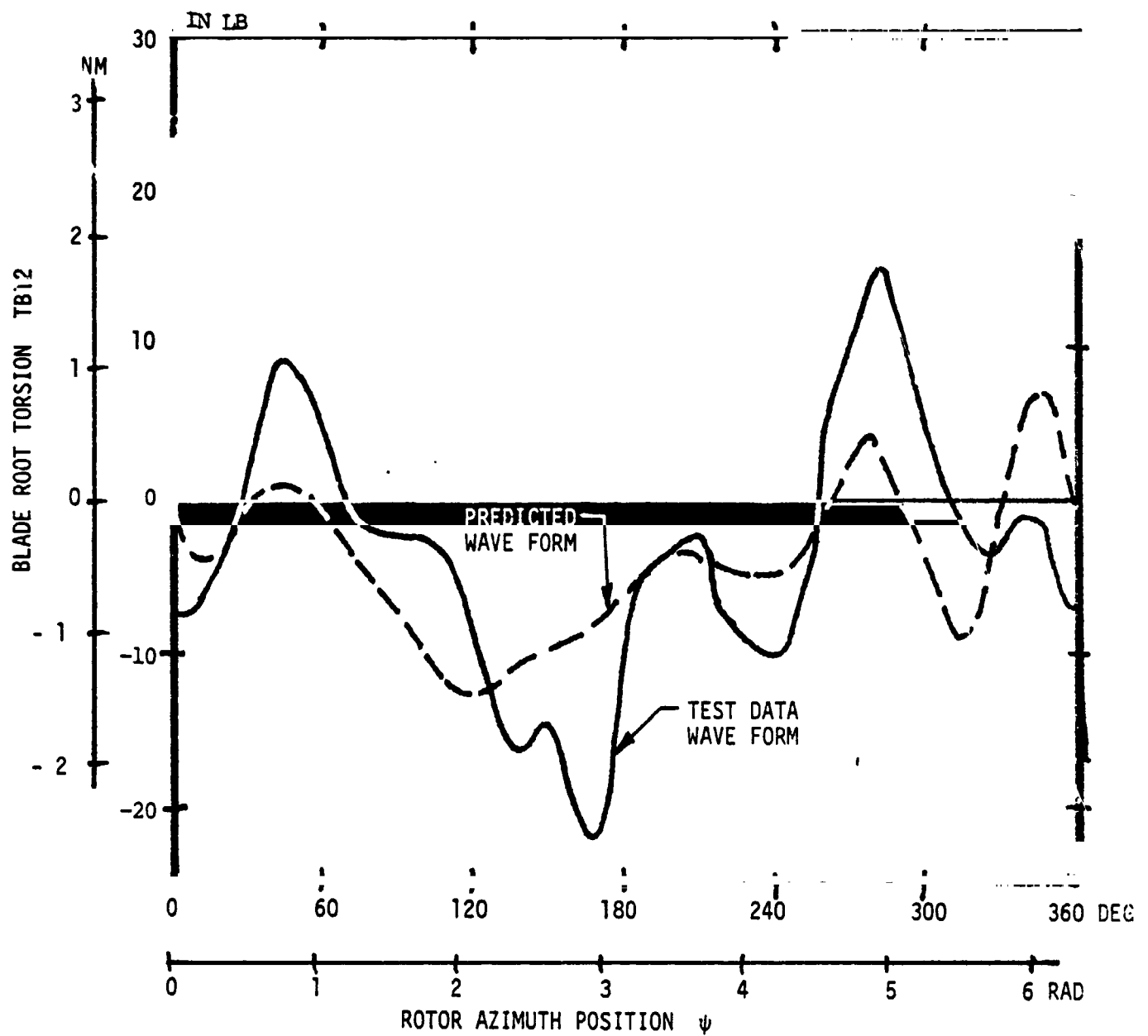


FIGURE 6.9.4 COMPARISON OF ROOT TORSION PREDICTION WITH TEST DATA
 $\mu = 0.53$; $C_T/\sigma = 0.08$; $X/qd^2\sigma = 0.05$

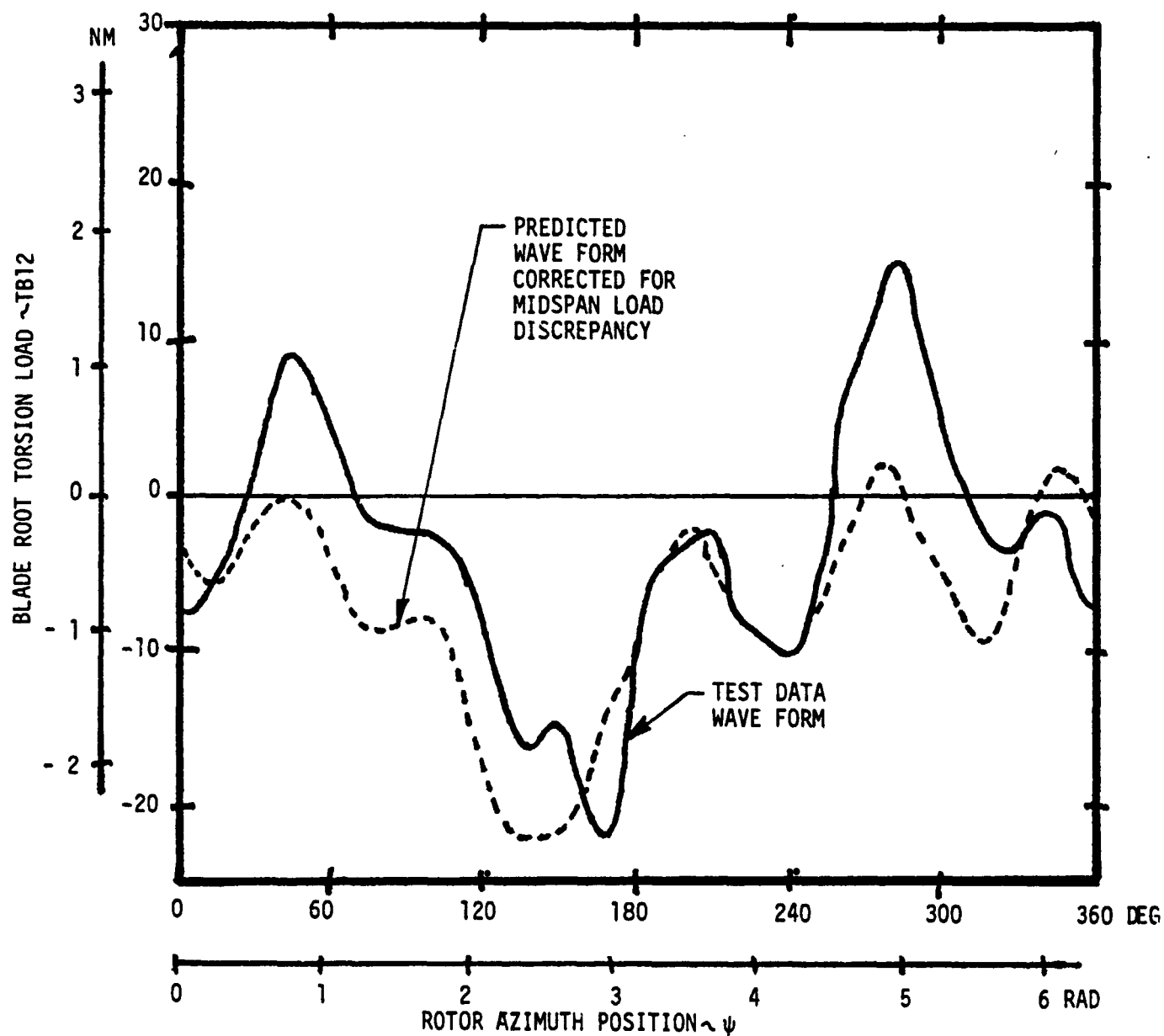


FIGURE 6.9.5 COMPARISON OF ROOT TORSION PREDICTION WITH TEST DATA-PREDICTION
CORRECTED FOR MID SPAN LOAD DISCREPANCY
 $\mu = 0.53$ $C_T/\sigma = 0.08$ $X/qd^2\sigma = 0.05$

6.10 Effect of Torsional Stiffness on High Advance Ratio Characteristics

At the end of the first portion of the test program, one lift limit test data run was performed at an advance ratio of 0.57 with a set of rotor blades that are geometrically the same but the torsional stiffness is reduced by approximately 45 percent. The basic test data is included in Appendix E of Volume 3 and a limited discussion of the major results and comparisons are included in this section. This testing was not required by the basic contract but is included here because of its implications on future rotor development.

Before presenting the performance and loads data it is necessary to establish the blade frequency trends with RPM to insure that there are no critical resonances at the operating conditions. The frequency spectrum for the model rotor blade that had a low torsional stiffness, as shown in Figure 6.10.1, was obtained from an RPM sweep at an advance ratio of 0.30 at a rotor lift coefficient of 0.06. The first torsion is at a frequency ratio of 4.4 at the normal operating tip speed of 620 ft/sec. There are no resonant frequency crossings near the normal operating speed of 2005 RPM.

As described in Section 6.1 the lift limit testing was accomplished with a sweep in rotor lift at a fixed propulsive force level of $X/qd^2\sigma = 0.05$. Figure 6.10.2 presents the rotor performance obtained during this lift limit test run at an advance

ratio of 0.57. The rotor performance obtained with the standard blade is compared with this torsionally soft blade which requires .0018 to .0014 less rotor power coefficient (C_P/σ_B) up to a rotor lift coefficient of 0.082. Beyond this lift level the rotor power required for the soft GJ blade increases very rapidly indicating stall and becomes the same as the standard blade. The maximum lift measured for the soft GJ blade is 0.086, the standard blade has reached a C_T'/σ of 0.094 and has not reached a maximum. Effective rotor drag variation with rotor lift is presented in Figure 6.10.3 and shows a difference of $\Delta C_{D_E}/\sigma_B = .0040$. The soft GJ blade was instrumented out of 55 percent of the radius but the standard blade was instrumented out to 80 percent and could account for this difference in C_{D_E}/σ_B . The maximum effective rotor lift to drag ratio is approximately 3.2 for the soft GJ blade and 2.9 for the standard blade not correcting for the difference in external instrumentation. A comparison of the alternating blade root torsion loads are presented in Figure 6.10.4. They both have approximately the same load at $C_T'/\sigma = 0.05$ but the load growth on the soft GJ blade is larger and becoming 20 percent higher at $C_T'/\sigma = 0.082$. Superimposed on this figure are wave forms for four lift levels. The lowest lift levels show similar wave forms but the steady is different and there is a negative stall at 30 degrees azimuth (ψ) and conventional or positive stall occurring at $\psi = 150$ and 240 degrees for the soft blade but not the standard blade. The same trend in the wave forms exist at $C_T'/\sigma = 0.069$. At a rotor lift

coefficient of 0.082 the only difference in wave forms is a larger steady load and a negative stall peak at $\psi = 230$ degrees for the soft blade.

The wave forms for the highest rotor lift coefficient trends are similar to those at $C_T/\sigma = 0.082$ but the magnitudes are larger. These loads and wave forms indicate that the blade winds up more causing higher alternating loads. There is very little difference in the effective lift drag ratio and the lift limit is reduced by at least 10 percent.

Further study of these results are required to understand where the increased loads are coming from and where the stall occurs. This is required to better understand the impact of torsional stiffness on the blade loads, to establish a method of defining rotor blades that will minimize loads and maximize performance.

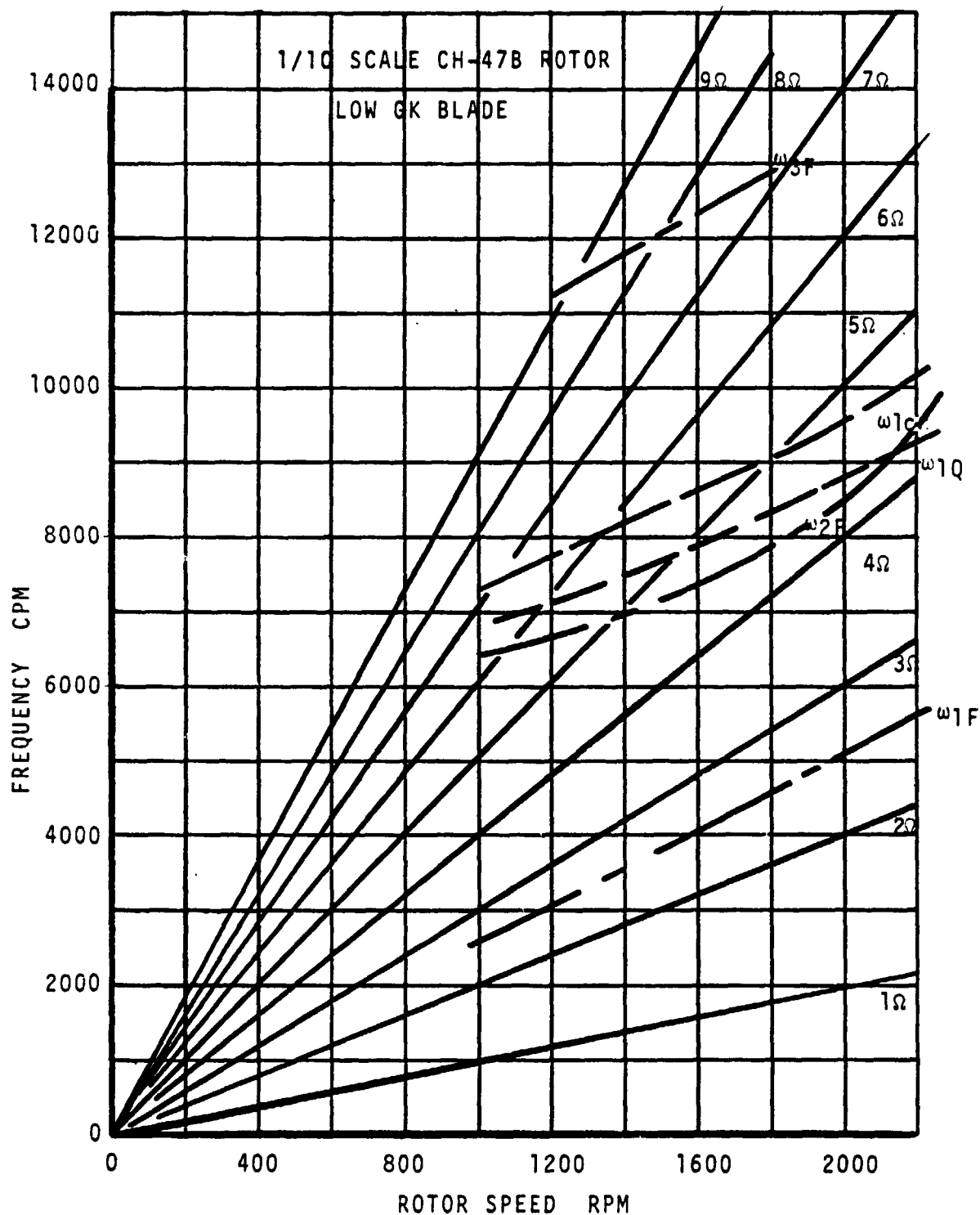


FIGURE 6.10.1 FREQUENCY SPECTRUM FOR TORSIONALLY SOFT BLADE

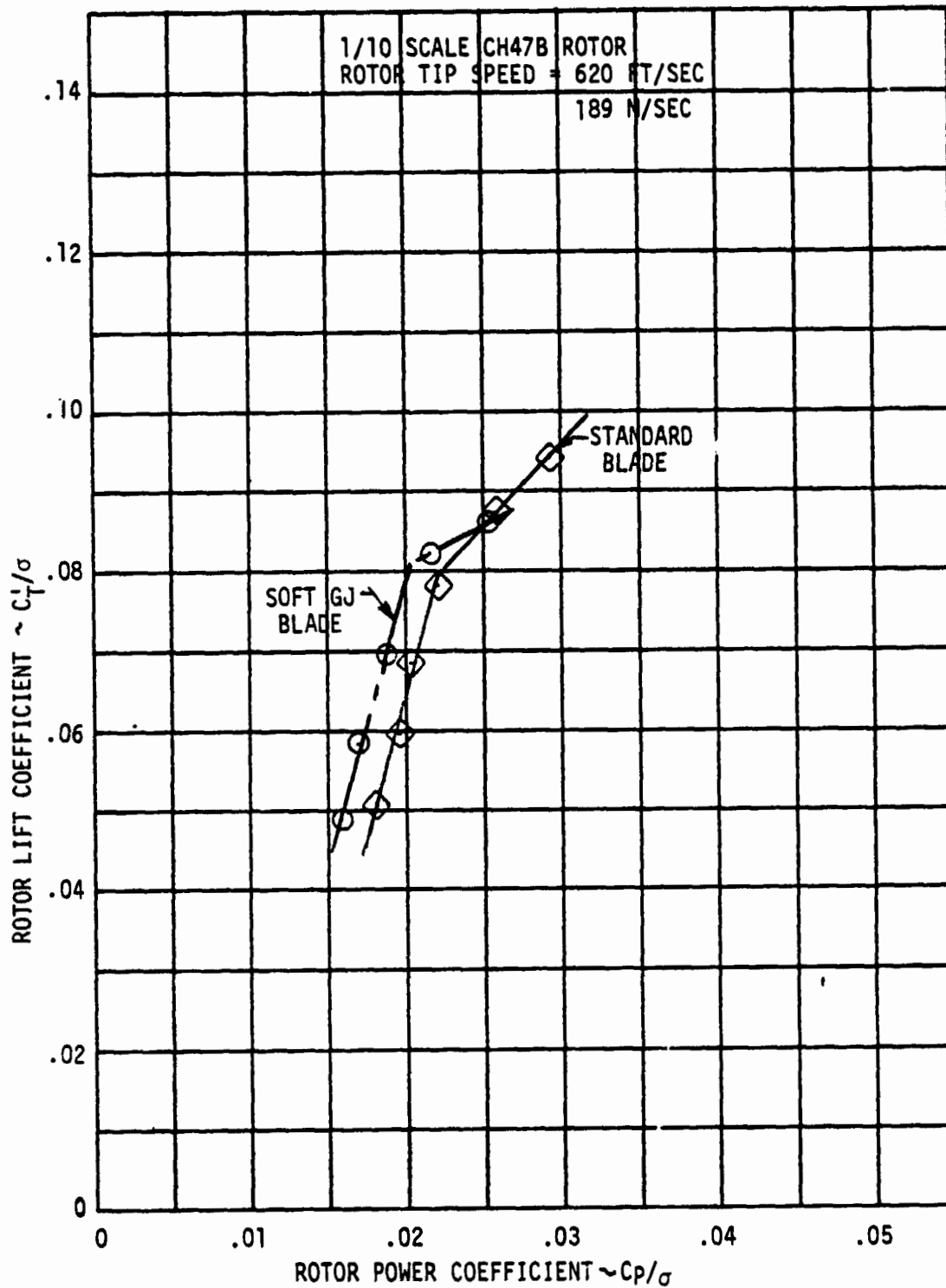


FIGURE 6.10.2 EFFECT OF TORSIONAL STIFFNESS ON ROTOR POWER
 $\mu = 0.57$ $X/qd^2\sigma = 0.05$

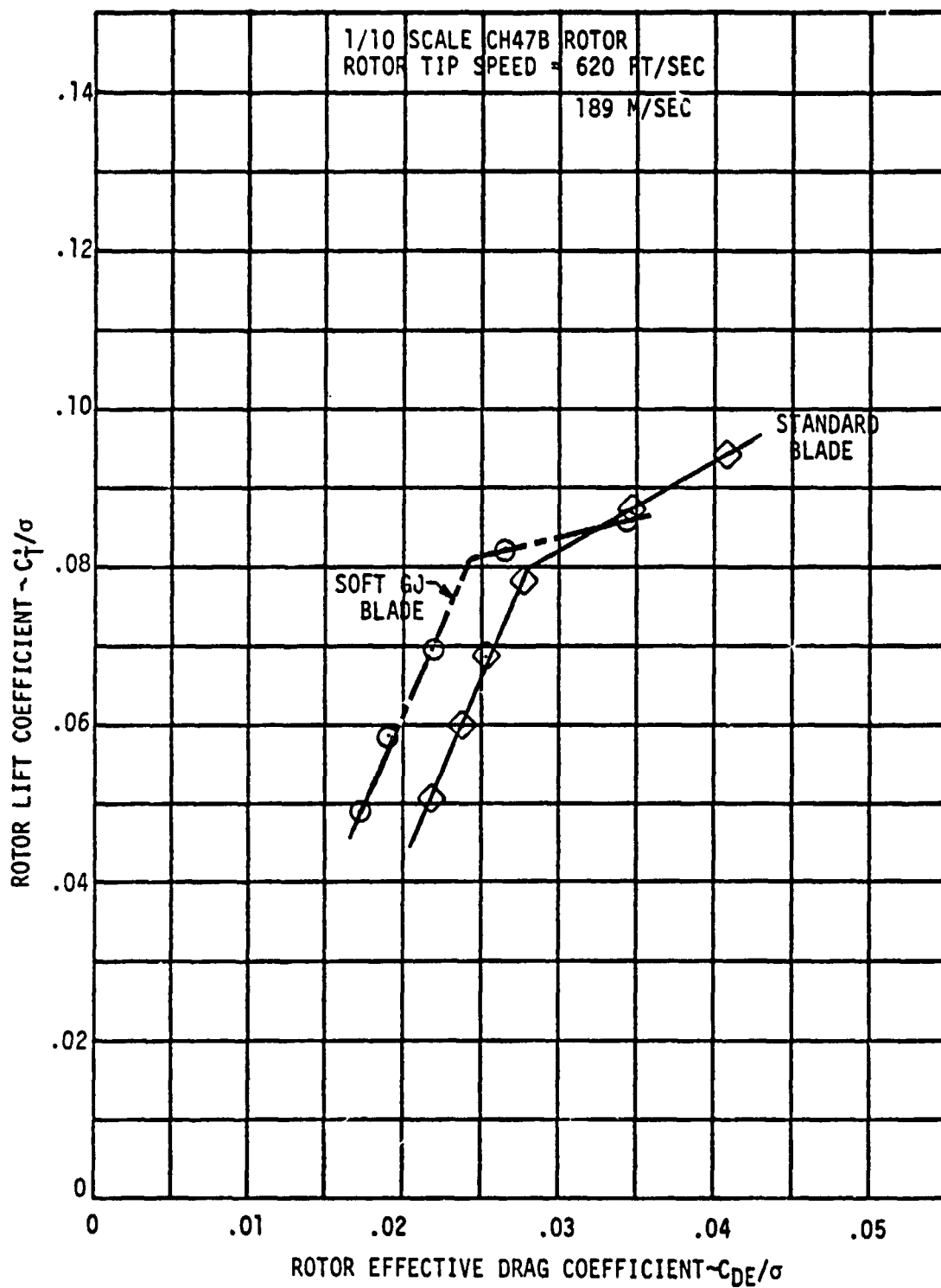


FIGURE 6.10.3 EFFECT OF TORSIONAL STIFFNESS ON ROTOR EFFECTIVE
DRAG $\mu = 0.57$ $X/qd^2\sigma = 0.05$

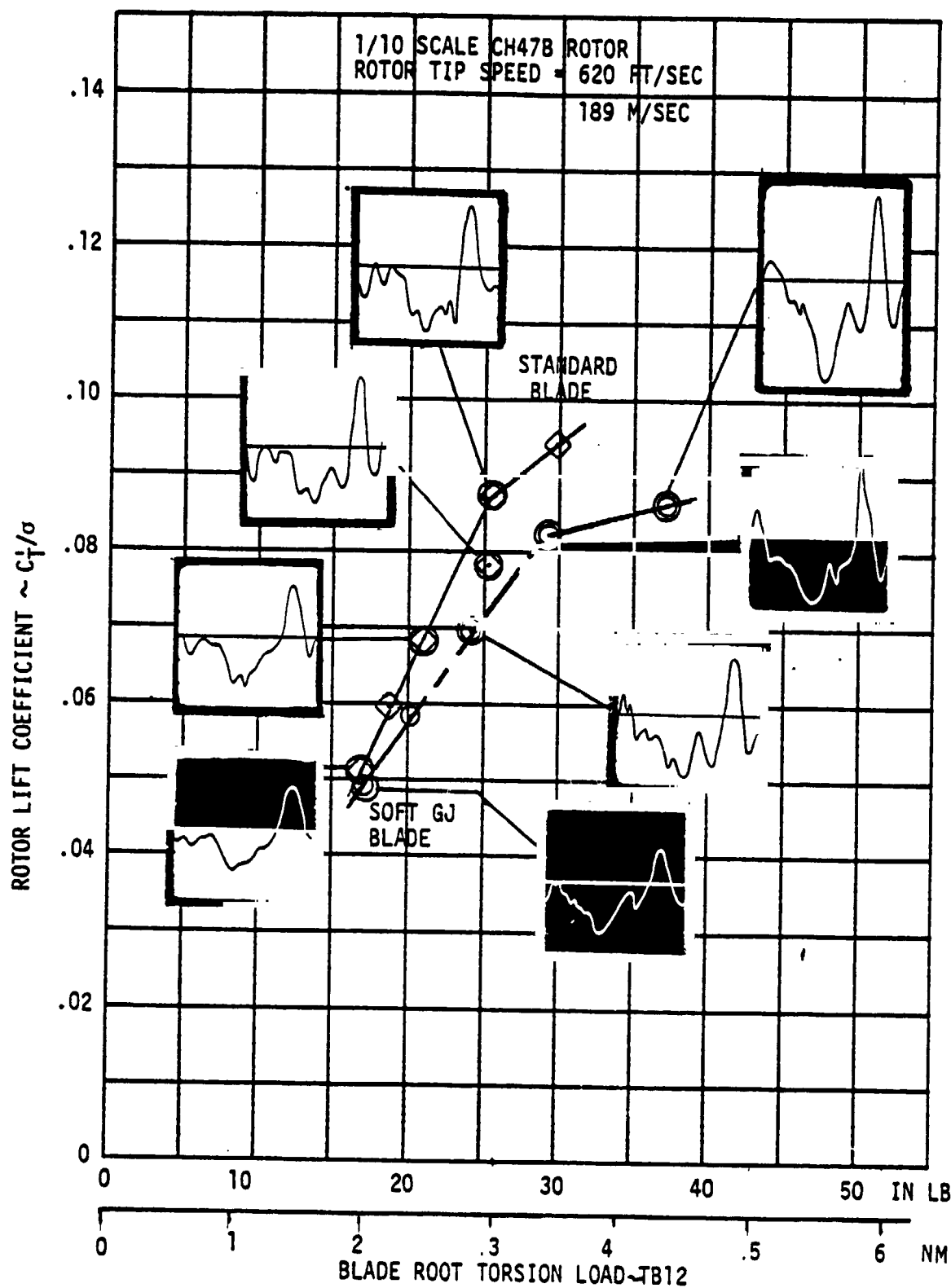


FIGURE 6.10.4 EFFECT OF TORSIONAL STIFFNESS ON BLADE ROOT
 TORSION LOAD $\mu = 0.57$ $X/qd^2\sigma = 0.05$

7.0 CONCLUSIONS

The overall objective of the Lift-Propulsive Force Limit Test Program was to conduct a wind tunnel investigation of a conventional helicopter rotor to determine the performance characteristics and limitations in high speed forward flight. In addressing this program objective and the specific test objectives with the test data analysis contained herein, the overall conclusion formulated is:

The conventional rotor can operate in high speed forward flight at useful levels of lift without auxiliary lift or auxiliary propulsion.

Operation of this six foot diameter rotor has been demonstrated at a rotor lift coefficient of 0.10 at 210 knots or at a reduced rotor lift coefficient of 0.08 up to 225 knots. This has been accomplished while operating at an equivalent flat plate drag area loading (GW/ft²) of 1500 LB/FT², compatible with an advanced helicopter level of drag cleanup.

Analysis of the individual test objectives has produced specific conclusions and they are listed below:

1. The maximum lift limit is defined by the aerodynamic capability of the rotor because increasing collective pitch produced no further increase in lift at the desired propulsive force level.

2. The maximum propulsive force developed by the model was limited by a model physical limit - the lag stops.
3. Propulsive force limit testing provided data that indicated the conventional rotor, even when operating at the advance ratio where the propulsive efficiency was the poorest, achieved 85 percent efficiency which is comparable to a propeller near its maximum efficiency.
4. There was a rapid rise in alternating blade root torsion load as the lift limit was approached resulting from inboard stall. At the lift limit, the load growth became almost asymptotic as a result of the mid and outboard blade stall combined with the inboard stall.
5. Measured rotor performance indicated a maximum effective lift to drag ratio of 9 was achieved at an advance ratio of 0.28 decreasing to 4.0 at 195 knots ($\mu = 0.53$). Estimating a correction for the external load instrumentation improves the capability to an effective lift to drag ratio of 13.5 and 7.0 for the same conditions.

6. There is no degradation in control power u_c to 90 percent of the maximum lift for advance ratios of 0.20 to 0.53.
7. Reducing advancing tip Mach number through reduced tip speed provided an increase in lift limits below $\mu = 0.50$ and above 0.60. Between $\mu = 0.50$ and 0.60 the lift limit is reduced by an increment in rotor lift $\Delta C_T^1/\sigma = 0.01$
8. Blade flapping response to step inputs in cyclic pitch appeared to be stable.
9. There are two distinct sets of operating conditions for the same lift and propulsive force requirements. One set of operating conditions has tip stall evident at lift levels as low as $C_T^1/\sigma = 0.06$.
10. An examination of the performance characteristics for a model configuration operating at a rotor lift coefficient of 0.08 operating at various propulsive force requirements indicated that a drag clean up from the current level ($X/qd^2\sigma = 0.10$) to that of an advanced helicopter ($X/qd^2\sigma = 0.05$) reduced the total power required by 25 to 30 percent.

11. A limited amount of test data was obtained at $\mu = 0.57$ on a rotor blade that was geometrically similar but with a torsional stiffness reduced by 45 percent. The rotor lift limit was reduced to $C'_T/\sigma = 0.086$ from approximately 0.10 and the alternating blade root torsion load sensitivity was significantly increased f . the soft GJ blade.

8.0 RECOMMENDATIONS

The data analysis trends developed and the conclusions summarized in Section 7.0 indicate that the conventional rotor can operate at useful levels of lift in the high speed without auxiliary lift or auxiliary propulsion. The analysis covered a wide range of subjects with a moderate amount of depth. There are a number of areas in the data analysis that a result is produced and the cause has not been completely identified. These areas require additional analysis directed at the following questions or tasks:

1. Can an improved blade load correlation be achieved for torsion? Also, what is the correlation of flap and chord bending?
2. Does reverse flow provide some relief in the lift distribution between $\mu = 0.45$ and 0.53 ?
3. For the basic tip speed operation, is the cause of the rapid drop in lift limit beyond an advance ratio of 0.53 driven by positive or negative stall?
4. Is the cause of the moderate rise in alternating blade torsion loads above $C_T^1/\sigma = 0.09$ a result of inboard stall? Does the nearly asymptotic use in torsion loads depend primarily on the mid and outboard stall or inboard stall?

5. Define the major areas producing lift and propulsive force with theory and compare with the qualitative lift distribution generated from the torsion and flap bending loads.
6. Is the improvement in lift limit below $\mu = 0.50$ and above 0.60, for reduced tip speed operation, an aerodynamic or an aeroelastic phenomena?
7. Is the reduction in lift limit between $\mu = 0.50$ and 0.60 an aerodynamic or an aeroelastic phenomena?
8. Does the reduced tip speed operation provide an improvement in performance at all advance ratios between 0.40 and 0.64?
9. What is the improvement in rotor lift limit achieved by the full scale rotor system?
10. Does the increased load growth demonstrated for the blade with reduced torsional stiffness result from increased blade wind up?

The major recommendation to be made is that additional data reduction and correlation of theory with test data must be performed. From this effort a better understanding of the rotor behavior in high speed can be developed. This can

provide a basis for expanding the operational capability of the conventional rotor and serve to guide the development of the next generation helicopter.

The next logical step is to develop a rotor system that reduces the impact of stall in high speed to improve the cruise efficiency and also integrates the geometric or structural requirements for improved hover capability. Having then defined a rotor that will achieve this, build and test it to verify the predicted characteristics or define the deficiencies in the technology and determine the modifications required to achieve the improved rotor system.